UNIVERSIDADE D
COIMBRA

João Rafael Cardoso de Brito Oliveira Abrantes

INFRARED THERMOGRAPHY AS A GROUND-BASED SENSING TOOL TO ASSESS SURFACE HYDROLOGIC PROCESSESS

Doctoral Thesis in Civil Engineering, in the scientific area of Hydraulics, Water Resources and Environment, supervised by Professor João Luís Mendes Pedroso de Lima and Professor Abelardo Antônio de Assunção Montenegro (UFRPE, Brazil), and submitted to the Department of Civil Engineering of the Faculty of Sciences and Technology of the University of Coimbra.

August 2019

Faculty of Sciences and Technology of the University of Coimbra
Department of Civil Engineering

INFRARED THERMOGRAPHY AS A GROUND-BASED SENSING TOOL TO ASSESS SURFACE HYDROLOGIC PROCESSES

João Rafael Cardoso de Brito Oliveira Abrantes

Doctoral Thesis in Civil Engineering, in the scientific area of Hydraulics, Water Resources and Environment, supervised by Professor João Luís Mendes Pedroso de Lima and Professor Abelardo Antônio de Assunção Montenegro (UFRPE, Brazil), and submitted to the Department of Civil Engineering of the Faculty of Sciences and Technology of the University of Coimbra.

August 2019

UNIVERSIDADE D
COIMBRA

Dedicated to the persons I love the most in this world:
my grandmother ***Fernanda***
my parents ***Cristina*** *and* ***Manel***
my sister ***Mariana***
my brother ***Tomás***

"The foolish man seeks happiness in the distance, the wise grows it under his feet."

- James Oppenheim

"There will come a time when you believe everything is finished. That will be the beginning."

- Louis L'Amour

ACKNOWLEDGEMENTS

I would like to express my gratitude and respect to my supervisors, without whom this Thesis would not have been possible. To Professor João Pedroso de Lima, whose creativity, imagination and inventiveness fostered my interest in scientific research. Professor João directly contributed to my success, by acknowledging my capacities, investing his time and resources in me, providing the so needed availability, patience, guidance and support whenever required and by transmitting to me his immense knowledge and insatiable thirst for science. To Professor Abelardo Montenegro, who believed in me and gave me the opportunity to work alongside him after completing my master's degree. For sure, that was a crucial moment that defined the following years. Professor Abelardo whose cooperation, knowledge and advises contributed to this Thesis and my, still short, research career. Thank you very much Professors for the supervision, but, above all, for the friendship.

I am thankful for the positive environment comprised of professors, researchers and colleagues that was indispensable to the fulfilment of this Thesis. To Professor Isabel Pedroso de Lima, Doctor Jacob Keizer, Professor Alexandre Silveira, Professor Rodrigo Moruzzi, Professor Nuno Simões and Professor Jorge Isidoro, for their expertise, cooperation and motivation throughout these years. To Raquel, Valdemir, Sérgio and Iraê for their help in the laboratory experiments. To Babar, Cleene, Isabela, Marcelle, Mousinho and Nazmul for their company and fun moments in the laboratory. To the laboratory technician Mr. Joaquim Cordeiro, for his suggestions, creativity and talent during the design and construction of some installations used in the experiments. Also, thanks for the pearls of wisdom learned during our lively talks.

To my closer friends (you know who you are) for the trusty words during the not so good times, the so much needed leisure and fun moments and, above all, the endless long-time friendship.

Last but not least, I would like to express my eternal love and gratitude to my family for their unconditional care, dedication and support expressed all over my life. To my grandmother Fernanda for all the affection and tenderness, to my parents Cristina and Manel for all the sacrifices they made to give me everything I could ask for, to my siblings Mariana and Tomás for their friendship and for instilling in me an almost paternal sense of responsibility, to my aunts Lucinda, Guiga and Gigi for being like second-mothers to me, to my cousins Teresa, Verónica and Artur, and, of course, to my beloved buddy Baloo.

To all: THANK YOU VERY MUCH!

FINANCIAL AND INSTITUTIONAL SUPPORT

The research presented in this Thesis was supported by the Doctoral grant SFRH/BD/103300/2014, financed by Foundation for Science and Technology (FCT), Portugal, through the National Strategic Reference Framework (QREN) and the Human Potential Operational Program (POPH), co-financed by the European Social Fund (ESF).

The research was also partially supported by the:

- Project PTDC/ECM/105446/2008, "Experimental and Numerical set-up for validation of the Dual-Drainage (sewer/surface) concept in an Urban Flooding Framework", and Project PTDC/ECM-HID/4259/2014 – POCI-01-0145-FEDER-016668, "HIRT - Modelling surface hydrologic processes based on infrared thermography at local and field scales", financed by the Foundation for Science and Technology (FCT), Portugal, through the Operational Programme 'Thematic Factors of Competitiveness' (COMPETE), co-financed by the European Regional Development Fund (ERDF);
- Strategic project UID/MAR/04292/2013, granted to MARE- Marine and Environmental Sciences Centre, Portugal, financed by the Foundation for Science and Technology (FCT);
- Project "RECARE - Preventing and Remediating degradation of soils in Europe through Land Care" (Grant Agreement 603498), financed by the European Union (EU);
- Project "Estudo do desempenho de tecnologias para a conservação de água e solo no Semiárido", within the Special Visiting Researcher program (Process 400757/2013-3), finance by the National Council of Scientific and Technological Development of the Ministry of Science and Technology (CNPq/MCT), Brazil, through the Science Without Borders program;
- Project "Análise de diferentes padrões de precipitação em estudos hidrológicos e conservacionistas em parcelas no Semiárido" (Process PBPG-1532-5.03/13), within the call FACEPE 14/2013, and Project "Pesquisa e tecnologias hídricas para o desenvolvimento do Semiárido de Pernambuco" (Process APQ-0300-5.03/17), within the call FACEPE 04/2017, financed by the Pernambuco State Research Support Foundation (FACEPE), Brazil;
- COST Action CA16219, "HARMONIOUS - Harmonization of UAS techniques for agricultural and natural ecosystems monitoring", financed by the European Cooperation in Science and Technology (COST), through the EU Framework Programme Horizon 2020.

Researchers from the following institutions were involved in the research:

- MARE - Marine and Environmental Sciences Centre, Portugal;
- CESAM - Centre for Environmental and Maritime Studies, Aveiro, Portugal;
- Department of Civil Engineering of the Faculty of Sciences and Technology of the University of Coimbra (FCTUC), Coimbra, Portugal;
- Department of Environment and Planning of the University of Aveiro (DAO/UA), Aveiro, Portugal;
- Department of Agricultural Engineering, Rural Federal University of Pernambuco (DEAGRI/UFRPE), Recife, PE, Brazil;
- Institute of Science and Technology, Federal University of Alfenas (ICT/UNIFAL-MG), Poços de Caldas, MG, Brazil.

MARE centro de ciências do mar e do ambiente
1 2 9 0 FACULDADE DE CIÊNCIAS E TECNOLOGIA UNIVERSIDADE D COIMBRA
DEPARTAMENTO DE ENGENHARIA CIVIL
universidade de aveiro cesam universidade de aveiro centro de estudos do ambiente e do mar
Unifal MG Universidade Federal de Alfenas
UNIVERSIDADE FEDERAL RURAL DE PERNAMBUCO
FCT Fundação para a Ciência e a Tecnologia
REPÚBLICA PORTUGUESA
COMPETE 2020
POCH
PORTUGAL 2020
UNIÃO EUROPEIA Fundo Social Europeu
cost EUROPEAN COOPERATION IN SCIENCE AND TECHNOLOGY
COST is supported by the EU Framework Programme Horizon 2020
CNPq Conselho Nacional de Desenvolvimento Científico e Tecnológico
FACEPE Fundação de Amparo à Ciência e Tecnologia do Estado de Pernambuco

ABSTRACT

The harmful impacts of surface runoff and associated water erosion on the environment and populations have been widely recognized throughout the history. Understanding and modelling these processes is, therefore, of crucial importance for engineers, scientists and policy makers in the field of *Hydraulics, Water Resources and Environment*, in order to predict beforehand their impacts and develop proper protection and conservation policies and technologies. Attempts to understand and investigate such processes encompass laboratory experiments, field monitoring and numerical modelling. Each one of these approaches has its purpose, advantages and disadvantages. One thing they all have in common is the necessity of cost-effective techniques to obtain good quality hydrologic data. A recent technological boost in infrared thermography has drawn the attention of the scientific community to the development and investigation of innovative measurement techniques based on these systems. However, not all the potential of these systems has been exploited so far and investigation is still needed.

The aim of this Thesis was to develop innovative techniques based on infrared thermography that can be used as sensing tools to assess different morphologic and hydraulic characteristics of the soil surface and flowing water, and investigate if the collected information can be useful to model and better understand surface hydrologic processes, namely surface runoff and water erosion.

The research developed in this doctoral study started by the development of innovative techniques based on infrared thermography to assess the morphology of the soil surface (microrelief and rills) and soil surface hydraulic characteristics (permeability, macroporosity, water repellency). These techniques were firstly developed in laboratory controlled conditions, in scenarios where some more common measuring techniques cannot be applied successfully. A follow up study to investigate the applicability of these techniques to assess soil water repellency in real field conditions was then carried out. Afterwards, the research focused on the investigation of thermal tracers to estimate basic hydraulic characteristics of shallow flows. The thermal tracer technique was compared to other more tradicional tracer techniques, such as dye and salt. A numerical approach to handle data from thermal tracers as an alternative method to estimate the velocity of shallow flows was then explored. This was done by fitting an analytical solution of an advection–dispersion transport equation to temperature data from thermal tracers. Finally, a two-dimensional (2D) numerical model of surface runoff, infiltration and water erosion was developed. The model combines the two-dimensional unsteady water flow equations on an infiltrating surface with a two-dimensional sediment transport equation, distinguishing between rill erosion, interrill erosion and sediment deposition. Numerical simulations were validated with data from laboratory rainfall simulation experiments on a bi-directional soil flume.

The research presented in this doctoral study revealed that infrared thermography can be used as a ground-based sensing tool for acquisition of information on soil surface characteristics and flow hydraulics. These techniques have shown great potential to: i) Estimate the spatial variability of soil surface morphology where other techniques cannot be applied (presence of organic residues concealing the soil surface); ii) Estimate the spatial variability of soil surface hydraulic characteristics in a faster and expedite way, instead of multiple time-consuming point measurements that need to be grouped or scaled to bring out spatial coherence; and iii) Estimate the surface flow velocity in the occurrence of very shallow flows where many measurement equipment cannot be used.

One big advantage of these techniques is the possibility of qualitative real time monitoring of the spatial dynamics of some key processes in surface hydrology, using only one infrared camera. However, in quantitative terms, the precision of some of these techniques relies on measurements with other more common techniques. As usual, such novel sensing tools will require extensive calibration and validation to be routinely adopted in field monitoring practices.

Observations from these techniques can be used to complement observations from other techniques. Also, techniques and equipment can be combined; e.g. dual cameras with optical and infrared sensors to combine both type of observations, infrared cameras couple with unmanned aerial vehicles to combine observations at different spatial scales.

No doubt, the information collected with these techniques can be useful to calibrate and validate numerical models of surface hydrology, such as surface runoff and water erosion, as well as to better understand the underlying processes.

Keywords

Surface hydrology; Measurement techniques; Infrared camera; Surface runoff; Water erosion; Numerical model

RESUMO

São conhecidos os vários impactos negativos do escoamento superficial e da erosão hídrica no meio ambiente e nas populações. Entender e modelar esses processos é, portanto, crucial para engenheiros, cientistas e responsáveis políticos na área da *Hidráulica, Recursos Hídricos e Ambiente*. Investigações desses processos abrangem desde experiências de laboratório, monitorizações de campo e modelações numéricas. Todas estas abordagens têm em comum a necessidade de técnicas economicamente viáveis para a obtenção de dados hidrológicos de boa qualidade. O recente salto tecnológico em termografia por infravermelhos tem chamado a atenção da comunidade científica para o desenvolvimento e investigação de técnicas inovadoras de medição baseadas nesses sistemas. No entanto, até ao momento, o seu potencial ainda não foi completamente explorado, sendo ncessário mais investigação.

Esta Tese teve como objetivo principal o desenvolvimento de técnicas inovadoras baseadas em termografia por infravermelha que possam ser usadas como ferramentas de deteção para avaliar diferentes características morfológicas e hidráulicas da superfície do solo e do escomento superficial, e investigar a utilidade dessa informação na melhoria da modelação e compreenção de processos hidrológicos superficiais, nomeadamente o escoamento superficial e a erosão hídrica.

A investigação desenvolvida neste estudo de doutoramento iniciou-se com o desenvolvimento de técnicas inovadoras baseadas em termografia por infravermelhos para avaliar a morfologia da superfície do solo (microrrelevo e sulcos) e características hidráulicas da superfície do solo (permeabilidade, macroporosidade e hidrofobicidade). Numa primeira fase, estas técnicas foram desenvolvidas em condições controladas de laboratório, em situaçoes onde não é possível aplicar com sucesso algumas técnicas de medição mais comuns. Numa segunda fase, efectuou-se um estudo para investigar a aplicabilidade dessas técnicas para avaliar a hidrofobicidade do solo em condições reais de campo. Posteriormente, a investigação centrou-se no estudo de traçadores térmicos para avaliar características hidráulicas de escoamentos superficiais pouco profundos. A técnica do traçador térmico foi comparada a outras técnicas de traçadores mais tradicionais, como corante e sal. De seguida, explorou-se uma abordagem numérica para lidar com dados de traçadores térmicos como um método alternativo para estimar a velocidade de escoamentos superficiais. Finalmente, foi desenvolvido um modelo numérico bidimensional (2D) de escoamento superficial, infiltração e erosão hídrica. O modelo combina as equações bidimensionais do escoamento numa superfície permeável com uma equação bidimensional de transporte de sedimentos, distinguindo entre erosão entre sulcos, erosão em sulcos e deposição de sedimentos. As simulações numéricas foram validadas com dados experimentais de simulação de chuva em laboratório num canal de terra bidirecional.

A investigação apresentada neste estudo de doutoramento revelou que a termografia por infravermelhos pode ser usada como uma ferramenta de aquisição de dados sobre as características da superfície do solo e do escoamento superficial. Estas técnicas mostraram grande potencial no sentido de: i) Estimar a variabilidade espacial da morfologia da superfície do solo onde outras técnicas não podem ser aplicadas (presença de resíduos orgânicos sobre a superfície do solo); ii) Estimar a variabilidade espacial de características hidráulicas da superfície do solo de forma mais rápida e expedita, em vez de múltiplas medições pontuais que precisam ser agrupadas para se obter coerência espacial; e iii) Estimar a velocidade superficial de escoamentos muito pouco profundos, onde muitos equipamentos de medição não podem ser usados.

Uma grande vantagem destas técnicas é a possibilidade de monitorização qualitativa em tempo real da dinâmica espacial de alguns processos chave em hidrologia de superfície, usando apenas uma câmara de infravermelhos. No entanto, em termos quantitativos, a precisão de algumas destas técnicas depende de medições com outras técnicas mais comuns. Como de costume, estas novas ferramentas de deteção vão necessitar de trabalhos extensivos de calibração e validação para serem adotadas como práticas comuns em monitorização de campo.

As observações com estas técnicas podem ser utilizadas para complementar observações de outras técnicas. Além disso, técnicas e equipamentos podem ser combinados; por exemplo, câmaras duplas com sensores óticos e infravermelhos para combinar observações; câmaras de infravermelhas acopladas a veículos aéreos não tripulados para combinar observações a diferentes escalas espaciais.

Sem dúvida, as informações obtidas com estas técnicas podem ser úteis para calibrar e validar modelos numéricos de hidrologia de superfície, como escoamento superficial e erosão hídrica, bem como para entender melhor os processos subjacentes.

Palavras-chave

Hidrologia de superfície; Técnicas de medição; Câmara de infravermelhos; Escoamento superficial; Erosão hídrica; Modelo numérico

TABLE OF CONTENTS

LIST OF FIGURES

LIST OF TABLES

"The measure of greatness in a scientific idea is the extent to which it stimulates thought and opens up new lines of research."

- Paul Dirac

"If we knew what it was we were doing, it wouldn't be called research, would it?"

- Albert Einstein (attributed)

1. INTRODUCTION

The first part of this chapter explains the motivation of the research, framing it in the field of *Hydraulics, Water Resources and Environment*. The second part presents the main research question to which this Thesis attempts to answer and a list of specific objectives of this Thesis. The third part outlines the organization of this Thesis with a brief summary of each chapter's content. Finally, the fourth part lists the publications compiled in this Thesis as well as a brief remark on other studies developed during this doctoral study.

1.1. Framework and motivation

Surface runoff harmful impacts on the environment and populations have been widely recognized throughout time. Surface runoff and associated water erosion processes (e.g. detachment, transport and deposition of sediments and pollutants) can contribute to the destruction of terrestrial ecosystems, unsustainable agriculture and deforestation due to soil degradation, to the eutrophication and destruction of aquatic ecosystems due to pollution of freshwater bodies, to the damage of hydraulic infrastructures due to deposition of sediments in water reservoirs and to the destruction of rural and urban structures, or even casualties, due to floods and landslides. Understanding and modelling surface runoff and water erosion is, therefore, crucial in order to predict beforehand their impacts and develop proper protection and conservation policies and technologies. This is a fundamental purpose of engineers, scientists and policy makers in the field of *Hydraulics, Water Resources and Environment* (PANAGOS and KATSOYIANNIS, 2019; VAN LEEUWEN et al. 2019).

Laboratory and field experiments can provide a detailed understanding of surface runoff and water erosion. However, due to the complexity of such processes, it is difficult to extrapolate the data from smaller scales (e.g. laboratory soil flume, field plot) to larger scales (e.g. hillslope, catchment). A robust mathematical model can provide a cost-effective and flexible tool by which many of the complex processes and scenarios at different scales can be quickly simulated in order to predict a problem and choose beforehand the best alternative of addressing it. However, as models' robustness increases, the parameterization complexity and data requirements increase as well. In many cases, the amount of data is not available or does not have good quality. Collecting such data can be challenging, expensive and time-consuming. Some measurement techniques present high costs, low portability and are only suited for laboratory conditions. Some have limited resolution and only provide punctual data that must be grouped or scaled to bring out spatial

coherence. Some may induce deformation to the soil surface or disturbance to the water flow. Some have high toxicological impact on the environment. Therefore, the necessity of good quality hydrologic data with lower costs, higher resolution and lower impact on the soil surface, flow and environment have been fostering engineers and scientists to develop new measurement techniques and modelling methodologies (KETEMA and DWARAKISH, 2019; PARSONS, 2019).

Infrared thermography is a versatile technique that allows to measure the spatial and temporal variability of temperature in a non-invasive and a non-destructive way. During the last decades, infrared cameras have undergone a great increase in portability, sensors accuracy and spatial resolution, together with faster measuring and processing times and a reduction of equipment costs. In the field of surface hydrology, this recent technological boost has increased the interest in the development and investigation of innovative measurement methods, such as non-invasive infrared systems coupled with the use of unmanned aerial vehicles, and new tracer methods (MANFREDA et al., 2018; TAURO et al., 2018). However, the scientific community recognizes that not all the potential of these innovative techniques has been exploited so far and investigation is needed. This aspect was considered has one of the 23 unsolved problems in hydrology (BLÖSCHL et al., 2019): *"How can we use innovative technologies to measure surface and subsurface properties, states and fluxes at a range of spatial and temporal scales?"* Therefore, the development of innovative techniques based on infrared thermography to be used in surface hydrology has shown to have huge potential for investigation and motivated a doctoral study that is now described in this Thesis.

1.2. Research question and objectives

The motivation behind this Thesis led to the following main research goal, formulated in the form of question: **Can information collected at the soil surface level with techniques based on infrared thermography be useful to model and better understand surface hydrologic processes?**

In order to attempt to provide an answer to this question, the following seven specific objectives were defined for this Thesis:

- **Objective 1.** To develop, in laboratory, an innovative technique based on infrared thermography to assess morphological characteristics of soil surface;
- **Objective 2.** To develop, in laboratory, innovative techniques based on infrared thermography to assess different hydraulic characteristics of soil surface;
- **Objective 3.** To investigate the applicability in real field conditions of an innovative technique based on infrared thermography to assess the hydraulic behaviour of the soil surface due to differences in soil water repellency;
- **Objective 4.** To identify the strengths and drawbacks of the techniques based on infrared thermography developed in this doctoral study;

- **Objective 5.** To investigate the use of thermal tracers and infrared video cameras to estimate the velocity of shallow flows;
- **Objective 6.** To develop a numerical approach to combine with thermal tracers to estimate basic hydraulic characteristics of shallow flows;
- **Objective 7.** To develop a two-dimensional (2D) rainfall induced water erosion numerical model.

1.3. Thesis structure

This Thesis was structured in 13 chapters. Their content is briefly summarized in the following paragraphs.

- **Chapter 1. Introduction.** This chapter presents an overview of the motivation of the research, framing it in the field of *Hydraulics, Water Resources and Environment*, identifies the objectives of the research and describes the organization of this document.
- **Chapter 2. Literature review.** This chapter presents a literature review on processes and conditioning factors in surface hydrology, with focus on surface runoff and water erosion. Presents a brief state of the art about some measurement techniques used in surface hydrology. Finally, introduces the concept of infrared thermography and its uses in surface hydrology.

Chapters 3 to 7 focus on the development and investigation of innovative techniques based on infrared thermography to assess soil surface morphologic and hydraulic characteristics. These innovative techniques were firstly developed in laboratory using soil flumes in specific controlled conditions, where some measuring techniques cannot be applied successfully. A follow up study to investigate the applicability of one of these techniques in real field conditions was then carried out. Thermal data acquired with infrared video cameras was analysed using proper processing software and numeric procedures developed for each investigation. The calibration and evaluation of these thermal data were performed using data obtained with more traditional and accepted techniques. The content of each chapter is summarized next:

- **Chapter 3. Can infrared thermography be used to estimate soil surface microrelief and rill morphology?** This chapter presents an innovative technique to map soil surface microrelief and rill morphology using infrared thermography. The technique starts by applying hot water over the soil surface. As it flows along the soil surface, it concentrates in the lower topographic elements (e.g. rills, surface depressions), which, consequently, will present higher temperatures. The technique was investigated in laboratory in a surface with artificially created rills and in a surface eroded by flowing water, in bare soil and in the presence of organic residues covering the soil surface. Soil surface elevation was measured with a relief meter;

- **Chapter 4. Prediction of skin surface soil permeability by infrared thermography: a soil flume experiment.** This chapter presents an innovative technique to map soil surface permeability and to identify preferential flow at the soil surface using infrared thermography. The technique starts by applying hot water over the soil surface. As it flows along the soil surface, it preferentially infiltrates and penetrates the soil in the higher permeability areas which, consequently, will present higher temperatures. The technique was investigated in laboratory, where different spatial patterns of soil surface permeability were created using different soils. Soil permeability was expressed in terms of saturated hydraulic conductivity measured using a constant head permeameter;
- **Chapter 5. Mapping soil surface macropores using infrared thermography: an exploratory laboratory study.** This chapter presents an innovative technique to detect the number, location and size of macropores at the soil surface using infrared thermography. The technique starts by applying hot water over the soil surface. As it flows along the soil surface, it briefly accumulates inside the macropores, which, consequently, will present higher temperatures. The technique was tested in laboratory, with macropores of different sizes artificially created at the soil surface;
- **Chapter 6. Assessing soil water repellency spatial variability using a thermographic technique: small-scale laboratory study.** This chapter presents an innovative technique to map areas of the soil surface that present different levels of water repellency. The technique starts by applying cold water over the soil surface. As it flows along the soil surface, it is repelled in the repellent areas and preferentially infiltrates in the non-repellent areas. Consequently, the non-repellent areas will present lower temperatures. The technique was firstly tested in laboratory, where some areas of the soil surface were artificially induced with different levels of water repellency. Soil water repellency was measured in terms of surface tension using the Molarity of an Ethanol Droplet test;
- **Chapter 7. Field assessment of soil water repellency using infrared thermography.** This chapter presents a follow-up study to investigate the applicability of the technique presented in the previous chapter in field conditions. While the experimental set-up and methodology were similar, the data treatment procedure had to be adapted. Field tests were carried in different sites, where the soil surface presented both naturally and artificially induced water repellency. Soil water repellency was measured in terms of surface tension using the Molarity of an Ethanol Droplet test.

Chapters 8 to 10 focus on the use of thermal tracers and infrared video cameras to estimate basic hydraulic characteristics of shallow flows. As in the previous chapters, thermal data acquired with was analysed using proper processing software and specifically developed numeric procedures. The content of each chapter is summarized next:

- **Chapter 8. Using a thermal tracer to estimate overland and rill flow velocities.** This chapter presents the investigation of thermal tracer techniques to estimate overland and rill

flow space-averaged velocities. Laboratory experiments using a soil flume consisted in the injection of a combined tracer (i.e. dyed-heated water, presenting the characteristics of a dye and a thermal tracer) into the flow. Its movement with the flowing water was visualised using infrared and optical video cameras. Therefore, results of the two techniques could be compared;

- **Chapter 9. Comparison of thermal, salt and dye tracing to estimate shallow flow velocities: novel triple-tracer approach.** This chapter presents the investigation of thermal tracer techniques to estimate the velocity of very shallow water flowing over different surfaces (e.g. smooth acrylic, rough sand, synthetic grass and stones), combining different surface slopes and flow discharges. Laboratory experiments using a hydraulic channel consisted in the injection of a triple tracer (i.e. dyed-salted-heated water, presenting the characteristics of a dye, a salt and a thermal tracer) into the flow. Its movement with the flowing water was visualised and tracked using infrared and optical video cameras and an electrical conductivity sensor. Therefore, results of the three techniques could be compared. Estimations of the mean flow velocity using discharge/depth measurements allowed to investigate in detail the conversion factors used to convert tracer surface flow velocity into actual mean flow velocity;
- **Chapter 10. Combining a thermal tracer with a transport model to estimate shallow flow velocities.** This chapter presents a numerical approach to handle data from thermal tracers as an alternative method to estimate the velocity of shallow flows, by fitting an analytical solution of an advection–dispersion transport equation to temperature data from thermal tracers. This is done by calibrating the velocity and dispersion coefficient terms of the equation. This numerical approach was first developed to be used with data from salt tracer. Thermal and salt tracer data from the triple tracer experiments presented in the previous chapter were used in this investigation.
- **Chapter 11. Two-dimensional (2D) numerical modelling of rainfall induced water erosion: comparison with laboratory rainfall-runoff simulations on a two-directional soil flume.** This chapter presents the conceptualization and validation of a two-dimensional (2D) water erosion numerical model. Surface runoff from rainfall was modelled using the 2D unsteady, non-uniform fully dynamic physically based Saint-Venant equations. Infiltration was modelled using a combined Horton-SCS empirical scheme. Water erosion was modelled using a 2D transport rate-based advection equation and a common detachment-transport-deposition approach, distinguishing between interrill erosion, rill erosion and sediment deposition. The governing equations were solved using an explicit finite-differences method based on the MacCormack operator-splitting scheme. Numerical simulations were validated with data from laboratory rainfall simulation experiments on a two-directional 2×2 m^2 soil flume set at 1% and 10% slopes in the x- and y-directions, respectively.

- **Chapter 12. Final remarks.** This chapter attempts to give an answer to the main research question of this Thesis, summarizes the overall conclusions, and, finally, presents suggestions for future investigations.
- **Chapter 13. References.** This chapter presents the list of the publications consulted in the course of this doctoral study, which are referenced in this Thesis.

1.4. Publications

Chapters 3 to 10 of this Thesis were published in international journals and are presented here as published by the journals, except for some layout changes, such as size, position and numbering of figures and tables. Chapter 11 was submitted to an international journal and is currently under review. It is presented here as submitted to the journal. References of the articles are presented next:

- **Chapter 3.** DE LIMA, J.L.M.P. and ABRANTES, J.R.C.B. (2014). Can infrared thermography be used to estimate soil surface microrelief and rill morphology? *Catena*, 113, 314-322. DOI:10.1016/j.catena.2013.08.011.
- **Chapter 4.** DE LIMA, J.L.M.P., ABRANTES, J.R.C.B., SILVA JR., V.P. and MONTENEGRO, A.A.A. (2014). Prediction of skin surface soil permeability by infrared thermography: a soil flume experiment. *Quantitative InfraRed Thermography Journal*, 11(2), 161-169. DOI:10.1080/17686733.2014.945325.
- **Chapter 5.** DE LIMA, J.L.M.P., ABRANTES, J.R.C.B., SILVA JR., V.P., DE LIMA, M.I.P. and MONTENEGRO, A.A.A. (2014). Mapping soil surface macropores using infrared thermography: an exploratory laboratory study. *The Scientific World Journal*, 2014, 84560. DOI:10.1155/2014/845460.
- **Chapter 6.** ABRANTES, J.R.C.B., DE LIMA, J.L.M.P., PRATS, S.A. and KEIZER, J.J. (2017). Assessing soil water repellency spatial variability using a thermographic technique: small-scale laboratory study. Geoderma, 287, 98-104. DOI:10.1016/j.geoderma.2016.08.014.
- **Chapter 7.** ABRANTES, J.R.C.B., DE LIMA, J.L.M.P., PRATS, S.A. and KEIZER, J.J. (2016). Field assessment of soil water repellency using infrared thermography. *Forum Geographic*, 15(2), 12-18. DOI:10.5775/fg.2016.019.s.
- **Chapter 8.** DE LIMA, J.L.M.P. and ABRANTES, J.R.C.B. (2014). Using a thermal tracer to estimate overland and rill flow velocities. *Earth Surface Processes and Landforms*, 3(10), 1293-1300. DOI:10.1002/esp.3523.
- **Chapter 9.** ABRANTES, J.R.C.B., MORUZZI, R.B., SILVEIRA, A. and DE LIMA, J.L.M.P. (2018). Comparison of thermal, salt and dye tracing to estimate shallow flow

velocities: novel triple tracer approach. *Journal of Hydrology*, 557, 362-377. DOI:10.1016/j.jhydrol.2017.12.048.

- **Chapter 10.** ABRANTES, J.R.C.B., MORUZZI, R.B., DE LIMA, J.L.M.P., SILVEIRA, A. and MONTENEGRO, A.A.A. (2019). Combining a thermal tracer with a transport model to estimate shallow flow velocities. *Physics and Chemistry of the Earth*, 109, 59-69. DOI:10.1016/j.pce.2018.12.005.
- **Chapter 11.** ABRANTES, J.R.C.B., SIMÕES, N.E. DE LIMA, J.L.M.P., and MONTENEGRO, A.A.A. Two-dimensional (2D) numerical modelling of overland flow, infiltration and erosion: comparison with laboratory data from rainfall simulations on a multi slope soil flume. Submitted to *Journal of Hydrology and Hydromechanics* in August 2019. Under review.

In the nine listed articles, first author position was typically assigned to the person that conceptualised the study and article itself, which varied between the author of this Thesis (J.R.C.B. Abrantes) and the main supervisor (J.L.M.P. de Lima). Independently of the authorship position, the author of this Thesis was always involved in all aspects of the presented articles: execution of the experiments, numerical simulations, data treatment, interpretation of results and writing, editing and review of the article.

The research conducted in this doctoral study also contributed to publications and presentations (oral and poster), authored and co-authored by the author of this Thesis, in several national and international scientific meetings. Also, it contributed to the emergence of some related studies and submission of articles in international journals authored and co-authored by the author of this Thesis. A list of these publications is presented in Appendix A.

During this doctoral study, from 2013 to 2019, the author of this Thesis was also involved in several other studies in the field of *Hydraulics, Water Resources and Environment*, namely: i) Laboratory and numerical modelling of the effect of soil and water conservation techniques (e.g. mulching) on surface runoff and water erosion; ii) Laboratory and numerical modelling of surface runoff and transport of sediments and pollutants in urban areas (e.g. roofs); and iii) Numerical modelling of the power output of a wave energy generation device. These studies contributed to publications in international journals, as well as publications and presentations in national and international scientific meetings, as listed in the Curriculum Vitae of the author.

"... we might say that the earth has a spirit of growth; that its flesh is the soil, its bones the arrangement and connection of the rocks of which the mountains are composed, its cartilage the tufa, and its blood the springs of water."

- Leonardo da Vinci

2. LITERATURE REVIEW

The first part of this review gives a summary of some components and processes in surface hydrology. The second part gives a description of the water erosion processes and modelling. The third part gives an overview of some conditioning factors in surface hydrology. The fourth part gives a state of the art about some measurement techniques used in surface hydrology to assess the characteristics of rainfall, soil morphology, soil cover, soil hydraulics and flow hydraulics. The fifth part introduces the concept of infrared thermography and its application in surface hydrology and presents some innovative techniques including the ones investigated during this doctoral study.

2.1. Components and processes in surface hydrology

For the purpose of this doctoral study it is important to first define what surface hydrology is, and clearly identify its components and processes involved. Surface hydrology is the branch of hydrology dealing with hydrological phenomena and processes which occur on the Earth's surface, emphasizing surface flows (WMO, 2012). Despite most of the definitions of surface hydrology found in the literature show some levels of discrepancy, this is a classification that fits within most of the works in this field.

In this section, among the various components in surface hydrology, main attention will be given to rainfall, infiltration and surface runoff.

2.1.1. Rainfall

Rainfall consists of liquid water falling to Earth as individual raindrops, which occur in varying numbers, sizes and fall speeds. Rainfall initiation is a two phase process: i) Saturation of air masses with water vapour; and ii) Water vapour condensation that converts the suspended water particles in the air into large water particles that become large enough so that they can get to the Earth before evaporating (e.g. SUMN, 1988). Saturation of air masses can occur by accumulation of water vapour originated by evaporation of water bodies (e.g. sea, aquifers) or by transpiration (e.g. plants, animals). Water condensation can occur by saturated air masses cooling and consequent reduction of condensation temperature, generally caused by the lifting of air masses (e.g. air mass moving over a mountain, differences in air mass densities, air masses collide originating an upward movement). These two phases can occur almost simultaneously or in two distinct phases, e.g. saturated air masses can be carried by wind to other locations before suffer condensation, so, rainfall will not in the same location where air saturation has occurred.

Rainfall plays a dominant role in many hydrologic and hydraulic studies, in both natural and urbanized catchments, regardless of the climate region. Water from rainfall is the major source of surface runoff leading to the occurrence of extreme flash flood events in natural (e.g. BEVEN et al., 1984; JINKANG et al., 2007; PAQUET et al., 2013; PASCHALIS et al., 2014) and urbanized catchments (e.g. FLETCHER et al., 2013; ISIDORO, 2012; SMITH et al., 2007). Rainfall intensity distribution is a key factor affecting the temporal variation of soil erosion (e.g. detachment of soil particles by splash erosion, rill network initiation and development) during a storm event (e.g. BERGER et al., 2010; DE LIMA et al., 2005, 2013a; MONTENEGRO et al., 2013a, 2013b; PARSONS and STONE, 2006; RÖMKENS et al., 2001), especially in semiarid regions (e.g. BAARTMAN et al., 2011; BOCHET et al., 2006; MONTENEGRO, 2013b) characterized by highly spatial and temporal irregular precipitation, with high intensity and low frequency rainfall events occurring mainly in the beginning of the rainy season when soil is more susceptible to erosion (e.g. DE LIMA et al., 2013b; SANTOS and MONTENEGRO, 2012; SANTOS et al., 2010). The amount of rain determines the crop productivity of rainfed agriculture and controls the development of water dependent ecosystems, especially in arid and semiarid regions (e.g. KALFF et al., 1985; ROCKSTRÖM et al., 2004, 2010). Rainfall temporal variability directly influences temporal fluctuations of groundwater levels (e.g. JAN et al., 2007; PADILLA et al., 2014; WU et al., 1996) and groundwater recharge amount presented a linear relationship with rainfall intensity (OWOR et al., 2009). Rainfall strongly influences the urban structure as well as landscape architecture, buildings and street furniture (e.g. GREENE, 2001). Rainfall intensity, duration and frequency are crucial parameters in the design of urban hydraulic structures, such as drainage systems, water treatment stations and flood control structures.

2.1.2. Infiltration

Infiltration is a key process in the rainfall runoff relationship. It is one of the most important soil parameters in watershed modelling (e.g. SINGH and WOOLHISER, 1976) and in the design and evaluation of both rainfed and irrigated agricultural systems (e.g. SINGH et al., 1999), since it controls the formation of surface runoff and plays a vital role in the water storage in the soil (i.e. soil moisture) which is responsible for the growth and development of crops.

According to HORTON (1933) infiltration divides rainfall into two parts. One part goes via overland flow and stream channels to the sea as surface runoff; the other goes initially into the soil and thence through groundwater again to the stream or else is returned to the air by evaporative processes. For more details see the review of Robert E. Horton's work by BEVEN (2004). Infiltration occurs at two distinct phases. At the beginning, when the water supply rate (e.g. rainfall, surface runoff from upslope areas) is lower than the infiltration capacity (i.e. the capacity of soil to absorb water) all water infiltrates into the soil. Thus, during the first phase, the speed at which soil is able to absorb water is greater than the water supply rate. As water continues to infiltrate, soil infiltration capacity decreases due to soil surface crusting, pore saturation by water or clogging by sediments and swelling of the clays (RÖMKENS et al., 1990). Infiltration capacity decreases with

a logarithmic behaviour, from its maximum when soil is completely dry to a minimum in saturated conditions (equivalent to saturated hydraulic conductivity). When the infiltration capacity is less than the water supply rate, water will start to pond on soil surface and, once depressions are filled, runoff over the soil surface will begin. This is the so called Hortonian overland flow or infiltration excess overland flow. After the water supply ends, the soil starts to dry, and the restoration of the infiltration capacity begins.

Infiltration is a dynamic process, both in time and space. In climates with contrasting seasons (e.g. Mediterranean environments) the infiltration capacity will vary in time due to the seasonal climatic fluctuations, which modify the antecedent soil moisture conditions (e.g. CERDÀ, 1996, 2010). Spatial variability is the consequence of the wide range of factors that control infiltration (e.g. SHARMA et al., 1980), such as, rainfall characteristics (e.g. intensity), soil hydraulic properties (e.g. permeability), soil surface conditions (e.g. slope, roughness, vegetation type and cover, rock fragment cover, crust cover), microclimatic properties and biological activities (e.g. MONTENEGRO et al., 2013a; POESEN et al., 1999; RODRÍGUEZ-CABALLERO et al., 2012; RÖMKENS et al., 2001; SOLÉ-BENET et al., 1997).

2.1.3. Surface runoff

There is no doubt that surface runoff has great impact in surface hydrology. It affects the local water balance and is the major responsible for water erosion and solute transport in natural and urbanized catchments. Surface runoff is a major controlling factor of the water level and water quality of surface water bodies (e.g. streams, rivers). Those water bodies show a fast reaction to the input of surface runoff and sediments and solutes (e.g. nutrients, pesticides) associated to it (e.g. DONG and WANG, 2013; BLANCHOUD et al., 2007; LOUCHART et al., 2001; TETZLAFF et al., 2013).

Surface runoff can be divided into overland flow, rill flow and stream flow. A full review on this topic can be found in HOGG (1982). Overland flow is the surface water that flows over the surface before it enters a defined channel. When overland flow concentrates in a defined channel it is called rill flow or stream flow, depending on the characteristics of the channel. Rills are narrow and shallow irregular incisions in the topsoil layer. Due to natural or artificial erosive processes rills may evolve into gullies and streams, large structures where stream flow takes place. According to VAN LOON (2001), the spatial and temporal transition between overland flow, rill flow and stream flow, can only be defined subjectively and approximately.

Surface runoff initiation can occur by two mechanisms (e.g. APPELS, 2013; VAN LOON, 2001). It can occur by saturation of the topsoil layer by excess of water input from above the surface, called Hortonian overland flow or excess infiltration overland flow (see section 2.1.2), or by saturation of the topsoil layer due to the rise of the groundwater table to the soil surface. This last mechanism is called saturation excess or Dunne overland flow (DUNNE and BLACK, 1970). The mechanism for surface runoff initiation depends on the hydraulic characteristics of the soil and water input. In hillslopes of semiarid regions, excess infiltration is the main mechanism of surface

runoff initiation (e.g. BUTZEN et al., 2014; GOMI et al., 2008; PEUGEOT et al., 1997) due to the low infiltration capacity soils and extreme but short rainfall events. These regions present high risks of suffer soil erosion by water. Surface runoff initiation by excess saturation is mostly related to wetlands and riparian zones and to shallow soils, during the wet seasons when the soil is completely saturated (e.g. MATUSHI et al., 2006; VERBIST et al., 2007; WILSON et al., 1991).

Surface runoff is highly variable in space and time, due to the spatial and temporal fluctuations of groundwater levels that affect the saturation levels of the soil and the wide range and heterogeneity of factors that control infiltration. While the first may affect surface runoff at the catchment scale (e.g. GABRIELLI et al., 2012; HEATHWAITE, 2010) the second affects surface runoff even at plot scale (e.g. MONTENEGRO et al., 2013a; POESEN et al., 1999; RÖMKENS et al., 2001). This variability combined with temporal and spatial dynamics of rainfall create a large variability in the initiation, rate, extent and duration of surface runoff and, consequently, in the soil erosion processes associated to it.

2.2. Water erosion

Water erosion is one of the most widespread forms of soil degradation, representing a main threat to the sustainability and productive capacity of agriculture, especially in arid and semiarid regions (e.g. BOARDMAN et al., 2009; CANTÓN et al., 2011; KAGABO et al., 2013; ROUTSCHEK et al., 2014). It can lead to decline in organic matter and nutrient contents, breakdown of soil structure and reduction of the water holding capacity.

According to STROOSNIJDER (2012), water erosion is the most important land degradation process of ten land degradation processes distinguished by the European Union.

2.2.1. Water erosion processes

Water erosion consists in the detachment, transport and deposition of sediments (soil particles) by the erosive forces of rainfall and surface runoff. Therefore, it directly comprises all the spatial and temporal variability aspects of rainfall and surface runoff and indirectly comprises the variable aspects of infiltration. Water erosion occurs in various forms (e.g. splash, sheet, rill, gully) depending on the stage of progress and on the surface structures where it occurs.

Generally, splash erosion is the first mechanism of sediments detachment in the rainfall-runoff process. It consists in the detachment of soil particles by raindrops, when their force of impact on the surface overcomes the interstitial forces holding the soil particles together (e.g. KINNELL, 2005). It provides for the allocation of small soil particles that can be transported by either arising or already generated surface runoff. As surface runoff starts to flow on soil surface, in the form of overland flow, sheet erosion starts. This is the detachment and transport of sediments by overland flow, in the form of a very thin broad sheet. Sediments may be dissolved or suspended in the

overland flow (e.g. JULIEN and SIMONS, 1985) and may have been detached by the splash erosion or by the own erosive power of the overland flow. As overland flow converges and becomes more concentrated, it becomes sufficiently erosive to form small shallow channels on the soil surface, called rills, and rill erosion starts. According to LOCH (1979) rill erosion can be the major mechanism of soil loss from sloping, cultivated land, and can detach and transport much higher sediment loads than sheet flow. As the erosive power increases, the small rills may converge to form gullies, and gully erosion starts (e.g. POESEN et al., 2003). Eventually, if enough water continues to flow in the rills and gullies, the erosional processes will originate well-defined channels, such as streams and rivers. At any point of the erosion process, flow may no longer be able to transport sediments (e.g. by reduction of flow velocity) and some may be deposited at the soil surface.

The combined mechanism of splash and sheet erosion is called interrill erosion and is mainly controlled by the kinetic energy of the raindrops, by the soil surface conditions (e.g. vegetation cover, rock fragment cover, microrelief) and by the soil texture and strength (e.g. FAN and WU, 1999; JOMAA et al., 2012; MEYER, 1981; MIURA et al., 2002). According to KNAPEN et al. (2007), soil erosion by concentrated flows in rills and gullies is highly dependent on flow conditions (e.g. flow velocity, flow depth and hydraulic roughness). Surface cover conditions, such as rock fragments and vegetation, soil compaction, texture and strength and plant roots also control rill initiation and development (e.g. POESEN et al., 1999; TORRI et al., 2012). The balance between interrill and rill erosion processes is highly dynamic and complex (e.g. GOVERS and POESEN, 1988) and, like overland and rill flows, it is difficult to define with precision the spatial and temporal transition between the two processes.

The detachment capacity and transport capacity are interrelated variables of the flow and they are the ones that control the detachment-deposition processes (e.g. ALI et al., 2013; COCHRANE and FLANAGAN, 1996; FINKNER et al., 1989; JULIEN and SIMONS, 1985; SLAYMAKER, 2003; YAN et al., 2008; ZHANG et al., 2009). The transport capacity of the flow is the maximum amount of sediment that a given flow can carry, for a given hydraulic condition, without deposition. The detachment capacity measures the ability of the flow to detach sediments and is dependent on soil erodibility properties and the shear stress acting on the sediment by the flow. These two variables determine respectively the lower and upper limit of sediment transport by runoff and their interaction that controls the patterns and magnitudes of erosion (SAAVEDRA, 2005). If the detachment capacity of the soil is significantly lower than the transport capacity then the amount and magnitude of soil erosion is limited by the detachment capacity, e.g. in clay soils where the binding forces of soil particles are large and resist detachment. If the detachment capacity is significantly greater than the transport capacity then the amount and magnitude of soil erosion is limited by the sediment transport capacity of runoff, e.g. for sandy soils that are easily detached.

2.2.2. Water erosion modelling

Modelling water erosion processes is a very useful tool to predict beforehand their environmental impact and to develop regulations, policies and techniques for soil and water conservation management. Laboratory and field studies using rainfall simulators have been widely used to investigate water erosion (e.g. CERDÀ et al., 1997; DE LIMA et al., 2003, 2008, 2009, 2011, 2013a; MARTÍNEZ-MURILLO et al., 2013; MONTENEGRO et al., 2013a, 2013b; PÉREZ-LATORRE et al., 2010). These studies enable a detailed exploration of a large range of hydrologic conditions occurring at the plot and hillslope scale.

Numerical modelling of water erosion is based on an understanding of the physical laws and processes that occur at the soil surface (e.g. rainfall, surface runoff, infiltration) at different scales (e.g. catchment, hillslope, plot). It describes the fundamental processes of sediment detachment, transport and deposition through mathematical relationships translating the components and processes occurring at the surface (e.g. JETTEN et al., 2003; SAAVEDRA, 2005). Mathematical models are cost-effective tools for improving our understanding of erosion processes and predict its effects on soil and water quality. A robust mathematical model can provide a cost-effective tool by which many scenarios can be simulated and compared in order to find the best alternative of addressing a particular problem. Generally, three main types of models are used to describe hydrologic processes: i) Empirical; ii) Conceptual; and iii) Physically based. The types of models differ in the physical processes simulated, in the model algorithms describing the processes and in the data dependency of the models. For more details see the review on theoretical consideration and types of models in surface hydrology in JAJARMIZADEH et al. (2012) and SINGH and WOOLHISER (2002) and the review of erosion and sediment transport models in BATISTA et al. (2019), DE VENTE et al. (2013) and MERRITT et al. (2003).

Empirical models are generally the simplest of the three main types, because they require less data and computational effort. They are based primarily on experiments and observations to characterize the hydrological processes. They are particularly useful as a first step in identifying the erosional processes, because they can be implemented in a situation with limited data and parameter inputs. However, they should not be extrapolated beyond their data range and are often criticized for employing unrealistic assumptions about the physics of the catchment system, for ignoring the heterogeneity of catchment inputs and characteristics. Maybe the most used water erosion empirical models are the Universal Soil Loss Equation (USLE, WISCHMEIER and SMITH, 1978) and the Revised USLE version (RUSLE, RENARD et al., 1997)

Conceptual models lie between empirical and physically based models. Traditionally, they include a general description of catchment processes, without including the specific details occurring in the complex process interactions. Conceptual models tend to suffer from problems associated with the identification of the parameter values.

Physically based models use mathematic equations stating the physical laws that govern the fundamental hydrological and erosion processes. These models are based on the understanding of

the physics of the erosion, using equations governing the transfer of mass, momentum and energy. Normally, they can be applied outside the range of conditions used for calibration and they can be evaluated from direct measurements, without the need for long hydrometeorological records. Therefore, they are limited only by the physical laws on which they are based. Some examples are the KINematic runoff and EROSion (KINEROS, WOOLHISER et al., 1990), the Water Erosion Prediction Project (WEPP, FLANAGAN and NEARING, 1995), or the EUROpean Soil Erosion Model (EUROSEM, MORGAN et al., 1998).

Physically based models are generally the most scientifically robust and flexible models and provide an understanding of the fundamental and non-stationary processes involved in the detachment, transport and deposition of sediments and provide an access to their spatial and temporal variation (NEARING, 2000). However, due to the complexity of such processes, fully physically based models have not yet become a practical tool. Their parametrisation is complex, and they are data intensive. Also, such data always carry a level of uncertainty, are expensive and time consuming and, therefore, most of the times the amount of data needed is not readily available (STROOSNIJDER, 2005).

Equations used for soil erosion and sediment transport resulting from rainfall induced overland flow vary significantly due to different understanding and treatments of the sediment detachment, transport and deposition mechanisms (FLANAGAN and NEARING, 1995; KINNELL, 200; MORGAN et al., 1998; WOOLHISER et al., 1990). A coupling approach is often used to describe the detachment-transport-deposition processes in water erosion modelling (e.g. e.g. DENG et al., 2008; LIU et al., 2006; NEARING et al., 1989). Usually, three fundamental water erosion processes are considered: i) Interrill erosion, that reflects the detachment and transport of sediments by the action of raindrops; ii) Rill erosion, that reflects the detachment and transport of sediments by the action of surface runoff; and iii) Sediment deposition, that reflects the settling down of sediments. Raindrop impact and/or surface runoff can detach sediments from the soil surface. A critical force needs to be exerted by either a raindrop or a flow before detachment occur. Transport of detached material can occur as the result of raindrops and flow acting singly or together. Sediment deposition occurs when the flow can no longer support the suspended sediments, usually as result of a decrease in the flow transport capacity. As flow conditions change, either detachment or deposition of sediments will be favoured. This approach assumes that the available flow energy is preferentially utilized for sediment transport and any excess energy will be used for sediment detachment.

Soil erosion by water is a complex process that mainly entails the processes of surface runoff and infiltration. Therefore, a spatial and temporal dynamic water erosion model, coupling infiltration and surface runoff, should be used. To simulate surface runoff over natural and artificial surfaces both the kinematic and diffusive wave approximations of the 1D and 2D Saint-Venant shallow water equations, stating the laws of conservation of mass and momentum, have been extensively used (e.g. DE LIMA and SINGH, 2002; GARCIA and KAHAWITA, 1986; GARCIA-NAVARRO and SAVIRON, 1992; SINGH, 1996). Water infiltration is usually modelled using the physically

based Richards equation for the movement of water in unsaturated soils derived from Darcy's law (e.g. RICHARDS, 1931) or empirical models, such as the Horton equation in its initial form (HORTON, 1933, 1940) or the modified Horton equation that is a combination between the Soil Conservation Service Curve Number method (SCS-CN) and a method derived from Horton equation (e.g. BAUER, 2010; GABELLANI et al., 2008).

In Chapter 11 of this Thesis, an original two-dimensional (2D) numerical model of soil erosion and sediment transport is presented. It is a spatial and temporal dynamic model combining physical and empirical laws, comprising three main modules: i) An overland flow module that solves the two-dimensional unsteady water flow equations on an infiltrating surface, using an explicit finite-difference method based on the MacCormack operator-splitting scheme (GARCIA and KAHAWITA, 1986; MACCORMACK, 1971; SIMÕES, 2006); ii) A soil infiltration module that uses a modified version of the empirical Horton's infiltration equation with a calibration methodology of its parameters based on formal analogies with the SCS-CN method (GABELLANI et al., 2008); and iii) A soil erosion and sediment transport module that solves the two-dimensional sediment transport equation, distinguishing between rill erosion, interrill erosion and sediment deposition (CAO et al., 2002; DENG et al., 2008). Specific procedures were used to handle the wet/dry front and, therefore, simulations can start on an initially dry surface. The performance of the model was evaluated by comparing its results with observed data from laboratory rainfall-runoff experiments on a two-directional free-drainage square soil flume.

2.3. Conditioning factors in surface hydrology

When studying and modelling surface runoff and water erosion, some of the most important parameters to be evaluated are related with the erosive characteristics of the rainfall (e.g. intensity, raindrop sizes) and their spatial variability (e.g. DE LIMA et al., 2005, 2013a; KINNEL, 2005; RÖMKENS et al., 2001), hydraulic characteristics of surface runoff (e.g. LEI et al., 1998; PARSONS and WAINWRIGHT, 2006), soil morphological characteristics such as rill morphology (e.g. width, depth) and soil surface microrelief (e.g. FAVIS-MORTLOCk et al., 2000; GÓMEZ and NEARING, 2005), soil surface cover with vegetation, organic residues and rock fragments (e.g. GOVERS et al., 2006; MONTENEGRO et al., 2013a, 2013b) and hydraulic characteristics of the soil, such as permeability, macroporosity and water repellency (e.g. BEVEN and GERMANN, 1982, 2013; DEBANO, 2000b). All these parameters are space and time variable functions of the water erosion evolutionary process and their non-static characteristic should not be neglected.

2.3.1. Rainfall characteristics

The spatial variability of rainfall is a major source of error in hydrological modelling (e.g. SMITH et al., 2004; TETZLAFF and UHLENBROOK, 2005). Especially for small catchments and hillslopes, when runoff processes respond directly to precipitation, detailed rainfall information is

necessary. The temporal variability of rainfall has a large impact on runoff generation and associated transport processes (e.g. DE LIMA et al., 2009; MANNAERTS and GABRIELS, 2000; TRUMAN et al., 2007), particularly in semiarid areas where transport by storm events spans different orders of magnitude (e.g. DE LIMA and GRASMAN, 1999; DE LIMA et al., 2002).

Rainfall intensity plays the most important role in the rainfall-runoff process and the resulting soil losses (e.g. DE LIMA et al., 2013a; MONTENEGRO et al., 2013a, 2013b; RÖMKENS et al., 2001). However, is the raindrop size that plays a major controlling factor in splash erosion. As raindrops increase in size, their terminal velocity and kinetic energy also increases. Therefore, larger drops have more erosive power to detach sediments from the soil surface. According to KINNEL (1982) splash loss per drop varied with the square of the drop mass.

2.3.2. Soil surface morphology

Soil surface morphological characteristics, such as the micro-topographic variations in soil surface elevation at a scale ranging from centimetres to millimetres or less (e.g. HUANG, 1998; PAZ-FERREIRO et al., 2008; VIDAL VÁZQUEZ et al., 2005), called microrelief, has been demonstrated to strongly influence several hydrological processes. They influence surface retention, infiltration, runoff, sediment transport, rill formation, rill erosion (e.g. DARBOUX et al., 2001; GÓMEZ and NEARING, 2005; RÖMKENS et al., 2001; KIDRON, 2007), surface sealing, surface crusting and soil moisture (e.g. FOHRER et al., 1999; RODRÍGUEZ-CABALLERO et al., 2012), evaporation and heat flux (e.g. PRICE et al., 1998). Microrelief is the result of several factors that affect the superficial layer of the soil over the time, such as water and wind erosion, agricultural practices (e.g. tillage, ploughing, mulching), vegetation (e.g. roots, mulch, shrubs, grass) and animal activity (e.g. ant mounds).

One problem related with the modelling of runoff-erosion processes (e.g. rill erosion models) is the effect of the change of microrelief over the time and area in which those processes occur (e.g. ZOBECK and ONSTAD, 1987). Erosional processes modify the soil surface and create a new specific surface. For example, runoff during the latest part of a rainfall event will flow over a soil surface that may be different from the surface encountered by runoff earlier in the storm (e.g. FAVIS-MORTLOCK et al., 2000). Also, larger rills will modify the local soil surface morphology in a greater extent than small rills. Thus, the development of greater rills will be more successful as they were more capable of capture and convey runoff and sediments. This constitutes a positive feedback loop, between microrelief and runoff-erosion processes (e.g. FAVIS-MORTLOCK, 1998).

2.3.3. Soil surface cover

It is generally recognized that surface cover by organic residues (e.g. mulch), inorganic materials (e.g. geotextiles), vegetation and rock fragments have a significant impact on soil erosion.

GOVERS et al. (2006) reported that intensity of water erosion is strongly related to the presence and density of rock fragments and vegetation (living plants and/or residues) on the soil.

Several investigations on the impact of mulching on runoff have been conducted, addressing the effect of cover densities on surface flow, soil moisture, evapotranspiration and soil temperature (e.g. COOK et al., 2006; MONTENEGRO et al., 2013a). JORDÁN et al. (2010) showed that long term mulching application improved physical and chemical properties of a semiarid soil in Spain. Increase in rainfall interception, delay in runoff generation, and reduction in runoff and sediment yield were observed under mulching conditions. An important aspect highlighted by the authors was the exhaustion of available erodible particles after storms longer than 30 minutes, thus reducing sediment transport. In a laboratory study, MONTENEGRO et al. (2013a) applied a sequence of intermittent rainfall patterns with different intensities and patterns, under the presence of different mulch cover densities. They found that mulching dramatically reduced erosion rates, especially during the rainfall events with higher intensity. Also, mulch increased infiltration and controlled temperature fluctuations in soil. PRATS et al. (2015, 2017) observed that mulching 1/3, 2/3 and 3/3 of the flume's length with forest residues at 70% ground cover, significantly reduced soil loss, but not runoff. At 50% ground cover, only the application of mulch over the whole plot was able to reduce soil loss significantly. Sieved forest residue mulch was less effective in reducing runoff (10%) but more effective in reducing erosion (65%), as compared to the straw mulch (25 and 50% runoff and soil loss reduction, respectively) in the study presented in ABRANTES et al. (2018b). In these studies (ABRANTES et al., 2018b; PRATS et al., 2015, 2017) the authors observed that mulching effectiveness decreased with water input. In a study by LOCH (2000), erosion from a simulated storm was greatly reduced by vegetation cover, declining approximately 98% from 0 to 47% of vegetative covers. According to LI et al. (2008) the presence of vegetation cover resulted in high infiltration rates, with unsaturated hydraulic conductivities significantly greater for the vegetated surface than for the rock fragment covered surface and bare soil surface.

Rock fragment cover has ambiguous effects on overland flow and infiltration rates. While studying the effect of rock fragments in the rain splash soil erosion, JOMAA et al. (2012) observed that the presence of rock fragments protected the soil from raindrop splashes and from sealing, therefore preserving the original soil structure and infiltration rate. However, this effect was conditioned by the size and spatial distribution of the rock fragments. POESEN et al. (1999) found that surface rock fragments are less efficient in decreasing concentrated flow erosion rates when the topsoil is dry, than when the topsoil is wet. Surface rock fragments seemed to protect the underlying soil more efficiently when it has been already wet for some time. According to LI et al. (2008) rock fragments had no obvious effect on water infiltration and soil hydraulic conductivity as compared with bare soils. In laboratory and field, PRATS et al. (2018) found that the presence of rocks, with 2 to 3 cm in size, on the top of the soil surface, significantly reduced soil loss. Surface runoff was reduced but not significantly.

2.3.4. Soil hydraulic characteristics

Water movement on soil and the associated transport of fertilizers, pesticides and other pollutants in the soil have significant impact on hydrological response and water quality (e.g. BEVEN et al., 2006; KÖHNE et al., 2009; VAN DER HEIJDEN et al., 2013).

Permeability is the measure of the soil's ability to allow water to flow through its pores or voids. It depends not only on the pores but also to how they are connected and is affected, amongst other factors, by land use, soil organisms, soil moisture and precipitation/irrigation. Permeability is one of the most important soil property of interest to engineer's purposes: i) Many hydrological models require estimations of permeability to predict overland flow; ii) Changes in permeability can provide an early warning of soil degradation, flood risk and erosion; and iii) Permeability is the key factor for the design of subsurface drainage systems.

Macropores and water flow in soils and substrates are complex and related to topics like preferential flow, non-equilibrium flow and dual-continuum, and have been the subject of many studies in the last decades (e.g. the reviews by BEVEN and GERMANN, in 1982, and, most recently, 30 years later, BEVEN and GERMANN, in 2013). Macropore is defined as a pore space which allows water to move through the soil under gravity without being restrained by capillary tension (BEVEN and GERMANN 1982) and can be formed by the cracking of the surface material or by biological activity (e.g. ants, earthworms, burrowing mammals, roots). Some root systems, earthworm and ant burrows extend for many metres below the surface and can have a significant effect on the infiltration rate. Robert E. Horton was already aware of the effects of macropores on infiltration (e.g. BEVEN, 2004). Since macropores affect soil permeability they directly influence other hydrological processes (e.g. surface runoff and associated transport processes). Macropores convey water to greater depths with higher speed, thus influencing water infiltration into the soil and solute transport. According to VILLHOLTH (1998) in shallow unsaturated soils the effect of macropore flow can be manifested through very short arrival times of surface-applied or derived substances to the groundwater. Macropores also directly affect the flow of air into the soil, the root growth of plants and biological activity (e.g. JARVIS, 2007; LUO et al., 2010; PERRET et al., 1999). Therefore, a high macroporosity enhances air and water movement in the soil, promoting also infiltration and root penetration.

Soil water repellency (also called soil hydrophobicity) is another characteristic of soil hydraulics that affects different aspects of surface hydrology. Soil water repellency can alter infiltration and water storage capacity of soils, enhancing infiltration by preferential flow and/or enhancing surface runoff generation and associated erosion (KEIZER et al., 2005b; LEIGHTON-BOYCE et al., 2007; RITSEMA and DEKKER, 1994; SHAKESBY et al., 1993; VIEIRA et al., 2014). Also, by altering water availability SWR can indirectly affect seed germination, seed establishment and plant growth (DOERR et al., 2000).

Repellent soils have been found in fire affected forest lands (BADÍA-VILLAS et al., 2014; KEIZER et al., 2008; MATAIX-SOLERA and DOERR, 2004; SHAKESBY, 2011), but also in

pine and eucalypt forest lands not affected by fires and in agricultural lands with high soil organic matter content (DOERR et al., 2000, KEIZER et al., 2007, SANTOS et al., 2013). Other factors, such as soil moisture (CHAU et al., 2014; FERREIRA et al., 2016; KEIZER et al., 2005a; LEIGHTON-BOYCE et al., 2005), presence of fungi and bacteria species (SCHAUMANN et al., 2007), soil texture and structure (URBANEK et al., 2007) and soil organic carbon content (WIJEWARDANA et al., 2016) have shown to cause and/or influence soil water repellency. However, its ultimate origin is the coating of soil particles with hydrophobic organic substances usually released by plants or decomposing plant material (DEKKER and RITSEMA, 1994; KEIZER et al., 2005c).

2.4. Measurement techniques in surface hydrology

2.4.1. Rainfall characteristics

Many studies of rain have typically concentrated on its average properties over sufficiently large volumes and time intervals, and not on characterizing the exact positions, sizes and fall speeds of the individual raindrops. In such case, the stochastic and discrete nature of rainfall at smaller spatial and temporal scales is usually treated only in a statistical sense. Some relatively recent developments have contributed to the increased interest of the hydrological community in the microstructure of rainfall and the attention devoted to understanding processes at the land surface, such as soil detachment and erosion by raindrop impact, infiltration of rain water into the soil, surface runoff and interception by vegetation canopies. In general, these are highly nonlinear processes to which every raindrop can make a significant contribution. One example is the use of weather radar for estimating the spatial and temporal distribution of rainfall (e.g. TETZLAFF and UHLENBROOK, 2005).

Some examples of earlier proposed techniques that provide indirect estimation of the number and size of the raindrops arriving at a surface during a particular sample interval, are: i) The flour method (e.g. BENTLEY, 1904); ii) The blotter paper stain method (e.g. MAGARVEY, 1957); and iii) The oil method (e.g. EIGEL and MOORE, 1983). PEARSON and MARTIN (1957) offer a review of early attempts to assess the number, size and fall speed of raindrops, at the edge of technological developments that have changed considerably the approaches used to obtain such data. These latter measurement techniques will work well for sparse raindrops, not a heavy rain (which will just spread all over the surfaces). Moreover, some of these simple techniques involve quite time-consuming data processing; in addition, their accuracy and efficiency are limited because they depend a lot on human measurement.

There have been some developments in relation to assessing raindrop properties. Examples of devices and early studies that provide instantaneous measurements of the number and size of raindrops, are the raindrop camera (e.g. JONES, 1992), the optical array probe

(e.g. KNOLLENBERG, 1970), the electromechanical disdrometers (e.g. JOSS and WALDVOGEL, 1969) and the optical spectrometers (e.g. BRADLEY and STOW, 1974). While offering the possibility to acquire high resolution data and continuous records, some of the latter techniques involve using expensive equipment and require the capability to handle and analyse large data sets. The absence of required conditions makes it still necessary to consider the possibility of using simplified methods to get insight into the drop size distribution.

2.4.2. Soil surface morphology

An accurate modelling of surface hydrological processes requires detailed information on soil surface microrelief and rill morphology with adequate resolution and precision (e.g. GOVERS et al., 2007; KAMPHORST and DUVAL, 2001; KAMPHORST et al., 2000; LEI et al., 1998; MANCILLA et al., 2005; NEARING, 1998; PLANCHON et al., 2001). A wide range of techniques can be used to characterise and measure the soil surface microrelief and rill morphology (e.g. width, depth) with an adequate resolution and precision for water erosion studies and modelling. Yet, this is a task that may require a large consumption of time and/or resources (e.g. JESTER and KLIK, 2005). Measurement techniques can be classified as contact and noncontact and two-dimensional (2D) and three-dimensional (3D).

The most common contact techniques, used to characterize soil surface roughness are profile or pin meters (e.g. GILLEY and KOTTWITZ, 1995), chain and set methods (e.g. MERRILL et al., 2001) and automatic relief meters (e.g. HANSEN et al., 1999). These techniques measure soil surface roughness along a single profile. The main benefits of these techniques are the low cost and easy handling. However, these techniques present limited resolution and may induce deformation to the soil surface.

Nowadays, there are very accurate noncontact techniques that allow the generation of digital elevation models with enough resolution for microrelief analysis, being the most commonly used the laser techniques (e.g. DARBOUX and HUANG, 2003; EITEL et al., 2011) and the photographic techniques like photogrammetry methods (e.g. RIEKE-ZAPP and NEARING, 2005; WARNER, 1995) and shadow analyses (e.g. GARCIA MORENO et al., 2008, 2010). While laser techniques consist mainly in 2D devices measuring roughness, photogrammetry is able to measure soil surface roughness in 3D giving a more realistic value of the roughness measure. Other noncontact techniques using ground based (e.g. SANKEY et al., 2011) and airborne (TURNER et al., 2014) light detection and ranging devices (LiDAR) and acoustic backscatter devices (e.g. OELZE et al., 2003; ZRIBI et al., 2014) have also been applied to characterize the surface morphology.

One of the main problems when assessing information on soil surface microrelief for water erosion studies is the presence of vegetation covering the soil surface (i.e. mulching). In fact, with high vegetation covers microrelief cannot be estimated by these techniques, since you measure the mulch characteristics instead of the soil surface bellow.

2.4.3. Soil hydraulic characteristics

Several experimental investigations have been carried out aiming to the development of measurement techniques for estimating soil hydraulic characteristics (e.g. HAVERKAMP et al., 2006; REYNOLDS and ELRICK, 1985; ŠIMŮNEK and HOPMANS, 2002; VEREECKEN et al., 2007).

In general, small scale measurement techniques rely on precise and time-consuming experimental procedures. In situ experimental measurements can be carried out in the field, based on small scale infiltration tests under saturated or unsaturated soil conditions. Among these methods, the double-ring infiltrometer, the Beerkan method developed by BRAUD et al. (2005) and the Guelph Permeameter method, proposed by REYNOLDS and ELRICK (1985) have been largely adopted (e.g. SILVA et al., 2012; XU et al., 2009). These methods can be conveniently applied to the field conditions because of the simple experimental apparatus. However, e.g. the ring methods cannot be used on a sloping soil surface. In such cases, experimental permeability measurements must be obtained in the laboratory using disturbed or undisturbed soil samples. Since, permeability is highly variable over different spatial scales, traditional permeability tests need to be grouped or scaled to bring out spatial coherence (WANG et al., 2001) in order to properly represent distributed patterns of variations and for distributed spatial analysis.

The development of simple cost-effective approaches for determining the occurrence of preferential flow (e.g. through macropores) is required to identify risks of agrochemical mobilisation to groundwater (e.g. HARDIE et al., 2013). A review of different approaches for identifying the occurrence and extent of preferential flow through the soil is presented in ALLAIRE et al. (2009). One approach identified by the author, is to use X-ray and magnetic resonance imaging (MRI) to observe the soil structure and soil porosity. These techniques resulted in very good representations of the network pore system with very high spatial resolution. However, these systems require staff with very specific technical knowledge, are very expensive and are difficult to handle. Also, most of the times, it is not possible to transport that equipment to the filed. Thus, requiring the transport of samples to the scanning site (e.g. hospital), which, in general, is not feasible.

Other approach identified by ALLAIRE et al. (2009) is to use dye tracers. The dye tracer technique (e.g. FLURY et al., 1994) consists in the application of a dye at the soil surface either with water or before water infiltration, excavation of the soil profile after a specified infiltration time, analysis of visual and/or photo interpretation of dye distribution with computer software. These approaches are easy to apply, inexpensive and gives a range of macroporosity levels and other features causing preferential flow. However, they are imprecise, the characteristics of the dye may affect interpretation, are destructive and labour intensive. According to ALLAIRE et al. (2009) much progress has recently been made in quantifying preferential flow in soil. In particular, dye tracing with image analysis has significantly evolved in recent years so that dye concentrations from photos can be quantified and even the type of interaction between macropores and the matrix can now be evaluated.

Regarding soil water repellency, the two most commonly used techniques to measure it are the Molarity of an Ethanol Droplet (MED) test, also known as Percentage of Ethanol test or Critical Surface Tension test (LETEY, 1969) and the Water Drop Penetration Time (WDPT) test (VAN'TWOUDT, 1959).The MED test uses the surface tension of an ethanol solution to indirectly measure the apparent surface tension of the soil surface, i.e. how strongly water is repelled. The WDPT determines how long repellency persists in the contact area of a water drop. Both the MED and WDPT tests provide quantitative data, but the subsequent classification or characterization of these data vary with the objective of the investigator and perception of what constitutes low or high repellency severity. Other techniques to measure soil water repellency include measurement of the water-soil contact angle (LETEY et al., 1962), measurement of ethanol and water ethanol sorptivity (TILLMAN et al., 1989), measurement of the water entry pressure head of a soil (CARRILLO et al., 1999), and the sessile drop method using a goniometer-fitted microscope (BACHMANN et al., 2000). Most of these techniques have been compared in various papers such as COSENTINO et al. (2010), DEKKER et al. (2009), KING (1981) and LETEY et al. (2000).

An important problem in assessing the hydrological role of soil water repellency is that most of the existing techniques to quantify soil water repellency require specialized equipment and are best suited for use in the laboratory (DEKKER et al., 2009). Some of these techniques require air-dried or oven-dried samples which may not be very representative of the conditions occurring in the field. Also, some of these techniques (e.g. WDPT) can be very time consuming in the presence of strong to extreme repellency. Other problem with most of the existing techniques is that they provide punctual data, not revealing the spatial extent of the repellency severity. At field and landscape scales, punctual measurements must be grouped or scaled to bring out spatial coherence, in order to properly map soil water repellency and represent distributed patterns of variations. This presents a laborious and time-consuming task.

2.4.4. Flow velocity

Most research related to hydraulics and hydrology relies on the accurate measurements of flow velocity. In particular, shallow flows that often occur in natural and urbanized drainage basins, have important implications, such as water erosion and water quality. Flow velocity is a basic hydraulic property of overland flow and its precise calculation is a necessary component of all process based hydrological models such as soil erosion and rill development models (e.g. GIMÉNEZ et al., 2004; GOVERS, 1992; WIRTZ et al., 2012), as well as in modelling sediment and solute transport by runoff (e.g. LEI et al., 2010; MÜGLER et al., 2011).

Flow velocity measuring techniques vary with water body dimension, its accessibility and characteristics. Recently, significant developments have been made in sensing technology, resulting in a wide spectrum of powerful and versatile options for high accuracy flow velocity data. However, measurement devices may have some limitations when operating outside their ideal measurement conditions. Particularly for shallow flows, the characterization of the velocity fields

is complicated, mostly because of their lack of depth (anything from several millimetres to a few centimetres) and other problems, such as variability of the channel bed due to erosion, presence of sediment and other debris in the flow or even the presence of vegetation concealing the measuring area. This restricts the use of many flow measuring devices.

For deeper water bodies (e.g. large rivers) flow velocity can be measured with current meters or acoustic Doppler techniques, such as acoustic Doppler velocimetry (ADV) or acoustic Doppler current profiler (ADCP), at determined monitoring sections (e.g. KIMIAGHALAM et al., 2016; MUSTE et al., 2004a, 2004b). Although intrusive, these techniques do provide a reliable characterization of the flow velocity vertical profile; however, these instruments cannot always be used in very shallow water. Other techniques, such as satellites, radars and microwave sensors, hand-held or coupled in a drone, can be used to estimate surface flow velocity accurately and non-intrusively (e.g. BJERKLIE, 2007; BJERKLIE et al., 2003; FULTON and OSTROWSKI, 2008); however, these methods are usually very costly and satellite data are typically applied to large water bodies.

For a long time, common techniques used in shallow flow velocity measurements for soil erosion studies were based on the determination of the travel time of a tracer across a defined section, in both laboratory (e.g. ABRAHAMS and ATKINSON, 1993; GIMÉNEZ and GOVERS, 2002) and field conditions (e.g. HORTON et al., 1934; WIRTZ et al., 2012). In fact, many researchers regard tracer methods as crude methods that yield a maximum flow velocity that must be corrected to give a mean velocity. However, in shallow muddy flows, with depths of a few millimetres to a few centimetres, it is not always possible to use the more sophisticated methods to measure true mean flow velocity, such as ADV, ACDP. When using tracers, the accuracy of the measurement depends to a great extent on the tracer added to the flow and on the quality of its detection in the flow. According to FLURY and WAI (2003) an ideal tracer for hydro-environmental research should have the following characteristics: i) Movement similar to water; ii) Be conservative, i.e. without degradation during the measurement time; iii) Not show sorption to other environment components (e.g. soil, sediments, rocks); iv) Be clearly distinguishable from the background of the system; v) Be detectable either by chemical analysis or by visualization; and vi) Low toxicological impact on the study environment.

Among the different materials that have been tested as tracers in flow velocity experiments are natural and radioactive isotopes (NIAZI et al., 2017), floating objects (TAURO et al., 2012a), fluorescent particles (TAURO et al., 2012a, 2012b, 2012c), bacteria (e.g. MAURICE et al., 2010), salts (e.g. CALKINS and DUNNE, 1970; DAY, 1977; LEI et al., 2005, 2010; SHI et al., 2012) and dyes (e.g. ABRAHAMS et al., 1986; DUNKERLEY, 2003; FLURY and FLÜHLER, 1993; HOLDEN et al., 2008; TAZIOLI, 2011). Depending on the used tracer, optical cameras (e.g. for dyes, floating objects), fluorometers (e.g. for fluorescent particles, fluorescent dyes) or electrical conductivity sensors (e.g. for salt tracers), can be used. A review of tracer technology in hydrologic studies is presented in LEIBUNDGUT et al. (2009).

Optical methods for flow characterization, such as particle image velocimetry (PIV) and particle tracking velocimetry (PTV), have seen great development and have been adjusted so that they can be used in natural environments (e.g. COZ et al., 2010; KANTOUSH et al., 2011; TAURO et al., 2014, 2016). These methods combine digital cameras and lasers to track the movement of particles (tracers) dispersed in the water (e.g. fluorescent particles, air bubbles, floating objects) and thereby better estimate the surface flow velocity. LEI et al. (2005) proposed an alternative methodology for determining shallow flow velocities based on an advection-dispersion solute transport model. This numerical technique consisted on fitting the analytical solution of the differential equation for solute transport in shallow flows to solute transport data obtained by means of a salt tracer. This fitting was done by minimising the sum of squared errors between modelled and experimentally observed data. This method has been used in several studies involving the determination of shallow flow velocity (BAN et al., 2016; CHEN et al., 2017; HUANG et al., 2018; LEI et al., 2010, 2013; RAHMA et al., 2013; SHI et al., 2012, 2016; ZHUANG et al., 2018).

2.5. Infrared thermography

2.5.1. Background, operating principles and applications

Infrared thermography is a technique with which it is possible to detect and measure the radiated infrared (thermal) energy emitted from the surface of a given material. Infrared energy is the electromagnetic radiation with wavelengths between 0.74 microns and 1000 microns, i.e. the zone in the electromagnetic spectrum between the visible light and microwaves. Every object with temperature above the absolute zero emits infrared energy and its emittance increases with temperature. Since the human eye can only detect a narrow range of wavelengths, between 0.4 to 0.7 microns (visible wavelength), infrared thermographic systems must be used to detect and measure the infrared radiation. These systems are mainly comprised of infrared cameras that use special lenses to detect the infrared radiation in their field of view, which is converted to digital signals. These signals are then processed and are converted to temperature values that are associated to a colour scale and are displayed as a thermal image (i.e. group of pixels each one with a colour associated to a temperature value) in a monitor associated to the camera or in a computer.

When using these systems, it is important to note that: i) Most common infrared cameras detect radiation in the long-wavelength infrared (8μm-14μm), not the entire infrared spectrum (materials in the temperature range from approximately -83 ºC to 726 ºC emit radiation in this spectral range); ii) Human eye transparent materials (e.g. transparent glass, transparent acrylic) can be opaque in the long-wavelength infrared, blocking the radiation emitted by the objects behind it; and iii) Two materials with different emissivity (physical property of any material), at the same temperature, may appear differently in the thermal image (the contrary can also happen, i.e. two materials with different emissivity, at different temperatures, may appear equal in the thermal image).

During the last decades, the development of thermographic systems has been rapidly growing. According to GADE and MOESLUND (2014), although infrared light was discovered by William Herschel around 1800, the first infrared scanning devices were only built in the late 1940s and 1950s, for the American military for the purpose of night vision. The first commercial products were only produced in 1983 and opened up a large area of new applications. According to ROGALSKI (2011), on the last 25 years array size has been increasing at an exponential rate, with the number of pixels doubling every 19 months. Recently Teledyne Imaging Sensors developed an infrared imaging sensor that combining a total of 35 arrays each with 2048 × 2048 pixels, producing an image with 147 megapixels.

Thermography is a versatile technique and allows us to measure the spatial and temporal variability of temperature in a non-invasive and a non-destructive way. Nowadays infrared thermography is used in a variety of fields (BAGAVATHIAPPAN et al., 2013; GADE and MOESLUND, 2014): i) In veterinary, to diagnose diseases, control reproductive processes, analyse animal behaviour, detect and estimate population sizes; ii) In food production, to obtain information about the quality, such as damage and bruises in fruits and vegetables; iii) In building inspection, to detect heat loss from buildings (e.g. thermal bridges), to detect termites; iv) To detect an anomalous gas and track to locate the source of the gas leak; v) In industry, as a diagnostic tool for electrical joints in power transmission systems, to evaluate specific properties in different materials, detect malfunctions in objects; vi) In motorized sports for dynamic analysis of the temperature of the tires during a race; v) For fire detection in particular homes, industrial facilities and forests; vi) For military purposes, to detect and locate the origin of a gunfire, detect mines, vi) In the surveillance and detection of intruders; vii) For safety applications like the detection of fall accidents or unusual inactivity; vii) In face recognition, to estimate anxiety levels, evaluate emotion of, drivers detection; viii) In medicine, to breast cancer detection, diabetes neuropathy, fever screening, dental diagnosis, brain imaging; and ix) In physical rehabilitation to monitor and interpret communications from people with motor impairments.

For more information about the background history of infrared thermography, operating principles, applications, types of sensors, composition of the lenses and other characteristics of the technology, along with the recent developments observed in this field, see the reviews by BAGAVATHIAPPAN et al. (2013), GADE and MOESLUND (2014) and ROGALSKI (2011).

2.5.2. Applications in surface hydrology

Infrared thermography has been successfully employed as a high spatial and temporal resolution non-intrusive imaging tool in surface hydrology. Some of the first hydrologic studies using infrared thermography, rely on satellite data, and date back to the 1970's and 1980's, after the launch of the first satellites equipped with infrared sensors. Infrared satellite imagery has been used to estimate rainfall over large space and time scales (GRIFFITH et al., 1978), to assess evapotranspiration over large agricultural regions (e.g. TACONET et al., 1986), to identify the potential of groundwater

flow, that can provide valuable input to the hydrological modelling, the selection of sites for solid waste disposal and non-point-source modelling (e.g. BOBBA et al., 1992). Satellite based infrared systems have been used to characterize temperature patterns in oceans (e.g. EMERY and YU, 1997) and lakes (e.g. HOOK et al., 2003).

Since the 1980's, thermal sensing has been used and has been proved to be particularly useful for the study of plant-water relations and to evaluate soil water deficit and crop water stress of several agricultural and horticultural crops. A few examples are sunflowers (HASHIMOTO et al., 1984), muskmelons (CLARKE 1997), grapevines (GRANT et al., 2007), soybean and cotton crops (O'SHAUGHNESSY et al., 2011) and olive orchards (EGEA et al., 2017). URRESTARAZU (2013) evaluate and determinate the capability of using infrared thermography as an early, rapid and simple method for diagnosing salt tolerance or the salt stress level of a crop.

During the last decades, thanks to the technological development of high resolution, cost-effective and robust handheld (i.e. portable) thermal imaging cameras, the use of infrared thermography techniques in surface hydrology have undergone a significant increase. The increase in sensors accuracy and spatial resolution, together with faster measurement and processing times and improved quality of the thermographic data, allow hydrologists to rapidly image real-time variations in temperature at high resolution in the field at scales from a few millimetres to several meters. These studies can be carried at the air level by attaching the camera to an airborne vehicle (e.g. drone) or at the ground level (e.g. hand-held, mounted on a tripod).

Differences between temperatures in a stream and surrounding sediments can be analysed to trace the movement of groundwater to and from streams, and to better understand the magnitudes and mechanisms of stream/groundwater exchanges (e.g. STONESTROM and CONSTANTZ, 2003). DANIELESCU et al. (2009), KELLY et al. (2018) and MEJÍAS et al. (2012) used infrared cameras mounted in aircrafts for mapping groundwater discharge in shallow estuaries and harbours, provided that there is a thermal contrast between groundwater and the receiving surface waters. Through handheld infrared data acquisition, CHEN et al. (2009) and SCHUETZ and WEILER (2011) mapped and quantified localized groundwater inflow into streams.

Thermal infrared remote sensing has proven effective for mapping temperature heterogeneity of streams and rivers (e.g. CARDENAS et al., 2008; TONOLLA et al., 2010). CARDENAS et al. (2008) verified that remotely sensed stream temperatures acquired with handheld infrared camera compared well with those measured with a digital thermometer. Thermal images shown a significant spatial and temporal stream thermal variability. Such results have consequences for thermally sensitive hydro-ecological processes and implications for their modelling. TONOLLA et al. (2010) quantified the spatial and temporal thermal heterogeneity of entire river floodplains, characterized aquatic and terrestrial floodplain habitat types, and quantified vertical temperature patterns within unsaturated gravel sediment deposits. In this study, an infrared camera was mounted on a tripod installed at the rim of steep mountains fringing on two floodplains, thereby allowing the entire valley bottom to be thermally mapped.

Climate change is altering river temperature regimes, modifying habitats temperatures and the dynamics of temperature sensitive species. The ability to map river temperature is therefore important for understanding the impacts of future warming (e.g. BAKER et al., 2019; DUGDALE et al., 2019). DUGDALE et al., 2013 used an infrared camera mounted on a helicopter platform to acquire thermal imagery of an Atlantic salmon river in Québec, Canada, with the objective of characterize the temporal variability in thermal refuges and broader scale water temperature complexity. According to BAKER et al. (2019), while ground-based infrared thermography can be useful for qualitatively identifying stream temperature differences, acquisition of absolute stream temperatures remains difficult due to interference from reflected radiation. In this study, analytical and empirical methods were used to extract absolute stream temperatures from infrared imagery. Since reflected temperatures and stream surface emissivity can be difficult to quantify, the empirical correction approach offered the best alternative.

PFISTER et al. (2010) used ground-based thermal imagery as a simple, practical tool, for mapping saturated area connectivity and dynamics. It was possible to discriminate between areas with snow cover, snow melt, soil seepage and stream water. It was possible to detect when and where variably saturated areas were active and when connectivity existed between the hillslope–riparian–stream systems. According to PFISTER et al. (2010), this was a simple and inexpensive technology for sequential mapping and characterisation of surface saturated areas and a useful complement to conventional tracer techniques.

More recently, innovative infrared thermography techniques with specific methodologies have been developed and tested to evaluate different hydraulic aspects of the soil (e.g. crust formations, evaporative fluxes, rock porosity, permeability, macroporosity, soil water repellency). Generally, these started with exploratory and proof of the concept studies performed under controlled laboratory conditions, thus proposing a wide range of ideas for further scientific researches aiming at implementing and validating these techniques, namely in real field conditions.

SOLIMAN et al. (2010) used infrared thermography to distinguishing soil surface crust formations. Two samples of surface crust formed under different conditions and one sample of a bedrock soil, with $6.0 \times 4.5 \times 2.5$ cm^3, were collected and used to evaluate the technique in laboratory. The technique consisted in heating the samples for 420 min, using two 500 W halogen lamps, and in recording the heating and later cooling with an infrared camera. Thermal inertia of the samples (i.e. heating and cooling rates) showed to be directly proportional to density and inversely proportional to porosity. Therefore, the two samples of surface crust presented higher thermal inertia. However, no significant differences were observed between the two surface crust samples, despite the differences in the formation process. The advantages this technique are: i) Minimum arrangements and instrumentation (a heat input source and a suitable infrared camera); ii) Non-invasive nature that requires minimum preparation of the samples and can estimate the thermal inertia from surface measurements; and iii) Allow multiple comparisons of samples extracted from different geomorphological units (e.g. comparing surface crusts formed in upstream and downstream of a

dry valley), where variation of thermal inertia is linked to variation of depositional environments and cementing processes. However, the technique requires large measurement time and it suits only in dry and low moisture content samples. SHAHRAEENI and OR (2010, 2011) presented a new method for the non-invasive determination of spatially and temporally resolved distributions of evaporative fluxes from heterogeneous porous surfaces based on infrared thermography. High resolution infrared imagery of evaporating surface temperature fields provides input to a surface energy balance simplified solution to yield the evaporation rate spatial distribution. In laboratory conditions, the authors studied evaporation patterns from surfaces of initially saturated sand columns containing sharp vertical textural contrasts (fine-sand inclusion in coarse-sand background) to evaluate the performance of the proposed method. Spatial and temporal infrared thermal data were numerically inverted to obtain evaporation flux values that are compared with rates of mass loss from direct weighing of the samples. MINEO and PAPPALARDO (2019), presented an innovative potential laboratory test for the indirect estimation of porosity of intact rock specimens. Their hypothesis was based on an existence of a relation between the cooling of previously heated rocks and their porosity. After an initial heating phase, the cooling of the rocks was monitored through infrared thermography. Results demonstrated that the cooling trend of rocks within the first 10 min of test represented a reliable index for the indirect quantification of their porosity.

Runoff initiation from raindrops falling onto an inclined planar impervious surface was investigated in a laboratory experiment by NEZLOBIN et al. (2013). The authors used an infrared camera to visualize different processes of runoff initiation, by applying simulated rainfall (water at a temperature of approximately 18 ºC) over an inclined planar impervious surface (at a temperature at around 23–24 ºC). The effect of the surface inclination on the runoff initiation process was evaluated. Infrared thermography allowed visualizing drop cluster formation, clusters merging, coalescence shrink and wetted trails at the surface.

One technique studied during this doctoral study was the estimation of raindrops size by means of infrared thermography (DE LIMA et al., 2015a). Rain samples were collected on pre-heated acrylic boards, which were exposed to rain during an instant, and thermograms were recorded. The area of the thermal stains (i.e. signatures of the raindrops) emerging on the board was measured and converted to drop diameters, applying a calibration equation. Diameters of natural raindrops, estimated using this technique, were compared with laser disdrometer measurements. Results confirmed the usefulness of this simple technique for sizing and counting raindrops, although it is unsatisfactory in light rain or drizzle situations.

An innovative technique to estimate soil surface microrelief and rill morphology using infrared thermography is presented in ABRANTES and DE LIMA (2014) and DE LIMA and ABRANTES (2014a). The technique was tested in laboratory in a surface with artificially created rills and in a surface eroded by flowing water, in bare soil conditions and in the presence of different mulch densities. Heated water was used to create a temperature gradient on the soil surface and high-

resolution soil surface thermal imaging were obtained using a portable infrared camera. The authors were able to generate 3D models of soil surface elevation for both bare soil and soil covered with organic residue. This technique is presented in Chapter 3 of this Thesis.

In DE LIMA et al. (2014b) a new technique to map soil surface permeability and to identify preferential flow at the soil surface using infrared thermography is presented. The technique was tested in a laboratory flume, where different scenarios were tested using soils with different permeability. Heated water was applied to the soil surface and preferentially infiltrated and penetrated the soil in the higher permeability areas which, consequently, presented higher temperatures that could be recorded with an infrared video camera. This technique is presented in Chapter 4 of this Thesis. Further tests were conducted in the field (data submitted for publication), where infrared thermography was used for estimating the soil moisture and unsaturated hydraulic conductivity of two distinct soils in the Mimoso representative catchment, located in the semiarid region of Pernambuco state, Brazil. Based on the obtained data, it was possible to estimate the unsaturated soil hydraulic conductivity of the two soils, relevant to the analysis of hydrological processes, such as infiltration.

Infrared thermography was used to map soil surface macroporosity. This technique was first studied in a laboratory soil flume (DE LIMA et al., 2014a). The technique consisted in applying heated water to the soil surface and register the brief accumulation of water in macropores (artificially created at the soil surface) with an infrared video camera. The technique allowed to estimate the number, location and size of macropores with different sizes. This study is presented in Chapter 5 of this Thesis. The technique was further applied in the field on natural soil conditions in DE LIMA et al. (2014c). Field tests were carried out in the campus of the Federal Rural University of Pernambuco (UFRPE), Recife, Brazil; and in the Mimoso representative catchment, located in the semiarid region of Pernambuco state, Brazil. The technique relied on heating the soil surface with hot air for mapping soil surface macropores. In contrast to the hot water firstly used in the laboratory (DE LIMA et al., 2014a), the hot air used in the field had no destructive impact on the soil.

A technique to map soil water repellency spatial variability using infrared thermography was also developed. The technique was firstly tested in small-scale laboratory soil flume experiments, where areas of the soil surface were artificially induced with repellency, and cold water was used to create a temperature gradient on the soil surface (ABRANTES et al., 2017). A follow-up study in field conditions with natural soil water repellency was conducted in a Pine (P. pinaster) and Eucalyptus (E. globulus) forest site located in Pinhal de Marrocos, Coimbra, Portugal (ABRANTES et al., 2016). These studies are presented in Chapters 6 and 7 of this Thesis.

Many authors have exploited the use of infrared cameras and thermal tracers to estimate flow velocity (e.g. DE LIMA, 2013). SCHUETZ et al. (2012) used infrared thermal imaging combined with the injection of heated water as an artificial tracer technique to characterize the spatial distribution of flow paths and to assess transport properties in a 65 m^2 experimentally constructed wetland with water depths between 0.1-0.2 m. For the studied conditions the authors observed that

heated water can be used as a conservative artificial tracer for plot scale experiments. LIANG et al. (2012) studied the feasibility of using thermal imaging to investigate the scalar transport process in shallow jet and wake flows with waters depths of 35 mm and 45 mm by adding warm water to the flow. The authors found that the thermal imaging technique has great potential as a quantitative flow visualisation technique for studying shallow turbulent dispersion characteristics. TAURO and GRIMALDI (2017) applied PTV techniques to track the movement a thermal tracer deployed in a natural stream, as a surface flow velocity measurement technique. Thermal videos were collected with infrared camera and ice dices were used as tracer. Due to the meagre quantity of tracing material and the simplicity of the experimental setup, the methodology showed to be promising and advantageous against standard optical methods. Specifically, the combined use of thermal images and PTV leads to reduced image pre-processing times and to accurate reconstruction of the surface flow velocity field. Also, optical image-based methods are more severely affected by illumination conditions and tracers' visibility. On the other hand, some drawbacks of this methodology were the practical handling of the ice dices, cost of thermal cameras, and higher degree of supervision in applying PTV rather than algorithms based on high-speed cross-correlation. Under controlled laboratory conditions, MUJTABA and DE LIMA (2018) tested the capability of cold oil droplets as a new thermal particle tracer to measure the velocity of shallow overland flows (< 2 mm depth) using an infrared-based PTV technique. Again, in this study, the authors stressed the potential of using thermal imaging to estimate the velocity of shallow water bodies, because of the tracer's conspicuous visibility and independence from illuminating conditions. LIN et al. (2019) tested several thermal tracers, in both small natural streams and laboratory conditions, and developed a proper tracking algorithm (i.e. PTV technique) to measure surface flow velocities. When applied to imagery from a thermal camera, their tracking algorithm outperformed commonly used tracking methods.

Part of the research developed in this doctoral study was dedicated to the development and validation of thermal tracer techniques. Firstly, overland and rill flow velocities were estimated by means of dye and thermal tracers and results of the two tracer techniques were compared (DE LIMA and ABRANTES, 2014b). Secondly, a triple tracer experiment was conducted to compare the thermal tracer technique with dye and salt tracer techniques under different hydraulic conditions, namely bottom slope, bottom roughness and flow depth (ABRANTES et al., 2018a). Thirdly, an analytical solution of an advection–dispersion transport equation was combined with thermal tracer data to estimate shallow flow velocity (ABRANTES et al., 2019). These studies are presented in Chapters 8, 9 and 10 of this Thesis. Field tests using thermal tracers were also carried out during the doctoral study, and were presented in DE LIMA et al., 2015b. In the field, thermography was particularly useful when dealing with very shallow water depths, where the current available options have many limitations, often challenged by minimum working depths of equipment, or other unfavourable conditions. The inexistence of constraints regarding the use of thermography in the presence of sediments (muddy flows), debris or rocks is another advantage (usually also a limitation for other methods).

"A rill in a barnyard and the Grand Canyon represent, in the main, stages of valley erosion that began some millions of years apart."

- George Gaylord Simpson

3. CAN INFRARED THERMOGRAPHY BE USED TO ESTIMATE SOIL SURFACE MICRORELIEEF AND RILL MORPHOLOGY?[1]

3.1. Abstract

This study presents a new technique to estimate soil microrelief using infrared thermography. This technique can be specifically useful to characterize soil surface microrelief, to identify preferential flow paths in mulching conditions and to estimate soil surface elevation where other microrelief measurement techniques cannot be successfully applied. Laboratory tests were carried out using two soil flumes where different scenarios were tested: scenarios with artificial rills created at the soil surface and scenarios with a surface eroded by flowing water. The technique was tested both in bare soil conditions and in the presence of different mulching surface cover densities. Heated water was used, and high-resolution soil surface thermal imaging was obtained using a portable infrared video camera.

The proposed technique allows us to identify different microrelief structures at the soil surface and to visualize preferential flow paths in mulching densities up to 4 t ha^{-1}. Where other microrelief measurement techniques cannot be used, the thermography allows obtaining 3D models of the soil surface elevation, with satisfactory accuracy, knowing only 4 points of the soil surface. Higher mulch cover densities (above 4 t ha^{-1}) strongly affected the performance of the technique.

Keywords

Soil microrelief; Measurement technique; Thermography; Rill visualization

3.2. Introduction

Microrelief is the spatial arrangement of the micro-topographic variations in soil surface elevation at a scale ranging from centimetres to millimetres or less (e.g. HUANG, 1998; VIDAL VÁZQUEZ et al., 2005; PAZ-FERREIRO et al., 2008). It is the result of several factors that affect the superficial layer of the soil over the time, such as: water erosion (e.g. splash, interrill and rill erosion), wind erosion, agricultural practices (e.g. tillage, ploughing, mulching), vegetation (e.g. roots, mulch, shrubs, grass) and animal activity (e.g. ant mounds).

[1] DE LIMA, J.L.M.P. and ABRANTES, J.R.C.B. (2014). Can infrared thermography be used to estimate soil surface microrelief and rill morphology? *CATENA*, 113, 314-322. DOI:10.1016/j.catena.2013.08.011.

Microrelief has been demonstrated to strongly influence several hydrological processes, such as infiltration, runoff, sediment transport, rill formation, rill erosion (e.g. DARBOUX et al., 2001; GÓMEZ and NEARING, 2005; KIDRON, 2007; RÖMKENS et al., 2001), surface sealing, surface crusting and soil moisture (e.g. FOHRER et al., 1999; RODRÍGUEZ-CABALLERO et al., 2012), evaporation and heat flux (e.g. PRICE et al., 1998). Most of the times, an accurate modelling of those hydrological processes, especially the runoff-erosion processes (e.g. rill erosion), require detailed information on soil surface microrelief and rill morphology with adequate resolution and precision (e.g. GOVERS et al., 2007; KAMPHORST and DUVAL, 2001; KAMPHORST et al., 2000; LEI et al., 1998; MANCILLA et al., 2005; NEARING, 1998; PLANCHON et al., 2001).

One problem related with the modelling of runoff-erosion processes (e.g. rill erosion models) is the effect of the change of microrelief over the time and area in which those processes occur (e.g. ZOBECK and ONSTAD, 1987). Erosional processes modify the soil surface and create a new specific surface. For example, runoff during the latest part of a rainfall event will flow over a soil surface that may be different from the surface encountered by runoff earlier in the storm (e.g. FAVIS-MORTLOCK et al., 2000). Also, larger rills will modify the local micro-topography in a greater extent than small rills. Thus, the development of greater rills will be more successful as they were more capable of capture and convey runoff and sediments. This constitutes a positive feedback loop, between microrelief and runoff-erosion processes (e.g. FAVIS-MORTLOCK, 1998).

A wide range of techniques can be used to characterise and measure the soil surface microrelief and rill morphology (e.g. width, depth) with an adequate resolution and precision for water erosion studies and modelling. Yet, this is a task that may require a large consumption of time and/or resources (e.g. JESTER and KLIK, 2005). Measurement techniques can be classified according to the sensing type as contact and noncontact techniques. The most common contact techniques, used to characterize soil surface roughness, are profile or pin meters (e.g. GILLEY and KOTTWITZ, 1995), chain and set methods (e.g. MERRILL et al., 2001) and automatic relief meters (e.g. HANSEN et al., 1999). The principal benefits of these techniques are the low cost and easy handling. However, these techniques present limited resolution and may induce deformation to the soil surface. Nowadays, there are very accurate noncontact techniques that allow the generation of digital elevation models with enough resolution for microrelief analysis, being the most common used: laser techniques (e.g. DARBOUX and HUANG, 2003; EITEL et al., 2011); and photographic techniques like photogrammetry methods (e.g. RIEKE-ZAPP and NEARING, 2005; WARNER, 1995) and shadow analyses (GARCIA MORENO et al., 2008).

In agricultural and rural areas of arid and semiarid regions, water erosion is one of the most important soil degradation processes (e.g. MARTINEZ-MENA, 2001; MAYOR et al., 2009; CANTÓN et al., 2011). Runoff-erosion modelling is of great significance to improve soil and water conservation management in those regions (HESSEL and TENGE, 2008). One of the main problems when assessing information on soil surface microrelief for water erosion studies in agricultural semiarid environments is the presence of vegetation covering the soil surface (i.e.

mulching) that is one of the most used soil and water conservation method in those areas (e.g. MONTENEGRO et al., 2013b; TOTIN et al., 2013). In fact, with high mulching covers microrelief cannot be estimated by these techniques, since you measure the mulch characteristics instead of the soil surface bellow.

This paper presents an innovative technique to estimate soil surface microrelief and rill morphology using infrared thermography. Infrared thermography has been successfully applied as a high-resolution imaging tool in hydrological studies: surface water temperature distributions (e.g. DANIELESCU et al., 2009) and groundwater–surface water interaction (e.g. MEJÍAS et al., 2012). In particular, studies carried with portable hand-held thermography systems have been recently increasing, due to their easy handling and easy adjustment of measurement distance and scale (e.g. CARDENAS et al., 2008; PFISTER et al., 2010; SCHUETZ et al., 2012).

The main goals of this study were: i) Verify if infrared thermography can be used to visualize preferential flow paths and to identify microrelief elements (e.g. rills, depressions, mounds, ridges) namely in the presence of mulch covering the soil surface; and ii) Try to generate a 3D model of the soil surface, knowing only a few (at least two) points of the real topography. The technique presented here pretends to be specifically useful when soil surface is covered with mulch, where other microrelief measurement techniques cannot be successfully applied.

3.3. Methodology

3.3.1. Experimental setup

A schematic representation of the experimental setup used in this study is shown in Figure 3.1. All experiments presented here were conducted in laboratory.

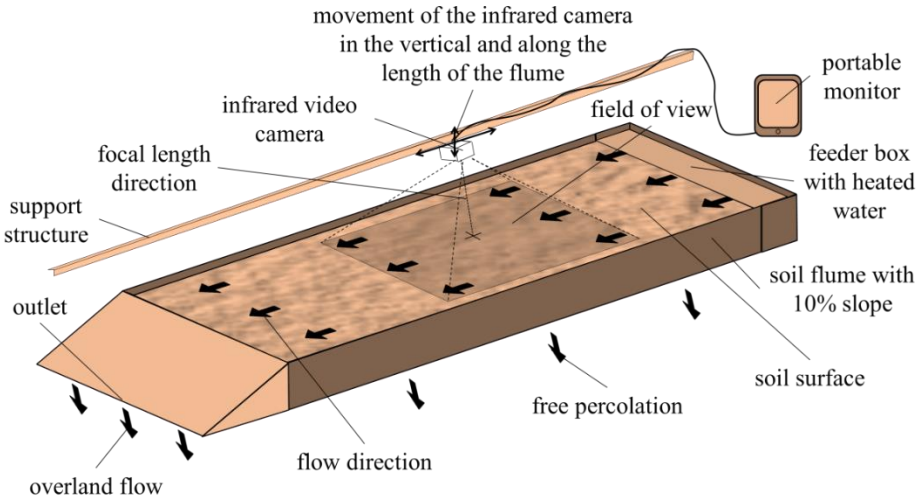

Figure 3.1. Sketch of the setup used in the laboratory tests (not at scale).

Soil flumes and soil characteristics

The experiments were carried out using two rectangular free drainage soil flumes set at a 10% slope: a narrower soil flume 0.3 m wide and a wider soil flume with a width of 1 m. Feeder boxes were installed at the upslope end of each flume which allowed the application of a constant and uniform flow of hot water to the soil surface of the flumes.

The sedimentary material used in the experiments consists of a sandy-loam soil and was collected from the right bank of River Mondego (Coimbra, Portugal). Clear signs of water erosion (e.g. rills, gullies) under natural rainfall were visible (DE LIMA et al., 2003). The soil presented 7% clay, 9% silt and 84% sand and was mainly composed of quartz, feldspars, quartzite, muscovite and clay minerals.

Both flumes and soil have been used in several research projects in the last years (e.g. DE LIMA et al., 2003, 2011, 2013a; MONTENEGRO et al., 2013a).

Infrared video camera

Soil surface and water temperatures (i.e. thermal videos and thermal imaging) were recorded with an Optris PI-160 portable infrared video camera (Optris GmbH, Germany) with an optical resolution of 160 × 120 pixels, a thermal resolution of 0.1 ºC, an accuracy of ±2%, a frame rate of 100 Hz and a lens with a field of view of 23° × 17° and focal length of 10 mm. The camera was attached to a metal support structure over the soil surface with the focal length direction perpendicular to the soil surface. The infrared camera can be moved in different directions, enabling the study of different sections with different sizes.

The camera converts the invisible infrared energy emitted by the soil surface and water into a 2D visual image. Because the imaging scale of the infrared camera is based on temperature emissivity coefficients of the materials, it must be taken into account that, for the working spectral range of the infrared camera (7.5-13.0 μm), water and soil emissivity coefficients are very similar and, therefore, the associated errors could be ignored.

3.3.2. Soil surface microrelief scenarios

Two study sections were defined at the surface of the flumes: i) A smaller section with 0.30 × 0.40 m^2 at the narrower flume; and ii) A larger section with 0.75 × 1.00 m^2 at the wider flume. The study sections were defined 0.5 m downslope of the feeder boxes.

Different soil surface microrelief scenarios were tested on both study sections: scenarios with artificial rills and scenarios on a surface eroded by flowing water where different mulch cover densities were applied. Figure 3.2 shows photographs of the soil surfaces of the two flumes.

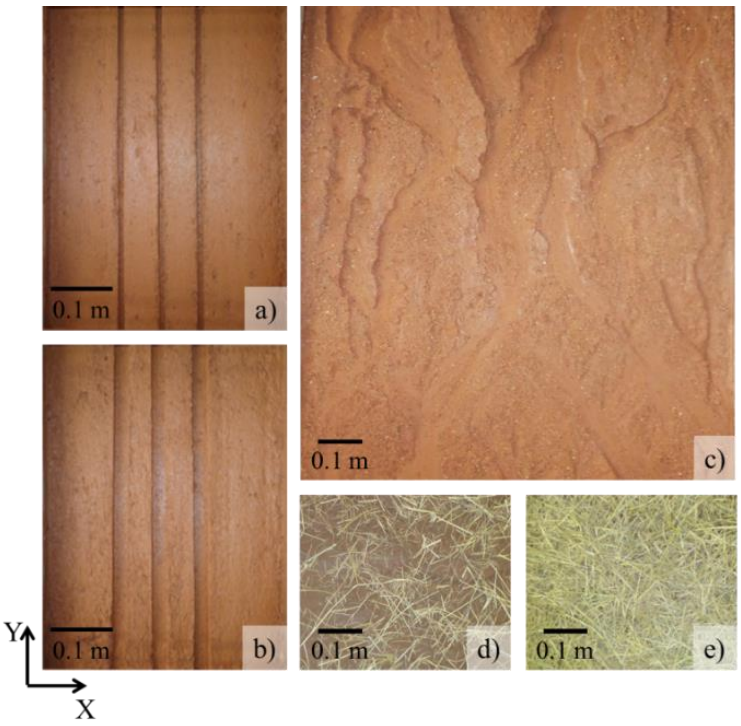

Figure 3.2. Photographs of the soil surface of the flumes: a) Small study section with three small artificially created rills; b) Small study section with three big artificially created rills; c) Bare soil with microrelief created by water erosion; d) Low mulching cover; and e) High mulching cover. X represents the distance along the width of the flumes and Y represents the distance along the length of the flumes.

Scenarios with artificial rills

Four scenarios with artificial rills were studied on the smaller section (narrower flume). The artificial rills created at the soil surface had three different sizes (depth and width): i) Small rills with 7 mm width and 7 mm deep; ii) Large rills with 12 mm width and 12 mm deep; and iii) Deep rills with 7 mm width and 18 mm deep. Figure 3.3 presents the soil surface elevation profiles of the four scenarios with artificial rills which were kept constant along the length of the study section.

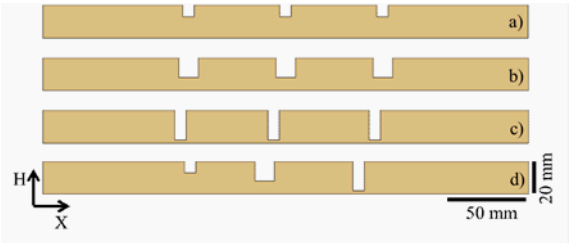

Figure 3.3. Soil surface elevation profiles of the scenarios with artificial rills: a) Scenario with three small rills (see Figure 3.2a); b) Scenario with three large rills (see Figure 3.2b); c) Scenario with three deep rills; and d) Scenario with a combination of three rills with different sizes. X represents the distance along the width of the flume and H represents the soil surface elevation.

Scenarios on the surface eroded by water

Six scenarios, with different mulching densities, were studied on the surface eroded by flowing water created on the larger study section (wider flume): i) Bare soil (see Figure 3.2c); ii) Low mulching cover with 0.5 t ha^{-1} density (see Figure 3.2d); iii) Medium low mulching cover with 1.0 t ha^{-1} density; iv) Medium mulching cover with 2.0 t ha^{-1}; v) Medium high mulching cover with 4.0 t ha^{-1}; and vi) High mulching cover with 8.0 t ha^{-1} density (see Figure 3.2e). Rice straw (Oryza sativa L. ssp. japonica) was adopted as mulching.

3.3.3. Experimental procedure

The air dried pre-sieved soil was manually spread along the flume and compacted, aiming to obtain a bulk density of approximately 1700 kg m^{-3} (original soil bulk density). A sharp straight-edged blade was used to produce a plane top surface. The soil was saturated and let to dry aiming to obtain a desired consistency that allowed the creation of different reliefs at the soil surface, both artificially and by water erosion. The artificial rills were created compressing rectangular wooden forms, of known geometry and dimensions, against the soil surface. Microrelief created by water erosion was obtained by applying a uniform water flux of approximately 500 ml s^{-1} over the soil surface, using the feeder box installed upslope of the flume, during 30 min. The rice straw, previously air dried, was applied uniformly along the study section trying not to disturb the soil surface microrelief.

The infrared thermography technique starts by applying to the soil surface, using the feeder boxes located upslope of the flumes, water heated (e.g. in an electric kettle) to a temperature of approximately 90ºC. Water was applied with the lowest possible discharge in order not to alter soil surface microrelief. As the heated water flows along the study section, uniformly distributed, it concentrates in the lower topographic elements (e.g. rills, surface depressions). Consequently, these features should present higher temperatures. On the contrary, the higher topographic elements (e.g. mounds) should present lower temperatures because the heated water does not concentrate there. The thermal videos of the soil surface were monitored throughout the experiments in the portable device. Three repetitions were conducted for each of the ten soil surface scenarios studied.

3.3.4. Data analyses

The thermal videos obtained with the infrared camera were analysed with the objective of identifying preferential flow paths and the existing microrelief elements on the soil surface (e.g. rills, depressions, mounds, ridges). Thermograms of the soil surface (i.e. snapshots of the thermal videos) were captured every second from the moment that the heated water reached the upstream end of the study sections. The characteristics of the thermograms of the studied sections (e.g. dimensions, number of pixels, pixel dimension) are shown in Table 3.1.

Table 3.1. Characteristics of the thermal imaging obtained with the infrared camera for the two studied sections.

Section	Smaller	Larger
Section dimension (m)	0.40 × 0.30	1.00 × 0.75
Optical resolution used (pixel)	144 × 108	160 × 120
Number of data points (pixel)	15552	19200
Pixel dimension (mm)	2.78 × 2.78	6.25 × 6.25

Temperature data extracted from the captured thermograms was converted into soil surface elevation data, to generate 3D digital soil surface elevation models. The digital elevation models were constructed by interpolation of the obtained data, using kringing method from Surfer 10 surface modelling program (Golden Software, Inc.).

Elevation data obtained with thermography was then compared with the real elevation data measured with a manual profile meter, by means of statistical indexes and regression analyses. Real elevation point data was measured at every 0.050 m and 0.001 m along the length and width of both study sections. In the surface eroded by flowing water, real elevation measurements were taken after the water erosion be induced. The surface remained almost the same during the experiments, because after surface eroded by water be created it was left to rest, aiming to obtain a consistency that allowed the application of the heated water without damage significantly the soil surface. Also, heated water was applied with the lowest possible discharge in order not to alter soil surface microrelief. For the experiments with the artificial rills, before each repetition of the experiments, the soil surface microrelief and rills were created artificially with wooden forms. So, for each scenario the microrelief was always the same.

Data conversion method

The conversion method consists in transforming the temperature data of the thermograms into elevation data using linear regressions comparing the real elevation of, at least, two points, chosen from the soil surface with their corresponding temperatures extracted from the thermograms.

The conversion method was tested using five sets with different number points selected from the soil surface: i) 2 points; ii) 4 points; iii) 6 points; iv) 8 points; and v) 10 points. Only the maximum of 10 points were chosen because the aim of the technique is to be as simple as possible and measuring soil surface elevation with precision is a laborious and time-consuming task. The points were selected randomly. Only one restriction was defined on choosing the points: approximately half of the points should be situated in lower microrelief elements (e.g. rills, depressions) and the other half should be situated in higher microrelief elements (e.g. mounds, ridges). Five tests were performed for each set of points, to ensure uniformity in the selection of points of the soil surface.

Statistical indexes

Random roughness (RR) is the index most commonly used in soil surface roughness and microrelief studies (e.g. PLANCHON et al., 2001; RODRÍGUEZ-CABALLERO et al., 2012). ALLMARAS et al. (1966) defined RR as the standard deviation (SD) of soil surface elevation after the slope and tillage effects were removed, the upper and lower 10% of the measurements were eliminated and with a log transformation of the raw data. However, in this study, RR was estimated simply as the SD of soil surface elevation after the slope effect was removed, without removing the effect of the rills, without the log transformation of the raw data (e.g. CURRENCY and LOVELY, 1970; KAMPHORST et al., 2000) and without remove the upper and lower 10% of the measurements (e.g. GARCIA MORENO et al., 2008; PAZ-FERREIRO, et al., 2008). RR was calculated using Equation 3.1, for both measured values with the profile meter and obtained values with thermography.

$$RR = \sqrt{\frac{1}{N}\sum_{i=1}^{N}\left(H_i - \bar{H}\right)^2} \tag{3.1}$$

where H_i is the elevation value at data point i, and $\bar{H}$ is the average elevation data point and N is the number of elevation data points. Minimum, maximum and average elevation values were also calculated.

Regular regression and frequency analyses were also performed to estimate the accuracy of the elevation data estimated with the technique presented in this study, comparing soil surface elevation data measured with the manual profile meter and obtained with thermography. Goodness of fit was evaluated based on the coefficient of correlation (r) and on the root mean square error (RMSE), calculated as Equations 3.2 and 3.3.

$$r = \frac{\sum_{i=1}^{N}\left(\left(Hobs_i - \overline{Hobs}\right)\times\left(Hsim_i - \overline{Hsim}\right)\right)}{\sqrt{\left(\sum_{i=1}^{N}\left(Hobs_i - \overline{Hobs}\right)^2\right)\times\left(\sum_{i=1}^{N}\left(Hsim_i - \overline{Hsim}\right)^2\right)}} \tag{3.2}$$

$$RMSE = \sqrt{\frac{1}{N}\sum_{i=1}^{N}\left(Hobs_i - Hsim_i\right)^2} \tag{3.3}$$

where $Hobs_i$ is the observed (measured with the profile meter) elevation value at data point i, $Hsim_i$ is the simulated (obtained with thermography) elevation value at data point i, $\overline{Hobs}$ is the average observed elevation data point, $\overline{Hsim}$ is the average simulated elevation data point and N is the number of elevation data points.

3.4. Results and discussion

3.4.1. Scenarios with artificial rills

Soil surface thermograms obtained for the scenarios with the artificially created rills are shown in Figure 3.4. The visualization of these thermograms allows us to identify the rills at the soil surface, perceptible by the vertical stripes with a lighter colour, which is the result of higher temperatures. This happened because the heated water flowed into the rills, where it has concentrated. The points at the top surface (i.e. points out of the rills) presented lower temperature, because the water in these places has not concentrated as much as in the rills. Some thermograms presented points at the top surface with a darker coloration (e.g. right side of Figure 3.4a and between the rills in Figure 3.4d). This could be related to the dispersion of the water as it flowed along the study section.

In the thermograms it is also possible to identify some differences in the width of the rills: e.g. in Figure 3.4b the rills with 12 mm thick present vertical stripes thicker than the rills with 7 mm thick of Figure 3.4c. Beyond the distinction of the widths it is also perceptible the difference of the depth between some rills: in Figure 3.4d the leftmost vertical stripe (rill with depth of 7 mm) presents a darker coloration than the other vertical stripes (rills with 12 mm and 18 mm depth).

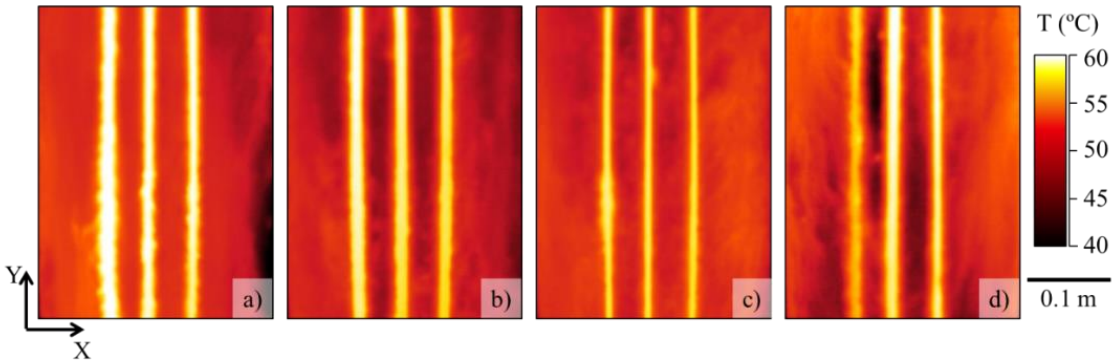

Figure 3.4. Thermograms of the soil surface with artificially created rills: a) Scenario with three small rills; b) Scenario with three large rills; c) Scenario with three deep rills; and d) Scenario with a combination of three rills with different sizes. X represents the distance along the width of the study section, Y represents the distance along the length of the study section and T represents the temperature of the soil surface.

Figure 3.5 presents a comparison between data measured with the manual profile meter and obtained with the thermographic technique. The variation, in time, of the correlation between the two types of data presented a similar trend in all the scenarios with artificial rills. As shown in Figure 3.5a, the fit increased in the first 5 seconds and then remained approximately constant, decreasing after, around, 20 seconds. That means that there is a considerable period of time when it is possible to use the thermal imaging obtained, without loose too much accuracy.

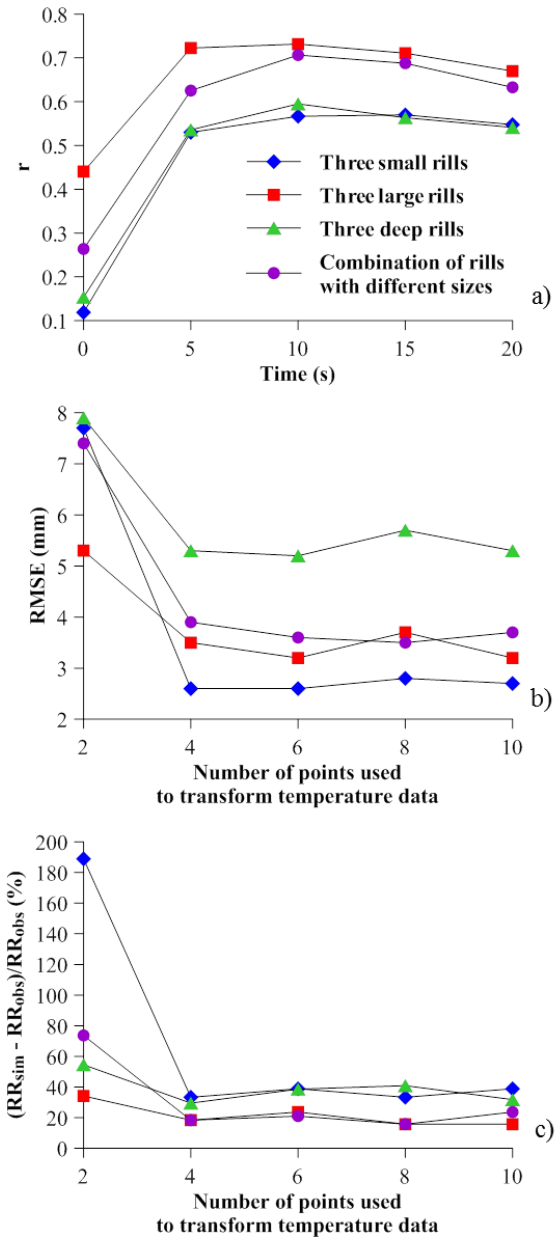

Figure 3.5. Comparison between soil surface elevation data measured with the manual profile meter (obs) and obtained with thermography (sim), for the scenarios with rills created artificially (see Table 3.2): a) Coefficient of correlation (r) over the time; b) Root mean square error (RMSE) for the different number of points used to convert the temperature data; and c) Relative differences of random roughness (RR), for the different number of points used to convert the temperature data

Thermograms obtained 10 seconds after the water reached the upstream of the small study section were chosen to test the performance of the thermographic technique. RMSE, RR and other parameters presented in Table 3.2 were used to evaluate the effect of the use of different number of points of the soil surface to transform the temperature data into elevation data. Both RMSE and RR (Figures 3.5b and 3.5c) clearly indicate that at least 4 points of the soil surface should be used. As more points were used the better of the performance of the technique. However, this improvement is not meaningful, and it may not compensate the effort in measuring soil surface

with precision. Minimum, maximum and average elevation values, shown in Table 3.2, also presented similar results: generally, the worst performance was obtained when only 2 points of the soil surface were used. In almost all the scenarios, the minimum elevation value was obtained with more accuracy that maximum elevation value.

Table 3.2. Soil surface microrelief parameters and indexes calculated for the scenarios with rills created artificially. Temperature data converted using 6 points of the soil surface.

			Parameter			Index	
Scenario	Technique	Data points used to convert temperature data	Hmean (mm)	Hmin (mm)	Hmax (mm)	RR (mm)	RMSE (mm)
Three small rills	Obtained with thermography	2	-4.7 (6.5)	-10.3 (2.1)	11.0 (9.3)	5.2 (2.4)	7.7 (6.1)
		4	-2.0 (0.8)	0-8.9 (1.4)	00.9 (0.7)	2.4 (0.3)	2.6 (0.5)
		6	-1.5 (1.3)	0-8.8 (2.1)	01.5 (1.1)	2.5 (0.4)	2.6 (0.5)
		8	-1.0 (1.9)	0-7.9 (2.4)	01.8 (1.8)	2.4 (0.3)	2.8 (0.5)
		10	-1.8 (1.1)	0-8.1 (2.0)	00.2 (0.8)	2.5 (0.4)	2.7 (0.9)
	Measured	-	-0.5	0-7.0	00	1.8	-
Three large rills	Obtained with thermography	2	-1.2 (0.8)	-13.2 (2.9)	02.6 (0.5)	5.1 (1.8)	5.3 (0.8)
		4	-1.7 (0.3)	-14.9 (2.1)	02.6 (1.3)	4.5 (0.3)	3.5 (0.4)
		6	-2.8 (2.0)	-16.4 (3.0)	01.5 (1.8)	4.7 (0.5)	3.2 (0.8)
		8	-2.7 (1.6)	-15.5 (2.3)	01.4 (1.4)	4.4 (0.3)	3.7 (0.5)
		10	-2.1 (0.8)	-14.9 (1.6)	02.0 (0.7)	4.4 (0.3)	3.2 (0.2)
	Measured	-	-1.4	-12.0	00	3.8	-
Three deep rills	Obtained with thermography	2	-0.3 (1.9)	-23.7 (4.1)	08.8 (3.6)	6.8 (1.5)	7.9 (1.6)
		4	-0.3 (2.5)	-19.8 (3.2)	07.4 (3.5)	5.7 (1.0)	5.3 (1.3)
		6	-1.2 (1.7)	-22.0 (1.5)	07.0 (2.0)	6.1 (0.3)	5.2 (0.3)
		8	-1.5 (2.6)	-22.6 (2.2)	06.8 (2.8)	6.2 (0.2)	5.7 (0.5)
		10	-1.0 (2.3)	-20.9 (2.8)	06.8 (2.4)	5.8 (0.5)	5.3 (0.5)
	Measured	-	-1.1	-18.0	00	4.4	-
Combination of rills	Obtained with thermography	2	-1.7 (6.7)	-23.3 (9.5)	13.9 (9.2)	6.6 (4.2)	7.4 (6.2)
		4	-1.0 (2.0)	-17.9 (3.1)	07.3 (2.9)	4.5 (0.8)	3.9 (0.6)
		6	-1.3 (1.4)	-18.4 (2.6)	07.1 (2.1)	4.6 (0.7)	3.6 (0.5)
		8	-1.9 (0.9)	-18.5 (4.1)	06.3 (0.8)	4.4 (0.9)	3.5 (0.7)
		10	-0.7 (1.5)	-17.3 (2.1)	11.0 (9.3)	4.7 (1.4)	3.7 (0.3)
	Measured	-	-1.1	-18.0	00	3.8	-

Hmean, average elevation data point; Hmin, minimum elevation data point; Hmax, maximum elevation data point; RR, random roughness; RMSE, root mean square error comparing elevation data obtained with thermography and elevation data measured with the manual profile meter. Average values and standard deviation (between brackets) of the repetitions.

Figure 3.6 shows the 3D representations of the soil surface elevation for the scenarios with artificial rills. These representations were constructed using elevation data converted from temperature data using 6 points of the soil surface. Although some 3D models present a top surface with a very smooth aspect, others present some roughness at the top surface. This rough aspect could be related to the erosive effect of the heated water. This effect confers some destructive feature to the technique, which means that it should be used carefully. Despite the use of a minimum discharge of heated water, in some tests the erosive effect of the water could not be completely eliminated. This effect could be minimized by letting the soil rest for a little longer after the compaction of the soil and creation of the rills.

The comparison between soil surface elevation profiles obtained with thermography and measured with the manual profile meter is shown in Figure 3.7. It can be seen that the sharp corners of the

real topography are not well represented by the thermographic technique. This smoothing effect could be caused by heat and turbulent diffusion.

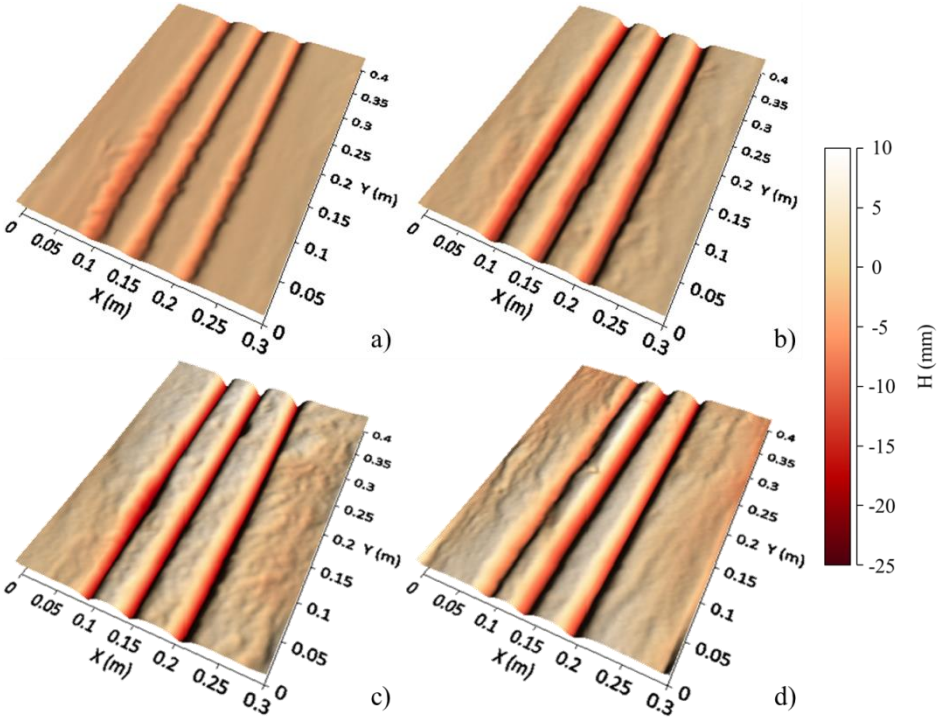

Figure 3.6. 3D models of the soil surface elevation obtained by thermography for the scenarios with rills created artificially: a) Scenario with three small rills; b) Scenario with three large rills; c) Scenario with three deep rills; and d) Scenario with a combination of three rills with different sizes. X represents the distance along the width of the study section, Y represents the distance along the length of the study section and H represents the soil surface elevation.

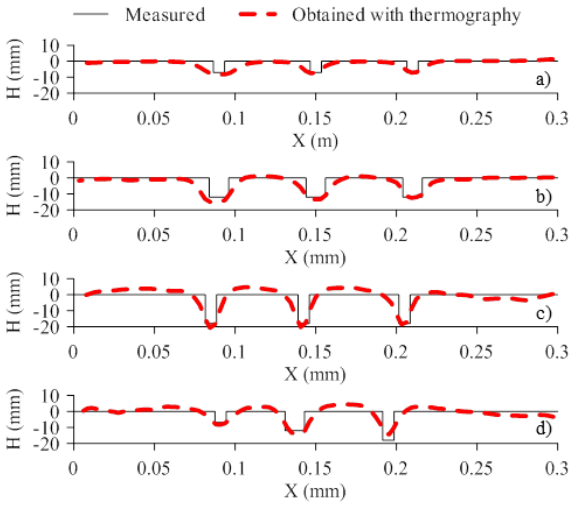

Figure 3.7. Soil surface elevation profiles obtained with thermography and measured with the manual profile meter, for the scenarios with artificial rills: a) Scenario with three small rills; b) Scenario with three large rills; c) Scenario with three deep rills; and d) Scenario with combination of three rills with different sizes. X represents the distance along the width of the study section and H represents the soil surface elevation.

3.4.2. Scenarios with surface eroded by water

The application of the technique in a surface covered by mulch is presented in Figure 3.8.

Initially the soil was subjected to erosion by moving water; afterwards soil mulching covers with different densities were applied. It can be seen that the presence of mulch affects the visualization of water flow with the infrared camera, because straw conceals the paths of the water at the surface of the soil. Also mulching creates a physical barrier to the flow altering the accumulation of water at the soil surface and the preferential flow paths. However, below densities of 2 t ha^{-1} (medium high mulching cover) it was still possible to identify satisfactory preferential flow paths and distinguish different microrelief elements.

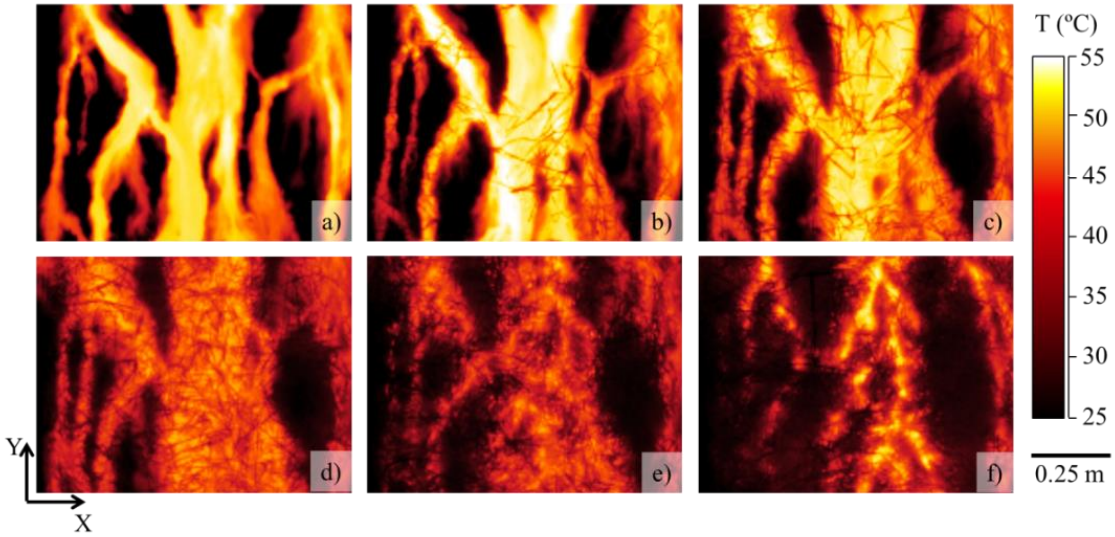

Figure 3.8. Thermograms of the surface eroded by water, for the scenarios with mulching cover: a) Bare soil; b) Low mulching cover; c) Medium low mulching cover; d) Medium mulching cover; e) Medium high mulching cover and f) High mulching cover. X represents the distance along the width of the study section, Y represents the distance along the length of the study section and T represents the temperature of the soil surface.

Higher mulching densities decreased the performance of the technique. Figure 3.9 shows a decrease of the coefficient of correlation and an increase of the RMSE for increasing mulching cover densities. For densities under 2 t ha^{-1} the performance of the technique was very similar. However, the application of 4 t ha^{-1} strongly decrease the performance of the thermographic technique in measuring soil surface elevation.

Relevant soil surface elevation data is presented in Table 3.3.

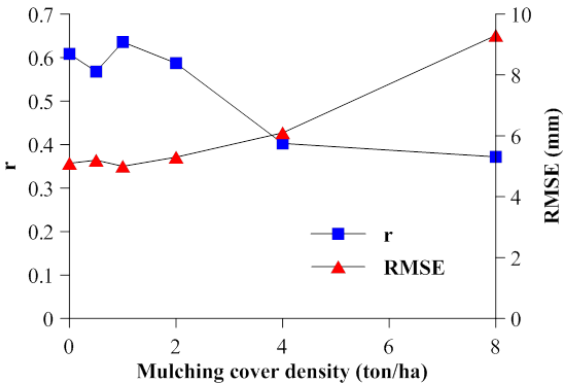

Figure 3.9. Coefficient of correlation (r) and root mean square error (RMSE) comparing soil surface elevation data measured with the manual profile meter and obtained with thermography, for different mulching cover scenarios (see Figure 3.8). Thermograms used were obtained by snapshots at 25 seconds.

Table 3.3. Soil surface microrelief parameters and indexes calculated for the mulching cover scenarios. Temperature data converted using 6 points of the soil surface.

		Parameter			Index	
Technique	Mulching cover density (t ha^{-1})	Hmean (mm)	Hmin (mm)	Hmax (mm)	RR (mm)	RMSE (mm)
Obtained with thermography	0	-13.0 (1.2)	-21.3 (2.5)	-7.3 (1.7)	4.2 (1.0)	5.1 (0.3)
	0,5	-11.6 (0.9)	-20.3 (3.9)	-6.5 (1.7)	3.9 (1.5)	5.2 (0.2)
	1	-13.3 (0.9)	-24.8 (4.4)	-5.1 (2.9)	5.1 (1.8)	5.0 (0.6)
	2	-13.5 (0.7)	-28.0 (5.6)	-3.5 (2.8)	5.3 (1.8)	5.3 (0.7)
	4	-14.2 (1.6)	-34.2 (6.5)	-6.2 (3.1)	7.2 (1.4)	6.1 (0.7)
	8	-15.8 (4.3)	-54.7 (8.5)	-5.3 (2.9)	8.1 (5.1)	9.3 (5.5)
Measured	-	-13.0	-30.4	-0.9	5.6	-

Hmean, average elevation data point; Hmin, minimum elevation data point; Hmax, maximum elevation data point; RR, random roughness; RMSE, root mean square error comparing elevation data obtained with thermography and elevation data measured with the manual profile meter. Average values and standard deviation (between brackets) of the repetitions.

Figure 3.10 presents the 3D models of the soil surface elevation obtained with the thermographic technique, converting data using 6 points of the real soil surface elevation.

As said before, the presence of higher mulching cover densities (i.e. 4 t ha^{-1} and above) affected the performance of the studied technique. The cumulative empirical frequency distribution is strongly affected by the presence of mulching, as it can be seen in Figure 3.11. For higher mulching densities the empirical cumulative frequency distribution deviates from the measured surface elevation distribution.

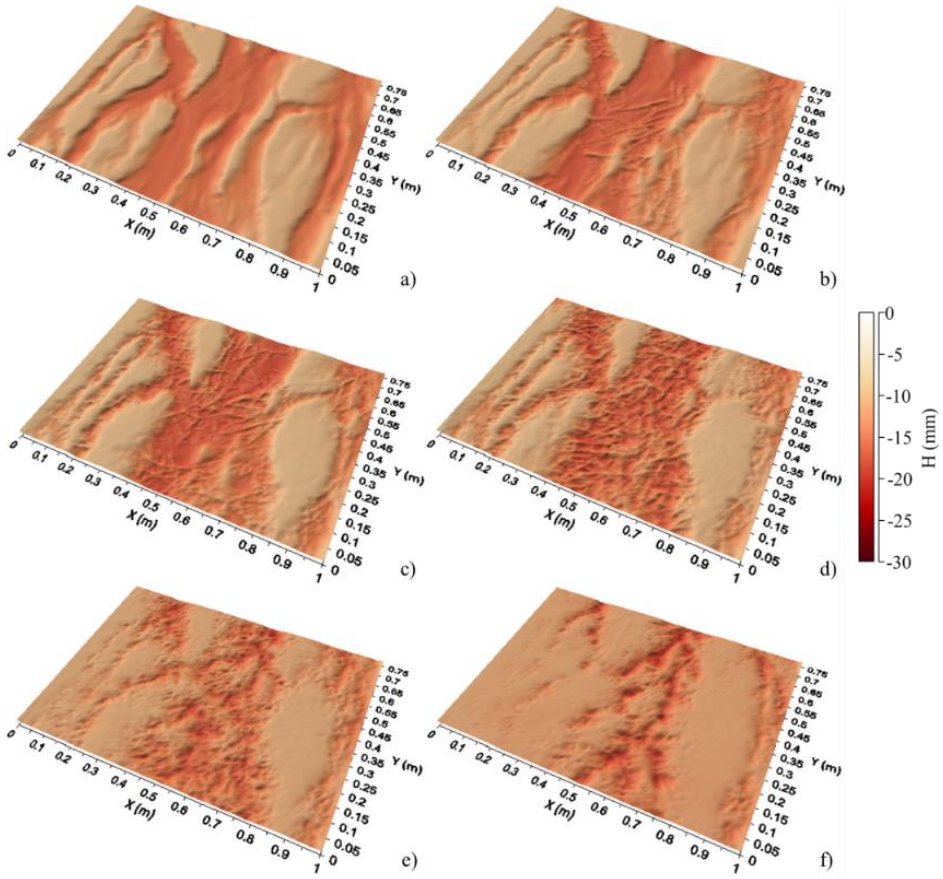

Figure 3.10. 3D models of the soil surface elevation obtained by thermography of the scenarios with surface eroded by water and mulching cover: a) Bare soil; b) Low mulching cover; c) Medium low mulching cover; d) Medium mulching cover; e) Medium high mulching cover and f) High mulching cover. X represents the distance along the width of the study section, Y represents the distance along the length of the study section and H represents the soil surface elevation.

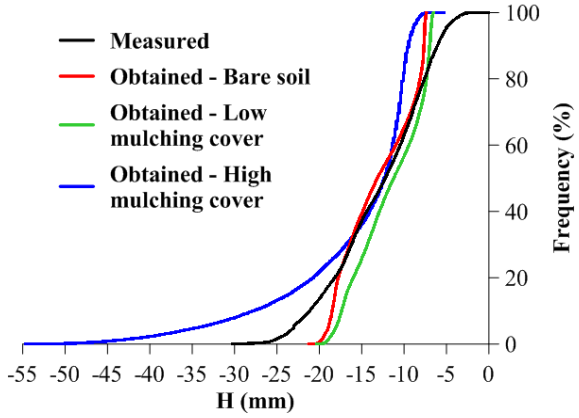

Figure 3.11. Cumulative frequency distribution of soil surface elevation data of the scenarios with surface eroded by water, measured with the manual profile meter and obtained with thermography for bare soil, low and high mulching cover densities. H represents the soil surface elevation.

3.5. Conclusion

This study presented a first approach to the use of an infrared thermography technique to estimate soil surface microrelief and visualize preferential flow paths, namely in the presence of mulch cover. It can be concluded that thermography:

- Can be used to visualize preferential flow paths and identify microrelief structures in the presence of mulch covering the soil surface up to densities of 2 t ha^{-1} (valid for rice straw);
- Can be used to estimate soil surface microrelief and obtain 3D models of the soil surface where other measurement techniques could not be applied.

The thermographic technique has shown to be of easy and fast application. The easy handling of the equipment required, and low cost compared with other techniques make this technique to be very usefully.

However, the following drawbacks can be appointed to the proposed thermographic technique:

- The precision of the technique in bare soil conditions was low compared with other techniques available (e.g. laser scanning). This is especially true for sharp edges that tend to be interpreted by this technique as being smoother;
- For high mulch cover densities (above 4 t ha^{-1}) the measurements of the soil surface temperatures are strongly affected;
- The technique can affect the soil surface microrelief (e.g. a second test will obtain a slightly different soil surface microrelief), especially in easily erodible soils. It should be applied carefully (e.g. use the lowest possible amount of heated water to avoid soil erosion).

"With reference to the expression 'infiltration capacity' I have found to my chagrin that there are particularly in the Soil Conservation Service men who allege that they do not have sufficient mental capacity to visualize the meaning of the word 'capacity' with but one of its well accepted uses in physics and hydraulics, viz. as a volume. The Oxford English Dictionary gives as the first definition of the word 'capacity': 'ability to take in; ability to receive or contain'. ... For the benefit of those having the limitations of mental capacity above suggested, it may be well to point out that infiltration capacity is a volume per unit of time. A third definition of 'capacity' given in the Oxford dictionary is 'mental or intellectual receiving power; ability to grasp or take in impressions, ideas, knowledge'. This is certainly something more than the size of a man's head."

- Robert E. Horton

4. PREDICTION OF SKIN SURFACE SOIL PERMEABILITY BY INFRARED THERMOGRAPHY: A SOIL FLUME EXPERIMENT[2]

4.1. Abstract

This study presents a new technique to map soil surface permeability using infrared thermography and to identify preferential flow. Laboratory tests were carried out using a soil flume where different scenarios were tested. Heated water was used to create a temperature gradient on the soil surface and high-resolution soil surface thermal imaging were obtained using a portable infrared camera. The technique was tested using soils with different permeability. The proposed technique successfully allows us to identify different soil surface permeability and to visualize preferential flows.

Keywords

Thermography; Soil permeability; Preferential flow; Laboratory experiments; Soil flume

4.2. Introduction

Permeability is the measure of the soil's ability to allow water to flow through its pores or voids. It depends not only on the pores but also to how they are connected. Skin permeability is affected, amongst other factors, by land use, soil organisms, soil moisture and precipitation/irrigation. Permeability is probably the most important soil property of interest to engineer's purposes. For example: i) Many hydrological models require estimations of permeability to predict overland flow; ii) Changes in permeability can provide an early warning of soil degradation, flood risk and erosion (DIS4ME, 2013); and iii) Permeability is the key factor for the design of subsurface drainage systems.

It is not possible to measure soil hydraulic properties everywhere by traditional methods. In general, small scale measurement techniques rely on precise and time-consuming experimental procedures. Several experimental investigations have been carried out over the last years aiming to the development of measurement techniques for estimating soil hydraulic characteristics

[2] DE LIMA, J.L.M.P., ABRANTES, J.R.C.B., SILVA JR., V.P. and MONTENEGRO, A.A.A. (2014). Prediction of skin surface soil permeability by infrared thermography: a soil flume experiment. *Quantitative InfraRed Thermography Journal*, 11(2), 161-169. DOI:10.1080/17686733.2014.945325.

(e.g. REYNOLDS and ELRICK, 1985; ŠIMŮNEK and HOPMANS, 2002; HAVERKAMP et al., 2006; VEREECKEN et al., 2007). In situ experimental measurements can be carried out in the field, based on small scale infiltration tests under saturated or unsaturated soil conditions. Among these methods, the double-ring infiltrometer, the Beerkan method developed by BRAUD et al. (2005) and the Guelph Permeameter method, proposed by REYNOLDS and ELRICK (1985) have been largely adopted (e.g. SILVA et al., 2012; XU et al., 2009). Large scale experiments (e.g. pumping tests) cannot capture the spatial variability of permeability. Experimental permeability measurements can also be obtained in the laboratory using disturbed or undisturbed soil samples. Permeability is highly variable over different spatial scales, strongly influencing hydrological processes. Hence, local scale traditional permeability tests need to be grouped or scaled to bring out spatial coherence (WANG et al., 2001) in order to properly represent distributed patterns of variations and for distributed spatial analysis.

Infrared thermography has been successfully applied as a high-resolution imaging tool in hydrological studies: surface water temperature distributions and groundwater-surface water interaction (e.g. DANIELESCU et al., 2009; MEJÍAS et al., 2012). Several recent studies have appeared, carried out using portable hand-held thermography cameras due to their easy handling and easy adjustment of measurement distance and scale (e.g. CARDENAS et al., 2008; DE LIMA and ABRANTES, 2014a, 2014b; PFISTER et al., 2010; SCHUETZ et al., 2012).

The main goals of this study were: i) Verify if infrared thermography can be used to map areas of lower and higher skin surface soil permeability; and ii) Verify if infrared thermography can be used to identify preferential infiltration fluxes at the soil surface. This study follows several articles that also made use of soil flumes in a controlled laboratory environment (e.g. DE LIMA and ABRANTES, 2014a, 2014b; DE LIMA et al., 2003, 2011; MONTENEGRO et al., 2013a), some of which have already used infrared thermography (DE LIMA and ABRANTES, 2014a, 2014b).

4.3. Materials and methods

4.3.1. Setup

A schematic representation of the experimental setup used in the study presented here is shown in Figure 4.1. The experiments were carried out using a 3.00 m long, 0.30 m wide and 0.12 m deep free drainage soil flume set at a 10% slope. A feeder box was installed at the upslope end of the flume which allowed the application of a volume of hot water uniformly to the soil surface.

The characteristics of the three substrates used in the experiments are presented in Table 4.1, including saturated hydraulic conductivity (soil permeability) and bulk density.

Skin soil surface temperature distributions (e.g. thermal images) were recorded with a portable infrared camera PI160 (Optris GmbH) with an optical resolution of 160 × 120 pixels, a thermal resolution of 0.1 ºC, an accuracy of ±2%, and a frame rate of 100 Hz. The camera was positioned

over the soil surface with the focal length direction perpendicular to the soil surface. A section of the flume with 0.50 × 0.30 m^2 was defined approximately 0.5 m of the hot water feeder box. The section was surveyed by the infrared video camera.

Four different scenarios were tested: three scenarios with only two substrates (Soil_1 and Soil_2) and one scenario with the three substrates (Soil_1, Soil_2 and Soil_3). Figure 4.2 shows sketches of the soil surfaces of the flume for the different scenarios studied.

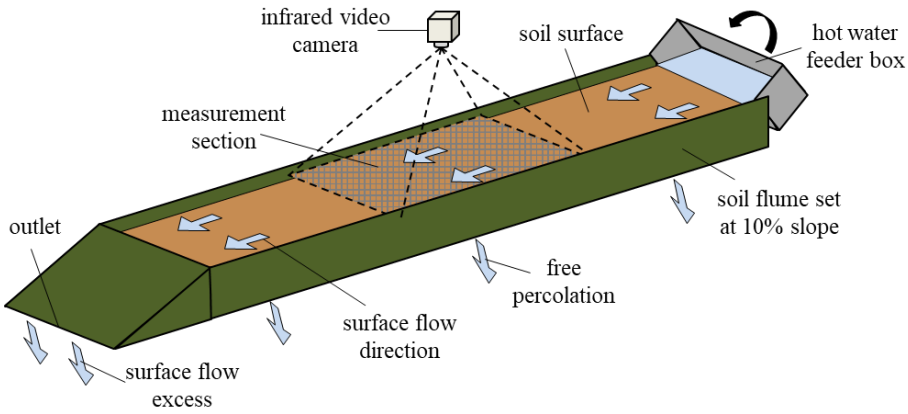

Figure 4.1. Sketch of the setup used in the laboratory tests (not at scale).

Table 4.1. Characteristics of the three substrates used in the laboratory experiments.

Material	Brief characterization	Saturated hydraulic conductivity (m s^{-1})**	Bulk density (kg m^{-3})	Origin
Soil_1	Loamy sand soil (substrate) presenting 4% silt, 11% clay and 82% sand*	4.33×10^{-6}	1750	Collected from the left bank of River Mondego (Coimbra, Portugal).
Soil_2	Sieved sand	4.23×10^{-4}	1500	
Soil_3	Mixture of 50% Soil_1 and 50% Soil_2	1.75×10^{-5}	1650	Mixed in the laboratory

* Dry sieving for particles larger than 0.25 mm and wet sieving for particles finer than 0.25 mm; ** Data obtained by using a constant head permeameter (30 mm layer of water over a 90 mm soil layer)

4.3.2. Experimental procedure

The air dried substrates were manually placed along the flume and compacted in order to obtain the different geometric shapes visualized in Figure 4.2, with the bulk densities shown in Table 4.1.Thin (0.10 mm) flexible plastic film was used to create the different geometric shapes and to separate the different substrates used avoiding mixing. A sharp straight-edged blade was used to produce a plane top surface.

The technique starts by applying to the soil surface, using the feeder box located upslope of the flume, approximately 1.5 L of heated water at a temperature between 80-85 ºC. Water was applied with the lowest possible discharge in order not to alter soil surface configuration. The volume of

applied water and discharge depend on the different characteristics of the soil (e.g. soil permeability) and measurement section (e.g. area, shape).

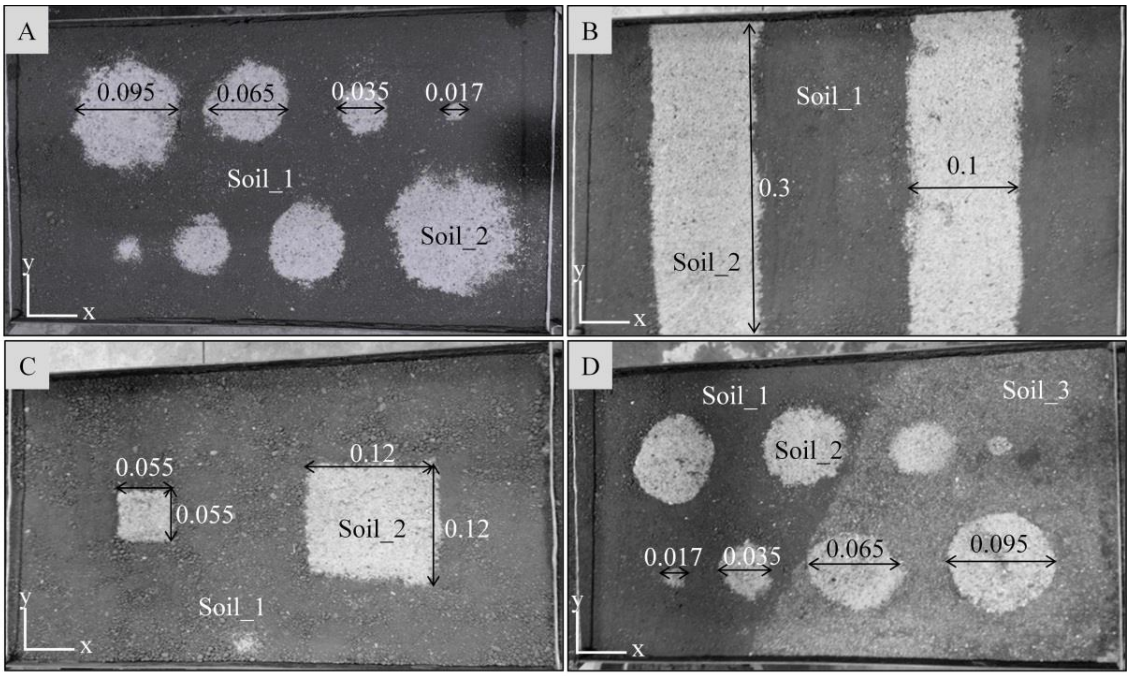

Figure 4.2. Photographs of the soil surface of the flumes for the four scenarios tested. The different soil can be distinguished by the different brightness. X represents the distance along the length of the flume and Y represents the distance along the width of the flume. Dimensions in metres.

As the heated water flows along the flume, uniformly distributed, part of the water infiltrates to the soil and part flows freely out of the flume through the downslope outlet, as overland flow. The heated water preferentially infiltrates and penetrates the soil in the higher permeability areas which, consequently, will present higher temperatures. The more heated water infiltrates the soil the higher will be the increase of temperature at the surface.

Thermal snapshots of the soil surface were taken just after overland flow has stopped (approximately 30 s).

4.3.3. Data analyses

The thermal videos obtained with the infrared camera were analysed with the objective of identifying preferential flow and spatial differences in soil surface permeability. For each scenario, the temperature data was converted into permeability data to generate soil surface permeability maps. The conversion method consists in transforming the temperature data of the thermograms into permeability data using linear regressions comparing the permeability of different points of the soil surface with their corresponding temperatures extracted from the thermograms. Three points for each substrate used were selected to convert the data. Permeability data (always positive) obtained with the infrared thermographic technique were compared with the measured values

obtained with a constant head permeameter (e.g. ELRICK and REYNOLDS, 1992; STOLTE, 1997), by means of statistical indexes and regression analyses.

Goodness of fit of soil surface permeability data was evaluated based on the coefficient of correlation (r) and on the root mean square error (RMSE), calculated as (Equations 4.1 and 4.2):

$$r = \frac{\sum_{i=1}^{N}\left(\left(Hobs_i - \overline{Hobs}\right)\times\left(Hsim_i - \overline{Hsim}\right)\right)}{\sqrt{\left(\sum_{i=1}^{N}\left(Hobs_i - \overline{Hobs}\right)^2\right)\times\left(\sum_{i=1}^{N}\left(Hsim_i - \overline{Hsim}\right)^2\right)}} \quad (4.1)$$

$$RMSE = \sqrt{\frac{1}{N}\sum_{i=1}^{N}\left(Hobs_i - Hsim_i\right)^2} \quad (4.2)$$

where $Hobs_i$ is the observed permeability value (measured with constant-head hydraulic conductivity test with permeameter) at data point i, $Hsim_i$ is the simulated permeability value (obtained with thermography) at data point i, $\overline{Hobs}$ and $\overline{Hsim}$ are the average measured or simulated permeability and N is the number of data points.

4.4. Results and interpretation

Thermograms of the four scenarios tested are presented in Figure 4.3. In the thermograms it is clearly perceptible the delimitation of the areas with different permeability. The visualization of thermograms allows us to identify the areas with higher permeability at the soil surface, perceptible by the lighter colouration, which is the result of higher temperatures. This happened because more heated water flowed into the soil in the higher permeability areas. Areas of lower surface permeability presented lower temperature, because less water has infiltrated in these places.

Despite the soil in the eight circle areas of the scenarios A and D presented the same high permeability (Soil_2), they have shown different surface temperatures. Infrared thermography cannot adequately represent the smaller areas of high permeability. Also, small differences in permeability are not easily detected, as shown in scenario D with Soil_1 and Soil_3.

Figure 4.4 presents a 3D representation of the permeability data obtained with the infrared thermography. The technique enables the characterization of the spatial distribution of the soil surface permeability.

Comparison between soil surface permeability obtained with thermography and measured with the constant head permeameter (e.g. ELRICK and REYNOLDS, 1992; STOLTE, 1997), along cross section lines, is shown in Figure 4.5. It can be seen that the sharp variation of permeability, artificially created on the soil flume, were not well represented by the thermography technique. This smoothing effect could be caused by higher diffusion of heat in those areas.

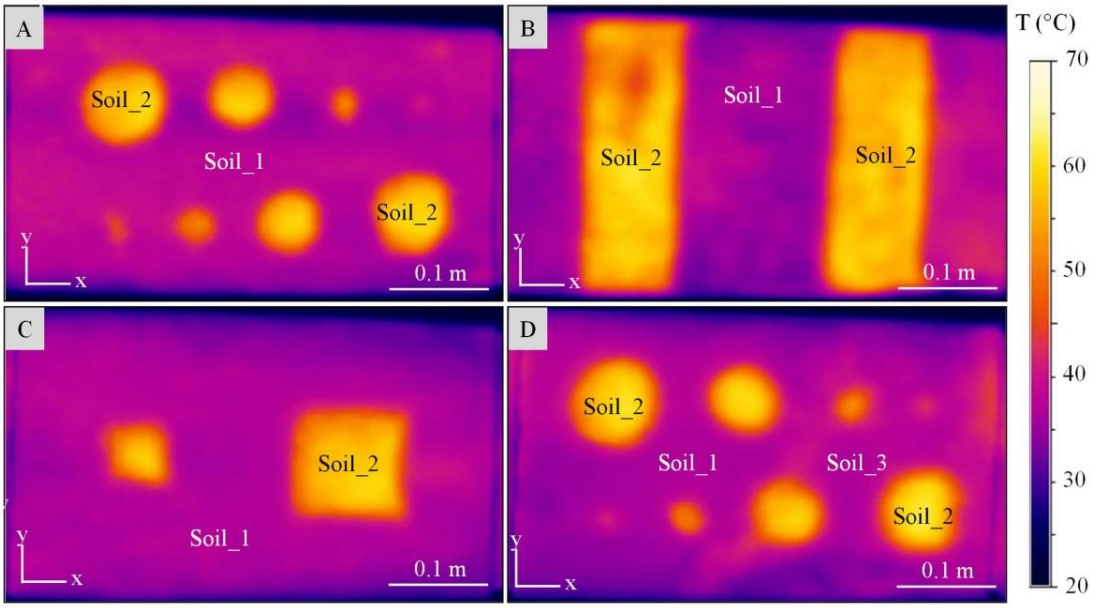

Figure 4.3. Thermograms of the soil surface for the four scenarios tested. X represents the distance along the length of the flume, Y represents the distance along the width of the flume and T represents the temperature of the soil surface recorded with the infrared video camera.

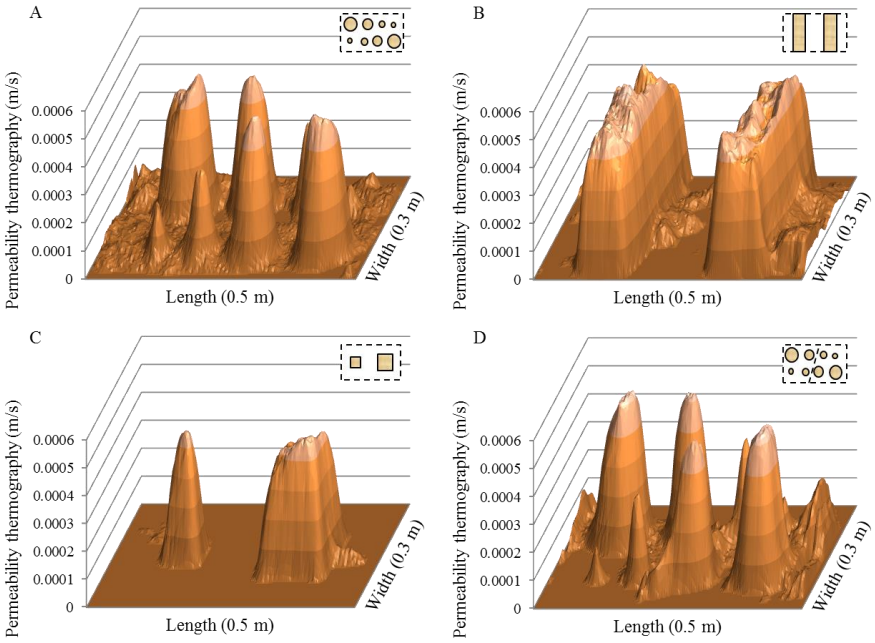

Figure 4.4. 3D view of the soil surface permeability obtained with thermography for the scenarios tested.

The technique is more efficient when characterizing larger high permeability areas. When areas of different sizes, with the same permeability, are presented the technique tended to slightly overestimate the permeability of larger areas and greatly underestimate permeability of smaller areas. This is clearly visible in graphs of the cross sections A.1 and A.2 of scenario A and cross sections D.1 and D.2 of scenario D.

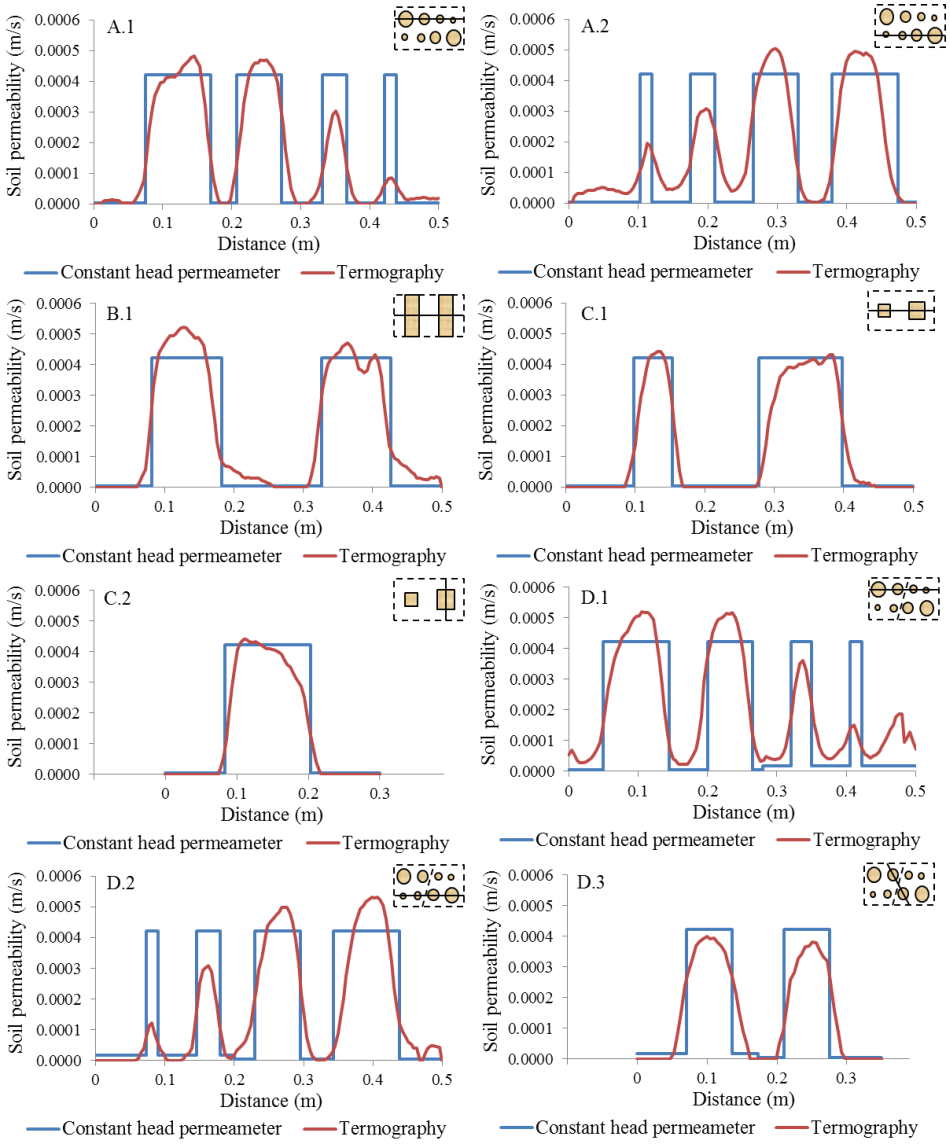

Figure 4.5. Comparison between soil surface permeability measured with the constant head permeameter (blue straight lines) and obtained with thermography (red curved lines), along longitudinal, transversal and oblique cross sections.

Coefficient of correlation (r) and root mean square error (RMSE) for the different scenarios are presented in Table 4.2. The success of the technique in representing the soil surface permeability of Scenarios B and C is shown by the high coefficient of correlation (r) of almost 1 and the lower values of error (RMSE).

Table 4.2. Goodness of fit of soil surface permeability data obtained with thermography.

Scenarios	Number of points	Coefficient of correlation, r (-)	Root mean square error, RMSE (m s^{-1})
A	9375	0.82	8.0×10^{-5}
B	9375	0.90	7.9×10^{-5}
C	9375	0.86	6.3×10^{-5}
D	9375	0.85	7.0×10^{-5}

Scenarios A and D, which presented circular high permeability areas (Soil_2) of different sizes presented lower values of r (approximately 0.5) and the higher values of RMSE. This is a consequence of the difficulty of the technique in represent, at the same time, areas with very distinct sizes (smaller circles with 7 mm radius and larger circles with 42 mm radius).

4.5. Conclusions

This technique can be specifically useful to identify preferential flow and to map areas of lower and higher surface permeability in a expedite way. It can be concluded that infrared thermography:

- Can be used to visualize preferential flow;
- Can be used to estimate the spatial variability of soil surface permeability;
- Can be used to map approximate surface permeability spatial variation.

The thermographic technique has shown to be of easy and fast application. The easy handling of the equipment required, and the small time spent compared with other techniques make this low-cost procedure very interesting and promising.

The following drawbacks of the proposed thermographic technique should however be appointed out:

- The precision of the technique has to rely on reliable measurements of permeability (in situ or laboratory);
- Sharp variations of permeability tend to be interpreted by this technique as being smoother;
- The technique can affect the soil surface characteristics (e.g. a second test will obtain a slightly different soil surface permeability map), especially in easily erodible soils, where sediment transport can alter surface composition, or a surface crust can be formed.

In field application it is expected to allow the identification of areas with similar permeability, therefore reducing the number of in situ random soil permeability tests (e.g. using double ring infiltrometer), which are time consuming techniques. Future work has to be carried out to verify the applicability of the proposed technique under different conditions, especially in field studies:

Test the influence of different soil surface conditions (e.g. soil surface roughness, initial soil moisture content) and the presence of vegetation and other obstructions to the overland flow;

Test the technique at different scales, by increasing the measurement area (flooding area), and observe how the technique is affected due to the need of higher amounts of heated water and loss of uniformity of the flow.

“Engineers like to solve problems. If there are no problems handily available, they will create their own problems.”

- Scott Adams

5. MAPPING SOIL SURFACE MACROPORES USING INFRARED THERMOGRAPHY: AN EXPLORATORY LABORATORY STUDY[3]

5.1. Abstract

Macropores and water flow in soils and substrates are complex and are related to topics like preferential flow, nonequilibrium flow, and dual continuum. Hence, the quantification of the number of macropores and the determination of their geometry are expected to provide a better understanding on the effects of pores on the soil's physical and hydraulic properties. This exploratory study aimed at evaluating the potential of using infrared thermography for mapping macroporosity at the soil surface and estimating the number and size of such macropores. The presented technique was applied to a small-scale study (laboratory soil flume).

Keywords

Thermography; Soil surface macropores; Laboratory experiments; Soil flume

5.2. Introduction

Macropores and water flow in soils and substrates are complex, are related to topics like preferential flow, nonequilibrium flow, and dual-continuum, and have been addressed by many studies in the last decades, e.g. the reviews by BEVEN and GERMANN (1982) and, most recently, 30 years later, BEVEN and GERMANN (2013). Since macropores affect soil permeability, they directly influence other hydrological processes (e.g. surface runoff and associated transport processes).

The water movement and the fertilizers, pesticides, and other pollutants transporting in the soil through macropores have significant impact on hydrological response and water quality (e.g. BEVEN et al., 2006). These structures convey water to greater depths with higher speed, thus influencing water infiltration into the soil and solute transport. The macropores also directly affect the air flow into the soil, the plants root growth, and biological activity (e.g. JARVIS, 2007; LUO et al., 2010; PERRET et al., 1999). Therefore, a high macroporosity enhances air and water movement in the soil, promoting also infiltration and root penetration.

[3] DE LIMA, J.L.M.P., ABRANTES, J.R.C.B., SILVA JR., V.P., DE LIMA, M.I.P. and MONTENEGRO, A.A.A. (2014). Mapping soil surface macropores using infrared thermography: an exploratory laboratory study. *The Scientific World Journal*, 2014, Article ID 84560. DOI:10.1155/2014/845460.

Recently, infrared thermography has been successfully applied as a tool for high resolution imaging in different hydrological studies, conducted at quite different spatial scales. Thermographic techniques are based on records of bodies' temperatures, which are taken at certain instants or over time and at a given space scale; this technology is allowing for a nonconventional acquisition of data and analysis of different processes and their time and space dynamics.

The use of portable infrared cameras or thermal imaging cameras has gained popularity due to their easy handling and adjustment of the vision field to a specific study area. DANIELESCU et al. (2009) and MEJÍAS et al. (2012) used infrared cameras mounted in aircrafts for mapping groundwater discharge in shallow estuaries, provided that there is a thermal contrast between groundwater and the receiving surface waters. CARDENAS et al. (2008) characterized the thermal heterogeneity in a small stream during different flow conditions. PFISTER et al. (2010) used ground-based thermal imagery as a simple, practical tool, for mapping saturated area connectivity and dynamics. It was possible to discriminate between areas with snow cover, snow melt, soil seepage, and stream water. It was possible to detect when and where variably saturated areas were active and when connectivity existed between the hillslope-riparian-stream systems. This was a simple and inexpensive technology for sequential mapping and characterisation of surface saturated areas and a useful complement to conventional tracer techniques. SCHUETZ et al. (2012) used infrared thermal imaging combined with the injection of heated water as an artificial tracer technique to characterize the spatial distribution of flow paths and to assess transport properties in a 65 m^2 experimentally constructed wetland with water depths between 0.1 and 0.2 m. For the studied conditions, the authors observed that heated water can be used as a conservative artificial tracer for plot scale experiments.

Infrared thermographic techniques studied in laboratory conditions were used to assess different surface hydrological processes. A technique to estimate soil surface microrelief and rill morphology using infrared thermography is presented in DE LIMA and ABRANTES (2014a). The authors were able to generate 3D models of soil surface elevation for both bare soil and soil covered with organic residue. In DE LIMA and ABRANTES (2014b) the authors estimated very shallow flow velocities (overland and rill flow), by injecting a thermal tracer (e.g. heated water) into very shallow flows and visualizing the leading edge of the tracer by means of infrared video. Soil flume laboratory experiments have been conducted for many years aiming at studying specific processes and interactions in controlled conditions allowing for repetitions in a short period of time (e.g. DE LIMA et al., 2003, 2005, 2011, 2013a; MONTENEGRO et al., 2013a, 2013b).

In situ small scale infiltration tests (e.g. profile or plot scale), under saturated or unsaturated soil conditions, normally have difficulty to cope with macropores. The quantification of the number of macropores, which are drivers of water, and the determination of their geometry will provide a better understanding of the effects of pores on the physical and hydraulic properties of the soil (e.g. SORACCO et al., 2012). Thus, this exploratory study aimed at evaluating the potential of using infrared thermography for mapping macroporosity at the soil surface and estimating the

number and size of such macropores. The presented technique was applied to a small laboratory scale study (i.e. soil flume). Thus, upscaling results to field, hillslope, and even plot scales will require further investigation, which is beyond the scope of the presented analysis.

5.3. Materials and methods

5.3.1. Laboratory setup

A schematic representation of the used exploratory laboratory setup is shown in Figure 5.1. The experiments were carried out using a 3.00 m long, 0.30 m wide, and 0.12 m deep free drainage soil flume, set at a 10% slope (round number also used in many other works). A feeder box installed at the upslope end of the flume allowed the application of a defined volume of hot water uniformly over the soil surface. A rectangular measuring area (0.50 × 0.30 m^2) with macropores was defined at the flume soil surface, approximately 0.5 m downstream of the hot water feeder box.

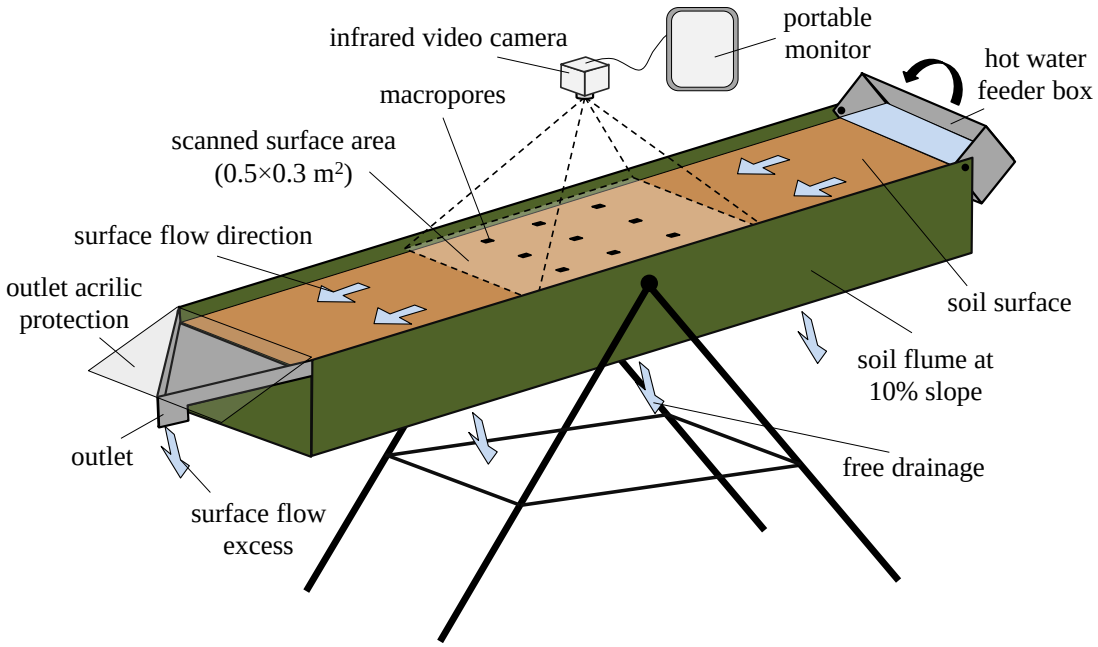

Figure 5.1. Sketch of the laboratory setup using a soil flume and an infrared video camera.

The experiments were carried out using a loamy-sand soil collected from the River Mondego banks (Coimbra, Portugal). The soil presented 6% clay, 11% silt, 82% sand, and a 1750 kg m^{-3} bulk density. Saturated hydraulic conductivity was 4.51 × 10^{-6} m s^{-1}, for the macropores-free soil.

Thermal videos of the soil surface were recorded with an Optris PI-160 portable infrared video camera (Optris GmbH, Germany) with an optical resolution of 160 × 120 pixels, a thermal resolution of 0.1 °C, an accuracy of ±2%, a frame rate of 100 Hz, and a lens with a view field of 23º × 27º and focal length of 10 mm. The camera was attached to a metal support structure 0.75 m

above the flume soil surface with the focal length direction perpendicular to the soil surface (Figure 5.1).

5.3.2. Soil surface macropores

Soil surface vertical macropores with three different rectangular cross section areas were artificially created to test the proposed thermographic technique: i) Large macropores with an area of 256 mm^2 (16 × 16 mm^2); ii) Medium macropores with an area of 120 mm^2 (12 × 10 mm^2); and iii) Small macropores with an area of 36 mm^2 (6 × 6 mm^2). The tests were conducted for four different macropores spatial arrangement's scenarios; these scenarios are shown in Figures 5.2: a) 9 large macropores (Scenario A); b) 9 medium macropores (Scenario B); c) 9 small macropores (Scenario C); and d) a combination of 3 large, 3 medium, and 3 small macropores (Scenario D). It should be noted that field conditions are quite different from a uniform plane surface, clean of stones, debris, and vegetation, with homogeneous colours and macropores with well-defined shapes, used in this exploratory study.

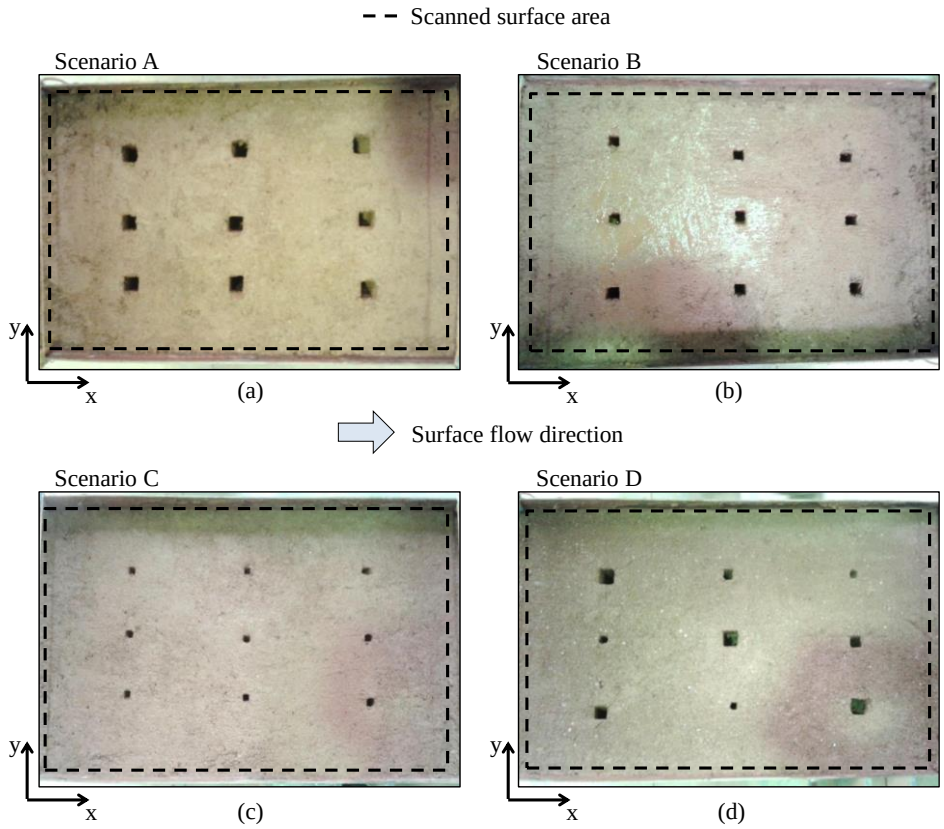

Figure 5.2. Top view (photographs) of the flume soil surface showing macropores of different sizes scattered in accordance to the four scenarios described in the text: a) Scenario A; b) Scenario B; c) Scenario C; and d) Scenario D. The x axis represents the downslope distance along the length of the flume and the y axis represents the distance across the width of the flume (the dashed line defines the measuring area with 0.50 × 0.30 m^2). See Figure 5.1.

5.3.3. Experimental procedure

Air dried pre-sieved soil was manually spread over the flume and gently tapped to obtain a soil layer with a uniform thickness of 0.10 m with a bulk density of 1750 kg m^{-3}. A sharp straight-edged blade was used to produce a smooth plane soil surface. The soil was saturated and left to dry, aiming to obtain a consistency that allowed the artificial creation of vertical macropores at the soil surface; this was carried out by perforating the soil layer, throughout its 0.10 m thickness, with rectangular cross-section metal rods that were described in section 5.3.2. After the creation of the macropores, the soil was again saturated.

The technique starts by applying approximately 1.5 L of heated water over the soil surface, at a temperature around 80-85 °C. The water was manually released using the feeder box located upslope of the flume (Figure 5.1). It was applied with the lowest possible discharge in order to guarantee flow depth uniformity over the measuring area, minimum soil surface disturbance, and the unaltered structure of the macropores by the flowing water. The volume of hot water used (and applied discharge) should be adjusted to the test's conditions (e.g. dimension of the measuring area, slope, water temperature, soil permeability, and dimension of macropores).

The hot water created a wave that covered uniformly the soil surface; along the flume, part of the water flows to the macropores, part infiltrates into the soil, and part flows out of the flume through the downslope outlet, as overland flow. The hot water briefly accumulates inside the macropores before exiting freely the soil layer due to the flume free drainage (Figure 5.1). Since macropores were filled with flowing hot water, they present higher temperatures in the thermal videos, recorded with the infrared video camera, which allowed the mapping of their spatial location and the estimation of their approximate area. Because the soil was close to the field capacity at the beginning of the experiments, the percentage of water infiltrated into the soil was very low compared to the percentage flowing into the macropores.

Soil surface thermal videos were recorded with the infrared camera throughout the experiments. However, thermograms of the surface of the overland flow layer did not provide any spatial variability of temperature. therefore, for each scenario (Figure 5.2), a thermogram of the soil surface was selected, corresponding to an instant just after (approximately 30 s) the passage of the wave of hot water through the scanned area; thermogram is a graphic record of temperature variations, and represent radiation in the infrared range of the electromagnetic spectrum, providing identification of pixels associated with different surface temperatures. Because, in general, macropores present higher temperatures, a threshold temperature (τ) can be selected that allows identifying the pixels associated with the macropores (i.e. pixels with temperature values above a given threshold temperature), thus distinguishing them from the remaining pixels that cover the soil surface scanned area (i.e. pixels with temperature values below the temperature threshold). The percentage of pixels that have temperature above the threshold temperature was called threshold percentage of pixels (α).

The number of macropores detected with this technique, as well as their area, depends upon the selected threshold temperature (τ). Higher threshold temperatures will lead to a detection of a lower number of macropores with smaller cross-section area (and, correspondingly, lower temperatures identified by the thermal images). On the contrary, lower threshold temperatures will lead to a detection of a higher number of macropores with bigger cross-section area. The lower-limit temperature from which all macropores are detected was called critical threshold temperature (τc). Selected threshold temperatures below τc will only lead to an increase of the macropores' area, since the maximum number of macropores was already detected.

5.4. Results and discussion

Thermograms for the four scenarios defined in section 5.3.2. are presented in Figure 5.3. In the thermograms, it is possible to identify the location of the different macropores, perceptible by the presence of groups of pixels exhibiting a brighter colour. These thermal marks are the result of the higher temperatures produced by the accumulation of flowing hot water in the macropores.

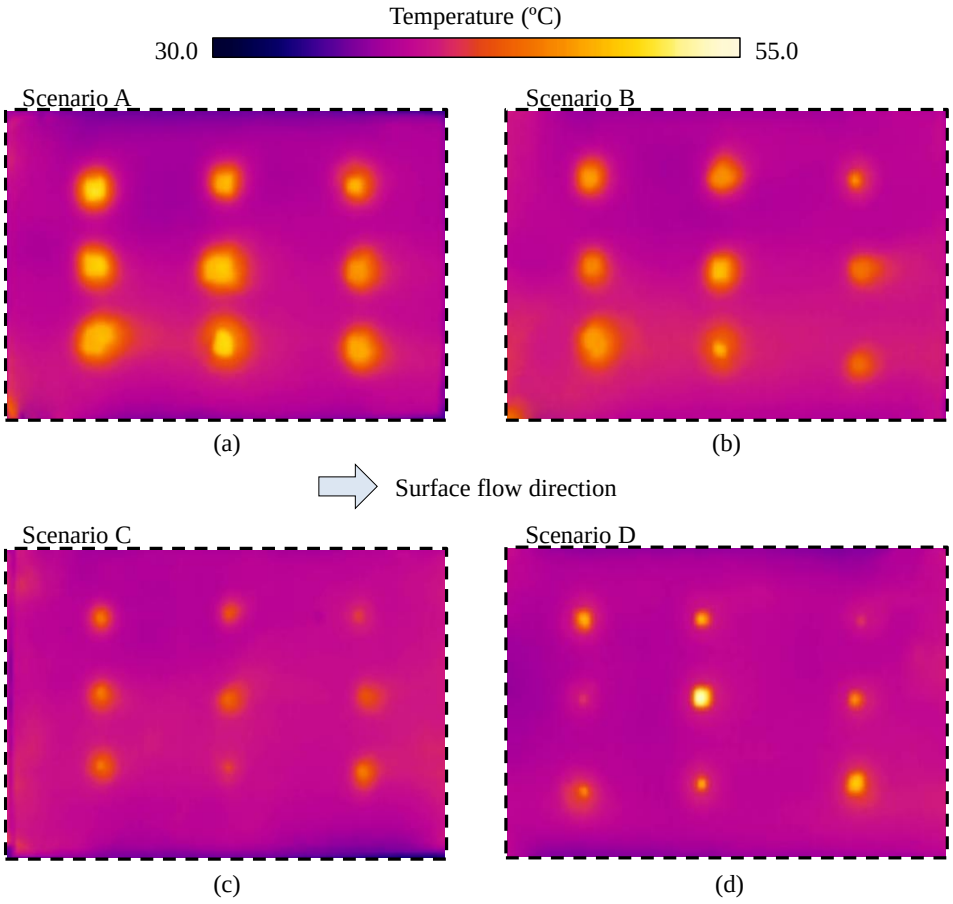

Figure 5.3. Thermograms of the soil surface for the four scenarios: a) Scenario A; b) Scenario B; c) Scenario C; and d) Scenario D. The dashed line defines the measuring area with 0.50×0.30 m^2. See also Figure 5.2.

Despite the rectangular shape of the macropores, the thermal marks identified visually in the thermograms are of approximate circular shapes. Also, the thermal marks are, in general, larger than the actual area of the macropores. This temperature smearing around the macropores is caused by thermal diffusion, by the higher infiltration of hot water around the macropores, and by the relatively low resolution of the camera.

In general, larger macropores led to larger thermal marks, exhibiting higher temperatures at the centre. Thermograms of Scenarios A, B and C, of Figures 5.3a to 5.3c, clearly show thermal marks with different areas, which are in accordance to the different areas of the macropores of each scenario. In the thermogram of Scenario D, in Figure 5.3d, it is also possible to distinguish the macropores of different areas in the same thermogram. Macropores concentrate water which flows into these hollows and are, therefore, in contact with more hot water. This is why macropores have a different temperature than the surrounding soil.

The relation between the threshold temperature (τ) and the number of macropores detected with thermography is shown in Figure 5.4 (right axis). The same graph shows the temperature cumulative frequency distribution of the pixels' temperature (T), corresponding to the four thermograms in Figure 5.3, curve up to 2.5% (left axis).

For each scenario, the critical threshold temperature (τc) and corresponding critical threshold percentage of pixels (αc) are identified in the figure. We highlight that both τc and αc depend on the area of the thermal marks in the thermograms: e.g. Scenario A, with only large macropores, leads to the highest τc and αc. The threshold τc depends also on the temperature of the hot water applied, the initial surface temperature and the macropores present at the soil surface. Therefore, is not possible to specify single τc or αc values, representative of all scenarios. Nevertheless, such values are essential for processing the data and mapping existing soil surface macropores. Therefore, bearing in mind the results obtained in our experiment for all the tests (Figure 5.4), we have further adopted a threshold percentage of pixels (α) of 2.5% for all scenarios, since in our tests we found always $\alpha c < 2.5\%$. For each scenario, the corresponding temperature frequency distribution curve (Figure 5.4) yields a specific value of the threshold temperature (τ) for $\alpha = 2.5\%$, which we have used to study the area and location of the macropores, using thermography.

Soil surface macropores were identified by applying to the temperature data the threshold temperature (τ) corresponding to $\alpha = 2.5\%$; the selected τ were subtracted to all temperature values from the thermograms: positive values, which correspond to pixels with temperature values above τ, are associated to the macropores.

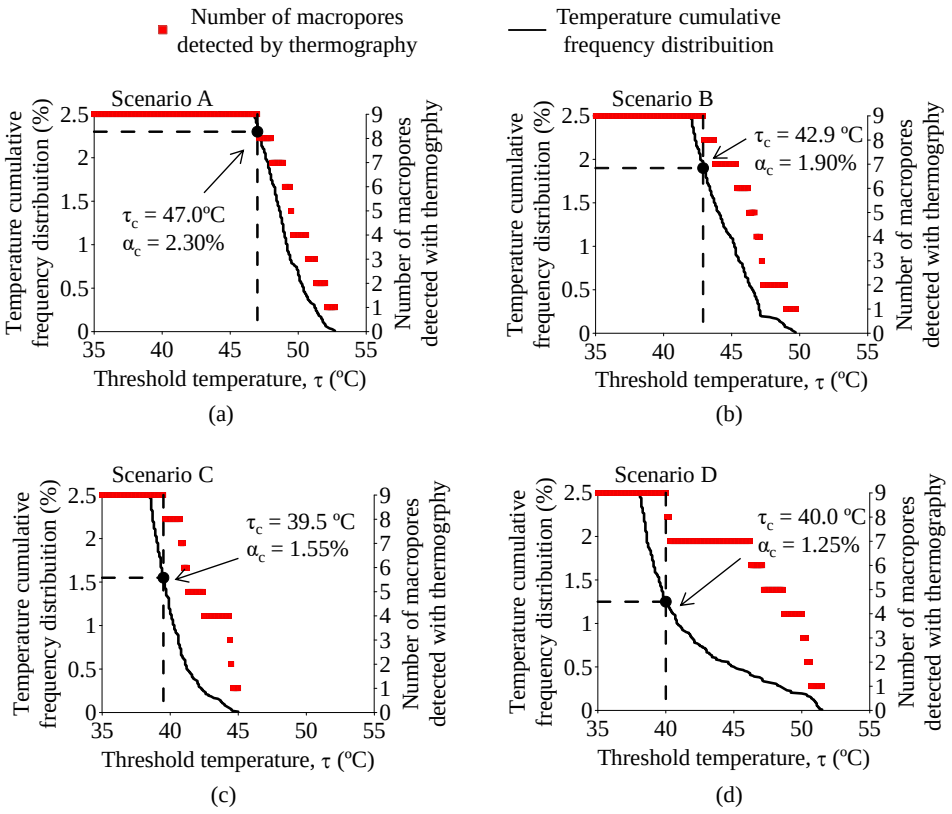

Figure 5.4. Relation between threshold temperature (τ) and the number of macropores detected with thermography, for the four scenarios: a) Scenario A; b) Scenario B; c) Scenario C; and d) Scenario D. Temperature cumulative frequency distribution curves are also plotted, up to 2.5%. Critical threshold temperature (τc) and corresponding critical threshold percentage of pixels (αc) are also identified.

The comparison between the boundaries of the actual macropores and the macropores' area detected with thermography is shown in Figure 5.5. The macropores' area detected with thermography was, in general, larger than their actual area. Therefore, the technique did not accurately estimate the actual area of the macropores, especially for the smaller ones. It is possible to observe in Figure 5.5d that the proposed technique can be used to distinguish macropores with different size (i.e. cross-section area), since larger macropores were detected with thermography as having also larger areas. This has already been suggested by observing the thermal marks in the thermograms in Figure 5.3 and the photographs in Figure 5.2.

Figure 5.6 shows the comparison between the position of the actual geometric centre of the macropores and their geometric centre detected using thermography. In general, the proposed technique allowed the correct estimation of the macropores' location. Although, the technique did not assess accurately the actual area of macropores, it clearly allowed mapping the macropores and identifying their spatial distribution and position across the studied soil surface area.

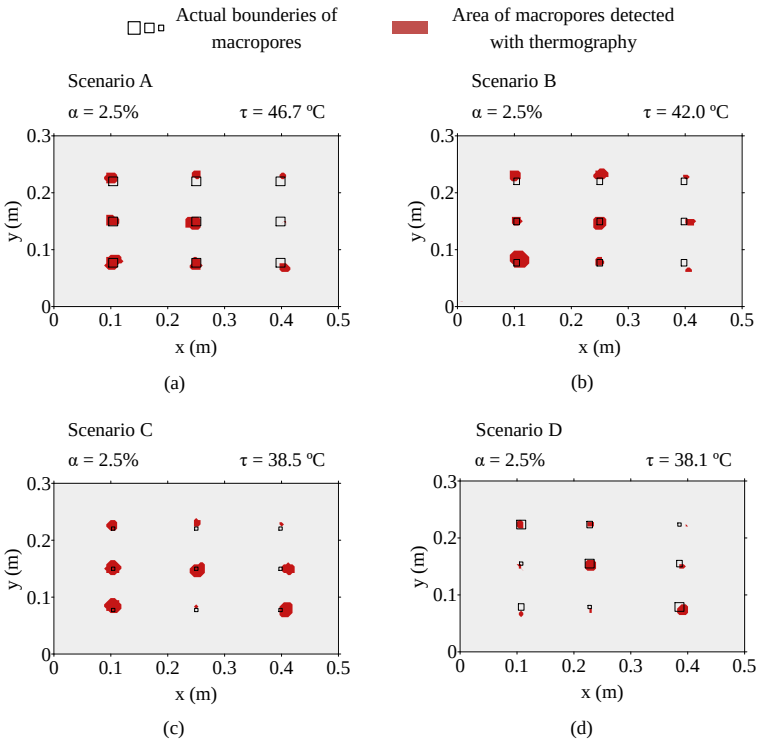

Figure 5.5. Comparison between the boundaries of the actual macropores and the area detected with thermography, for the four scenarios. Across the area scanned by the thermographic camera, the macropores are located using (x,y) coordinates: The x axis represents the downslope distance along the length of the flume (0.5 m) and the y axis represents the distance across the width of the flume (0.3 m). See also Figures 5.2 and 5.3.

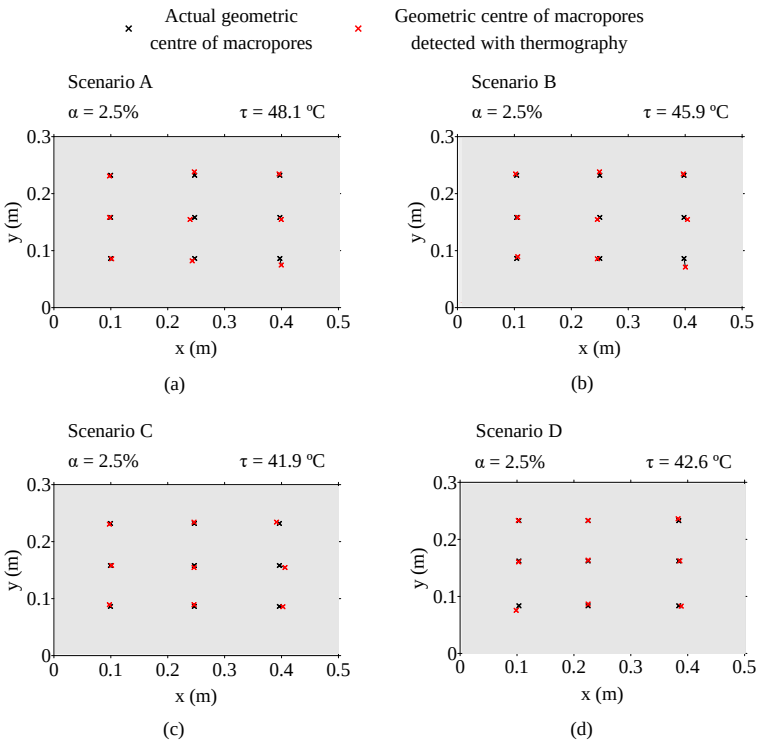

Figure 5.6. Comparison between the actual geometric centre of the macropores and their geometric centre detected using thermography, for four scenarios. See Figure 5.5.

5.5. Conclusions

A novel technique to detect and characterize soil surface macropores based on infrared thermography was presented and discussed, based on exploratory laboratory soil flume experiments. For our laboratory conditions, the thermographic technique was successful in identifying the presence of macropores at the soil surface, providing a low cost and fast methodology to map soil surface macropores. Although uncertainties arise during the analysis about the macropores boundaries at the soil surface, which therefore restricts the quantification of their shape and size, the technique seems promising and able to identify macropores' spatial distribution with satisfactory accuracy.

Only extensive field work can, in fact, reveal the relevance of the technique in real (field) conditions. Future work has to be carried out to verify the applicability of the proposed technique under different field conditions, such as e.g. soil type, dimensions of scanned area, surface microrelief and roughness, presence of vegetation, stones and other obstructions, which is beyond the scope of the presented analysis.

“Start by doing what's necessary; then do what's possible; and suddenly you are doing the impossible.”

- Unknown

6. ASSESSING SOIL WATER REPELLENCY SPATIAL VARIABILITY USING A THERMOGRAPHIC TECHNIQUE: AN EXPLORATORY STUDY USING A SMALL-SCALE LABORATORY SOIL FLUME[4]

6.1. Abstract

This exploratory study presents a technique to assess soil water repellency (SWR) spatial variability based on infrared thermography. Small-scale laboratory tests were carried out using a soil flume and a loamy-sand soil, where SWR was induced on soil surface with waterproofing spray and repellent areas were mapped through thermal imaging, using a portable infrared video camera. Cold water was used to create a temperature gradient on the soil surface in order to assess SWR.

The technique was, in overall terms, successful in mapping SWR spatial variability, distinguishing repellent from wettable areas as well as distinguishing between areas with different levels of SWR severity, in particular, between areas with extreme as opposed to low to medium SWR. The proposed technique apparently has high potential to contribute to a better understanding of the hydrological impacts of different spatial patterns of SWR due to its capacity to monitor in real time the dynamics of these impacts.

Keywords

Soil water repellency; Infrared thermography; Spatial variability; Laboratory soil flume experiments

6.2. Introduction

Soil water repellency (SWR) is now recognised as a global phenomenon with important implications for hydrology and, therefore, of major concern to both hydrogeologists and land managers over a century (DEBANO, 2000b).SWR can alter infiltration and water storage capacity of soils, enhancing infiltration by preferential flow and/or surface runoff generation and associated erosion (KEIZER et al., 2005b; LEIGHTON-BOYCE et al., 2007; RITSEMA and DEKKER, 1994;

[4] ABRANTES, J.R.C.B., DE LIMA, J.L.M.P., PRATS, S.A. and KEIZER, J.J. (2017). Assessing soil water repellency spatial variability using a thermographic technique: small-scale laboratory study. *Geoderma*, 287, 98-104. DOI:10.1016/j.geoderma.2016.08.014.

SHAKESBY et al., 1993). Also, by altering water availability SWR can indirectly affect seed germination, seed establishment and plant growth (DOERR et al., 2000). A large number of studies have indicated a variety of factors causing and influencing SWR, such as soil moisture (CHAU et al., 2014; FERREIRA et al., 2016; KEIZER et al., 2005a; LEIGHTON-BOYCE et al., 2005), incidence of fires (BADÍA-VILLAS et al., 2014; DEBANO, 2000b; KEIZER et al., 2008; MATAIX-SOLERA and DOERR, 2004), presence of fungi and bacteria species (SCHAUMANN et al., 2007), soil texture and structure (URBANEK et al., 2007) and soil organic carbon content (WIJEWARDANA et al., 2016). However, the ultimate origin of SWR is the coating of soil particles with hydrophobic organic substances usually released by plants or decomposing plant material (DEKKER and RITSEMA, 1994; KEIZER et al., 2005c).

The two most commonly used techniques to measure SWR are the Molarity of an Ethanol Droplet (MED) test, also known as Percentage of Ethanol test or Critical Surface Tension test (LETEY, 1969) and the Water Drop Penetration Time (WDPT) test (VAN'TWOUDT, 1959).The MED test uses the surface tension of an ethanol solution to indirectly measure the apparent surface tension of the soil surface, i.e. how strongly water is repelled. The WDPT determines how long SWR persists in the contact area of a water drop. Both the MED and WDPT tests provide quantitative data, but the subsequent classification or characterization of these data vary with the objective of the investigator and perception of what constitutes low or high SWR severity. Also, although SWR strength and persistence are often related somehow, this relationship is not always clear or consistent (DEKKER and RITSEMA, 1994; KEIZER et al., 2008). Other techniques to measure SWR include measurement of the water-soil contact angle (LETEY et al., 1962), measurement of ethanol and water ethanol sorptivity and using their ratio as SWR index (TILLMAN et al., 1989), measurement of the water entry pressure head of a soil, which is a function of water-soil contact angle (CARRILLO et al., 1999), and the sessile drop method using a goniometer-fitted microscope (BACHMANN et al., 2000). Most of these techniques have been compared in various papers such as COSENTINO et al. (2010), DEKKER et al. (2009), KING (1981) and LETEY et al. (2000).

An important problem in assessing the hydrological role of SWR is that most of the existing techniques to quantify SWR require specialized equipment and are best suited for use in the laboratory (DEKKER et al., 2009). Also, some of these techniques require air-dried or oven-dried samples which may not be very representative of the conditions occurring in the field. The WDPT test can be performed on field-moist samples for the actual persistence of SWR (COSENTINO et al., 2010), or on dried samples for the potential persistence of SWR (DEKKER and RITSEMA, 1994). However, while the WDPT method demonstrates infinite resolution in severe SWR assessment, it lacks the precision required to distinguish intermediate degrees of soil repellency (DEKKER and RITSEMA, 1994). Also, WDPT results do not have an obvious physical meaning, and the technique can be very time consuming in the presence of strong to extreme SWR such as prevailing in eucalypt plantations (e.g. DOERR et al., 1998; KEIZER et al., 2005c; LEIGHTON-BOYCE et al., 2005). The MED test is usually more practical and more rapid than WDPT test and has therefore been widely applied in especially intensive field monitoring studies (e.g. KEIZER et

al., 2005c; 2007, 2008; MALVAR et al., 2016; SANTOS et al., 2013). Furthermore, its results are related to the water-soil contact angle and, therefore, physically meaningful. However, MED test results poorly predict the soil wetting behaviour (DOERR and THOMAS, 2000). Other problem with most of the existing techniques to quantify SWR is that they provide punctual data, not revealing the spatial extent of the SWR severity. At field and landscape scales, punctual measurements must be grouped or scaled to bring out spatial coherence, in order to properly map SWR and represent distributed patterns of variations. This presents a laborious and time-consuming task. Moreover, the limited surface area sampled by the MED and WDPT tests contributes to wide variability about the mean values (DEKKER and RITSEMA, 1994).

Infrared thermography is a versatile, accurate and fast technique of monitoring surface temperature and has been used in a variety of fields, such as military surveillance, medical diagnosis, industrial processes optimisation and building inspections. Its widespread use in different studies has been increasing due to recent reductions in the prices of infrared cameras and substantial enhancements of their portability and spatial resolution. In surface hydrology, it has been successfully employed as a high spatial and temporal resolution non-invasive and non-destructive imaging tool to access groundwater discharges into estuaries (MEJÍAS et al., 2012) and streams (CHEN et al., 2009), quantify thermal heterogeneity of streams (BONAR and PETRE, 2015) and floodplains (TONOLLA et al., 2010), and map saturated area connectivity and dynamics (PFISTER et al., 2010). Combining thermal imaging with the injection of hot water, as an artificial tracer technique, SCHUETZ et al. (2012) characterized the spatial distribution of flow paths and assessed flow transport properties, while DE LIMA and ABRANTES (2014b) and DE LIMA et al. (2015b) estimated very shallow overland and rill flow velocities. Some authors developed techniques based on infrared thermography to assess different processes that occur at the soil surface level, such as crust formation (SOLIMAN et al., 2010), evaporative fluxes (SHAHRAEENI and Or, 2010) microrelief and rill morphology (DE LIMA and ABRANTES, 2014a), permeability and preferential infiltration fluxes (DE LIMA et al., 2014b) and macroporosity (DE LIMA et al., 2014a, 2014c).

The main goal of this exploratory study was to investigate if infrared thermography can be used to assess SWR severity and spatial distribution.

6.3. Material and methods

6.3.1. Experimental setup

A schematic representation of the experimental setup used in this study is presented in Figure 6.1. The experiments were carried out using a 1.00 m × 0.75 m free drainage soil flume, with a depth of 0.05 m, set at 10% slope gradient (round number used in previous studies, e.g. DE LIMA and ABRANTES, 2014a, 2014b; DE LIMA et al., 2014a, 2014b). The soil used in the experiments was

collected from the banks of Mondego River in Coimbra, Portugal, and was classified as loamy-sand, according to USDA (1993), comprising 82.6 ± 2.4% sand (2.0-0.05 mm), 10.7 ± 0.4% silt (0.05-0.002 mm) and 6.7 ± 0.1% clay (< 0.002 mm). The soil presented an organic matter content of 0.86 ± 0.05% and a saturated hydraulic conductivity of 4.51×10^{-6} m s^{-1}, for a bulk density of 1750 kg m^{-3}. A feeder box was installed at the upslope end of the flume, which allowed the uniform application of determined volumes of cold water to the soil surface.

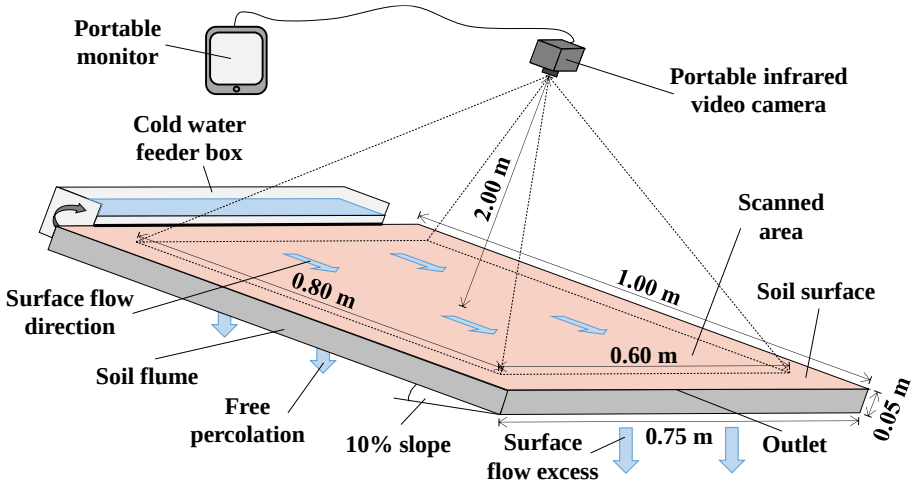

Figure 6.1. Scheme of the setup used in the laboratory tests (not at scale).

An Optris PI-160 portable infrared video camera (Optris GmbH, Germany) was used to record soil surface and water temperatures. The infrared camera converts the invisible infrared energy (working spectral range of 7.5-13.0 μm) emitted by a surface into temperature values that are then converted into a visual image (i.e. thermogram). The camera had an optical resolution of 160 × 120 pixels, a thermal resolution of 0.1 ºC, a frame rate of 100 Hz and a lens with a field of view of 23° × 17°. The camera was attached to a support structure with the focal direction perpendicular to the soil surface of the flume, at a distance of 2.0 m (Figure 6.1).

A rectangular area with 0.80 m × 0.60 m was defined at the soil surface and was scanned with the infrared video camera (Figure 6.1), providing thermal imaging with a pixel size of 0.005 m × 0.005 m. The scanned area was defined smaller than the soil flume to avoid border effects of the flume sides, to avoid higher turbulence near the feeder box caused by the application of cold water to the soil surface and to avoid the downstream effect of the surface excess water flowing out through the outlet.

6.3.2. Soil water repellency (SWR)

To test the proposed technique, 32 rectangular areas of the soil surface, each of 0.06 m × 0.04 m, were induced with different levels of SWR. SWR severity in each of these repellent areas as well as in the surrounding wettable areas (i.e. without SWR) was determined at the soil surface using the Molarity of an Ethanol Droplet (MED) test. To this end, three drops of an ethanol solution were

applied to a determined point of the soil surface using a dropper bottle held immediately above the soil surface. If only one drop infiltrated within 5 s, three drops of the solution with the next highest ethanol concentration were applied subsequently. On the contrary, if two or three drops infiltrated within 5 s, three drops of the solution with next lowest ethanol concentration were applied subsequently. The level of SWR assigned was that of the lowest ethanol concentration at which two or three drops infiltrated within 5 s. Adapted from DOERR et al. (1998), SWR severity was divided in 5 descriptive classes, where the 1st (0% ethanol) denotes no SWR and the 5th (36 and 50% ethanol) denotes extreme SWR. The seven ethanol concentrations used in the MED test and their respective surface tensions and descriptive severity classes are presented in Table 6.1.

Table 6.1. Ethanol concentrations (percentage of volume), respective apparent surface tensions and associated descriptive severity classes used in this study (adapted from DOERR et al., 1998).

Ethanol (%)	0	3	13	18	24	36	50
Surface tension (mN m^{-1})	72.1	60.9	46.3	42.3	38.6	33.1	31.0
Severity class	None	Low	Moderate	Severe		Extreme	

The thermographic technique was applied to two scenarios, with different spatial patterns of SWR severity, as shown in Figure 6.2: i) Scenario 1 with higher levels of SWR severity (13-50% ethanol); and ii) Scenario 2 with lower levels of SWR severity (3-24% ethanol).

6.3.3. Experimental procedure

Air dried pre-sieved soil was manually spread over the flume and compacted to obtain a soil layer with a uniform thickness of 0.05 m with a bulk density of 1750 kg m^{-3}. A sharp straight-edged blade was used to produce a smooth soil surface. After, the soil was saturated and let to dry, aiming to obtain a consistency that allowed the application of a waterproofing spray without disturbing the soil surface.

Since the soil used in the experiments did not present SWR, SWR was induced with different levels of severity (Figure 6.2), by applying a waterproofing spray (composed of hydrocarbons C9-C12, n-alkanes, isoalkanes, cyclics and aromatics) at different distances of the soil surface (between 0.05 and 0.50 m) and with different application durations (between 1 and 5 s). According to DOERR et al. (2000) hydrocarbons are also the main components of natural substances potentially responsible for SWR. To control the rectangular shape of the induced repellent areas during the application of the waterproofing spray, a plastic sheet was used to cover the wettable areas of the soil surface. The application of a waterproofing spray allowed to create spatial patterns of SWR using the same soil, instead of using different soils in different states of SWR that would possibly present different physical and chemical characteristics. After this application, the soil was let to dry again until the waterproofing spray dried out and soil surface temperature became uniform. Therefore, the repellent and wettable areas on the soil surface could not be distinguished visually or thermally before the tests (see Figure 6.2 and Figure 6.3a, showing visual and thermal images of the soil surface of Scenario 1 before the tests). So, given the initial uniformity of soil surface temperature

and of other characteristics (e.g. roughness, soil chemical characteristics, soil depth), the only relevant characteristic that changes is the SWR induced on the soil surface.

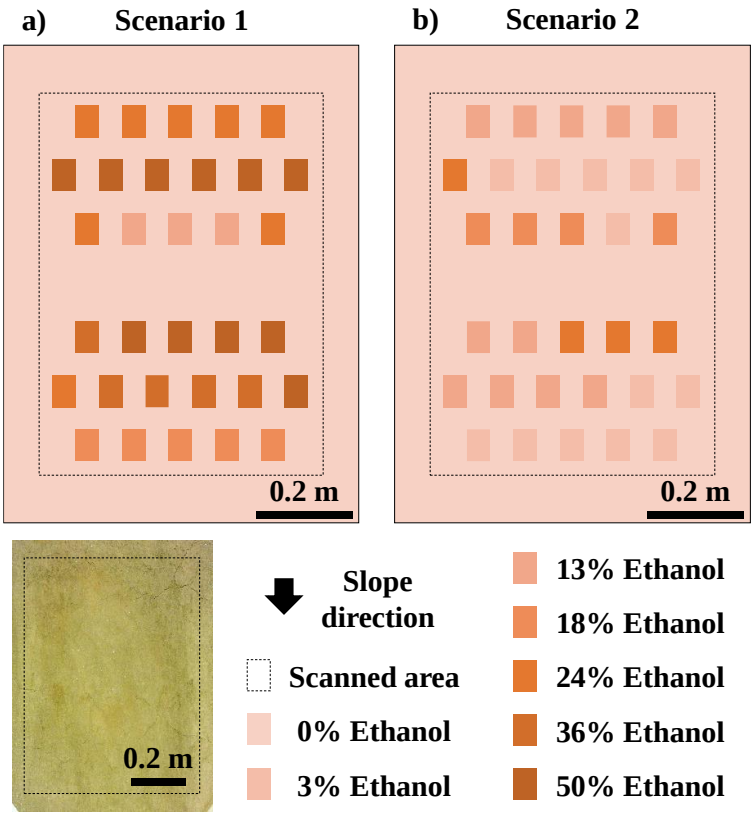

Figure 6.2. SWR severity spatial patterns, in terms of percentage of ethanol, for the two tested scenarios: a) Scenario 1; and b) Scenario 2. The photography of the soil surface of Scenario 1 after induced SWR (lower left corner) shows that repellent areas could not be visually distinguished from wettable areas.

The proposed thermographic technique started by applying approximately 4.0 L of cold water, at a temperature of 10-15 ºC (cooled in a refrigerator), over the soil surface. In previous studies of the authors using infrared thermography to assess soil surface properties (DE LIMA and ABRANTES, 2014a; DE LIMA et al., 2014a, 2014b), hot water at a temperature of 80-85 ºC was used instead of cold water. However, cold water was preferred in this study for its better performance and also its easiness in future replication under field studies. The use of cold water in the field, will provide a largest temperature contrast between soil and water, especially for dry and warm antecedent weather conditions when SWR is expected to be most severe and, thus, to have greatest impact on infiltration and runoff generation. The water was released manually by turning over the feeder box located upslope of the flume (Figure 6.1). The feeder box was tipped in a quick and fast movement in order to achieve a uniform discharge and a flow depth uniformity over the measuring area but, at the same time, to induce minimum soil surface disturbances. The volume of water and consequent applied discharge was adjusted to the conditions of the test (e.g. dimension of the measuring area, slope, water temperature) and soil characteristics (e.g. permeability, roughness, macroporosity).

Thermal videos of the soil surface and water were recorded with the portable infrared video camera throughout the tests. These videos were then analysed with the objective of identifying the repellent and wettable areas. For each scenario, a thermogram (i.e. snapshot of the thermal video) was selected and its temperatures were plotted against the corresponding SWR severity in terms of percentage of ethanol classes. In order to map SWR severity spatial pattern with the thermographic technique, the temperature of the thermograms was converted into percentage of ethanol classes using a relation between the recorded temperatures and the actual SWR. Spatial patterns of percentage of ethanol classes measured using the MED test and predicted on the basis of the thermographic technique were then compared.

6.4. Results and discussion

Because the infrared camera converts the infrared radiation into temperature values based on the materials emissivity coefficients, it should be noted that water and soil emissivity coefficients are very similar in the operational spectral range of the present camera. Also, the proposed technique does not aim to assess the exact actual temperatures of the soil surface and water but rather the differences in temperature between repellent and wettable areas.

A chronological sequence of thermograms obtained for Scenario 1 (Figure 6.2a), from an instant just before the cold water application to an instant after the passage of the water wave through the scanned area is shown in Figure 6.3, illustrating how works the proposed technique. At the beginning of the test (Figure 6.3a) soil surface temperature was almost uniform, with a mean value of 26.3 ºC and a standard deviation of 0.4 ºC; therefore, it was not possible to distinguish between wettable and repellent areas. As the water flowed down the flume over the soil surface (Figure 6.3b), it started to be repelled in the repellent areas (Figure 6.3c), starting to result in thermal differences between warmer repellent areas and cooler wettable areas. After the passage of the water wave through the measuring area (Figure 6.3d), repellent areas could be clearly distinguished based on their lighter (reddish) colouration associated with higher temperatures (see colour scale in Figure 6.3). Furthermore, stronger levels of SWR were associated with higher temperatures, as illustrated in Figure 6.3 through the areas where SWR corresponded to the ethanol classes of 18 and 50%. After the water had exited from the soil flume (Figures 6.3e, 6.3f, 6.3g), thermal differences between the wettable and repellent areas first increased for some instants. Then the thermal differences again decreased when soil surface temperature became once more spatially uniform as at the beginning of the test.

The imaging results were, in fact, driven by differences in soil water content, as observed in DE LIMA et al. (2014b). Differences in soil water content were consequence of differences in SWR severity. In wettable areas more cooled water flowed into the soil, therefore these areas presented lower temperatures. Repellent areas presented higher temperatures, because less cooled water has infiltrated in these places.

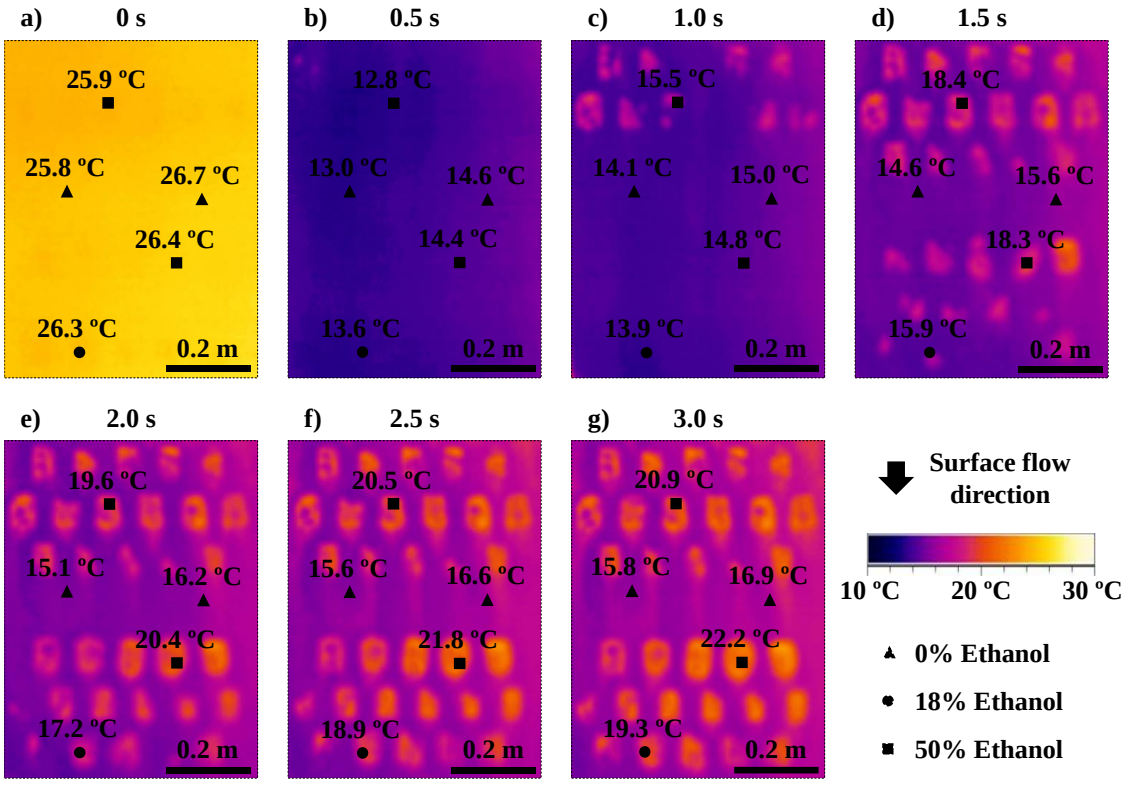

Figure 6.3. Chronological sequence of thermograms obtained during the application of the thermographic technique in Scenario 1: a) Instant just before the water application (0 s) where repellent areas cannot be identified; b) During the passage of the cold water wave (0.5 s); and c) d) e) f) and g) After the passage of the water wave through the scanned area (1.0, 1.5, 2.0, 2.5 and 3.0 s).

The thermograms of the two tested scenarios after the passage of the water wave through the scanned area (i.e. 3 s after the water application) are shown in Figure 6.4. This specific instant was chosen because it revealed the strongest thermal differences between the wettable and repellent areas and, thus, allowed evaluating the best possible performance of the proposed technique. Both thermograms allowed to distinguish repellent areas from wettable areas. Areas with higher SWR severity were more clearly perceptible than areas with lower SWR severity, as was evident from a comparison of the two thermograms with the scenarios' respective spatial SWR patterns (see Figure 6.2). Areas with severe and extreme SWR, which were more frequent in Scenario 1 than in Scenario 2, revealed the highest recorded temperatures. In contrast, some of the areas with low SWR in Scenario 2, especially those located on the 2nd and 6th rows, could not be distinguished in terms of soil surface temperature from wettable areas. Likewise, in DE LIMA et al. (2014b), while higher surface soil permeability differences were clearly perceptible, smaller differences were not so easily detected.

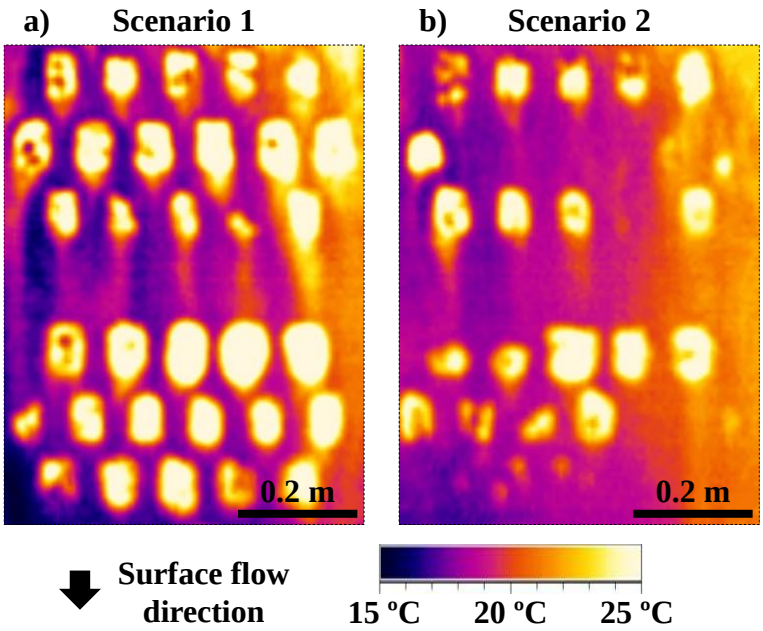

Figure 6.4. Thermograms of the soil surface of 3 s after the water application for the two tested scenarios: a) Scenario 1; and b) Scenario 2. Notice that the colour scale is different from the one in Figure 6.3.

The thermograms revealed some deformations of the rectangular areas where SWR was induced, suggesting a leaching of SWR from these areas in the downslope direction. These deformations could be artefacts of the present technique but, at the same time, could also reflect heat diffusion, or transport of repellent soil particles by the water wave, as observed in DE LIMA and ABRANTES (2014a) and in DE LIMA et al. (2014b). The thermograms also revealed a tendency to record higher temperatures in the right side of the measuring area, which was attributed to a slightly lower flow depth in this region during the passage of the cold water through the measuring area.

Figure 6.5 presents the frequency distribution of the temperature, in classes of 5 ºC, and their median values, plotted against the seven percentage of ethanol classes. In the case of both scenarios, the median temperatures increased monotonically with increasing ethanol class and, thus, level of SWR. Furthermore, the median temperature for each ethanol class differed little between the two scenarios, attesting to the reproducibility of results between different experiments. Worth mentioning in this respect is that small variations in both soil surface temperature and the temperature of the applied water are difficult to avoid, and, in this particular case, could help explain the differences in the temperature distributions between the two scenarios, most noticeably at the ethanol class of 24%.

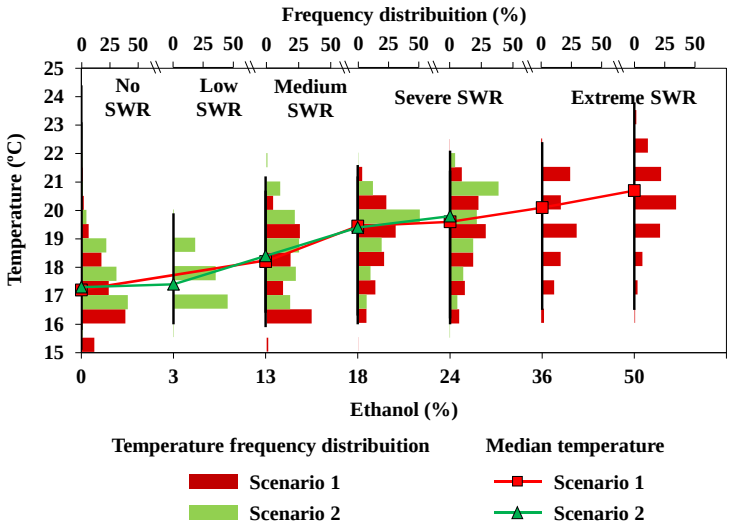

Figure 6.5. Temperature frequency distributions (classes of 5 ºC), and median temperatures plotted against the corresponding percentage of ethanol classes.

Figure 6.6 illustrates the two empirical functions for converting the temperatures extracted from the thermograms into percentage of ethanol classes. Both functions were derived from the information shown in Figure 6.5, assuming that the median temperatures varied linearly between two consecutive percentage of ethanol classes and that the midpoints of the linear variations defined the boundaries of the functions for each class. The lower and upper boundaries, respectively of the lower and higher percentage of ethanol classes, corresponded to the minimum and maximum recorded temperatures.

Applying in turn these functions to the thermograms allowed mapping the spatial patterns of SWR for both scenarios, as shown in Figure 6.7. A single empirical function covering the conditions of the two scenarios would be more valuable. However, the two scenarios did not presented the same levels of SWR (Scenario 1 presented SWR levels from 3 to 24% of ethanol and Scenario 2 presented SWR levels from 13 to 50% of Ethanol). Therefore, if such single empirical function was applied levels of SWR that only exist in Scenario 1 will also appear in Scenario 2 and vice versa.

Figure 6.8 compares the percentage of ethanol as measured using the MED test with those predicted on the basis of the thermograms and derived empirical functions. This is done for some longitudinal and transversal cross sections of the scanned area. The thermography based predictions were more reliable in the cases of none and medium to extreme SWR, even though medium to severe ethanol classes were often overestimated. This overestimating effect was observed in previous studies of the authors (DE LIMA and ABRANTES, 2014a; DE LIMA et al., 2014b). In the case of low SWR its presence was not always correctly predicted.

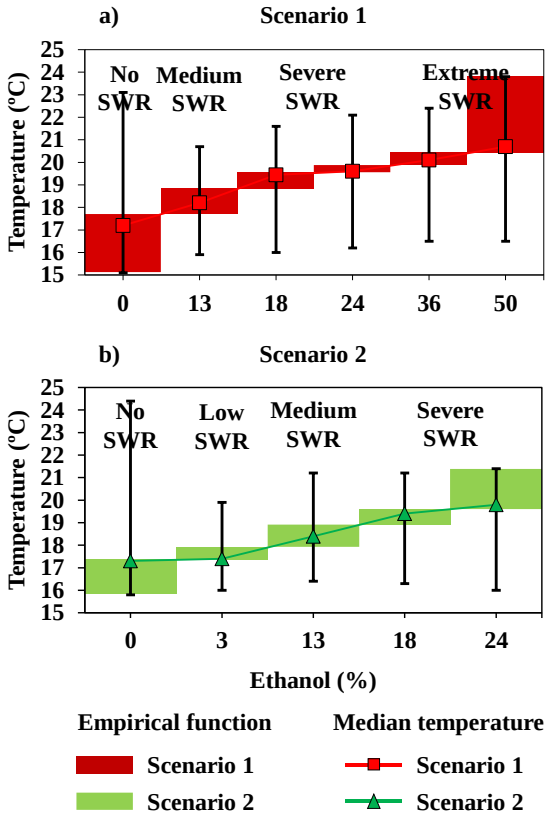

Figure 6.6. Empirical functions (filled areas) used to convert temperature data into percentage of ethanol classes: a) Scenario 1; and b) Scenario 2.

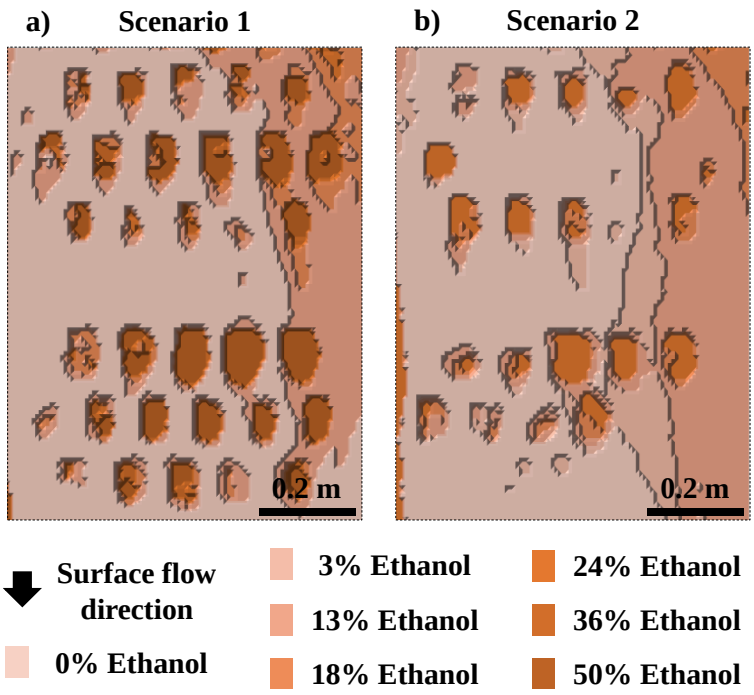

Figure 6.7. SWR spatial distribution, in terms of percentage of ethanol, obtained with the thermographic technique: a) Scenario 1; and b) Scenario 2. See corresponding thermograms in Figure 6.4.

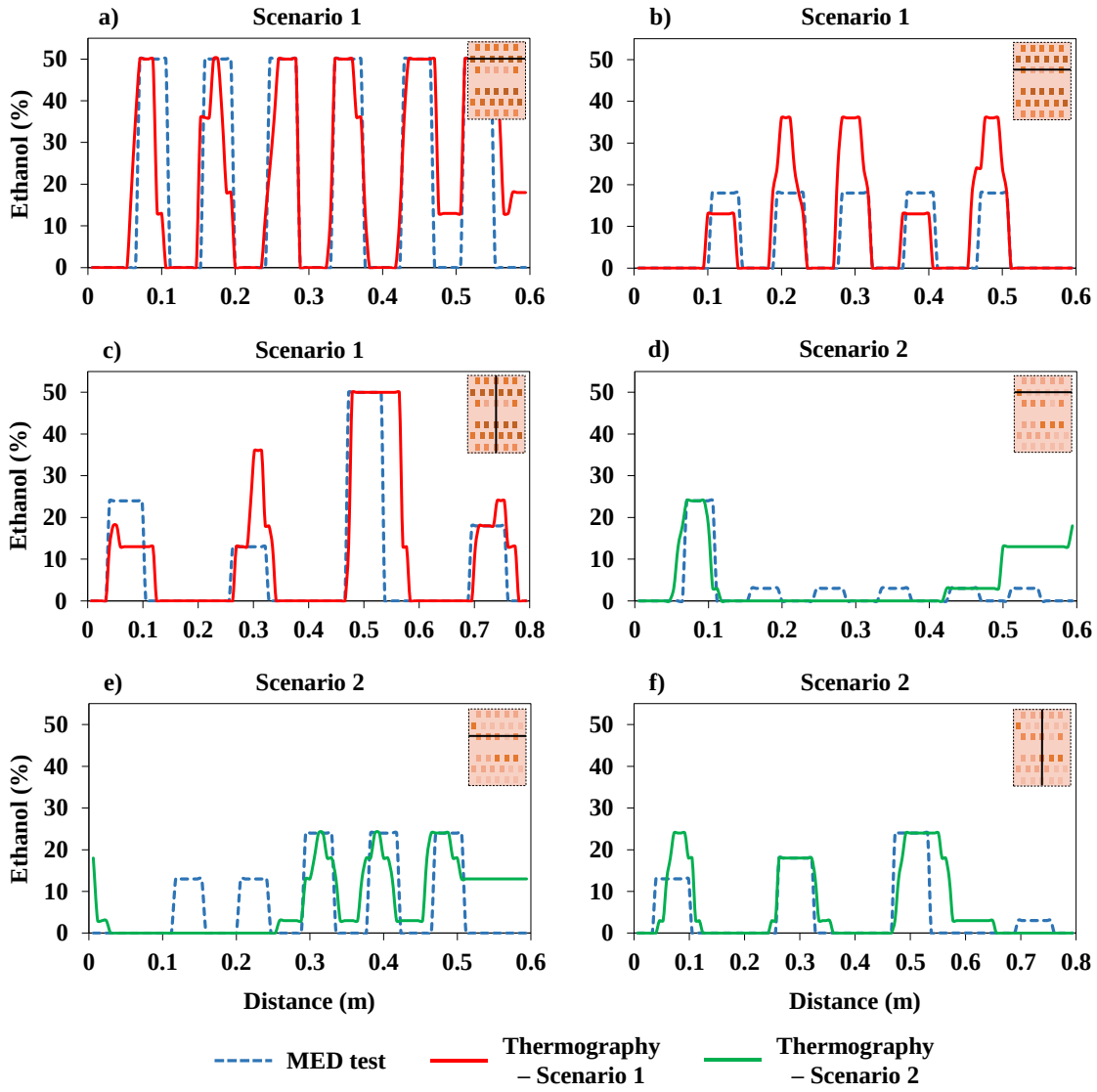

Figure 6.8. Comparison of SWR, in terms of percentage of ethanol, predicted on the basis of thermography and measured using the MED test, along longitudinal and transversal cross sections shown in the upper right corner of the plots (see SWR spatial distribution obtained with thermography and measured with the MED test in Figures 6.2 and 6.7).

6.5. Conclusions

In the present small-scale exploratory laboratory study, a technique based on infrared thermography was tested for assessing water repellency at the soil surface (SWR) and mapping its spatial variability. The technique proved to be of easy and fast application and, in overall terms, successful in distinguishing areas that were water repellent from areas that were wettable as well as in distinguishing between areas with different levels of SWR, in particular, between areas with extreme as opposed to low to medium SWR.

The proposed technique, however, also presented some drawbacks: i) It performed poorly in identifying areas with low SWR; ii) It may require measurements of SWR as a basis for accurate

predictions, as the underlying equation may depend strongly on local soil conditions as well as experimental aspects (e.g. temperature of the applied water); iii) It may interfere with the spatial SWR patterns themselves, by leaching, and, as such, is not necessarily a non-destructive technique; and iv) It may also affect the soil surface characteristics, especially in easily erodible soils.

Overall, the proposed technique apparently has high potential to contribute to a better understanding of the hydrological impacts of different spatial patterns of SWR due to its capacity to monitor in real time the dynamics of these impacts (e.g. establish critical thresholds when SWR is diminished, i.e. to look into when SWR areas turn from runoff sources to runoff sinks).

Results of this exploratory study suggest that is worthwhile to explore this technique in the field. Only extensive field work can, in fact, reveal the suitability of the technique in real conditions. Further work is therefore suggested for a more robust assessment of the applicability of the proposed technique, under field conditions with the presence of natural SWR. Future testing should analyse the impacts of applying different amounts of water and in different regimes, and evaluate the technique at different spatial scales and for different spatial patterns of SWR as well as different soil surface conditions in terms of, e.g. random roughness and cover of stones and mulch, which is beyond the scope of the presented analysis. Also, future tests should include SWR measurements with other techniques, such as the WDPT test, and measurements of soil water content to study its relation with the SWR.

"Each soil has had its own history. Like a river, a mountain, a forest, or any natural thing, its present condition is due to the influences of many things and events of the past."

- Charles Kellogg

7. FIELD ASSESSMENT OF SOIL WATER REPELLENCY USING INFRARED THERMOGRAPHY[5]

7.1. Abstract

This study aimed to evaluate the applicability of an infrared thermography technique relying on cooling the soil surface with cold water for assessing soil water repellency (SWR) severity under field conditions. This study is a follow-up of earlier exploratory small-scale laboratory tests, where SWR spatial variability was mapped and repellent areas could be clearly detected on the thermal imaging due to their higher temperatures, thus distinguishing them from the remaining wettable areas.

Field tests were carried out, where both natural and artificial SWR were mapped through thermal imaging, using a portable infrared video camera. Cold water was used to create a temperature gradient on the soil surface in order to assess SWR. Naturally repellent soils were found in a pine and eucalyptus forest and artificial SWR was induced with a waterproofing spray. The molarity of an ethanol droplet (MED) test was used to measure both natural and artificial SWR severity.

The technique was, in overall terms, successful in mapping SWR spatial variability, distinguishing repellent from wettable areas as well as distinguishing different levels of SWR severity. Only extensive testing can, ultimately, validate the technique and reveal its suitability in different field conditions (e.g. surface roughness, surface cover, spatial scale).

Keywords

Soil water repellency; Infrared thermography; Field tests

7.2. Introduction

Soil water repellency (SWR) is recognized as a key hydrological and geomorphological process since the earlier part of the 20th century. However, first observations of this phenomenon were reported in the later part of the 18th century (DEBANO, 2000a, DOERR et al., 2000). SWR is a major concern to hydrogeologists and land managers since it can alter infiltration and solute

[5] ABRANTES, J.R.C.B., DE LIMA, J.L.M.P., PRATS, S.A. and KEIZER, J.J. (2016). Field assessment of soil water repellency using infrared thermography. *Forum Geographic*, 15(2), 12-18. DOI:10.5775/fg.2016.019.s.

transport into the soil, enhancing surface runoff and associated erosion and affecting seed germination and plant growth, triggering land degradation processes (KEIZER et al., 2005b; LEIGHTON-BOYCE et al., 2007; RITSEMA and DEKKER, 1994; SHAKESBY et al., 1993).

SWR is originated by the coating of soil particles with hydrophobic organic substances usually released by plants or decomposing plant material (DEKKER and RITSEMA, 1994; KEIZER et al., 2005c). Repellent soils have been found in fire affected forest lands (BADÍA-VILLAS et al., 2014; KEIZER et al., 2008; MATAIX-SOLERA and DOERR, 2004), but also in pine and eucalypt forest lands not affected by fires and in agricultural lands with high soil organic matter content (DOERR et al., 2000, KEIZER et al., 2007, SANTOS et al., 2013).

One of the most commonly used technique to measure SWR is the Molarity of an Ethanol Droplet (MED) test (LETEY, 1969), which measures the surface tension between an ethanol solution and the soil surface to indirectly determine how strongly the water is repelled. It provides quantitative data, but the subsequent classification or characterization of these data varies with the objective of the investigator and perception of what constitutes low or high SWR severity. The MED test is a practical and quick test and has therefore been widely applied in especially intensive field monitoring studies (KEIZER et al., 2005c; 2007, 2008; MALVAR et al., 2016; SANTOS et al., 2013). Other techniques used to measure SWR include measurement of the time taken by a water drop to completely penetrate into the soil, measurement of the water-soil contact angle, measurement of ethanol and water ethanol sorptivity, measurement of the water entry pressure head of a soil and the sessile drop method (DEKKER et al., 2009; KING, 1981). However, these techniques only provide punctual data that must be grouped or scaled to bring out spatial coherence, in order to properly map spatial variations of SWR at field and landscape scales.

Infrared thermography based methods have been used as high resolution imaging tools in hydrology (BONAR and PETRE, 2015; MEJÍAS et al., 2012; SCHUETZ et al., 2012) and physical geography (DEHVARI and HECK, 2007; POHL and VAN GENDEREN, 1998; RICCHETTI, 2001), in particular those using portable hand-held infrared cameras have been increasing due to recent reductions in their prices and substantial enhancements of their portability and spatial resolution. In recent studies, infrared thermographic techniques were used by the authors to assess different soil surface hydrological processes in laboratory and field conditions (ABRANTES and DE LIMA, 2014; ABRANTES et al., 2017; DE LIMA and ABRANTES, 2014a, 2014b; DE LIMA et al., 2014a, 2014b, 2014c, 2015a, 2015b).

This study aimed to evaluate the applicability of a field infrared thermography technique relying on cooling the soil surface with cold water for assessing small-scale SWR severity under field conditions. This study is a follow-up of exploratory small-scale laboratory tests presented in ABRANTES et al. (2017) where SWR spatial variability was mapped and repellent areas could be clearly detected on the thermal imaging due to their different coloration associated with higher temperatures, thus distinguishing them from the remaining wettable areas.

7.3. Study area and soil surface repellency

The field tests presented in this study (Figure 7.1) were conducted in a Pine (P. pinaster) and Eucalyptus (E. globulus) forest site located in Pinhal de Marrocos, Coimbra, Portugal, in the surroundings of the Department of Civil Engineering of the Faculty of Sciences and Technology of the University of Coimbra. The soils in this site were loamy sand soils with a surface slope between 15-20%. Soil surface was dry at the beginning of the tests.

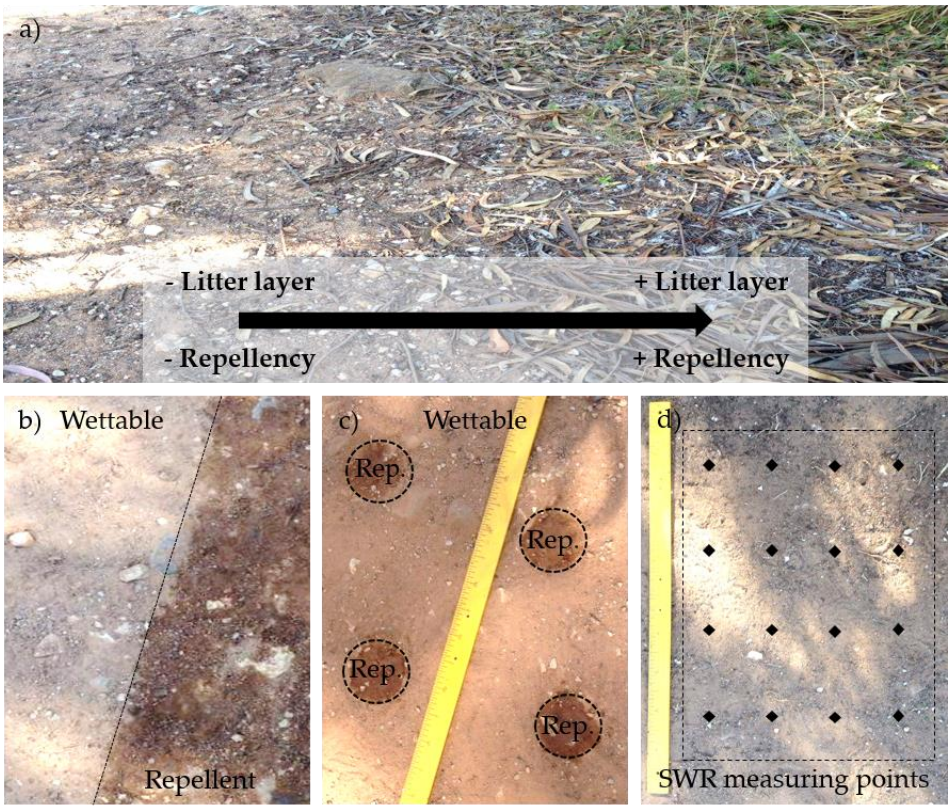

Figure 7.1. Photographs of: a) study area with observation of the increasing layer of litter and, consequently, increasing SWR; b) and c) scenarios 5 and 6, respectively, with representation of the boundary between the wettable and the induced repellent areas (photographs taken immediately after application of the waterproofing spray); and d) location of the places where the MED test was used to measure the SWR in the scanned area, after removal of the litter layer.

The thermographic technique was tested in 6 areas of the study site, each with approximately 0.65×0.85 m^2. The areas presented different characteristics (Figure 7.1a), such as areas with bare soil surface in open patches of the tree canopy (i.e. wettable soil surface) and areas with soil surface covered with a thick litter layer of pine and eucalyptus residues (i.e. repellent soil surface). Some wettable areas of the soil surface were also induced with artificial repellency by applying a waterproofing spray. This allowed to test the technique in different soil surface repellent conditions, ranging from wettable to extremely repellent: scenario 1 with wettable soil surface; scenario 2 with low SWR; scenario 3 with moderate SWR; scenario 4 with severe SWR; scenario 5 with half of the

area artificially induced with extreme repellency (Figure 7.1b); and scenario 6 with circular areas artificially induced with extreme repellency (Figure 7.1c).

SWR severity was determined at the soil surface after removal of the litter layer, using the MED test (following proceeding used in ABRANTES et al., 2017). SWR severity was divided in 5 repellency intensity classes, according to the ethanol concentration, as follows (adapted from DOERR et al., 1998): class 0, wettable (0%); class 1, low repellency (1, 3 and 5%); class 2, moderate repellency (8.5 and 13%); class 3, severe repellency (18 and 24%) and class 4, extreme repellency (36, 50% and more). In each scenario, SWR measurements were conducted randomly at the soil surface on 16 points in a regular pattern, as shown in Figure 7.1d.

7.4. Infrared thermographic technique

A schematic representation of the experimental setup used in this study is presented in Figure 7.2. The proposed thermographic technique tested previously in laboratory (ABRANTES et al., 2017), started by applying approximately 4.0 L of cold water, at a temperature of 6.3 ± 0.5 ºC (cooled in a refrigerator), over the soil surface. The water was released manually by turning over a feeder box located upslope of the scanned area (Figure 7.2). The feeder box was tipped in a quick and fast movement in order to achieve a uniform discharge and a flow depth uniformity over the scanned area but, at the same time, to induce minimum soil surface disturbances.

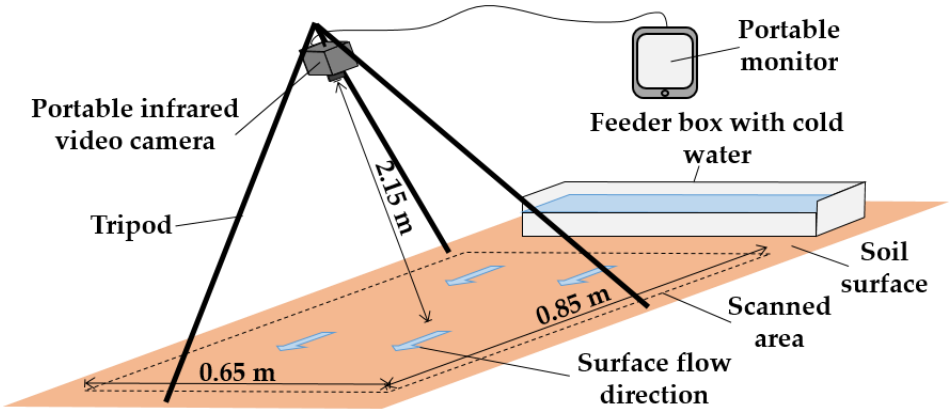

Figure 7.2. Scheme of the setup used in the field tests (not at scale).

Thermal videos of the soil surface and water were recorded with an Optris PI-160 portable infrared video camera (Optris GmbH, Germany) with an optical resolution of 160 × 120 pixels. The camera was attached to a support structure with the focal direction perpendicular to the soil surface, at a distance of 2.15 m (Figure 7.2).

These videos were then analysed with the objective of distinguish repellent from wettable areas as well as identify different levels of SWR. For each scenario, two thermograms (i.e. snapshot of the thermal video) were selected and its temperatures were analysed: one corresponding to an instant

just before the cold water application; and other corresponding to an instant just after the passage of the cold water wave through the scanned area, approximately 5 s after the cold water application. This specific instant was chosen because, in general, it revealed the strongest thermal differences between wettable and repellent areas and, thus, allowed evaluating the best possible performance of the proposed technique.

7.5. Results and discussion

Thermograms of the six scenarios studied in the field experimental tests, using the proposed infrared thermography technique, are presented in Figure 7.3. Each thermogram comprises a total of 19200 pixels (i.e. temperature data points), each one with a size of 28.8 mm^2.

At the beginning of the tests, soil surface temperature was not exactly the same in all scenarios. Average soil surface temperature of scenarios with previous presence of a litter layer of forest residues (removed at the beginning of the tests and before thermal images were captured) was lower than bare soil scenarios (average values of 22.2 and 24.0 ºC, respectively). Before the application of the thermographic technique (i.e. application of the cold water on the soil surface), the extremely repellent area induced with waterproofing spray could not be distinguished from the wettable area in scenario 5 (Figure 7.3e left). However, circular extremely repellent areas, induced with waterproofing spray, in scenario 6 showed slightly lower temperatures than the remaining wettable area. Even so, these thermal differences were not significant and, by themselves, were not sufficient to identify the extremely repellent areas.

As the cold water flowed down the scanned areas, it started to be repelled in the repellent areas. Therefore, after the passage of the water wave through the scanned areas, scenarios with stronger levels of SWR presented higher average temperatures (cold water was repelled), as opposed to scenarios with no (wettable soil) and lower levels of SWR, where more cold water infiltrated into the soil, thereby cooling it. Extremely repellent areas induced with waterproofing spray in scenarios 5 and 6 (Figures 7.3e and 7.3f) could be clearly distinguished from the wettable area, based on their lighter colouration associated with higher temperatures (also observed in ABRANTES et al., 2017).

Imaging results were driven by soil water content as a result of infiltration differences (also observed in DE LIMA et al., 2014b). As stated before, in wettable areas more cooled water flowed into the soil, therefore these areas presented lower temperatures. Repellent areas presented higher temperatures, because less cooled water has infiltrated in these places since it was repelled. Therefore, these imaging results are a clear indicator of the drainage pattern of each studied scenario, especially Figures 7.3c and 7.3d.

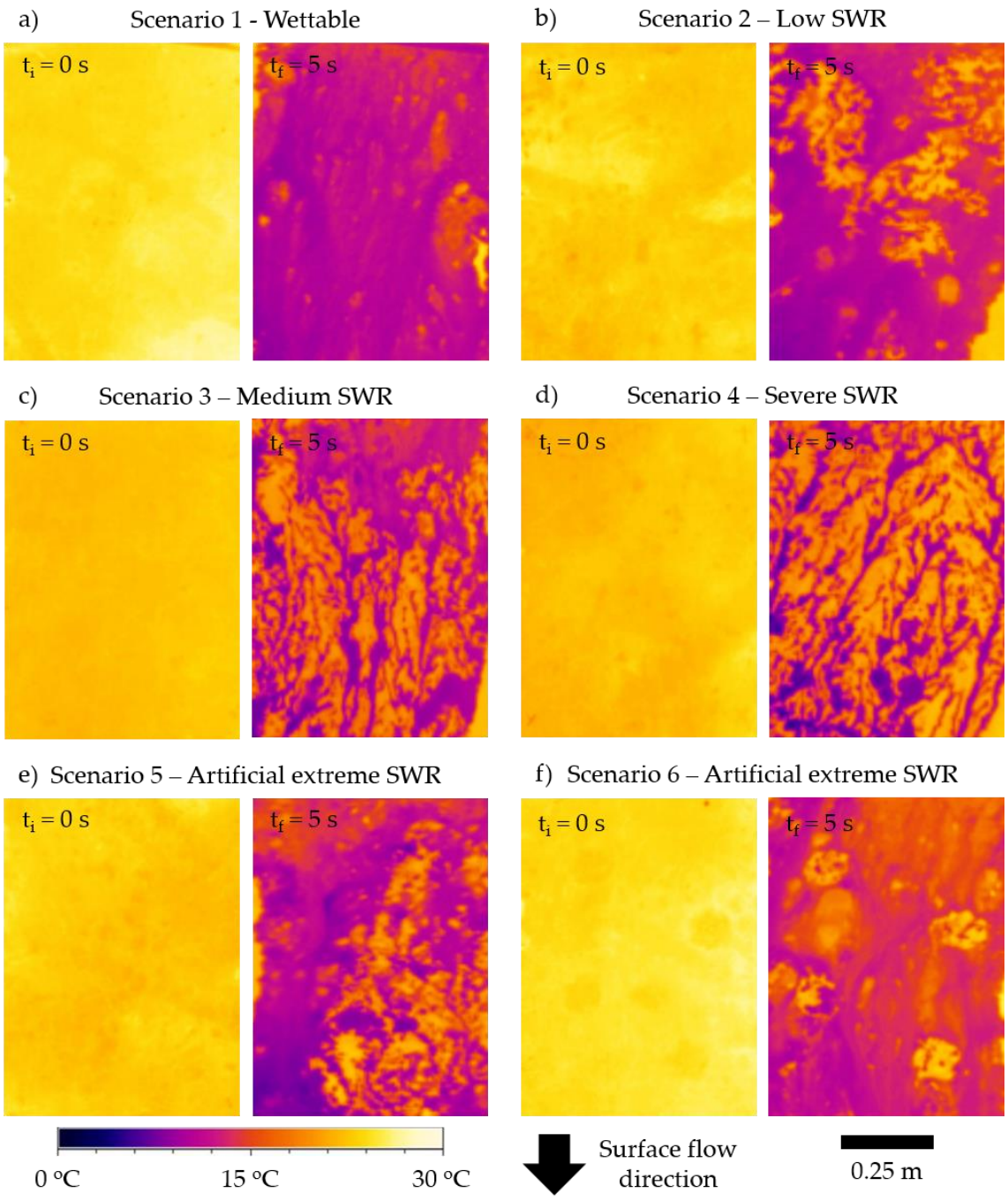

Figure 7.3. Unprocessed soil surface thermograms of the six scenarios studied in the field tests, before (t_i = 0 s) and after (t_f = 5 s) the application of the thermographic technique (i.e. application of the cold water on the soil surface): a) scenario 1 with wettable soil surface; b) scenario 2 with low SWR; c) scenario 3 with moderate SWR; d) scenario 4 with severe SWR; e) scenario 5 with half of the area artificially induced with extreme repellency; and f) scenario 6 with circular areas artificially induced with extreme repellency.

Since the application of the thermographic technique only lasted 5 s (i.e. time taken from the application of the cold water to its passage through the scanned area), temperature exchange between the soil surface (and/or water flowing at the soil surface) and the atmosphere was considered negligible.

The thermogram of scenario 6 presented some deformations of the circular areas, where extreme SWR was induced, suggesting leaching of SWR from these areas in the downslope direction (also observed in ABRANTES et al., 2017). These deformations could result/reflect the transport of repellent soil particles by the water wave and/or heat diffusion, as observed in DE LIMA and ABRANTES (2014a) and DE LIMA et al. (2014b).

As stated before, soil surface temperature at the beginning of the tests (i.e. prior to cold water application) was not exactly the same in all scenarios; therefore, the temperature in the thermograms was corrected by subtracting the temperature of the thermograms before the cold water application (T_i at t_i = 0 s) to the temperature of the thermograms after the cold water application (T_f at t_f = 5 s), as schematized in Figure 7.4 for scenario 1. Since the temperature of the cold water applied to the soil surface was approximately equal in all tested scenarios (6.3 ± 0.5 ºC) a correction of this temperature was not done. However, a similar correction should be considered if the temperature of the applied water would not equal.

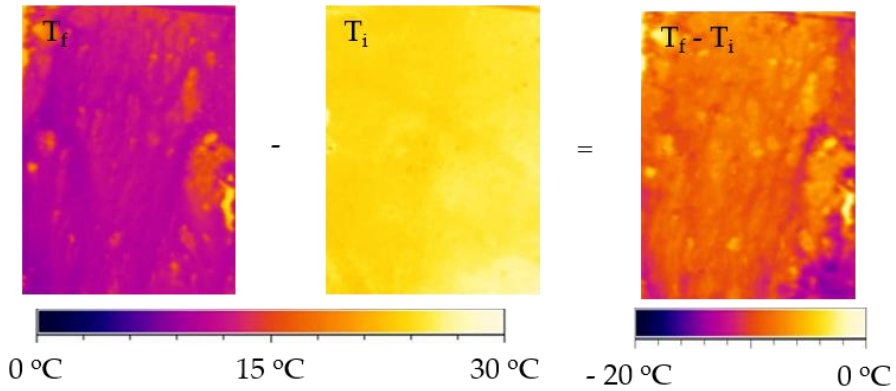

Figure 7.4. Scheme of the procedure used in the temperature correction of the soil surface thermograms, for scenario 1.

The correction procedure resulted in the final thermograms is shown in Figure 7.5, for all tested scenarios. With this correction, temperature of all thermograms can be compared without interference of the initial temperature of the soil surface. This is relevant because average soil surface temperature of scenarios with previous presence of a litter layer of forest residues was lower than bare soil scenarios.

As shown in Figure 7.5, scenarios with stronger levels of SWR presented a corrected temperature (i.e. temperature difference) closer to 0 ºC, since its final temperature was more similar to the initial temperature, due to lower cold water infiltration. By contrast, scenarios with no and lower levels of SWR presented average lower corrected temperatures, due to higher infiltration of cold water into the soil. This is shown in the graph of the Figure 7.5g which presents the average corrected temperatures, extracted from the processed thermograms, and plotted against the 5 SWR severity classes measured with the MED test.

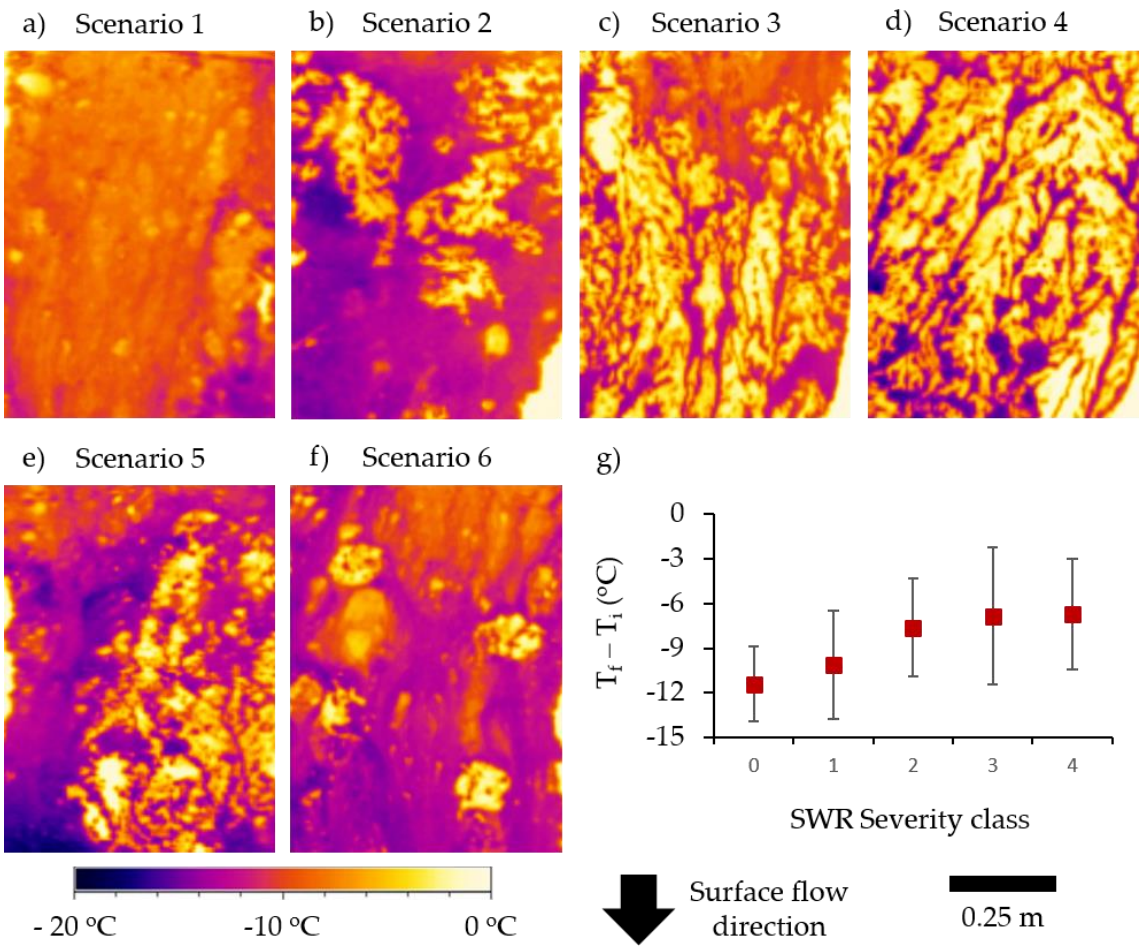

Figure 7.5. a), b), c), d), e) and f) Thermograms of the soil surface after the correction procedure, for all tested scenarios; and g) Average and standard deviation (19200 data points) of the corrected temperatures plotted against the 5 SWR severity classes measured with the MED test (class 0 – wettable, class 1 - low SWR, class 2 - moderate SWR, class 3 - severe SWR and class 4 - extreme SWR).

Figure 7.6 shows corrected temperatures extracted from the thermograms, for some cross sections of the scanned area, for all tested scenarios. The longitudinal (Figure 7.6a) as well as transversal (Figure 7.6b) cross sections revealed that average corrected temperatures contrasted markedly between scenarios 1, 2 and 3-4. However, almost no difference was observed between the average corrected temperature of scenarios 3 and 4. For the induced extreme SWR scenarios (scenario 5 in Figure 6c and scenario 6 in Figure 7.6d) a clear distinction existed between the corrected temperature in the repellent and wettable areas.

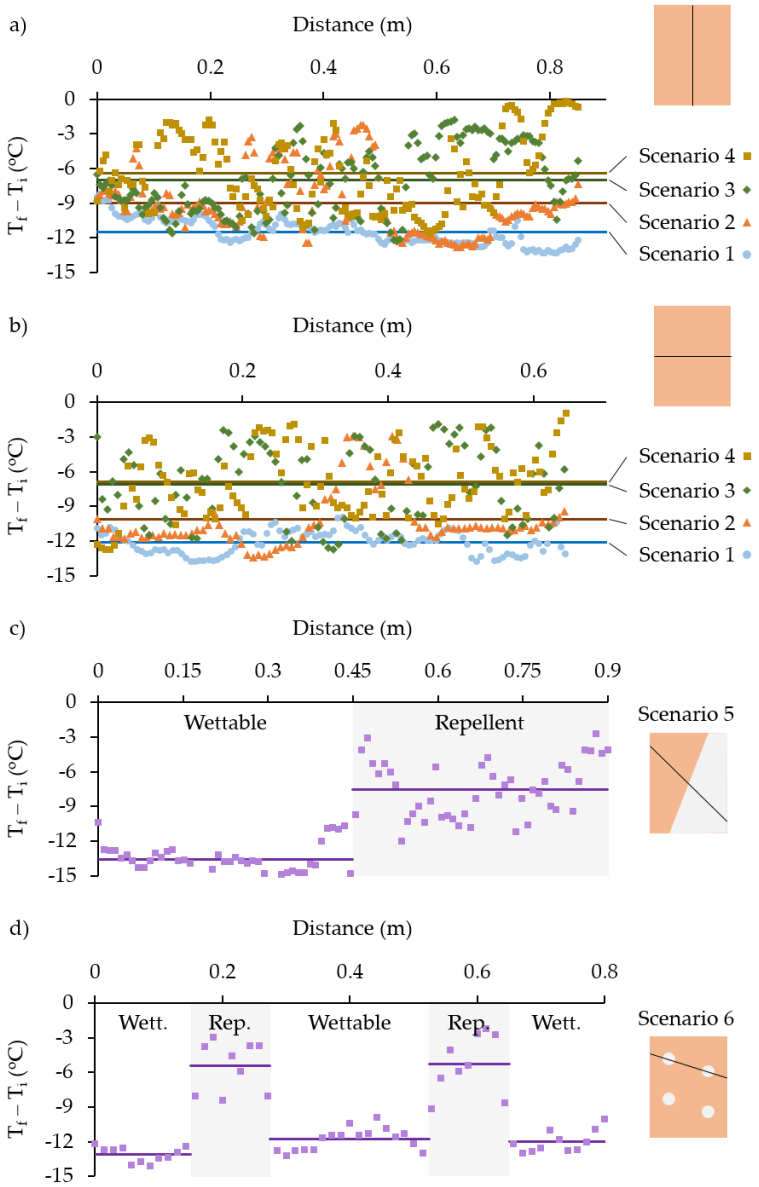

Figure 7.6. Soil surface corrected temperature (data points and average lines), for some cross sections of the scanned area (shown in the right side of the plots): a) Longitudinal cross sections for scenarios 1, 2, 3 and 4 (160 data points); b) Transversal cross sections for scenarios 1, 2, 3 and 4 (120 data points); c) Cross section for scenario 5 (90 data points); and d) Cross section for scenario 6 (60 points).

7.6. Conclusion

In the present field study, a technique based on infrared thermography was tested for assessing water repellency at the soil surface (SWR). The technique proved to be an easy and fast way for gathering a high resolution SWR map in small scale field plots, allowing thermograms with 19200 data points versus the 16 MED measurements. The technique was, in general, successful in distinguishing areas that were water repellent from areas that were wettable as well as in distinguishing between areas with different levels of SWR. Overall, the proposed technique

apparently has high potential to contribute to a better understanding of the hydrological impacts of SWR, by also revealing the drainage pattern of the field plots.

However, the proposed technique presented some drawbacks: i) It may require measurements of SWR as a basis for accurate predictions; ii) It can only be applied to relatively flat sloping soil surfaces and its results may depend strongly on experimental aspects (e.g. temperature of applied water), as well as on local soil conditions, such as roughness, temperature, moisture and macroporosity, which could create preferential infiltration patterns even in highly repellent areas; and iii) It may affect the soil surface characteristics, especially in easily erodible soils and it may alter SWR levels and, especially through leaching, SWR spatial patterns.

Results of this study suggest that is worthwhile to explore this technique. Only extensive testing can, in fact, validate the technique and reveal its suitability under different field conditions (e.g. surface roughness, surface cover, spatial scale).

"The movement of heavenly bodies despite their distance from earth have presented fewer difficulties to me than the movement of water which is within my reach."

- Galileo

8. USING A THERMAL TRACER TO ESTIMATE OVERLAND AND RILL FLOW VELOCITIES[6]

8.1. Abstract

Flow velocity is a basic hydraulic property of surface flows and its precise calculation is necessary for process based hydrological models, such as soil erosion and rill development models, as well as for modelling sediment and solute transport by runoff. This study presents a technique based on infrared thermography to visualize very shallow flows and allow a quantitative measurement of overland flow and rill flow velocities. Laboratory experiments were conducted to compare the traditional dye tracer technique with this new thermal tracer technique by injecting a combined tracer (heated dye) into shallow flowing surface water.

The leading edge tracer velocities estimated by means of infrared video and by the usual real imaging video were compared. The results show that thermal tracers can be used to estimate both overland and rill flow velocities, since measurements are similar to those resulting from using dye tracers. The main advantage of using thermography was the higher visibility of the leading edge of the injected tracer compared with the real image videos.

Keywords

Shallow flow velocity; Thermal tracer; Infrared thermography

8.2 Introduction

Shallow flows (e.g. overland flow, rill flow) often occur in natural and urbanized drainage basins and have important implications (e.g. water erosion, water quality). The understanding and modelling of these flows are necessary in surface hydrology and soil and water conservation studies. Flow velocity is a basic hydraulic property of overland flow and its precise calculation is a necessary component of all process based hydrological models such as soil erosion and rill development models (e.g. GOVERS, 1992; GIMÉNEZ et al., 2004; WIRTZ et al., 2012), as well as in modelling sediment and solute transport by runoff (e.g. LEI et al., 2010; MÜGLER et al., 2011).

[6] DE LIMA, J.L.M.P. and ABRANTES, J.R.C.B. (2014). Using a thermal tracer to estimate overland and rill flow velocities. *Earth Surface Processes and Landforms*, 3(10), 1293-1300. DOI:10.1002/esp.3523.

For a long time, common techniques used in shallow flow velocity measurements for soil erosion studies were based on the determination of the travel time of a tracer across a defined section, in both laboratory (e.g. ABRAHAMS and ATKINSON, 1993; GIMÉNEZ and GOVERS, 2002) and field conditions (e.g. HORTON et al., 1934; WIRTZ et al., 2012). More recently, a tracer technique that combined high speed digital cameras and laser scanners, and called Large Scale Particle Image Velocimetry (LSPIV), was used to estimate the temporal and spatial variability of shallow flow velocities and flow depths (e.g. JODEAU et al., 2008; KIM et al., 2008; LEGOUT et al., 2012).

According to FLURY and WAI (2003) an ideal water tracer has the following characteristics: i) Movement similar to water, without sorption to soils, sediments or rocks and without degradation during the measurement time; ii) Low background concentration, i.e. clearly discernible from the background of the system; iii) Behaviour unaffected by changes in the water chemistry (e.g. pH); iv) Detectable either by chemical analysis or by visualization; and v) Low toxicological impact on the study environment. Different materials have been tested as water tracers in flow velocity experiments (e.g. chemicals, gases, natural and radioactive isotopes, magnetized materials, fluorescent particles, floating objects, dyes, electrolytes). Dyes of different colours, fluorescent dyes, fluorescent particles and electrolytes are the tracer materials most often used to measure flow velocity in soil erosion studies (e.g. ABRAHAMS et al., 1986; LEI et al., 2005, 2010; SHI et al., 2012; TATARD et al., 2008; TAURO et al., 2012a, 2012b). The usual procedure to estimate the mean flow velocity with dye and electrolyte tracers is to measure the time from the injection of the tracer to the arrival of the leading edge of the tracer concentration at a sampling point and then divide this figure by the travel distance to give the leading edge velocity. The travel time of the leading edge of the tracer concentration is usually observed visually in the case of dye tracers and is measured using an electric conductivity sensor in the case of salt tracers. The leading edge velocity is then multiplied by a correction factor to obtain the mean flow velocity (e.g. DUNKERLEY, 2001; LI et al., 1996; ZHANG et al., 2010).

Infrared thermography has been successfully employed in hydrological studies as a high spatial and temporal resolution non-intrusive imaging tool to measure water surface temperatures and detect thermal sources: e.g. infrared thermography techniques were used to detect and quantify discharges of groundwater and freshwater into nutrient-sensitive estuaries and coastal bays (e.g. DANIELESCU et al., 2009; MEJÍAS et al., 2012). In particular, more field studies with portable hand-held infrared thermography systems have been carried out recently because the equipment is easy to handle and the measurement distance and scale are easy to adjust (e.g. CARDENAS et al., 2008; PFISTER et al., 2010; SCHUETZ et al., 2012).

Some authors have studied the use of infrared thermography and thermal tracers to measure shallow flow velocities. SCHUETZ et al. (2012) used infrared thermal imaging combined with the injection of heated water as an artificial tracer technique to characterize the spatial distribution of flow paths and to assess transport properties in a 65 m^2 experimentally constructed wetland with water depths between 0.1-0.2 m. For the studied conditions the authors observed that heated water can be used

as a conservative artificial tracer for plot scale experiments. LIANG et al. (2012) studied the feasibility of using thermal imaging to investigate the scalar transport process in shallow jet and wake flows with waters depths of 35 mm and 45 mm by adding warm water to the water flow. The authors found that the thermal imaging technique has great potential as a quantitative flow visualisation technique for studying shallow turbulent dispersion characteristics.

The purpose of this study is to describe a technique based on infrared thermography to visualize very shallow flows and enable a quantitative measurement of overland flow and rill flow velocities. Laboratory experiments were conducted to compare the traditional dye tracer technique with this new thermal tracer technique by injecting a combined tracer (heated dye) into these shallow flowing surface waters. In fact, for these deeper flows, dye tracing is considered by many a crude method that yields a maximum flow speed that has to be scaled to yield mean speed. However, in these muddy flows, with depths of a few millimetres, it is not possible to use far more sophisticated methods of measuring true mean flow speed that are reported in the literature for surface flows, namely river flows. In this study the leading edge tracer velocities estimated by means of infrared video and by a regular real imaging video were compared. The novelty of the proposed technique for computing mean velocity of overland flow and rill flow lies in the tracer characteristics. A thermal tracer is used instead of a dye tracer. The scientific question that arises from this paper is: Can a thermal tracer be used to estimate very shallow flow velocities?

8.3. Materials and methods

8.3.1. Laboratory set-ups

Two slightly different laboratory set-ups were used for the qualitative and quantitative comparison of the thermal tracer technique and dye tracer technique, one for the estimation of overland flow velocity (Figure 8.1a) and the other for rill flow velocity estimation (Figure 8.1b). Both experiments were carried out in a 3.0 m long and 0.3 m wide soil flume, adjusted to a 10% slope, with a water supply system installed upstream of the flume. The water supply system comprised a constant head tank and a feeder tank and allowed the application of a known constant flow of water to the flume soil surface.

8.3.2. Soil

The soil was a sandy loam collected from the banks of River Mondego (Coimbra, Portugal), exhibiting clear signs of water erosion (e.g. DE LIMA et al., 2003). The soil consisted of 7% clay, 9% silt and 84% sand and was mainly composed of quartz, feldspars, quartzite, muscovite and clay minerals. Standard laboratory permeability tests estimated saturated hydraulic conductivity of around 5.7×10^{-5} m s^{-1}. The sieved soil was uniformly spread in the flume, positioned horizontally, and a sharp straight-edged blade was used to remove excess soil to obtain a flat plane surface. The

soil in the flume was gently tapped with a wooden block to compact it and to reproduce a uniform bulk density of approximately 1700 kg m^{-3}. The soil was then saturated and left to dry until it gained a consistency that allowed the eroding effect of the water flux to be minimized and so preserve the soil surface characteristics throughout the experiments.

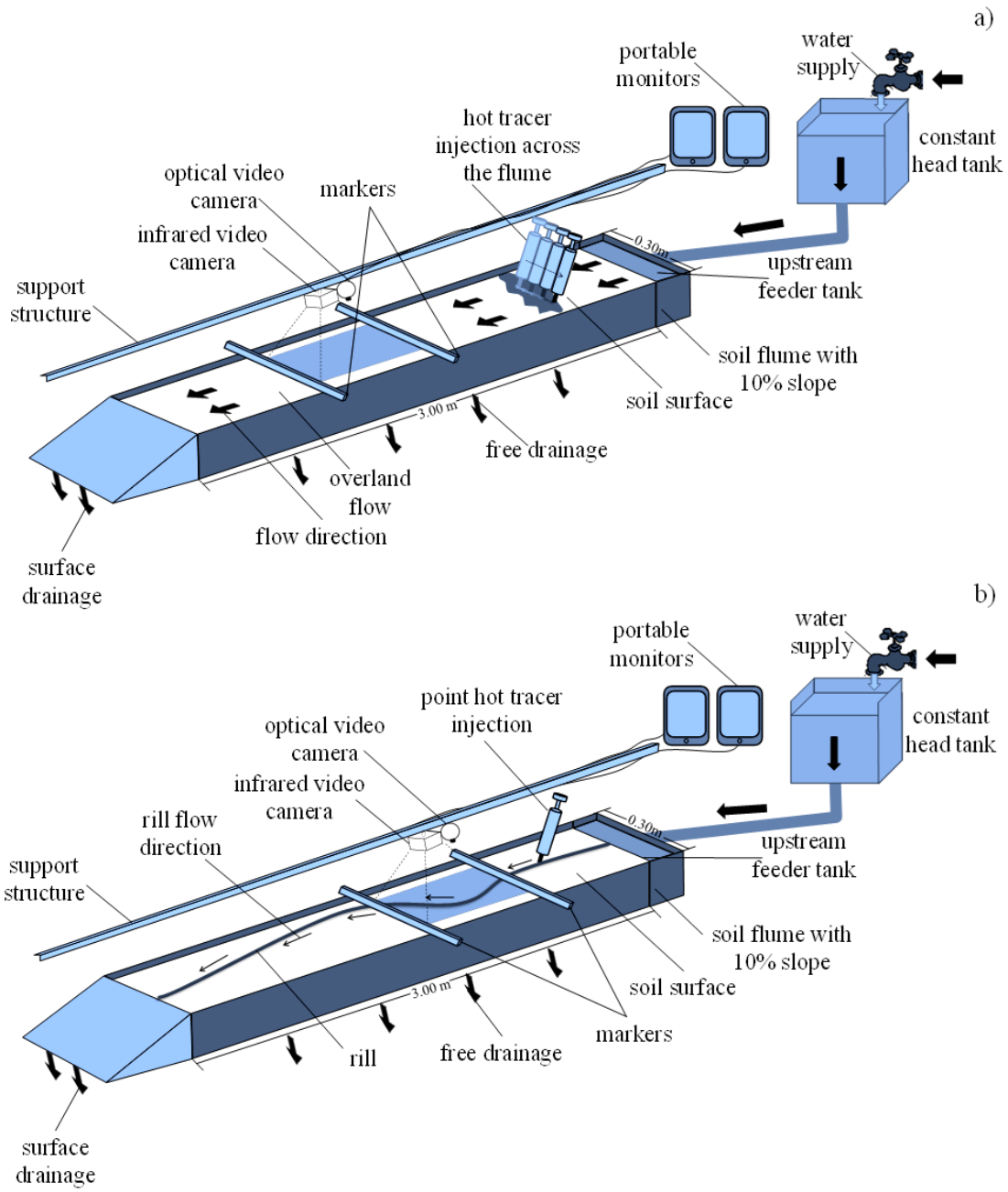

Figure 8.1. Schematic representation of the laboratory set-up (not to scale) for: a) Overland flow tests; and b) Rill flow tests.

The first series of experiments to measure overland flow velocity were performed on the uniformly smooth plane surface, without any rough protuberances or other microtopographic elements. For the second set of experiments an artificial rill was created along the length of the flume by compressing a malleable plastic form against the soil surface. The rill had an average depth of

8.9 ± 0.3 mm and width of 16.4 ± 2.3 mm and was fixed by spreading sieved white cement powder over the entire rill.

8.3.3. Tracers

To be able to compare the flow velocities measured with the thermal tracer and the dye tracer, the two techniques were tested simultaneously in a combined tracer comprising both dye and thermal characteristics. This was accomplished by heating the dye tracer solution, well above the average surface flow water temperature which varied from 18 ºC to 20 ºC.

In the first set of experiments (overland flow tests), non-fat milk heated to a temperature of approximately 80 ºC was used as a combined tracer. Non-fat milk was used because it can be heated to high temperatures and it is visible when injected into the water flow due to the dark brownish colour of the wetted soil surface. Also, it presents a similar density to other tracer solutions. In the rill flow tests, heated blue litmus tracer at a temperature of approximately 80 ºC was used as a combined tracer, due to the contrast with the whitish colour of the surface. The temperature of 80 ºC was used for convenience: after heating the water in an electric kettle, it was transferred to the cups for application on the flow.

Differences in water density and viscosity, which change slightly with temperature, do not seem to have a visible influence on the dispersion of the dye tracer in these experiments, due to: i) Small injected tracer volume (< 22 ml for overland flow and < 5 ml for rill flow); ii) Short sampling time (< 4 s for overland flow and < 2 s for rill flow); and iii) Short sampling length (0.5 m). Relative differences between tracer leading edge velocities measured with the same dye tracer at 15 ºC and 85 ºC were always less than 8%, under the tested experimental conditions, which is similar to the relative errors for the same temperature. This is explained by the variability induced by the manual implementation of this technique.

8.3.4. Video recording systems

Thermal videos and imaging of the soil surface and water were recorded with an Optris PI 160 portable infrared video camera (Optris GmbH, Germany). Specifications of the infrared video camera are presented in Table 8.1.

Table 8.1. Infrared video camera basic specifications

Specification	Unit	Value
Optical resolution	pixel	160 × 120
Field of view (FOV)	º	23 × 17
Focal length	mm	10
Frame rate	Hz	100
Thermal resolution	ºC	0,1
Accuracy	%	±2
Spectral range	µm	7.5-13.0

Real image videos were recorded with a regular optical video camera, Logitech QuickCam E 3500 Plus, using the respective product software, Logitech Webcam Software 1.1 (Logitech, Switzerland), with a digital resolution of 320 × 240 pixels and a frame rate of 15 Hz. Both cameras were attached to a metal support structure 0.75 m above the soil surface with the focal length direction perpendicular to the soil surface. This distance guaranties good coverage of the soil flume section being analysed. The cameras were side by side and so the angle of view slightly differed.

The infrared video camera converts the invisible infrared energy emitted by the wetted soil surface and water into a 2D visual image. Because the imaging scale of the infrared camera is based on the temperature emissivity coefficients of the materials, it must be taken into account that the water and wetted soil emissivity coefficients are very similar for the working spectral range of the infrared camera (7.5-13.0 μm) and, therefore, the associated errors could be ignored. To improve the visualization of the dye tracer in the real image videos, the flume was positioned to minimize the reflections of light in the water flow.

8.3.5. Laboratory procedure

Flow velocity was measured for different flow discharge rates (19, 70 and 157 ml s^{-1} for overland flow and 6, 19, 37, 77 and 151 ml s^{-1} for rill flow) and volumes of tracer. Initially, the discharge applied to the soil flume surface through the feeder tank was controlled manually by the water supply system installed at the upstream end of the flume. Volumetric discharge was measured periodically at the downstream end.

Once discharge became stable, the velocity measurements were taken at the measuring section with the optical and infrared video cameras. The measuring section was established 1.0 m downslope of the feeder tank and had a length of 0.50 m. This length was limited by the area covered by the thermograph video camera. Although other distances could be used, 0.50 m was sufficient and guarantied precision with respect to thermal pixel size.

The combined tracer (dye plus thermal tracer) was injected at approximately 0.5 m upslope of the measuring section to minimize the interference of the injection volume in the velocity measurements. The movement of the combined tracer along the measuring section was recorded with both the infrared and real image video cameras. This resulted in two independent videos for each tracer injection.

Both videos were monitored in portable devices throughout the experiments in order to estimate the velocity of the leading edge through manual evaluation of the video frames of its passage over the measuring section. Three repetitions were performed for each flow discharge rate and volume of tracer injected.

8.4. Results and discussion

Real image and thermal videos were visualized and analysed separately with appropriate software, in order to estimate flow velocities and compare the two tracer techniques. Real image videos were analysed using a common media player software, Windows Media Player 11 (Microsoft Corporation, USA), and thermal videos were analysed using a process imager software, Optris PI Connect (Optris GmbH, Germany). For comparison purposes, the flow velocities were estimated by measuring the travel time of the leading edge of the injected tracer over the measuring section. Figure 8.2 shows video snapshots of the measuring sections. These illustrate the differences between dye and thermal tracer in the rill flow tests. The combined tracer is clearly more visible in the thermal videos and the leading edge is more perceptible.

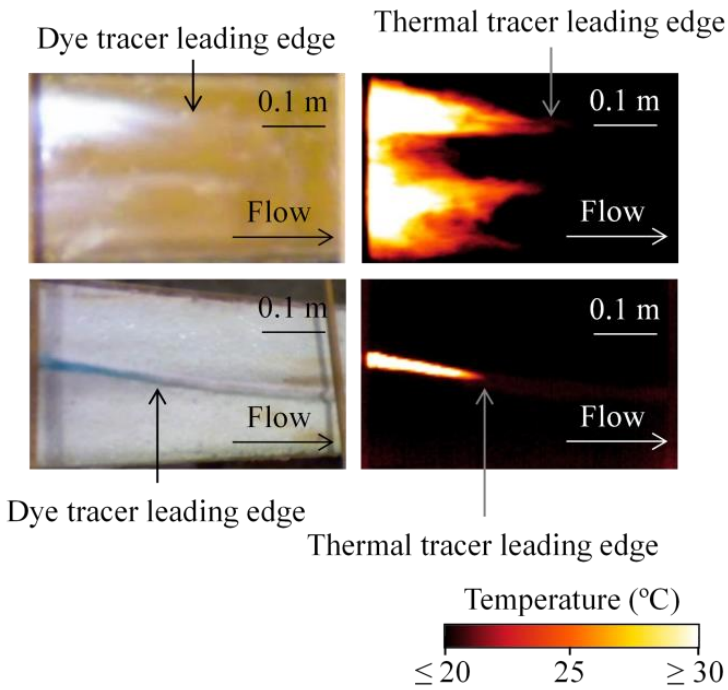

Figure 8.2. Comparison between real imaging (left) and thermal imaging snapshots (right) of the soil surface, during the overland flow (up) and rill flow tests (down). Flow and surface temperature are approximately 20 ºC.

When the thermal tracer is injected in the overland flow its dispersion can be seen (Figure 8.3). Whereas the thermal tracer leading edge movement is well defined and well-shaped, the remaining volume of injected tracer leaves a thermal mark that takes some time to disappear from the thermal videos. That mark is the residue of the tracer in the flow and is produced by the heating of the soil surface as the thermal tracer passes over it. For repetitive injections this effect could be reduced by reducing the amount of applied tracer and by reducing the temperature.

Injected tracer leading edge velocities measured with both dye and thermal tracer techniques are presented in Table 8.2 for the overland flow and Table 8.3 for the rill flow tests.

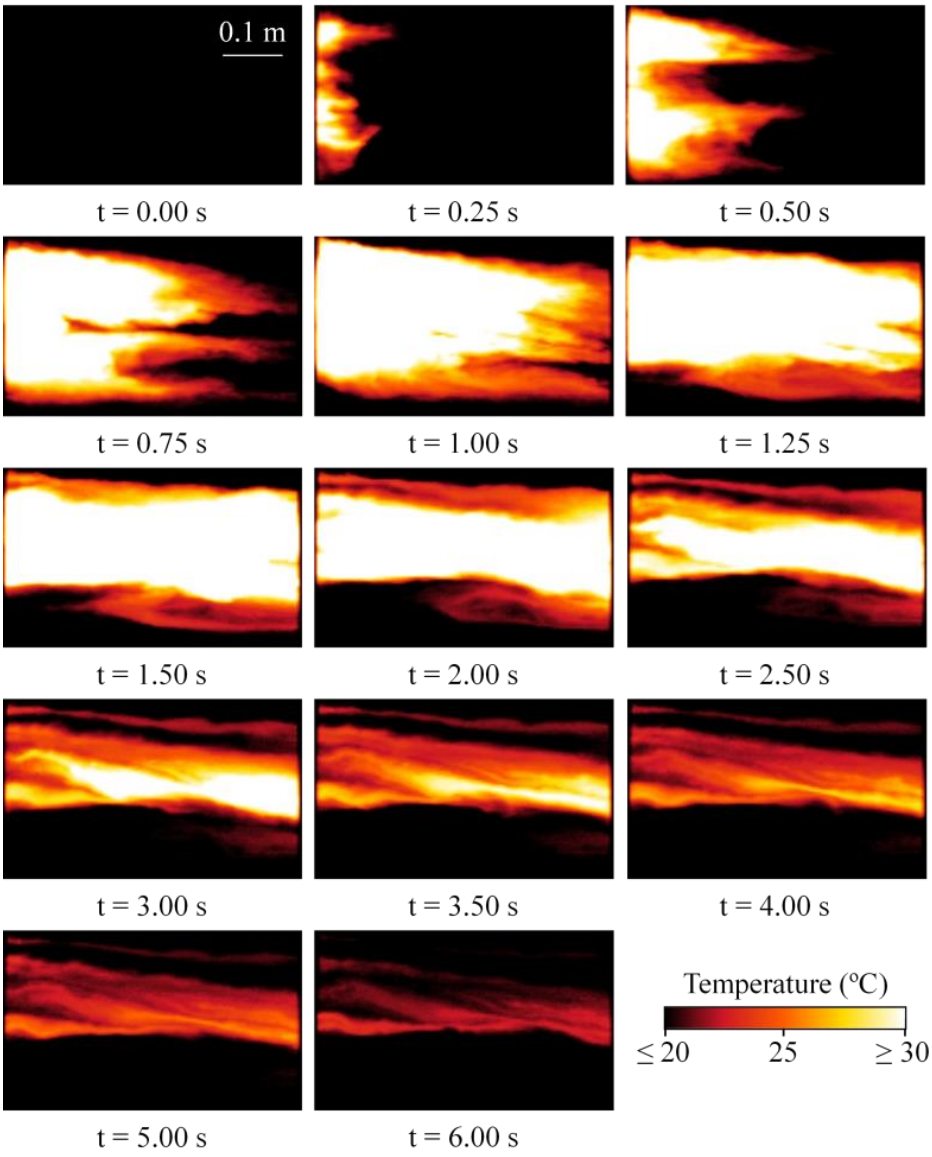

Figure 8.3. Chronological sequence of thermal imaging snapshots for overland flow tests. Flow and surface temperature are approximately 20 ºC.

Table 8.2. Overland flow test results (average of three repetitions).

		Flow velocity, U (m s^{-1})	
Discharge, Q (ml s^{-1})	Volume of tracer, Vtr (ml)	Thermal tracer	Dye tracer
19	9	0.134	0.134
	19	0.164	0.164
	22	0.254	0.254
	Mean	0.184	0.184
	S.D.	0.051	0.051
70	7	0.239	0.239
	13	0.284	0.269
	19	0.313	0.299
	Mean	0.279	0.269
	S.D.	0.031	0.024
157	13	0.328	0.313
	19	0.343	0.328
	22	0.358	0.343
	Mean	0.343	0.328
	S.D.	0.012	0.012

Table 8.3. Rill flow test results for discharges (average of three repetitions).

		Flow velocity, U (m s^{-1})	
Discharge, Q (ml s^{-1})	Volume of tracer, Vtr (ml)	Thermal tracer	Dye tracer
6	0.2	-	-
	0.4	-	-
	0.6	0.314	0.319
	0.8	0.326	0.324
	1.0	0.336	0.333
	2.0	0.344	0.338
	3.0	0.347	0.350
	4.0	0.352	0.355
	5.0	0.360	0.364
	Mean	0.340	0.340
	S.D.	0.015	0.015
19	0.2	-	-
	0.4	0.435	-
	0.6	0.435	0.414
	0.8	0.447	0.429
	1.0	0.449	0.455
	2.0	0.460	0.452
	3.0	0.466	0.453
	4.0	0.470	0.474
	5.0	0.475	0.471
	Mean	0.455	0.450
	S.D.	0.015	0.020
37	0.2	-	-
	0.4	0.495	-
	0.6	0.498	0.506
	0.8	0.509	0.485
	1.0	0.512	0.494
	2.0	0.519	0.500
	3.0	0.521	0.520
	4.0	0.523	0.511
	5.0	0.526	0.522
	Mean	0.513	0.505
	S.D.	0.011	0.012
77	0.2	0.579	-
	0.4	0.589	-
	0.6	0.594	0.585
	0.8	0.604	0.598
	1.0	0.608	0.598
	2.0	0.613	0.598
	3.0	0.613	0.600
	4.0	0.612	0.603
	5.0	0.615	0.604
	Mean	0.603	0.598
	S.D.	0.012	0.006
151	0.2	0.631	-
	0.4	0.631	-
	0.6	0.633	0.615
	0.8	0.637	0.637
	1.0	0.639	0.619
	2.0	0.641	0.624
	3.0	0.644	0.631
	4.0	0.644	0.638
	5.0	0.652	0.637
	Mean	0.639	0.629
	S.D.	0.006	0.009

Since the objective of this study was to compare dye and thermal tracer techniques, no attempt was made to estimate the actual mean flow velocity for the entire cross-sectional area. The velocity values presented in this paper were therefore not submitted to any correction factor, as suggested by many authors (e.g. DUNKERLEY, 2001; LI et al., 1996; ZHANG et al., 2010).

Figure 8.4 shows that the injected tracer leading edge velocities estimated by both techniques are similar for all flow discharges and volumes of tracer used. In both the overland and rill flow tests the differences between the two techniques increased with higher flow discharge. However, standard deviation (S.D.) decreased for higher discharges, which is related to the relative importance of the volume of tracer used, as can be seen in Figure 8.5.

Larger volumes of tracer lead to higher flow velocities; this is clearly more relevant for small discharges where the influence of the volume of injected tracer is more noticeable (Figure 8.5). The optimal volume of tracer is the smallest amount that permits the application of the technique, i.e. clearly visualization of the leading edge movement.

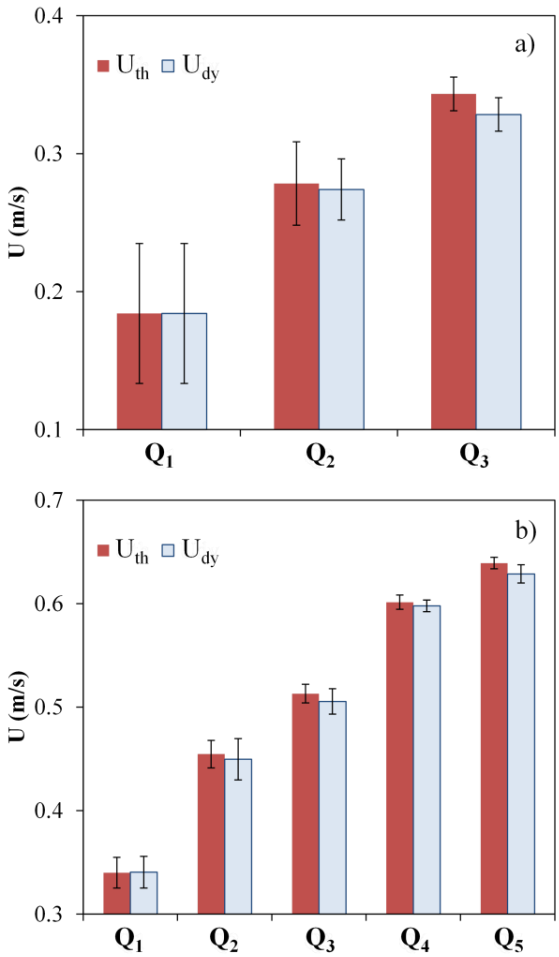

Figure 8.4. Injected tracer leading edge velocities measured: a) Overland flow tests; and b) Rill flow tests. Mean and standard deviation for all repetitions for each flow discharge. The vertical scale is not the same in the two graphs.

In Figure 8.5b it can be seen that for some small volumes of combined tracer it was only possible to estimate the flow velocity with the thermal tracer technique, because the dye tracer was not perceptible. For lower discharges, the visualization of the thermal tracer was more difficult.

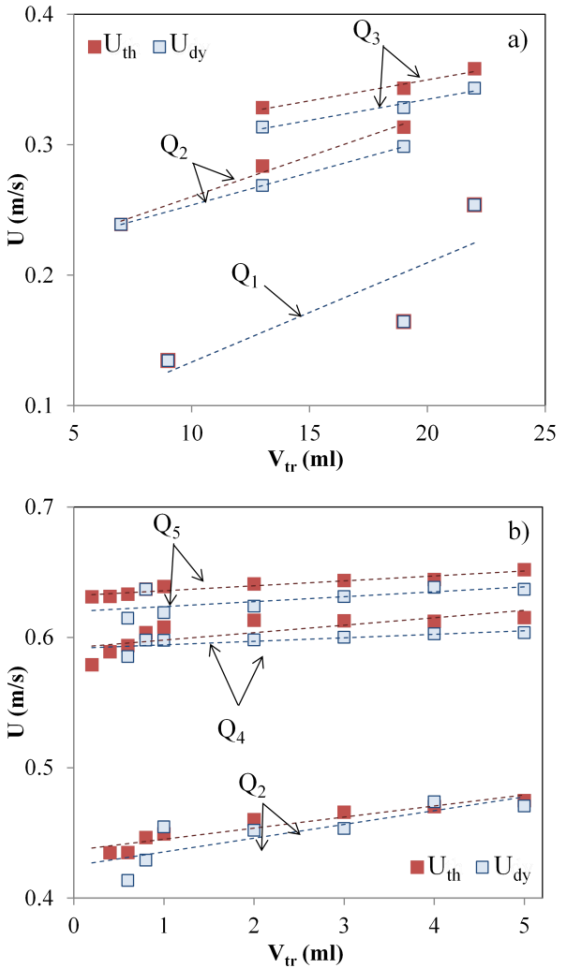

Figure 8.5. Injected tracer leading edge velocities measured as function of the volume of tracer: a) Overland flow test results for discharges of 19 ml s^{-1} (Q1), 70 ml s^{-1} (Q2) and 157 ml s^{-1} (Q3); and b) Rill flow test results for discharges of 19 ml s^{-1} (Q2), 77 ml s^{-1} (Q4) and 151 ml s^{-1} (Q5). Dashed curves are only indicative of a trend.

The two techniques studied yielded very similar results, as can be seen in Figure 8.6; the comparison between the velocities measured using dye tracer and thermal tracer showed a good correlation, with a coefficient of determination (r^2) of 0.96 and a linear regression of almost a 1:1 line. Higher discharges and velocities lead to larger differences between the results of the two techniques.

Relative differences between the two tracer techniques (Figure 8.7) increased with higher flow discharge and flow velocity to a maximum of around 5%, under the tested conditions. Also timing errors, unavoidable in the use of video imagery, due to frame rate of the recording system, increase with flow velocity, especially when using short flow path lengths for the tracer measurements.

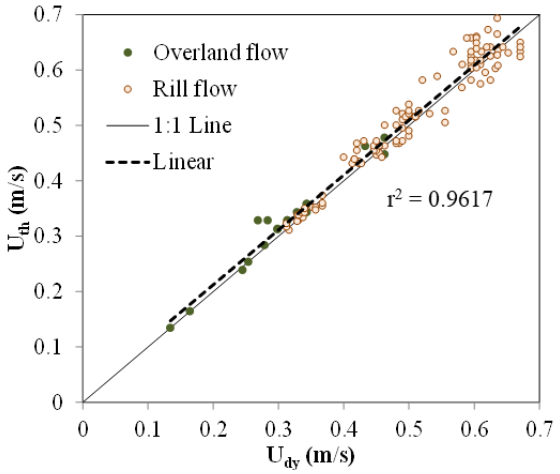

Figure 8.6. Comparison between velocities measured by the dye tracer technique (U_{dy}) and by the thermal tracer technique (U_{th}), for both the overland and rill flow tests. 1:1 line and linear regression of all data were also plotted.

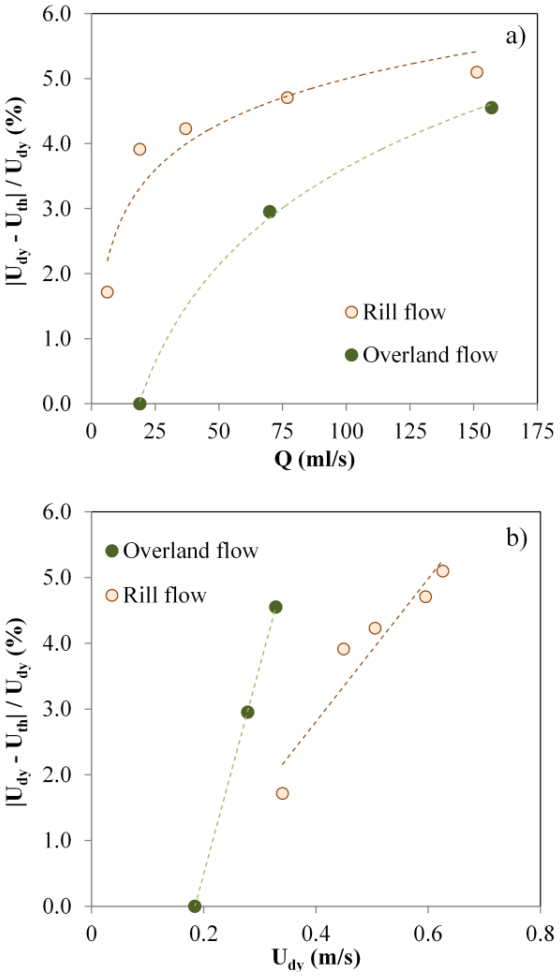

Figure 8.7. Relative differences between velocities measured by the dye tracer technique (U_{dy}) and by the thermal tracer technique (U_{th}), as a function of: a) Discharge; and b) Injected tracer leading edge velocity measured with dye tracer technique. Dashed curves are only indicative of a trend.

8.5. Conclusions

The results show that thermal tracers can be used to estimate both overland and rill flow velocities; measurements are similar to those observed using dye tracers, a technique widely used to estimate shallow flow velocities, and shows potential for field application.

The main advantage of using thermography was the higher visibility of the leading edge of the injected tracer compared with the real image videos. The thermal tracer technique allowed the estimation of flow velocities for smaller amounts of tracer. In some tests the injected volume of combined tracer was too small to be perceptible on the real image videos, but it was clearly visible in the thermal videos. Lower volumes of tracer lead to smaller disturbances in the actual flow velocity measurements. The thermal tracer technique also measures the flow velocity in a cleaner and more ecological way, without leaving any residue in the water or the soil and with very little temporal and spatial disturbance of the environment. Also, when compared with other flow velocity measurement techniques, the chief merit of the thermography technique is that it involves a very simple experimental setup; there is no need to insert an instrument in the water which makes this approach appropriate for low depth flows. Also, it can allow continuous monitoring of flow velocity observations. It would not be reasonable to think a sensor station that colours the flow every hour, while with the thermal tracer it could be possible. The main reason is the environmental impact of the dye tracers.

Some disadvantages of the technique were the need for a hot tracer (in field studies this might be an obstacle) and the cost of the infrared video camera compared to the cost of an everyday optical camera.

"Water is fluid, soft, and yielding. But water will wear away rock, which is rigid and cannot yield. As a rule, whatever is fluid, soft, and yielding will overcome whatever is rigid and hard. This is another paradox: What is soft is strong."

- Lao-Tzu

9. COMPARISON OF THERMAL, SALT AND DYE TRACING TO ESTIMATE SHALLOW FLOW VELOCITIES: NOVEL TRIPLE-TRACER APPROACH[7]

9.1. Abstract

The accurate measurement of shallow flow velocities is crucial to understand and model the dynamics of sediment and pollutant transport by overland flow. In this study, a novel triple-tracer approach was used to re-evaluate and compare the traditional and well established dye and salt tracer techniques with the more recent thermal tracer technique in estimating shallow flow velocities. For this purpose, a triple tracer (i.e. dyed-salted-heated water) was used. Optical and infrared video cameras and an electrical conductivity sensor were used to detect the tracers in the flow. Leading edge and centroid velocities of the tracers were measured, and the correction factors used to determine the actual mean flow velocities from tracer measured velocities were compared and investigated. Experiments were carried out for different flow discharges (32-1813 ml s^{-1}) on smooth acrylic, sand, stones and synthetic grass bed surfaces with 0.8, 4.4 and 13.2% slopes.

The results showed that thermal tracers can be used to estimate shallow flow velocities, since the three techniques yielded very similar results without significant differences between them. The main advantages of the thermal tracer were that the movement of the tracer along the measuring section was more easily visible than it was in the real image videos and that it was possible to measure space-averaged flow velocities instead of only one velocity value, with the salt tracer. The correction factors used to determine the actual mean velocity of overland flow varied directly with Reynolds and Froude numbers, flow velocity and slope and inversely with flow depth and bed roughness. In shallow flows, velocity estimation using tracers entails considerable uncertainty and caution must be taken with these measurements, especially in field studies where these variables vary appreciably in space and time.

Keywords

Shallow flow velocity; Thermal tracer; Infrared thermography

[7] ABRANTES, J.R.C.B., MORUZZI, R.B., SILVEIRA, A. and DE LIMA, J.L.M.P. (2018). Comparison of thermal, salt and dye tracing to estimate shallow flow velocities: novel triple tracer approach. *Journal of Hydrology*, 557, 362-377. DOI:10.1016/j.jhydrol.2017.12.048.

9.2. Introduction

Flow velocity is a basic hydraulic property of shallow flows (e.g. overland flow, rill flow, stream flow) and most hydro-environmental research relies on its accurate measurement (e.g. GIMÉNEZ et al., 2004; GOVERS, 1992; TAKKEN and GOVERS 2000). Shallow flows can occur in natural and urbanized basins (e.g. hillslopes, drainage systems) and their characterization is crucial for runoff, erosion and water quality modelling (e.g. KREIBICH et al., 2009; MÜGLER et al., 2011).

Flow velocity measuring techniques vary with water body dimension, its accessibility and characteristics. Recently, significant developments have been made in sensing technology, resulting in a wide spectrum of powerful and versatile options for high accuracy flow velocity data. However, measurement devices may have some limitations when operating outside their ideal measurement conditions. Particularly for shallow flows, the characterization of the velocity fields is complicated, mostly because of their lack of depth (anything from several millimetres to a few centimetres) and other problems, such as variability of the channel bed due to erosion, presence of sediment and other debris in the flow or even the presence of vegetation concealing the measuring area. This restricts the use of many flow measuring devices.

For deeper water bodies (e.g. large rivers) flow velocity can be measured with current meters or acoustic Doppler techniques, such as acoustic Doppler velocimetry (ADV) or acoustic Doppler current profiler (ADCP), at determined monitoring sections (e.g. KIMIAGHALAM et al., 2016; MUSTE et al., 2004a, 2004b). Although intrusive, these techniques do provide a reliable characterization of the flow velocity vertical profile; however, these instruments cannot always be used in very shallow water. Other techniques, such as satellites, radars and microwave sensors, hand-held or coupled in a drone, can be used to estimate surface flow velocity accurately and non-intrusively (e.g. BJERKLIE, 2007; BJERKLIE et al., 2003; FULTON and OSTROWSKI, 2008); however, these methods are usually very costly and satellite data are typically applied to large water bodies.

For a long time, less accurate and less costly techniques used for shallow flow velocity measurements were based on determining the travel time of a tracer across a predefined section. In fact, many researchers regard tracer methods as crude methods that yield a maximum flow velocity that has to be corrected to give a mean velocity. However, in shallow muddy flows, with depths of a few millimetres to a few centimetres, it is not always possible to use the more sophisticated methods to measure true mean flow velocity, such as ADV, ACDP. When using tracers, the accuracy of the measurement depends to a great extent on the tracer added to the flow and on the quality of its detection in the flow. According to FLURY and WAI (2003) an ideal tracer for hydro-environmental research should have the following characteristics: i) Movement similar to water; ii) Be conservative, i.e. without degradation during the measurement time; iii) Not show sorption to other environment components (e.g. soil, sediments, rocks); iv) Be clearly distinguishable from the background of the system; v) Be detectable either by chemical analysis or by visualization; and vi) Low toxicological impact on the study environment. Among the different materials that have

been tested as tracers in flow velocity experiments are natural and radioactive isotopes (NIAZI et al., 2017), floating objects (TAURO et al., 2012a), fluorescent particles (TAURO et al., 2012b, 2012c), bacteria (e.g. MAURICE et al., 2010), salts (e.g. CALKINS and DUNNE, 1970; DAY, 1977; LEI et al., 2005, 2010; SHI et al., 2012) and dyes (e.g. ABRAHAMS et al., 1986; DUNKERLEY, 2003; FLURY and FLÜHLER, 1993; HOLDEN et al., 2008; TAZIOLI, 2011). Depending on the used tracer, optical cameras (e.g. for dyes, floating objects), fluorometers (e.g. for fluorescent particles, fluorescent dyes) or electrical conductivity sensors (e.g. for salt tracers), can be used. A review of tracer technology in hydrologic studies is presented in LEIBUNDGUT et al. (2009). A more recent approach uses thermal tracers (e.g. water hotter or colder than the flow) that can be detected by infrared sensor equipment (e.g. infrared video camera). Thermal tracers were tested as instruments to measure flow velocities (BONNER et al., 2017; DE LIMA and ABRANTES, 2014b; DE LIMA et al., 2015; SCHUETZ et al., 2012), as well as for assessing microrelief (ABRANTES and DE LIMA, 2014; DE LIMA and ABRANTES 2014a), permeability (DE LIMA et al., 2014b), macroporosity (DE LIMA et al., 2014a, 2014c) and repellency of the soil surface (ABRANTES et al., 2016, 2017).

Traditionally, estimation of the mean flow velocity using tracers would consist of measuring the time from the injection of the tracer to its arrival at a sampling point and then dividing this figure by the travel distance. With dye tracers, the leading edge velocity is usually measured, since it is frequently regarded as the surface velocity of the flow. With salt tracers, the leading edge, peak or centroid of the tracer's concentration at the sampling point are measured. The leading edge is regarded as the surface velocity of the flow and the peak and centroid can be labelled as mean theoretical velocities, if retention of the salt in the water flow is assumed. However, especially in soil erosion processes, there can be constant exchanges of salt between the soil surface and water flow as the soil absorbs the salts, or the salts are dissolved from the detached soil materials. Also, infiltration processes lead to a decrease in the total amount of salt at the sampling point. Therefore, none of the measured velocities are considered the actual mean velocity of the flow. A correction factor has to be applied to obtain the mean flow velocity (e.g. HORTON et al., 1934). This correction factor varies with the flow characteristics such as velocity, depth, Reynolds number and Froude number, with the concentration of sediments in the flow and with the bed surface characteristics such as slope and roughness (DUNKERLEY, 2001; EMMETT, 1970; LI and ABRAHAMS, 1997; LI et al., 1996; PLANCHON et al., 2005; ZHANG et al., 2010).

Optical methods for flow characterization, such as particle image velocimetry (PIV) and particle tracking velocimetry (PTV), have seen great development and have been adjusted so that they can be used in natural environments (e.g. COZ et al., 2010; KANTOUSH et al., 2011, TAURO et al., 2014, 2016). These methods combine digital cameras and lasers to track the movement of particles dispersed in the water (e.g. fluorescent particles, air bubbles, floating objects) and thereby estimate the surface flow velocity. Based on these optical methods, TAURO and GRIMALDI (2017) used an infrared camera to track thermal particles (ice cubes) to monitor stream surface velocity.

In the present study, laboratory experiments were conducted to compare the traditional dye and salt tracer techniques to the more recent thermal tracer technique for estimating shallow flow velocities and investigating the effects of a wide range of hydraulic conditions on the correction factor used to determine mean flow velocity. This was done by adding a triple tracer (i.e. dyed-salted-heated water) into shallow flows and detecting its passage with optical and infrared video cameras and an electrical conductivity sensor. Experiments were carried out considering different bed surfaces (smooth acrylic, sand, stones and synthetic grass), flow discharges (32-1813 ml s^{-1}) and bed slopes (0.8, 4.4 and 13.2%), resulting in flow velocities from 0.02-0.85 m s^{-1}, flow depths from 1.4-46.0 mm, Reynolds numbers from 785-19000 and Froude numbers from 0.05-4.66. For the salt and thermal tracers, leading edge and centroid velocities of the tracers were measured. For the dye tracer, only the leading edge velocity was measured. Correction factors used to determine mean flow velocity were calculated by comparing triple-tracer measured velocities with velocities calculated from measured discharges and flow depths. This novel triple-tracer approach can give insight into the measurement of shallow flow velocities and provide a useful tool to re-evaluate and compare the three techniques.

9.3. Material and methods

9.3.1. Hydraulic channel and simulated flows

Dye, salt and thermal tracer techniques were compared using the laboratory setup schematized in Figure 9.1. It comprised a hydraulic channel 3.00 m long and 0.15 m wide that uses a water recirculation circuit with a 500 L reservoir, a pump and a flow control valve. The channel bed and walls are made of smooth, transparent acrylic sheets, and are thus impermeable.

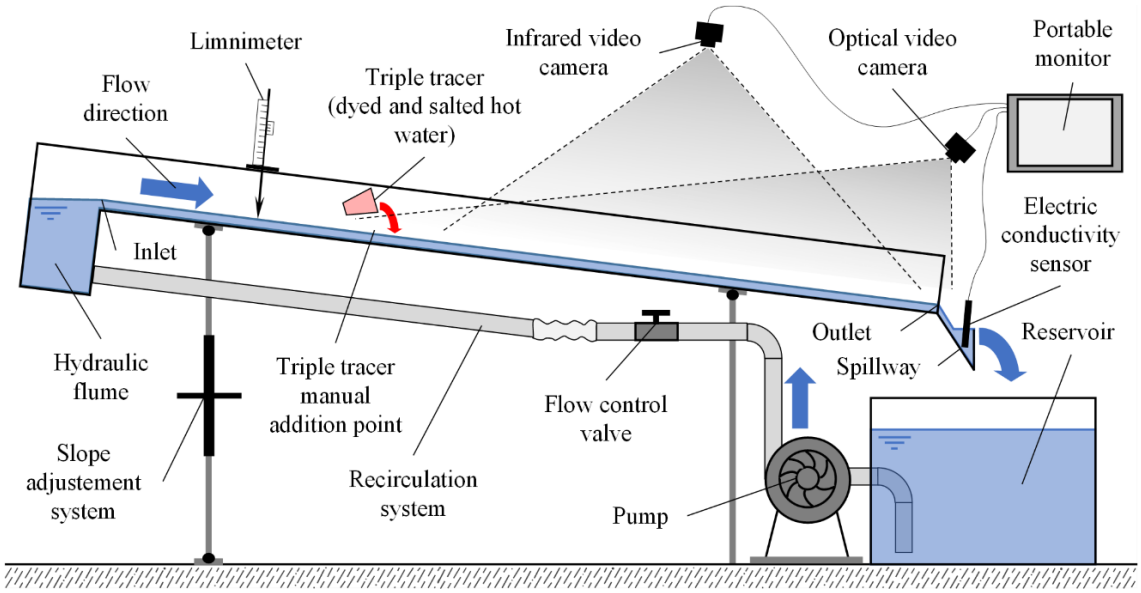

Figure 9.1. Scheme (side view) of the laboratory setup used in the triple-tracer experiments.

The setup allows a manual adjustment of the bed slope. The channel has free inflow and outflow and so flow velocity and flow depth are controlled by the flow discharge, bed slope and bed surface roughness.

Shallow flow velocity measurements were taken on four different bed surfaces, as shown in Figure 9.2: i) Smooth acrylic; ii) Sand; iii) Stones; and iv) Synthetic grass. Smooth acrylic tests were performed on the smooth, transparent acrylic sheet of the channel bed. For the sand tests, < 1.2 mm sieved sand particles were homogeneously glued to an acrylic board that was placed over the channel bed. Stone tests were performed by uniformly distributing 10-20 mm sieved stones over the channel bed. For the last tests, an 8.5 mm height synthetic grass carpet was fixed to the channel bed. Three bed slopes of 0.8, 4.4 and 13.2% were considered for each surface.

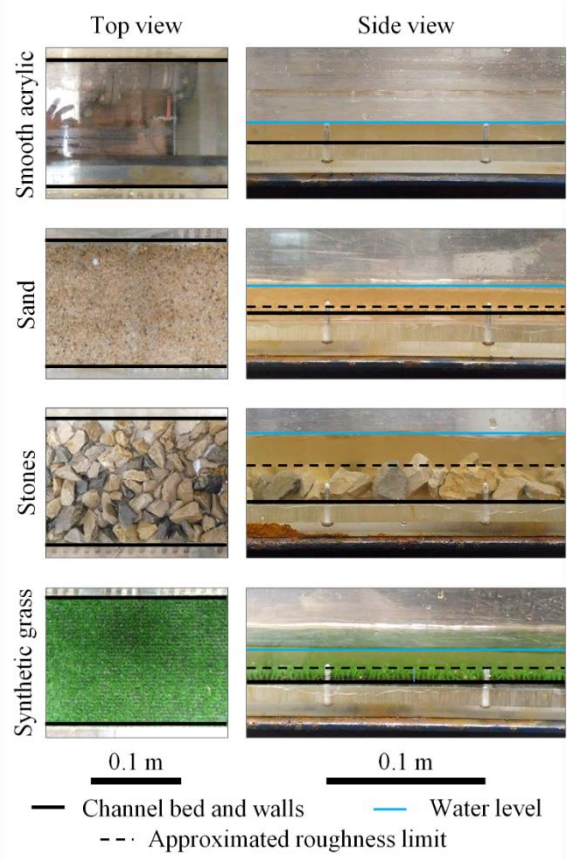

Figure 9.2. Photographs of the hydraulic channel (top view without flowing water; side view with flowing water), for the four bed surfaces tested. Channel walls and bed surface and approximate water levels and roughness limits are marked.

Flow velocity was measured for a total of 32 different flow conditions, combining four bed surfaces, three bed slopes and different flow discharges, as summarized in Table 9.1. For each flow condition, flow velocity was measured in triplicate, using the triple tracer, and flow depth was measured using a precision limnimeter. Flow discharge was controlled manually by the flow control valve in the recirculation system and was measured at the channel outlet by the volumetric method.

At the end of each set of tests (i.e. when bed surface was changed) the water from the reservoir was removed and replaced for fresh water to avoid excessive accumulation of the tracers' concentration in the recirculating water and avoid affecting the precision of the flow velocity measurements: during the experiments, average flow water temperature and electric conductivity varied between 28.0-31.9 ºC and 198-445 µS cm^{-1}, respectively.

9.3.2. Triple tracer

To be able to compare shallow flow velocities measured with dye, salt and thermal tracers, the three techniques were tested simultaneously in a triple tracer combining dyed-salted-heated water. This was made by adding dye and common table salt to tap water and heating this solution to a temperature well above the average flow water temperature. Common food colouring solutions (E104 yellow quinolone, E122 red carmoisine, E133 brilliant blue FCF and E147 green) and common table salt, in a ratio of 50 g of dye and 5 g of salt per litre of water, were used. These concentrations were established in preliminary tests and shown to be detectable in the flow either by visualization (dye tracer) or by the electrical conductivity sensor (salt tracer). Average tracer temperature immediately before addition to the flow was 71.3 ± 5.2 ºC. This was after heating the tracer in an electric kettle to boiling point and transferring it to a cup for adding to the flow. Any differences between flow and tracer density and viscosity due to differences in temperature, salt and dye concentrations should be minimal and should not have a significant influence on the transport of the triple tracer in the flow.

A volume of 10 ml of triple tracer per 100 ml s-1 of flow discharge was used in each flow velocity measurement. This ratio of tracer to flow discharge was appropriate for enabling the triple tracer to be detected in the flow with the three techniques. Also, in DE LIMA and ABRANTES (2014b), this ratio showed minor differences between flow velocities measured with thermal and dye tracers. The triple tracer was manually added to the flow in a quick movement, 2.1 m upslope of the channel outlet (as shown in Figure 9.1) and half-way across it.

9.3.3. Tracer detection systems

The movement of the triple tracer in the flow was recorded with an infrared and a real image video camera and was detected with an electrical conductivity sensor at a spillway installed next to the outlet. The videos and the electrical conductivity were all monitored by portable devices throughout the experiments.

Infrared video camera

Thermal videos were recorded with an Optris PI-160 infrared video camera (from Optris GmbH, Germany) and monitored on a laptop using PI Connect software (from Optris GmbH, Germany). The infrared video camera has an optical resolution of 160 × 120 pixels, a thermal resolution of

0.1 °C, an accuracy of ±2%, a frame rate of 120 Hz, a lens with a field of view of 23° × 17° and covers the spectral range of 7.5-13.0 μm.

The camera was fixed to a metal structure 4 m above the channel bed, with the focal direction perpendicular to the soil surface to ensure minimum angular distortion. The field of view covered 1.6 m of the channel bed in the flow direction (0.1-1.7 m upslope of the outlet and 0.4-2.0 m downslope of the triple tracer addition point) and the entire width of 0.15 m, providing thermal imaging with 156 × 13 pixels.

Electrical conductivity sensor

Electrical conductivity was monitored with a CON-BTA conductivity sensor (from Vernier Software & Technology LLC, USA) using the respective LabQuest portable interface (from Vernier Software & Technology LLC, USA). The sensor was placed in a spillway installed next to the channel outlet. The spillway was used to produce a minimum water column of approximately 30 mm needed for the measurements.

Electrical conductivity data was collected with a temporal resolution of 0.2 s in mid-channel of 0-2000 μS cm^{-1}, with an accuracy of ±3%. The sensor has an automatic mechanism for temperature compensation between 5-35 ºC, enough to offset the temperature of the tracer observed at the channel outlet.

Optical video camera

Real image videos were recorded with a regular optical video camera GoPro Hero 3 (from GoPro Inc., USA) and monitored on a laptop using the product software GoPro Studio (from GoPro Inc., USA). The optical video camera has a digital resolution of 1920 × 1080 pixels, a frame rate of 30 Hz and a lens with a field of view of 120° × 70°. The camera was attached to a metal structure with the focal direction diagonal to the channel bed to ensure good coverage of the point where the triple tracer was added to the flow, its movement along the channel and its exit via the outlet.

9.3.4. Data analyses

Thermal and real image videos and electrical conductivity data were analysed separately using proper software to estimate flow velocity and compare the three tracer techniques. For the thermal and salt tracers, flow velocity was estimated considering the leading edge and centroid of the tracers as they passed through the measurement sections. Only the leading edge velocity was estimated for the dye tracer.

Thermal data

Thermal data was analysed according to the scheme shown in Figure 9.3. A series of 11 thermograms (i.e. thermal images) was extracted from each thermal video: the first corresponded

to an instant (t_0) just before the triple tracer addition to the flow and the rest corresponded to the instants t_1 to t_{10}, as the triple tracer in the flow passed through the measurement section (1.6 m and 156 pixels length and 0.15 m and 13 pixels width in a total of 2028 pixels). Figure 9.3a shows the images for instant t_0 and t_1 to t_3.

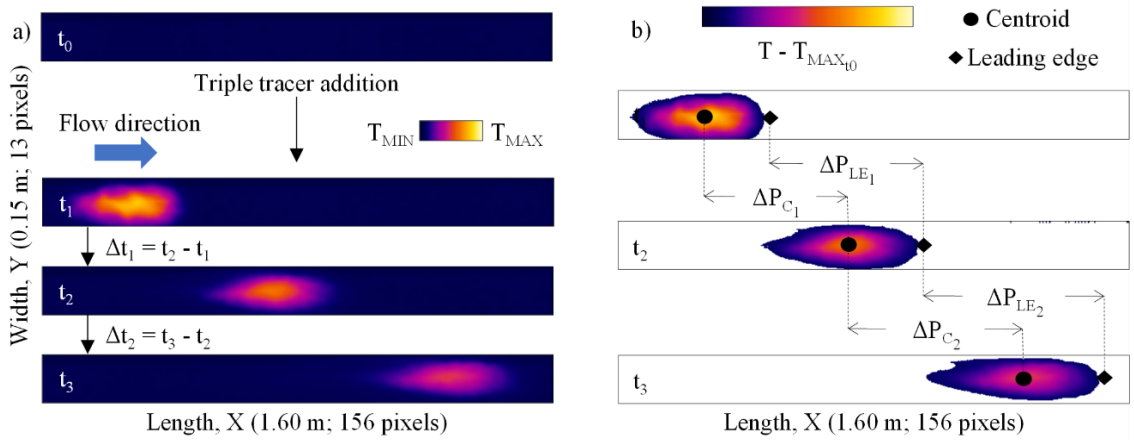

Figure 9.3. Scheme of the procedure used in the flow velocity measurement from thermal tracer: a) Time series of thermograms extracted from the thermal videos; b) Identification of the leading edge and centroid of the thermal tracer in the flow for flow velocity measurement.

A threshold temperature was established for each series of thermograms, as the maximum flow temperature observed in the instant t_0 (T_{MAXt0}). The threshold temperature enables the temperatures associated with the tracer to be identified (i.e. pixels with temperature values above the threshold temperature), thus distinguishing them from the other flow temperatures (i.e. pixels with temperature values below the temperature threshold).

The threshold temperature was subtracted from the temperature of the thermograms to give the thermograms in Figure 9.3b. It was then possible to specify the position of the leading edge at each instant (P_{LE}), as the first pixel at the front of the thermal tracer (i.e. in X direction) with a temperature value above the threshold temperature and the position of the centroid at each instant (P_C), calculated according to the moment equation (Equation 9.1):

$$P_C = \frac{\sum_{x=1}^{156}\sum_{y=1}^{13} T_{xy} \times P_{xy}}{\sum_{x=1}^{156}\sum_{y=1}^{13} T_{xy}} \quad (9.1)$$

where T_{xy} is the temperature (ºC) of the pixel xy, after subtraction of the threshold value T_{MAXt0}, P_{xy} is the location (m) of the pixel xy, x denotes the direction along the length of the channel (X direction with 156 pixels) and y denotes the direction across the width of the channel (Y direction with 13 pixels).

The velocity of the leading edge ($Vthe_{LE}$) and centroid ($Vthe_C$) of the thermal tracer was calculated by dividing the travelled distance (ΔPLE and ΔPC in Figure 9.3b) by the time interval between two consecutive instants (Δt in Figure 9.3a).

Electrical conductivity data

Electrical conductivity data was used to measure the velocity of the leading edge ($Vsal_{LE}$) and centroid ($Vsal_C$) of the salt tracer, as shown in Figure 9.4. As with the thermal tracer, a threshold salt concentration was used to distinguish concentrations associated with the tracer from the background flow concentration, and this was subtracted from the measured salt concentration during the passage of tracer. This threshold was set at the maximum salt concentration in the flow observed in the 5 s before the addition of the tracer (EC_{MAX5s}). The leading edge ($Vsal_{LE}$) and centroid ($Vsal_C$) velocity of the salt tracer was calculated by dividing the distance travelled from the addition of the tracer to the detection section (2.1 m) by the time taken from the triple tracer addition to the first rise in conductivity above the threshold value (i.e. arrival of the leading edge, t_{LE}) and by the time it takes for the centroid of the salt concentration (t_C) to arrive, calculated by the moment equation (Equation 9.2):

$$t_C = \frac{\sum_{t=t_{LE}}^{t_{LE}+t_B} EC_t \times t}{\sum_{t=t_{LE}}^{t_{LE}+t_B} EC_t} \tag{9.2}$$

where EC_t is the electrical conductivity (μS cm^{-1}) at time t (s), after subtraction of the threshold value EC_{MAX5s} and t_B is the base time (s) of the conductivity graphs, from the initial rise in conductivity above the threshold value to the decay below the threshold value.

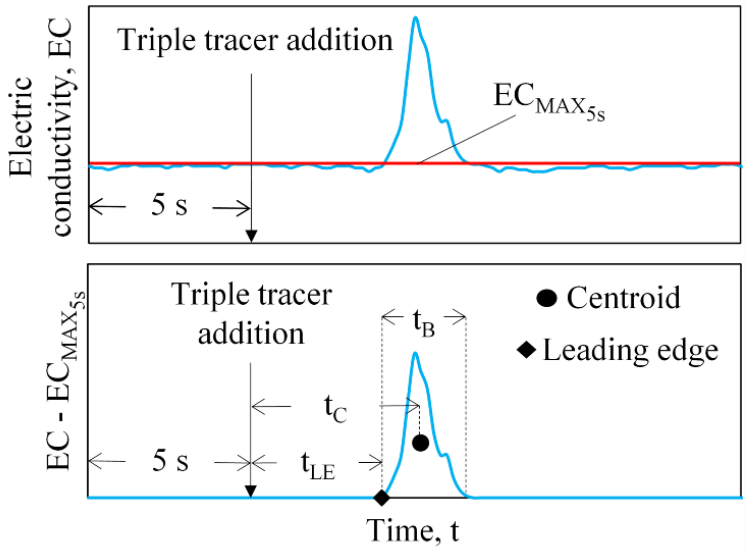

Figure 9.4. Scheme of the procedure used in the analyses of the electrical conductivity data for measurement of the flow velocity.

Optical data

For the dye tracer, only the leading edge velocities ($Vdye_{LE}$) were determined, following commonly used procedure, by measuring the travel time of leading edge (Δt) during its passage over three measuring sections, as illustrated in Figure 9.5.

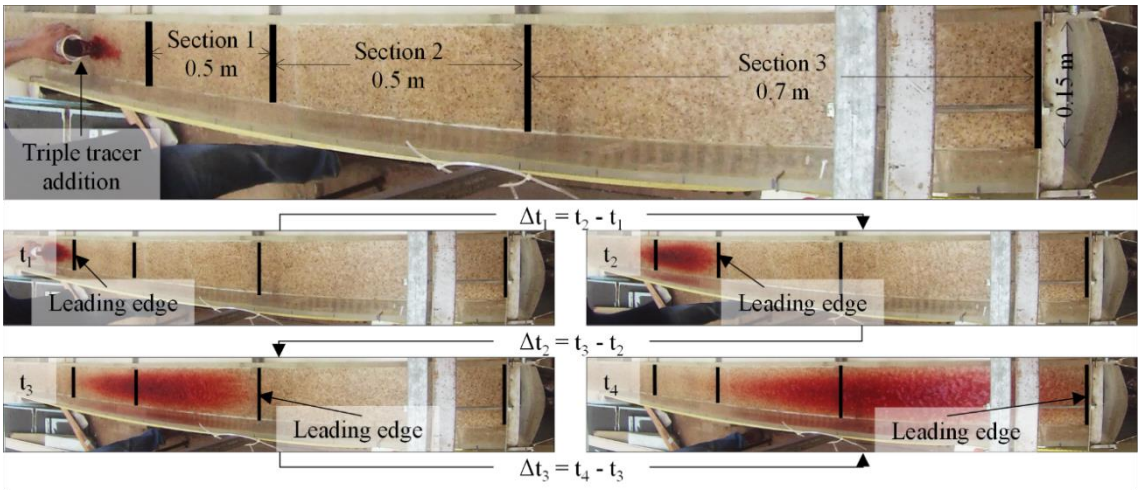

Figure 9.5. Series of photographs of a sand surface experiment with the passage of the dye tracer identified by the four measuring sections used to measure the flow velocity.

The first two sections were 0.5 m in length and were at a distance of 0.4-0.9 m and 0.9-1.4 m from the triple tracer addition point. The third section was 0.7 m in length and covered the final stretch of the channel, at a distance of 1.4-2.1 m from the triple tracer addition point. The travel time was determined from visualizing the real image videos recorded with the optical video camera.

Flow discharge/depth data

Flow discharge (measured at the channel outlet) and flow depth (measured with a precision limnimeter) data were used to calculate mean flow velocity (Vm) for all simulated flows, using Equation 9.3:

$$Vm = \frac{Q}{h \times w} \tag{9.3}$$

where Q is the flow discharge ($m^3\ s^{-1}$), h is the measured flow depth (m) and w is the width of the hydraulic channel (m).

Mean flow velocity and flow depth were used to calculate the Reynolds number (Re) and Froude number (Fr), according to Equations 9.4 and 9.5 (EMMETT, 1970):

$$Re = \frac{4 \times R_h \times Vm}{\nu} \tag{9.4}$$

$$Fr = \frac{Vm}{\sqrt{g \times h}} \quad (9.5)$$

where R_h is the hydraulic radius (m), ν is the kinematic viscosity of the water (7.842×10^{-7} m^2 s^{-1} at the average flow temperature of 30.4 ºC observed during the experiments) and g is the gravitational acceleration (9.807 m s^{-2}). The hydraulic radius was used instead of the flow depth to calculate the Reynolds number, due to the high flow depth values (reaching almost 1/3 of flow width) in the synthetic grass bed surface tests.

9.4. Results and discussion

9.4.1. Triple-tracer velocities

The triple-tracer experiments outlined in this study allowed the simultaneous measurement of thermal, salt and dye tracer velocity, and consequently the comparison of the three techniques. Table 9.1 shows results of the triple-tracer experiments, for all simulated flows: leading edge and centroid velocities estimated by thermal ($Vthe_{LE}$ and $Vthe_C$), salt ($Vsal_{LE}$ and $Vsal_C$) and dye ($Vdye_{LE}$) tracers and mean flow velocities (Vm). Comparison of the tracer velocities is shown in Figure 9.6.

In the stone bed surface tests and some of the synthetic grass bed surfaces it was not possible to calculate the mean flow velocity using discharge/depth measurements (n.a. in Table 9.1), since flow depth measurements failed either because of the size of the stones influenced flow depth or because the flow depths were very shallow, sometimes not even covering the stones or the synthetic grass. Thermal tracer velocities for some smaller discharges were also not successfully measured (as discussed below). During the sand bed surface tests of 13.2 % bed slope, the glued sand started to peel off from the acrylic board that was placed over the channel bed; therefore, these results were not considered.

As can be seen in Table 9.1, for the four tested bed surfaces (smooth acrylic, sand, stones and synthetic grass) and three slopes (0.8, 4.4 and 13.2%), simulated discharges varied from 32-1813 ml s^{-1}, resulting in measured flow depths from 1.4-46.0 mm and calculated mean flow velocities from 0.02-0.85 m s^{-1}, Reynolds numbers from 785-19000 and Froude numbers from 0.05-4.70.

Thermal, salt and dye tracer techniques yielded very similar results with a good correlation with one another, as can be seen in Figure 9.6 ($r^2 > 0.94$ and linear regressions with average angular coefficients of 1.127 ± 0.011 and average intercept constants of 0.018 ± 0.008). Generally, the thermal tracer technique resulted in slightly higher velocities than the other two techniques, with differences increasing with the measured velocity. Similar results were reported by DE LIMA and ABRANTES (2014b) when comparing dye and thermal tracers. Differences between the thermal and the salt tracing were slightly higher for the centroid velocities.

Table 9.1. Overall results of the triple tracer experiments.

	Slope S (%)	Discharge Q (ml s^{-1})	Mean flow velocity Vm (m s^{-1})	Tracer velocity (m s^{-1})*				
				Thermal		Salt		Dye
				Leading edge $Vthe_{LE}$	Centroid $Vthe_C$	Leading edge $Vsal_{LE}$	Centroid $Vsal_C$	Leading edge $Vdye_{LE}$
Smooth acrylic	0.8	650	0.475	0.608 ± 0.013	0.608 ± 0.009	0.596 ± 0.033	0.547 ± 0.040	0.559 ± 0.008
	0.8	856	0.516	0.703 ± 0.014	0.684 ± 0.010	0.639 ± 0.019	0.547 ± 0.047	0.629 ± 0.013
	0.8	1158	0.580	0.762 ± 0.008	0.772 ± 0.020	0.637 ± 0.020	0.597 ± 0.027	0.709 ± 0.004
	4.4	420	0.529	0.645 ± 0.012	0.639 ± 0.005	0.595 ± 0.043	0.552 ± 0.019	0.585 ± 0.016
	4.4	696	0.623	0.828 ± 0.048	0.791 ± 0.016	0.717 ± 0.134	0.649 ± 0.071	0.715 ± 0.006
	13.2	71	0.345	0.572 ± 0.058	0.378 ± 0.025	0.591 ± 0.009	0.460 ± 0.014	0.540 ± 0.015
	13.2	164	0.619	0.777 ± 0.082	0.683 ± 0.015	0.725 ± 0.063	0.573 ± 0.030	0.630 ± 0.021
	13.2	450	0.851	1.036 ± 0.018	0.944 ± 0.024	0.901 ± 0.095	0.945 ± 0.039	0.944 ± 0.027
Sand	0.8	47	0.035	0.092 ± 0.002	0.081 ± 0.005	0.080 ± 0.008	0.106 ± 0.003	n.a.
	0.8	81	0.070	0.116 ± 0.002	0.121 ± 0.007	0.138 ± 0.001	0.108 ± 0.006	0.114 ± 0.006
	0.8	210	0.079	0.172 ± 0.005	0.166 ± 0.005	0.156 ± 0.015	0.143 ± 0.009	0.163 ± 0.004
	4.4	72	0.033	0.105 ± 0.002	0.102 ± 0.005	0.122 ± 0.006	0.095 ± 0.004	n.a.
	4.4	259	0.178	0.332 ± 0.009	0.269 ± 0.004	0.317 ± 0.001	0.252 ± 0.002	0.343 ± 0.003
	4.4	884	0.371	0.639 ± 0.017	0.530 ± 0.007	0.538 ± 0.049	0.441 ± 0.010	0.581 ± 0.028

* Tracer velocities are averages ± standard deviation of three repetitions; n.a. for not applicable (not able to measure)

Table 9.1. Overall results of the triple tracer experiments (Continuation).

	Slope, S (%)	Discharge, Q (ml s^{-1})	Mean flow velocity, Vm (m s^{-1})	Tracer velocity (m s^{-1})*				
				Thermal		Salt		Dye
				Leading edge, $Vthe_{LE}$	Centroid, $Vthe_{C}$	Leading edge, $Vsal_{LE}$	Centroid, $Vsal_{C}$	Leading edge, $Vdye_{LE}$
Stones	0.8	219	n.a.	0.130 ± 0.010	0.084 ± 0.009	0.117 ± 0.009	0.087 ± 0.002	0.132 ± 0.001
	0.8	864	n.a.	0.359 ± 0.040	0.240 ± 0.008	0.313 ± 0.019	0.187 ± 0.003	0.277 ± 0.005
	0.8	1813	n.a.	0.411 ± 0.032	0.342 ± 0.102	0.382 ± 0.088	0.288 ± 0.053	0.369 ± 0.009
	4.4	256	n.a.	0.144 ± 0.004	0.099 ± 0.002	0.138 ± 0.011	0.100 ± 0.003	0.155 ± 0.007
	4.4	547	n.a.	0.306 ± 0.041	0.170 ± 0.010	0.247 ± 0.007	0.167 ± 0.003	0.263 ± 0.002
	4.4	1131	n.a.	0.466 ± 0.040	0.375 ± 0.015	0.398 ± 0.033	0.248 ± 0.005	0.422 ± 0.054
	13.2	32	n.a.	0.059 ± 0.013	0.050 ± 0.009	0.084 ± 0.002	0.065 ± 0.001	n.a.
	13.2	102	n.a.	0.092 ± 0.004	0.095 ± 0.005	0.096 ± 0.001	0.085 ± 0.001	0.088 ± 0.014
	13.2	753	n.a.	0.351 ± 0.012	0.274 ± 0.005	0.374 ± 0.018	0.247 ± 0.003	0.451 ± 0.059
Synthetic grass	0.8	94	0.025	0.084 ± 0.003	0.089 ± 0.001	0.109 ± 0.002	0.052 ± 0.006	n.a.
	0.8	438	0.080	0.192 ± 0.014	0.181 ± 0.006	0.225 ± 0.006	0.151 ± 0.008	0.205 ± 0.005
	0.8	1067	0.156	0.338 ± 0.006	0.299 ± 0.007	0.307 ± 0.007	0.194 ± 0.025	0.255 ± 0.011
	4.4	75	n.a.	0.043 ± 0.010	0.049 ± 0.005	0.072 ± 0.002	0.058 ± 0.001	n.a.
	4.4	549	0.207	0.432 ± 0.009	0.312 ± 0.009	0.472 ± 0.026	0.284 ± 0.009	0.339 ± 0.014
	4.4	1103	0.417	0.688 ± 0.014	0.530 ± 0.035	0.564 ± 0.030	0.371 ± 0.007	0.555 ± 0.027
	13.2	52	n.a.	0.045 ± 0.002	0.036 ± 0.002	0.062 ± 0.004	0.055 ± 0.002	n.a.
	13.2	202	0.118	0.175 ± 0.015	0.147 ± 0.008	0.210 ± 0.014	0.147 ± 0.007	0.239 ± 0.042
	13.2	1239	0.461	0.834 ± 0.012	0.703 ± 0.075	0.752 ± 0.052	0.545 ± 0.060	0.831 ± 0.006

* Tracer velocities are averages ± standard deviation of three repetitions; n.a. for not applicable (not able to measure)

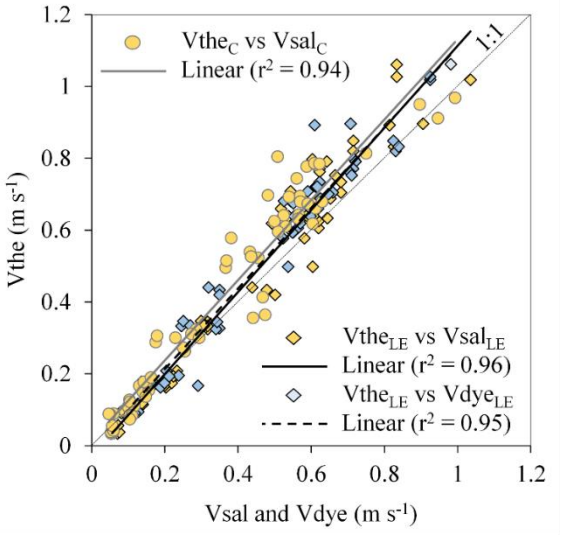

Figure 9.6. Comparison between thermal (Vthe), salt (Vsal) and dye (Vdye) tracer velocities for all simulated flows (subscripts LE and C stand for leading edge and centroid, respectively).

Thermal tracer velocities

Figure 9.7 presents results of the thermal tracer flow velocity measurements. Two flow conditions are shown for each tested bed surface, corresponding to the lowest and highest calculated mean flow velocity (see Table 9.1). Two snapshots (time interval of 1 s) of the thermal videos of the passage of the thermal tracer along the channel are shown for each flow condition.

The movement of the thermal tracer along the channel was always visible for all simulated flows; however, whereas for higher flow velocities its movement is well defined and well-shaped throughout the channel's length, for lower flow velocities its movement in some cases was only visible during the initial part of the measurement section (e.g. for stone bed surface with a discharge of 32 ml s^{-1} and a 13.2% slope). This is related to the non-conservative aspect of the thermal tracer, i.e. temperature diffusion. Lower velocities seem to result in higher temperature diffusion, which can be seen by the dimension of the thermal marks (i.e. pixels with temperature above the threshold value) and maximum temperature values of the tracer (T_{MAX} in Figure 9.7) as it passes along the channel. Overall, lower velocities have lower thermal marks and lower T_{MAX}. Larger bed roughness elements (e.g. stones) also induced higher tracer diffusion and lower tracer conservation, either by the higher dissipation of flow energy or by heat transfer between flow and the rough element.

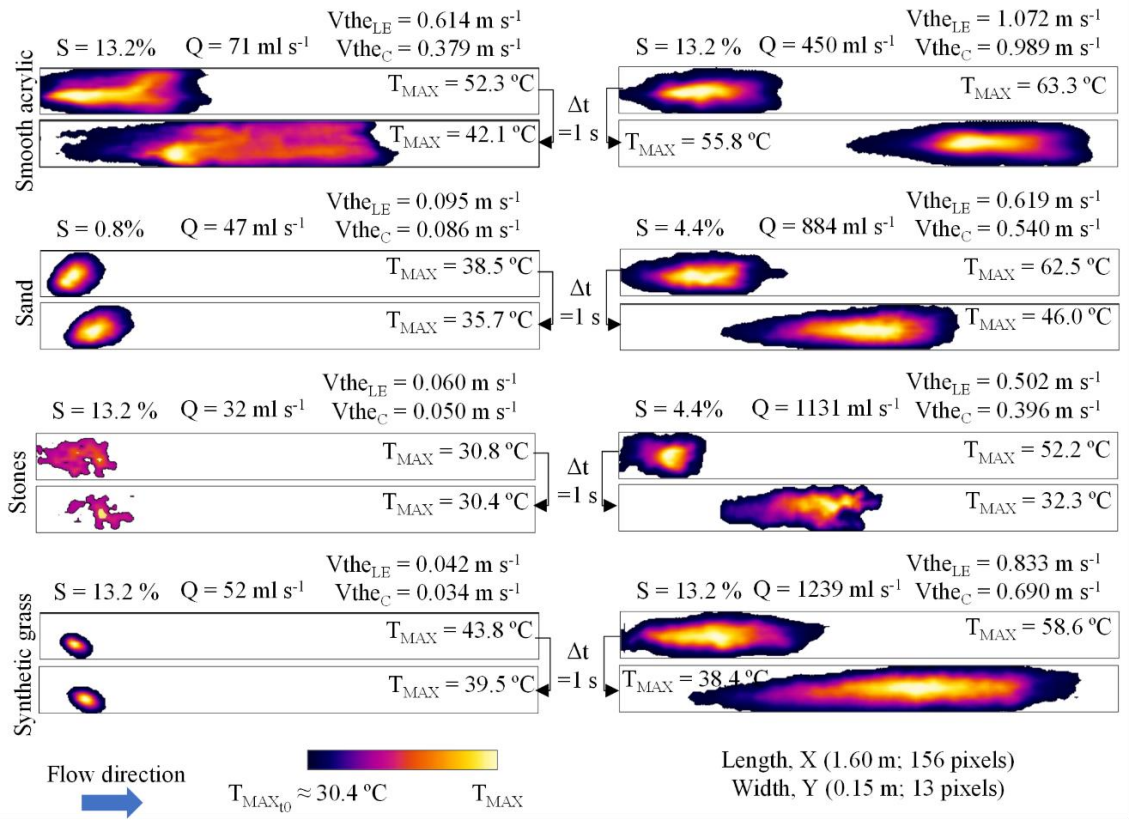

Figure 9.7. Snapshots of the passage of the thermal tracer along the channel for two flow conditions for each tested bed surface. S is the surface slope, Q is the discharge, $Vthe_{LE}$ and $Vthe_C$ are the thermal tracer leading edge and centroid velocities, T_{MAX} and T_{MAXt0} are the maximum and threshold temperatures.

One aspect that should be taken into account in the previous observation is that, in general, higher flow velocities were the result of higher discharges and therefore a higher volume of tracer, which facilitates the conservation of the thermal tracer during its passage along the channel. However, for lower flow velocities and lower discharges, the lower volumes of tracer did not facilitate their conservation for the length of the channel. Therefore, one way to improve the conservation of the thermal tracer is to increase the volume of added tracer; however, this will increase the error in estimating the flow velocity, since larger volumes of tracer interfere with velocity, especially for smaller discharges where the influence of the volume of added tracer would be more noticeable (DE LIMA and ABRANTES, 2014b; DE LIMA et al., 2015b). Therefore, the optimal volume of thermal tracer will be the smallest amount that permits the application of the technique, i.e. clear visualization of the movement of the tracer in the flow.

An alternative to the presented methodology is to introduce a temperature sensor in the water flow instead of using the infrared camera to detect the movement of the thermal tracer; however, introducing a sensor in the water will perturb the flow itself and in these very shallow flows of millimetres to a few centimetres, it is not always possible to properly measure the temperature with a sensor, since these type of sensors usually need a minimum water depth to perform correct measurements.

Another way to diminish the non-conservative aspect of the thermal tracer is by reducing the distance between the tracer addition point and the measuring section; however, this will again increase the error in estimating the flow velocity, since the tracer addition can cause disturbances in the flow that are more noticeable closer to the addition point and for smaller discharges. This can be seen in Figure 9.8, which shows that estimated thermal velocities vary with the distance from the tracer addition point. On the one hand, higher velocities closer to the tracer addition point can be caused by the disturbance of the tracer addition, even considering the distance of 0.4 m between the tracer addition point and the beginning of the measurement area. On the other hand, the non-conservative aspect of the thermal tracer causes a decrease in estimated thermal velocity with increasing distance to the tracer addition point.

The tracer temperature decreases as the distance to the tracer addition point increases and, therefore, tracer temperature slowly dissipates in the background water temperature. This effect had more impact on the leading edge velocity (Figure 9.8a) than on the centroid velocity (Figure 9.8b) because the temperature dissipation occurs first in the interface between the tracer and the water. This effect also increases as bed roughness increases and flow velocity decreases and is stronger for the stone bed surface and weaker for the smooth acrylic bed surface (i.e. higher heat transfer between flow and the rough element).

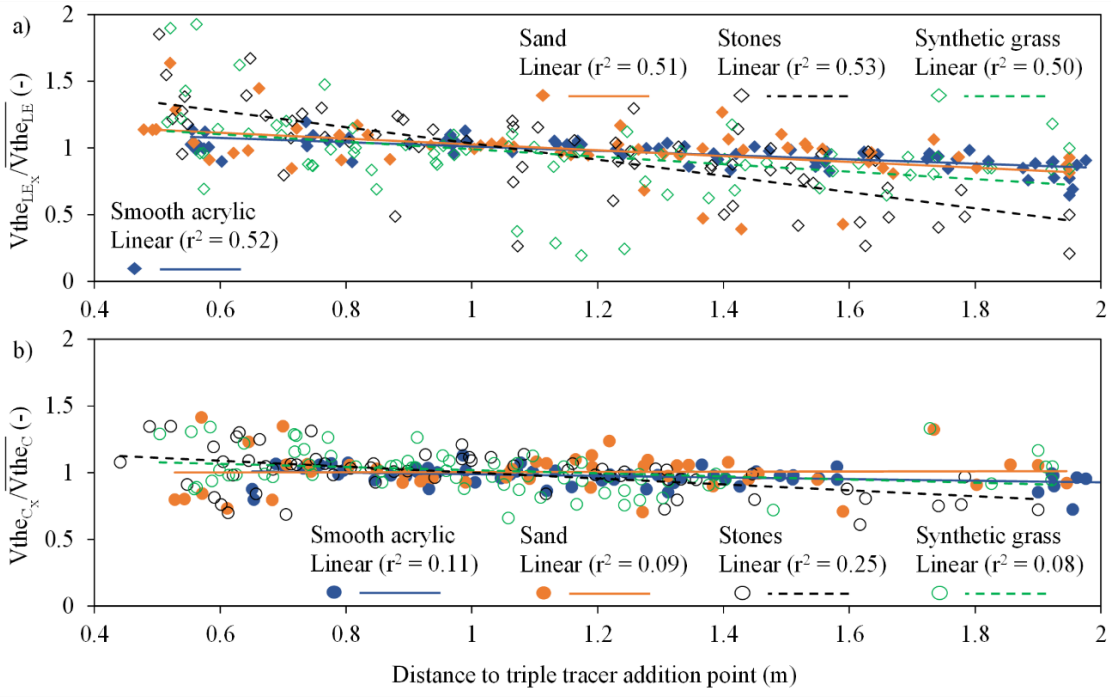

Figure 9.8. Thermal tracer estimated flow velocities as function of the distance to triple tracer addition point: a) Leading edge velocity; and b) Centroid velocity. The flow velocity is presented as a ratio between flow velocity at different locations along the length of the channel ($Vthe_{LEx}$ and $Vthe_{Cx}$) and the mean flow velocity along the entire channel ($\overline{Vthe_{LE}}$ and $\overline{Vthe_{C}}$).

Another aspect to be considered when using a thermal tracer is its temperature. A higher tracer temperature will improve the conservation of the tracer without significantly compromising velocity measurements. In previous experiments, DE LIMA and ABRANTES (2014b) found that the relative differences between the leading edge velocities of tracers at 15 and 85 ºC were similar to the relative differences between tracers at the same temperature, as result of the variability induced by the manual addition of the tracer.

Salt tracer velocities

Salt transport graphs (i.e. electrical conductivity) recorded at the channel outlet for two flow conditions and the four different tested bed surfaces are shown in Figure 9.9 (same tests presented in Figure 9.7 for thermal tracer). For all experiments, it was always possible to detect the passage of the salt in the outlet and therefore measure the flow velocity either by the leading edge or the centroid. Unlike the thermal and dye tracers, the salt tracer only gave a one-off measurement of flow velocity.

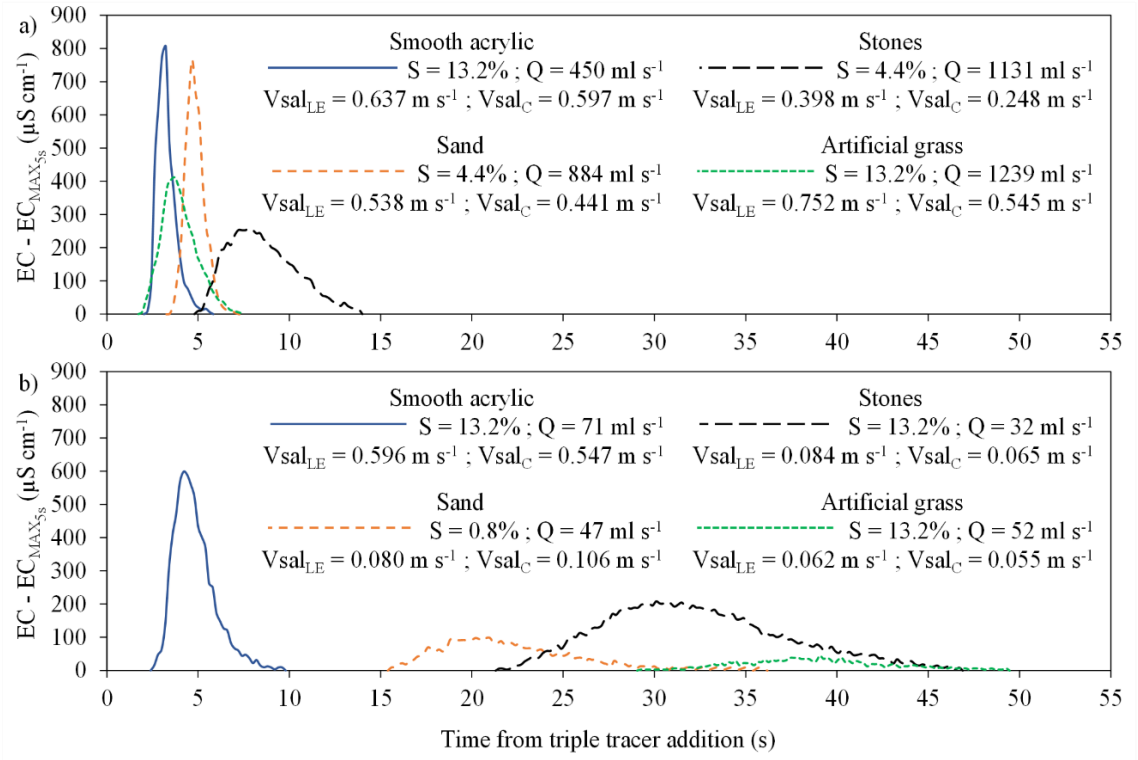

Figure 9.9. Salt transport graphs for two flow conditions for each tested bed surface: a) Higher velocities; and b) Lower velocities. S is the surface slope, Q is the discharge, $Vsal_{LE}$ and $Vsal_C$ are the salt tracer leading edge and centroid velocities, EC is the electrical conductivity and EC_{MAX5s} is the threshold electrical conductivity.

In general, higher mean velocities (see Table 9.1) lead to an earlier rise and peak of the salt transport graph, resulting in higher leading edge ($Vsal_{LE}$) and centroid velocities ($Vsal_C$). As the estimated salt velocities increased, so did the salt transport peak, while the base transport time (i.e. time from

the initial rise in conductivity above the threshold value to the decay below the threshold value) decreased.

The relation between the estimated salt velocities ($Vsal_{LE}$ and $Vsal_C$) and the total mass of salt transported by the flow, presented as a ratio of the total mass of salt detected by the electrical conductivity sensor at the channel outlet (M_{transp}) to the total mass of salt added to the flow (M_{added}), is shown in Figure 9.10. Similar to the thermal tracer, the non-conservative aspect of the salt tracer decreases with flow velocity, since salt transport increases. A major concern when using salt tracers to measure flow velocity is how to ensure that the salt is completely dissolved in the flow so that it can be properly detected (DAY, 1977). In the present study, salt was added as an aqueous solution with hot water, which greatly helped the salt to mix in the flow. Therefore, the decrease of salt transport with lower flow velocity would be closely related to the bed surface roughness. In fact, the average ratio of salt transport for the different tested bed surfaces was 1.02 ± 0.07, 0.85 ± 0.13, 0.87 ± 0.13 and 0.74 ± 0.30 for the smooth acrylic, sand, stones and synthetic grass, respectively.

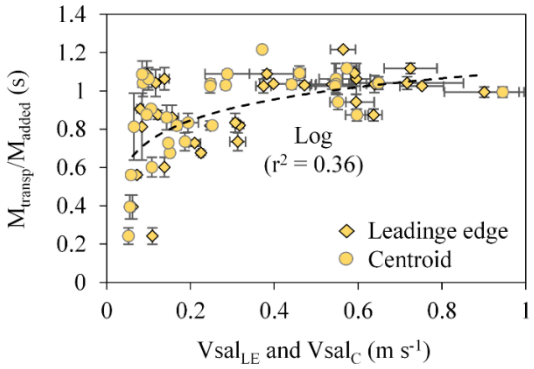

Figure 9.10. Relation between estimated leading edge and centroid salt velocities ($Vsal_{LE}$ and $Vsal_C$) and the ratio between mass of transported (M_{transp}) and added (M_{added}) salt. Vertical bars indicate standard deviation.

One way to improve the conservation of the salt tracer is to increase salt concentration and decrease the distance from the tracer addition point to the sampling point. It should be noted, however, that, similar to the thermal tracer, salt tracer velocities tend to decrease with increasing distance from the salt addition point (CALKINS and DUNNE, 1970; PLANCHON et al., 2005). At the same time, higher salt concentration would need a longer mixing time to ensure the salt is properly dissolved in the flow. Therefore, when using a salt tracer, the salt solubility, concentration, addition method (e.g. dry or as an aqueous solution), flow conditions (e.g. discharge, depth, velocity), bed surface roughness and mixing length must all be taken into consideration.

Dye tracer velocities

Figure 9.11 presents the results of the dye tracer flow velocity measurements (same tests presented in Figures 9.7 and 9.9 for thermal and salt tracers, respectively). Two snapshots of the real image

videos of the dye tracer passing along the 0.5 m measuring section (Section 2 in Figure 9.5) are shown for each flow condition.

It was not always possible to estimate flow velocity with the dye tracer for the tested flow conditions. This was because for lower discharges, and thus for lower volumes of added tracer, the dye tracer could not be visualized as it passed along the channel (see Figure 9.11 and n.a. in Table 9.1). This is related to the non-conservative aspect of the dye tracer and, as with the thermal and salt tracers, it was more evident for lower flow velocities in the higher bed surface roughness tests.

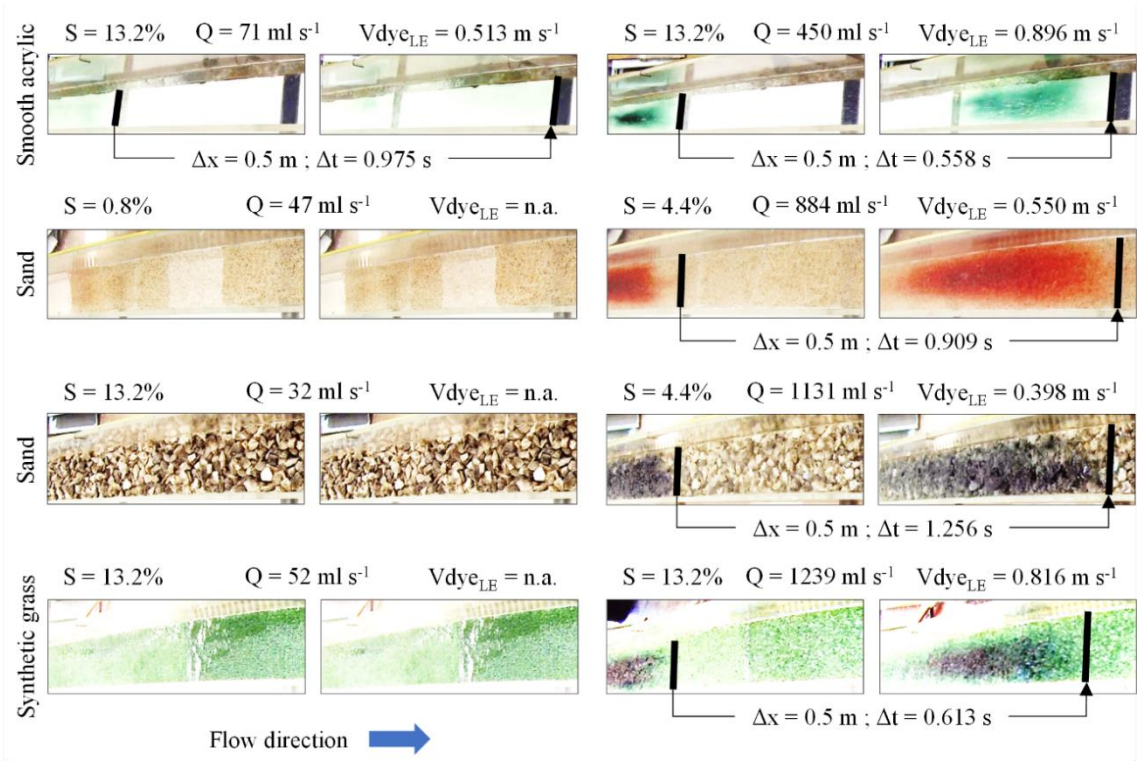

Figure 9.11. Photographs of the passage of the dye tracer in a measuring section (Section 2 in Figure 9.5) for two flow conditions for each tested bed surface. S is the surface slope, Q is the discharge, $Vdye_{LE}$ is the dye leading edge velocity, Δx is the measuring section length and Δt is the time interval.

One way to increase the conservation of the dye tracer is to increase the dye concentration and decrease the distance from the tracer addition point to the sampling point. But as with the thermal and salt tracers, the dye tracer leading edge flow velocity decreases with increasing distance from the tracer addition point (Figure 9.12). Furthermore, timing errors, unavoidable due to human reaction time and the frame rate of the recording system, will tend to increase with shorter measurement lengths (DE LIMA and ABRANTES, 2014b; DUNKERLEY, 2003). Other way to improve dye tracing performance is to use an automated mechanism of detecting the passage of the dye tracer such as the ones used in DUNKERLEY (2003) and HOLDEN et al. (2008).

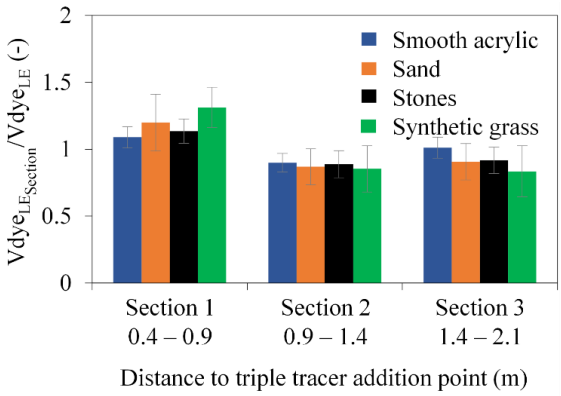

Figure 9.12. Ratio between dye tracer leading edge velocities for the three measuring sections ($Vdye_{LESection}$) and the mean dye tracer velocity along the entire channel ($Vdye_{LE}$).

9.4.2. Advantages and disadvantages of the tracer techniques

Overall, the main advantages of the thermal tracer technique over the dye tracer technique were: i) Higher visibility of the tracer in the thermal videos compared with the real image videos; ii) Estimation of flow velocities using smaller volume of tracer, and, therefore, smaller disturbances in the actual flow velocity; and iii) Easy estimation of centroid velocities that are very difficult to obtain from dye tracer measurements, since they require more sophisticated image processing and specific light conditions that may not be always available, especially in field tests. The main advantages of the thermal tracer technique over the salt tracer technique were: i) The visualization of the movement of the thermal tracer along the measuring section; ii) The possibility of measuring space-averaged flow velocities using only one infrared video camera instead of only one velocity value using only one electrolyte sensor (space-averaged salt tracer velocities would require multiple sensors placed along the flume); iii) The possibility of measuring the flow velocity without the need of introducing any instrument (sensor) in the flow, causing less disturbances in the actual flow velocity; and iv) The non-necessity of a minimum water depth, which usually is needed to accurately measure the salt concentration with an electrolyte sensor. The thermal tracer also offers a cleaner and more ecologically friendly way of measuring in situ flow velocities than the dye and salt tracers do, since it leaves no residue in the water or the soil and causes very little temporal and spatial disturbance to the environment.

Overall, the main disadvantages of the thermal tracer technique over the dye and salt tracers techniques were: i) High price of an infrared video camera compared with a regular optical video camera or an electrolyte sensor, despite recent falls in the cost of infrared equipment; and ii) The need to have an energy source to heat or cool the water rather than simply having to add colouring or salt might be an obstacle, especially in remote field studies. The thermal tracer showed less conservation in the flow than the salt tracer and the accuracy of the measurement seemed to depend more on the volume and/or temperature of the tracer than on the concentration of the salt. Measuring

flow velocity using the dye tracer can be faster and more intuitive than the thermal tracer, since the movement of the tracer can be simply observed by the operator without using any recording equipment (e.g. camera, sensor), which can be especially useful in field applications.

9.4.3. α and β correction factors

Figure 9.13 presents the comparison between mean flow velocities (Vm) calculated from flow discharge/depth measurements and the leading edge and centroid velocities measured with the triple-tracer technique. Results of the stone bed surface tests were not considered, since it was not possible to calculate mean flow velocity.

Leading edge and centroid tracer velocities presented a good correlation with mean flow velocity ($r^2 > 0.89$ in Figure 9.13). As expected, tracer velocities were higher than mean flow velocity, with higher values for the leading edge. In fact, as stated before, leading edge is regarded as the surface velocity of the flow, i.e. the theoretical maximum (or near maximum) value of the flow velocity profile. In turn, centroid velocity is regarded as the theoretical mean value of the flow velocity profile, if conservation of the tracer in the flow is assumed. However, since none of the tracers exhibited absolute conservation during the experiments, centroid velocities were slightly higher than mean flow velocity.

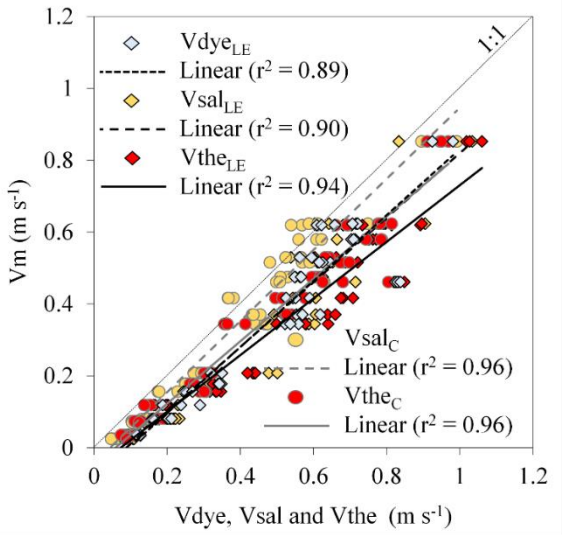

Figure 9.13. Comparison between mean flow velocities (Vm) and thermal (Vthe), salt (Vsal) and dye (Vdye) tracer velocities for all simulated flows (subscripts LE and C stand for leading edge and centroid, respectively).

Since tracer velocities were higher than mean flow velocity, a correction factor must be used to convert the measured tracer velocities into actual mean flow velocities. In this study, two correction factors were considered: i) α as the ratio between the mean flow velocity (Vm) and the leading edge velocity measured by means of the triple-tracer technique ($Vthe_{LE}$, $Vsal_{LE}$ and $Vdye_{LE}$); and ii) β as the ratio between the mean flow velocity (Vm) and the centroid velocity, measured by means of thermal and salt tracers ($Vthe_C$ and $Vsal_C$). Thermal, salt and dye tracer correction factors α and β

calculated for the smooth acrylic, sand and synthetic grass (stone bed surface results were not considered) are shown in Figure 9.14. As can be seen, there are no significant differences in the α and β values for the tracer techniques. Thermal, salt and dye α correction factors ranged from 0.283-0.879, 0.225-1.034 and 0.277-1.017 with average values of 0.595 ± 0.166, 0.626 ± 0.219 and 0.676 ± 0.193, respectively. Thermal and salt β correction factors ranged from 0.274-0.967 and 0.320-1.149 with average values of 0.666 ± 0.187 and 0.774 ± 0.223, respectively.

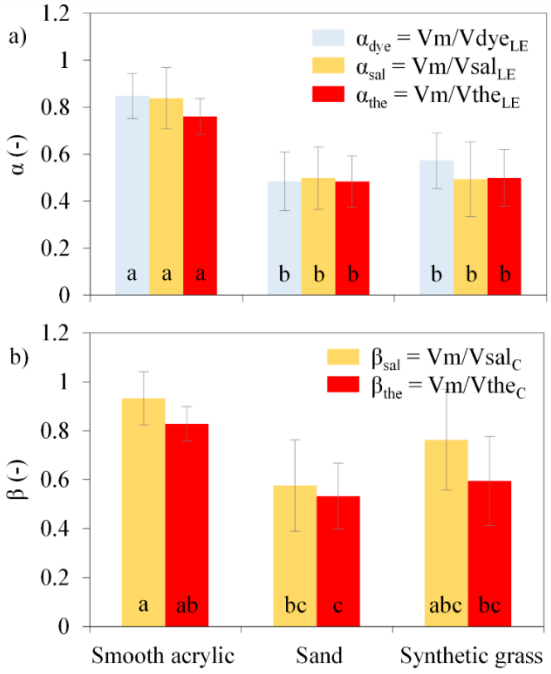

Figure 9.14. Correction factors derived from the triple-tracer experiments, for the smooth acrylic, sand and synthetic grass bed surfaces: a) α; and b) β. Columns with the same lowercase letter do not differ significantly for Tukey's test ($p < 0.05$).

The observed range of α included Horton's theoretical value of 0.67 for an infinitely wide, perfect laminar flow on a smooth and immobile bed (HORTON et al., 1934) and the α lower boundary of 0.225 agrees with the range of approximately 0.2-0.9 found in previous studies (DUNKERLEY, 2001; EMMETT, 1970; LI and ABRAHAMS, 1997; LI et al., 1996; PLANCHON et al., 2005; ZHANG et al., 2010); however, the upper boundary was higher (1.034). For all simulated flows, observed β values were higher than the α values, which is in line with the theory that tracer centroid velocities are mean theoretical velocities, if conservation of the tracer is assumed. Lower and upper boundaries of β (0.274-1.149) exceeded the range of 0.7-0.9 observed by LI et al. (1996) and 0.6-1.0 observed by PLANCHON et al. (2005). However, all previous studies presented a broad variety of findings and conclusions, without actually defining fixed conversion factors or relations. In fact, the variation of α and β is the result of a very complex relation between the shape of the flow velocity profile and the flow characteristics (e.g. velocity, depth, Reynolds number, Froude number) and the bed surface characteristics (e.g. roughness, slope).

As shown in Figure 9.14, significant differences were found for α and β (the latter to a lesser extent) between the smooth acrylic bed surface and the rough bed surfaces (sand and synthetic grass), with α and β being smaller for the rough bed surfaces. These findings are in agreement with EMMETT (1970) who found smaller α in field experiments than in laboratory experiments, since natural field soil surfaces had a wider range of roughness elements than the laboratory sand surfaces. Roughness elements will perturb the flow and give rise to steeper velocity profiles with a wider gap between the flow velocity profile mean and maximum (i.e. flow surface velocity) values, which implies lower α values. DUNKERLEY (2001) also observed a tenuous inverse relation between roughness and α.

Correction factors increased with increasing Reynolds number (Re) and Froude number (Fr), as shown in Figure 9.15. Here, only thermal correction factors are presented, though it should be noted that salt and dye correction factors showed similar behaviour. An increase in Re and Fr increases flow turbulence and flow speed, which results in a better mixing of the flow, and a less steep velocity profile, approaching the flow velocity profile mean and maximum values. Therefore, a smaller correction of the tracer velocities is required (i.e. correction factors closer to 1).

The variation of α and β with Re reported in previous studies largely depends on the studied flow regime (i.e. range of Re). EMMETT (1970) found lower values of α for laminar flow (Re < 2000), which increased during transitional flow (Re between 2000-8000), with the highest being for turbulent flow (Re > 8000). LI et al. (1996) observed an increase of α and β with Re in the transitional flow regime. LI and ABRAHAMS (1997) observed lower values of α in laminar flow, without a distinct trend with Re, a steep rise of α in the transitional flow and a slight rise in the turbulent range. DUNKERLEY (2001), too, did not find any relation between α and Re in the subcritical laminar range (Re between 100-500). In the present study, the variation of α and β with Re was tenuous (power regressions with r^2 of 0.26 and 0.29 in Figure 9.15a) and no clear distinction could be made between the different bed surfaces and the different flow regimes, thus the best fit was achieved when all data was plotted together. Only a slight distinction was found between a rise in the laminar and transitional phase (Re < 8000) and a slight decrease during the turbulent phase (Re > 8000). The rise in the laminar and transitional phase, without any distinction between them, was also noted in ZHANG et al. (2010). The slight decrease during the turbulent phase has not been reported in previous studies, but the highest Re studied previously was 13000 in LI and ABRAHAMS (1997) and LI et al. (1996) whereas in the present study a maximum of 19000 was reached.

In the present study, a stronger correlation was found with the variation of α and β with the Froude number. Here, the variation of Fr was closely related to the roughness of the surface of the bed; on the smooth acrylic bed surface the flow was supercritical (Fr > 1), with Fr between 1.60-4.70, and on the sand and synthetic grass surfaces the flow varied from subcritical (Fr < 1) to critical (Fr ≈ 1), with Fr between 0.05-1.09 (Figure 9.15b). As stated before, higher roughness leads to lower correction factors. The variation of α and β with Fr, was also observed previously in LI and

ABRAHAMS (1997) with Fr varying between 0.4-3.2. Such relations were not clear in other studies, e.g. LI et al. (1996) and ZHANG et al. (2010) only studied critical to supercritical flow, and DUNKERLEY (2001) only studied subcritical flow.

Variation of the correction factors with flow velocity, flow depth and bed slope was further analysed. The correction factors α and β both increased with flow velocity regardless of the flow regime, as shown in Figure 9.16, since these variations were similar for the laminar and turbulent flow and for the subcritical and supercritical flow. Best fit was thus achieved when all data were plotted together. Similar results have been reported in the literature (DUNKERLEY, 2001; EMMETT, 1970; LI and ABRAHAMS, 1997; LI et al., 1996; PLANCHON et al., 2005; ZHANG et al., 2010).

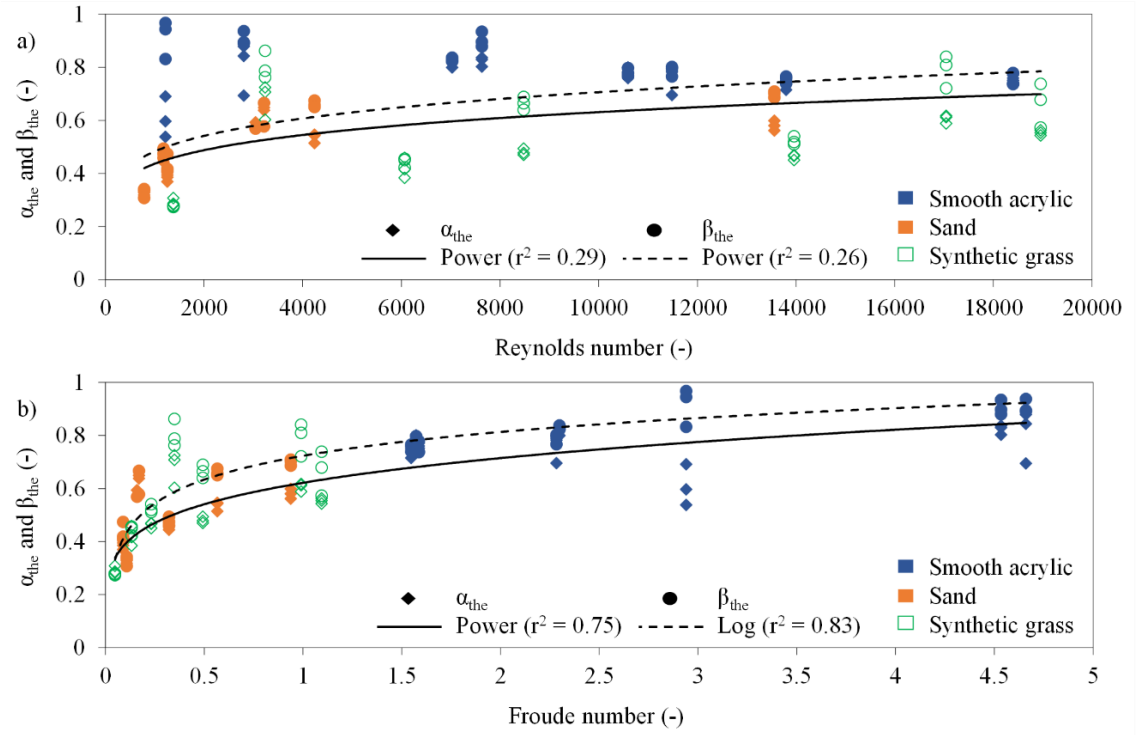

Figure 9.15. Variation of thermal α and β with: a) Reynolds number; and b) Froude number.

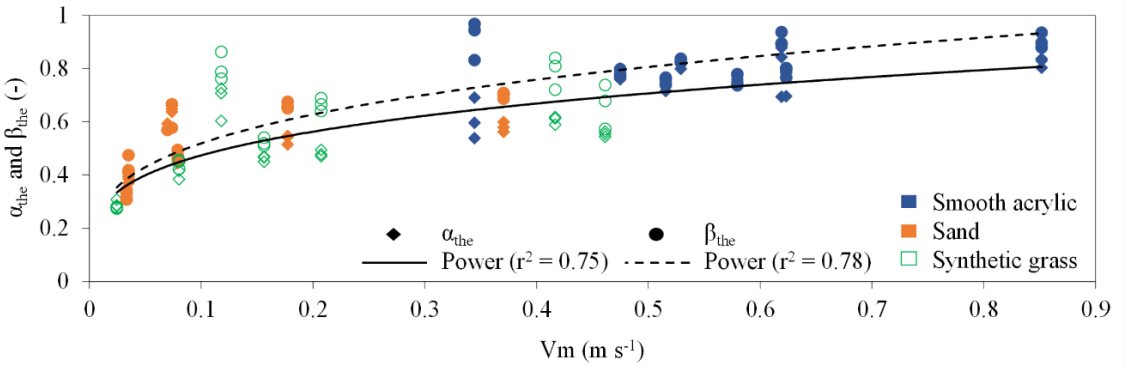

Figure 9.16. Variation of thermal α and β with mean flow velocity (Vm).

The variation of α with flow depth and bed slope is shown in Figures 9.17 and 9.18. Here, only α is presented, though it should be noted that β showed similar behaviour. These variations depended on the flow regime, since they differed between the laminar and transitional plus turbulent flow. No differences were observed between subcritical and supercritical flow, however. Therefore, best fit was achieved when laminar and transitional plus turbulent data were plotted separately, has shown in Figure 9.17. In Figure 9.18 data was plotted separately by surface bed. In this situation, best fit was achieved when transitional plus turbulent data was plotted individually. When separating data by bed surface, no clear relation was observed for laminar flow.

In the present study, α decreased with flow depth; this can be attributed to lower flow velocities observed for the rough surfaces that had the higher flow depths. As stated before, higher roughness leads to lower correction factors. The decrease in α with flow depth was also described in DUNKERLEY (2001) and in LI and ABRAHAMS (1997) for laminar flow. However, in LI and ABRAHAMS (1997), LI et al. (1996) and ZHANG et al. (2010) an increase of α with flow depth for transactional and turbulent flow was observed. Each of the three previous studies used only one type of bed surface: smooth acrylic bed surface in LI et al. (1996), and sand bed surface in LI and ABRAHAMS (1997) and ZHANG et al. (2010). In the present study, an increase of α with flow depth was only observed for transitional flow on the sand bed surface, as shown in Figure 9.18a. In this case, as stated by ZHANG et al. (2010), the influence of grain roughness on flow velocity profile may decrease as flow depth increases, resulting in smoother velocity profiles.

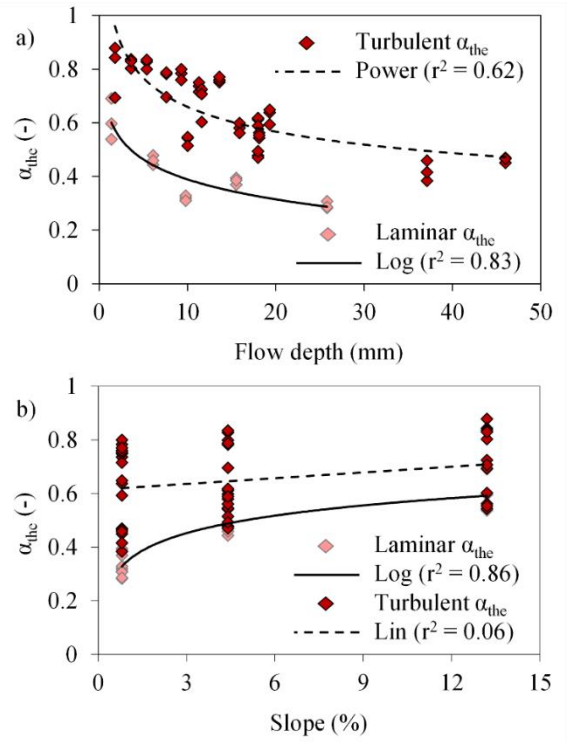

Figure 9.17. Graphs for α for laminar and turbulent flows, against: a) Flow depth; and b) Bed slope. Turbulent flow includes the transitional phase (Re > 2000).

The variation of α with bed slope varied considerably with flow regime; while no clear relation was observed for turbulent flow, for laminar flow there was a positive logarithmic relation with good correlation (r^2 = 0.86). Therefore, slope played an important role in controlling the shape of the flow velocity profile in the laminar range. In fact, for a given flow discharge, as slope gradient increased so did flow velocity, and flow depth decreased.

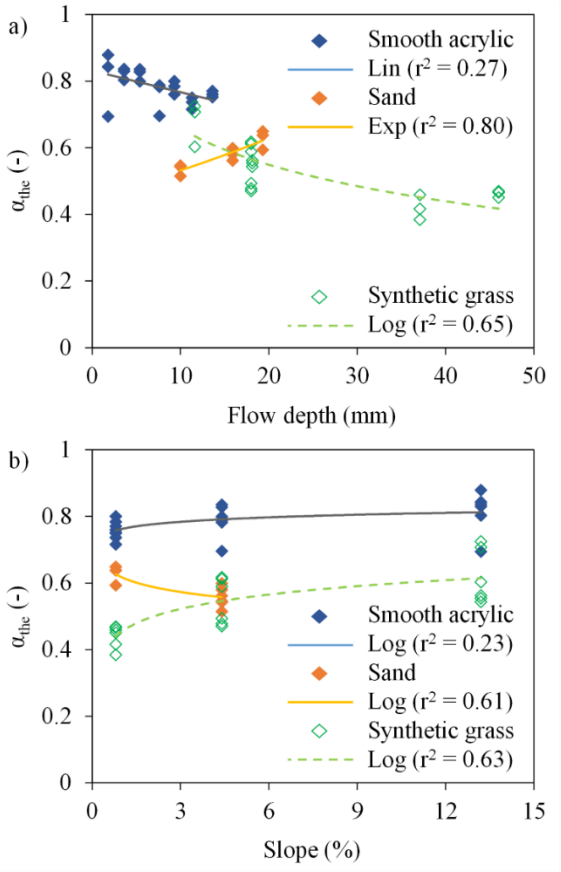

Figure 9.18. Graphs for α observed for the turbulent flows in the different bed surfaces, against: a) Flow depth; and b) Bed slope. Turbulent flow includes the transitional phase (Re > 2000).

As shown before, an increase in flow velocity results in higher α values. Previous studies had different results; in LI et al. (1996) and ZHANG et al. (2010), α decreased with slope for transitional and turbulent flow, but in LI and ABRAHAMS (1997) α did not vary with slope for laminar, transitional or turbulent flow. However, it should be remembered that only one type of bed surface was used in these studies. In the present study, a decrease of α with bed slope was only observed for transitional flow on the sand bed surface, as shown in Figure 9.18b.

9.5. Conclusions

To better understand and model the dynamics of sediment and pollutant transport by overland flow, flow velocities must be measured. Traditional dye and salt tracer techniques and the more recent thermal tracer technique have been used to measure flow velocity, especially in shallow muddy overland flows in the field. In this study, a novel triple-tracer approach was tested, using dyed-salted-heated water. This novel approach gave insight into the measurement of shallow flow velocities and proved to be a useful tool to compare the three techniques. However, it is worth mentioning that despite the improvement achieved by using this triple-tracer approach, many difficulties remained in evaluating shallow flow velocity measurements because of the complexity and spatial and temporal variability of shallow flow. Also, the simultaneous addition of the three tracers may limit each other to their best measurement precisions and the effect of the heated water on dye and salt and vice-versa, although presumably minimal, is not fully known.

Results showed that thermal tracing can be used to estimate shallow flow velocities, since the results are similar to those given by other traditional and well-established flow velocity measurement techniques, such as dye and salt tracing. In general, thermal tracer velocities were slightly higher, followed by dye and salt tracer velocities; however, no significant differences were observed between them.

In these triple-tracer experiments, the volume of added tracer was one of the most important limiting factors of the thermal and dye tracer techniques, whereas for the salt tracer this limitation was not so noticeable. It should be noticed that, the ideal volume for each tracer should be different and, therefore, the triple-tracer approach may has conditioned the best performance of each method. However, it is also true that the optimal volume of tracer should be the smallest amount that creates the smallest disturbance to the actual flow velocity and, at the same time, permits its clear visualization. In this case, the dye tracer was the less successful technique, since for some lower discharges and lower volumes of added tracer it was not always possible to estimate flow velocity with the dye tracer.

For field applications, the dye tracer technique seems to be faster and simpler, especially if only in situ visual observation is performed (i.e. no recording device). However, the involvement of human perception and reaction time is more prone to timing errors. If an optical video camera is used, the operator should ensure that light conditions are suitable to post imaging analyses, especially if the centroid velocity of the dye tracer is to be measured. For large scale field applications (e.g. hillslope scale) the salt tracer seems to be more appropriate due to the higher conservation. However, the movement of the salt tracer along the measuring section and the possibility of measuring space-averaged flow velocities can only be achieved by installing multiple sensors, which can ultimately cause higher disturbance to the actual flow velocity. Also, many sensors require a minimum water depth that may not be available during shallow flow monitoring. Thermal tracer allows to clearly visualise the movement of the tracer along the measuring section with high accuracy. However, it

requires more expensive equipment (i.e. infrared video camera) and an energy source to heat the tracer.

The results showed that the correction factors used to estimate the mean velocity of overland flow from the tracer's leading edge and centroid velocity measurements depend on the flow regime, since they increased with higher Reynolds and Froude numbers. In this study, the correction factors varied directly with flow velocity and slope and inversely with flow depth and bed roughness. In soil erosion and solute transport studies these variables greatly vary in space and time, especially in the field. Therefore, velocity estimation from tracers involves a large amount of uncertainty and caution is required when using these measurements. Data presented in this study can provide new insights on correction factors used in tracing velocity estimation, which is a field not yet clearly understood.

Clear flowing water was used in this study. Further studies are therefore required to investigate the effect of sediment load on the thermal tracer performance and on the respective correction factors. Also, to achieve the best calibration of the thermal tracer technique, further tests should be conducted using different volumes of tracer at different temperatures (hotter and colder water than the flow) and different measuring sections.

“Research always takes three times longer than planned, even after taking this rule into account.”

- Unknown

10. COMBINING A THERMAL TRACER WITH A TRANSPORT MODEL TO ESTIMATE SHALLOW FLOW VELOCITIES[8]

10.1. Abstract

For a long time, tracer techniques based on dyes, salts and more recently heat have been used to estimate shallow flow velocities. Traditionally, flow velocity estimation using tracers would consist of tracking the movement of the leading edge or the centroid of the tracer with the flow. An alternative methodology uses an analytical solution of an advection–dispersion transport equation as the mathematical foundation for measuring shallow water flow velocity from tracer measurements.

The main goal of the present study was to ascertain whether this alternative numerical methodology can be used with temperature data from thermal tracer measurements. Salt and thermal tracer techniques were applied simultaneously by injecting a double tracer of salted-heated water into different shallow flows simulated in a laboratory hydraulic flume. Simulated flows combined different bed surfaces (smooth acrylic sheet, rough sand board and synthetic grass carpet), flow discharges (from 47 to 1239 ml s^{-1}) and bed slopes (0.8, 4.4 and 13.2%), resulting in a wide range of hydraulic conditions. Velocities determined with the abovementioned methodology were compared with those estimated by measuring the tracers' leading edge and centroid and with mean flow velocity calculated using discharge/depth measurements.

Results from combining this alternative numerical methodology with thermal tracer data were similar to results from the salt tracer. Also, the proposed alternative numerical methodology predicted the mean flow velocity calculated from discharge/depth measurements better than the measurements of the leading edge and centroid of the tracers.

Keywords

Thermal tracer; Salt tracer; Advection-dispersion transport equation; Shallow flow velocity; Hydraulic flume

[8] ABRANTES, J.R.C.B., MORUZZI, R.B., DE LIMA, J.L.M.P., SILVEIRA, A. and MONTENEGRO, A.A.A. (2019). Combining a thermal tracer with a transport model to estimate shallow flow velocities. *Physics and Chemistry of the Earth*, 109, 59-69. DOI:10.1016/j.pce.2018.12.005.

10.2. Introduction

Shallow flows can occur in natural and urbanised basins (e.g. hillslopes, drainage systems) and the accurate measurement of their velocity has been of great concern to hydro-environmental researchers since it would help to better understand and model the dynamics of sediment and pollutant transport.

For a long time, tracer techniques have been used to estimate flow velocity. Many people regard them as crude methods compared with far more sophisticated and accurate methods, such as those based on acoustic and ultrasonic technologies (e.g. ADV, ACDP). However, those technologies may have some limitations if used outside their ideal measurement conditions, and therefore they cannot always be used, particularly in the case of very shallow flows with depths of millimetres to a few centimetres. The most common materials used as tracers in flow velocity estimation are dyes (e.g. ABRAHAMS et al., 1986; DUNKERLEY, 2003; FLURY and FLÜHLER, 1993; HOLDEN et al., 2008; TAZIOLI, 2011) and salts (e.g. CALKINS and DUNNE, 1970; COMINA et al., 2014; COMITI et al., 2007; DAY, 1977; TATARD et al., 2008). The movement of the dye with the flow can be seen with the naked eye or using optical recording equipment. The passage of the salt can be detected by an electrical conductivity sensor placed in contact with the flow.

A more recent approach in flow velocity measurement uses thermal tracers (e.g. hot water, ice cubes) that can be detected by an infrared camera (ABRANTES et al., 2018a; DE LIMA and ABRANTES, 2014b; DE LIMA et al., 2015b, 2018; SCHUETZ et al., 2012; TAURO and GRIMALDI, 2017). Results show that thermal tracers can be used to estimate shallow flow velocities, since the results are similar to those given by other traditional and well-established flow velocity measurement techniques, such as dye tracers (ABRANTES et al., 2018a; DE LIMA and ABRANTES, 2014b), salt tracers (ABRANTES et al., 2018a; SCHUETZ et al., 2012), current flow meters (TAURO and GRIMALDI, 2017) and ADV equipment (DE LIMA et al., 2015b). One advantage of thermal tracers is that the tracer is more visible in the thermal images than the dye tracer is in the optical images. Thermal tracers can be especially useful when vegetation is concealing the measuring area. Another advantage is the possibility of measuring space-averaged flow velocity, which for salt tracers can only be achieved by installing multiple sensors. Some disadvantages of thermal tracers are the equipment costs and tracer handling. Also, thermal tracers have been shown to be less conservative than salt tracers, which can be important for large scale field applications (e.g. hillslope scale).

Traditionally, flow velocity estimation using tracers would involve measuring the time from the injection of the tracer to its arrival at a sampling point and then dividing this figure by the travel distance. With dyes, the velocity of the leading edge is usually measured. With salts, either the leading edge or centroid of the tracer's concentration at the sampling point is usually measured. The leading edge is regarded as the surface flow velocity and the centroid is regarded as the mean theoretical flow velocity. However, the non-conservative aspects of the tracers, such as advection and diffusion processes, infiltration and constant exchanges between the soil surface and water

flow, mean that none of the measured velocities can be considered the actual mean flow velocity. Therefore, correction factors have to be applied to obtain the mean flow velocity (HORTON et al., 1934). Such correction factors vary with the flow characteristics (e.g. velocity, depth, regime) and bed surface characteristics (e.g. slope, roughness), as studied in ABRANTES et al. (2018a), DUNKERLEY (2001), EMMETT (1970), LI and ABRAHAMS (1997), LI et al. (1996), PLANCHON et al. (2005) and ZHANG et al. (2010).

An alternative methodology for determining shallow flow velocities based on the advection-dispersion solute transport model was proposed in LEI et al. (2005). This numerical technique consists of fitting the analytical solution of the differential equation for solute transport in shallow flows to solute transport data obtained by means of a salt tracer, i.e. the solute is a salt and its transport in flow is detected by means of electrical conductivity sensors. This fitting is done by minimising the sum of squared errors between modelled and experimentally observed data. This method has been used in a number of studies involving the determination of shallow flow velocity (BAN et al., 2016; CHEN et al., 2017; HUANG et al., 2018; LEI et al., 2010, 2013; RAHMA et al., 2013; SHI et al., 2012, 2016; ZHUANG et al., 2018); it estimates flow velocity more accurately and shows high stability relative to more traditional tracer techniques (e.g. measuring the leading edge or centroid of the tracer). This methodology takes into account the physical processes of advective transport caused by the shifting of the solute field (i.e. concentrated particles) due to the flow movement and diffusive transport by which solute from particles of higher concentration is transferred to particles of lower concentration that are in physical contact (Flick's law).

The main goal of the present study was to ascertain whether the numerical methodology proposed in LEI et al. (2005) could be adapted to temperature data obtained from thermal tracer experiments, first shown in ABRANTES et al. (2018a). In fact, as with solute transport, heat transport in flowing water is governed by advective transport caused by the translation of the energy field (i.e. heated particles) as result of the flow movement and diffusive transport due to the transfer of energy from higher temperature particles to lower temperature particles that are in physical contact (Fourier's law). Therefore, heat transport in flowing water can be described using a differential transport equation that takes both diffusive and advective transport into account, such as the one used for solute transport.

The analogy of comparison between solute and heat transport has been made in previous investigations. SCHUETZ et al. (2012) used thermal imaging and injections of heated-salted water as an artificial tracer method to experimentally characterise the spatial distribution of flow paths and to assess solute transport properties in shallow water in a constructed wetland. They found that, at relatively small temporal and spatial scales, heated water can be regarded as a conservative tracer with similar behaviour to salt tracer, and it allows the quantitative determination of transport parameters such as flow velocity and hydrodynamic dispersion. Comparing salt and thermal tracer techniques, ABRANTES et al. (2018a) observed that, for a small measuring section, the transport of heat and solute was similar and differences between the two tracers were insignificant. The

studies by ABRANTES et al. (2018a) and SCHUETZ et al. (2012) show that differences between the salt and thermal tracers' conservative properties are of the same magnitude as method errors (e.g. different response times of the equipment , different measurement temporal frequency of the equipment, differences between initial tracer temperature and concentration).

Numerical studies of solute and heat transport in saturated porous media (i.e. groundwater flow) were performed by e.g. de MARSILY (1986), RAU et al. (2012) and VANDENBOHEDE et al. (2009). Here, the same advection-dispersion transport model was used for both solute and heat transport. Differences between solute and heat transport are simulated by the hydrodynamic and thermal dispersion coefficients that represent both advective and diffusive transport mechanisms. In these situations (i.e. groundwater flow in porous media) the similarity between heat and solute transport is an approximation that may lack some precision because mass diffusion is orders of magnitude greater in water than in minerals, whereas thermal diffusion is comparable in the two media. However, in the present study, a single medium is considered (i.e. surface shallow flowing water) and therefore differences between media are not important. Furthermore, in such shallow flowing water with high flow rates, solute and heat transport processes are advection dominated (i.e. the effect of the mechanical advection greatly exceeds that of the molecular diffusion), and hydrodynamic and thermal dispersivity coefficients due to advection are considered to be approximately equal.

For the purpose of this study, the analytical solution of the differential advection-dispersion transport equation in shallow flows was fitted both to electrical conductivity data obtained with an electrical conductivity sensor (salt tracer technique) and to temperature data obtained with an infrared video camera (thermal tracer technique). The tracer techniques were applied simultaneously by injecting a double tracer of salted-heated water into different shallow flows simulated in a laboratory hydraulic flume. Simulated flows combined different bed surfaces (smooth acrylic sheet, rough sand board and synthetic grass carpet), flow discharges (from 47 to 1239 ml s^{-1}) and bed slopes (0.8, 4.4 and 13.2%), resulting in a wide range of hydraulic conditions. Velocities determined with the abovementioned methodology were compared with those estimated from measuring the tracers' leading edge and centroid and with mean flow velocity calculated using discharge/depth measurements.

With this adapted methodology the authors seek to combine the advantages of the thermal tracers shown in ABRANTES et al. (2018a), DE LIMA and ABRANTES (2014b), DE LIMA et al. (2015b), SCHUETZ et al. (2012) and TAURO and GRIMALDI (2017) with the advantages of the numerical methodology proposed in LEI et al. (2005).

10.3. Methodology

10.3.1. Solute and heat transport model

The transport of a solute or heat in flowing water is a complicated process that occurs under the influence of both advection and diffusion. It can be defined in general terms by a one-dimensional (1D) differential advection-dispersion transport equation, assuming steady flow (i.e. constant flow velocity and discharge), as follows:

$$\frac{\partial G}{\partial t} = \frac{\partial}{\partial x}\left(D\frac{\partial G}{\partial x} \right) - U\frac{\partial G}{\partial x} \tag{10.1}$$

where G represents either the solute concentration (C in kg m^{-3}, proportional to the electrical conductivity, EC in µS cm^{-1}) governed by the Fick's law of solute transport or the tracer temperature (T in ºC) governed by Fourier's law of heat transport, D represents either the hydrodynamic dispersion coefficient (D_H in m^2 s^{-1}) or the thermal dispersion coefficient (D_T in m^2 s^{-1}), U is the flow velocity (in m s^{-1}) and represents the movement of the heat or solute with the flow, x is the distance to the solute injection point in the flow direction (in m) and t is time from the instant of solute injection (in s).

10.3.2. Analytical solution, initial and boundary conditions

An analytical solution to Equation 10.1 that uses the Laplace's transformation, is given in LEI et al. (2005). In general terms:

$$G(x,t) = G_0 \frac{x}{2t\sqrt{\pi D \times t}} \exp\left(\frac{U \times x}{2D} \right) \exp\left(-\frac{U^2 t}{4D} \right) \exp\left(-\frac{x^2}{4D \times t} \right) \tag{10.2}$$

with the following initial (Equation 10.2a) and boundary (Equation 10.2b) conditions:

$$G(x,0) = 0, \quad \text{for} \quad x \geq 0 \tag{10.2a}$$

$$G(0,t) = G_0 \times \delta(t) \quad \text{and} \quad G(\infty,t) = 0, \quad \text{for} \quad t > 0 \tag{10.2b}$$

where G_0 represents either the amount of injected solute concentration (C_0 in kg s m^{-3}, proportional to the electrical conductivity, EC_0 in µS s cm^{-1}) or the amount of injected tracer temperature (T_0 in ºC s) and δ(t) is a generalized function that represents the tracer injection in time (in s^{-1}).

This analytical solution assumes that the tracer injection at the upper boundary occurs in a unit pulse input. In reality, a unit pulse input is never achievable. However, if a very short time for tracer injection at a constant rate is assumed (Equation 10.2c), this analytical solution produces satisfactory results (LEI et al., 2005).

$$\delta(t) = \frac{1}{t_i} \tag{10.2c}$$

where t_i is the time for tracer injection (in s^{-1}).

If conservation of the tracers in the flowing water is assumed, G_0 can be calculated as the integral area of the measured electrical conductivity or temperature curves with time (Equation 10.3). However, since both tracers are not fully conservative, this is only an approximation of the real value of G_0.

$$G_0 = \int_0^{\infty} G(x,t)\ dt \tag{10.3}$$

Therefore, in this generalised analytical solution, two parameters need to be determined to describe the transport of a solute or heat in the flow, i.e. D_H and U in the case of solute transport and D_T and U in the case of heat transport. They can be determined by fitting the analytical solution to solute or heat transport data obtained experimentally. For this purpose, solute transport data obtained with an electrical conductivity sensor and temperature data obtained with an infrared video camera from combined salt and thermal tracer experiments, described in ABRANTES et al. (2018a), were used.

10.4. Experimental methodology

10.4.1. Setup and simulated flows

The 3.00 m long by 0.15 m wide hydraulic flume (Figure 10.1) was used to simulate flows in this study. The flume uses a water recirculation circuit with a 500 L reservoir, a pump and a flow control valve. The setup allows the manual adjustment of the bed slope. The flume has free inflow and outflow and so flow velocity and depth are controlled by the flow discharge, bed slope and bed surface roughness.

A total of 23 different flow conditions (velocities) were simulated, involving three bed surfaces (smooth acrylic sheet, rough sand board and synthetic grass carpet), three bed slopes (0.8, 4.4 and 13.2%) and different flow discharges (between 47-1239 ml s^{-1}), as summarised in Table 10.1. Smooth acrylic simulations were performed on the bed's smooth acrylic sheet. For the rough sand simulations, < 1.2 mm sieved sand particles were glued to an acrylic board that was fixed to the flume bed. For the synthetic grass simulations, an 8.5 mm thick synthetic grass carpet was fixed to the flume bed. Photographs, from above, of the three bed surfaces used in the experiments are shown in Figure 10.2.

For each simulated flow, flow depth was measured using a point gauge (Figure 10.1a) and flow discharge was measured at the flume outlet by the volumetric method.

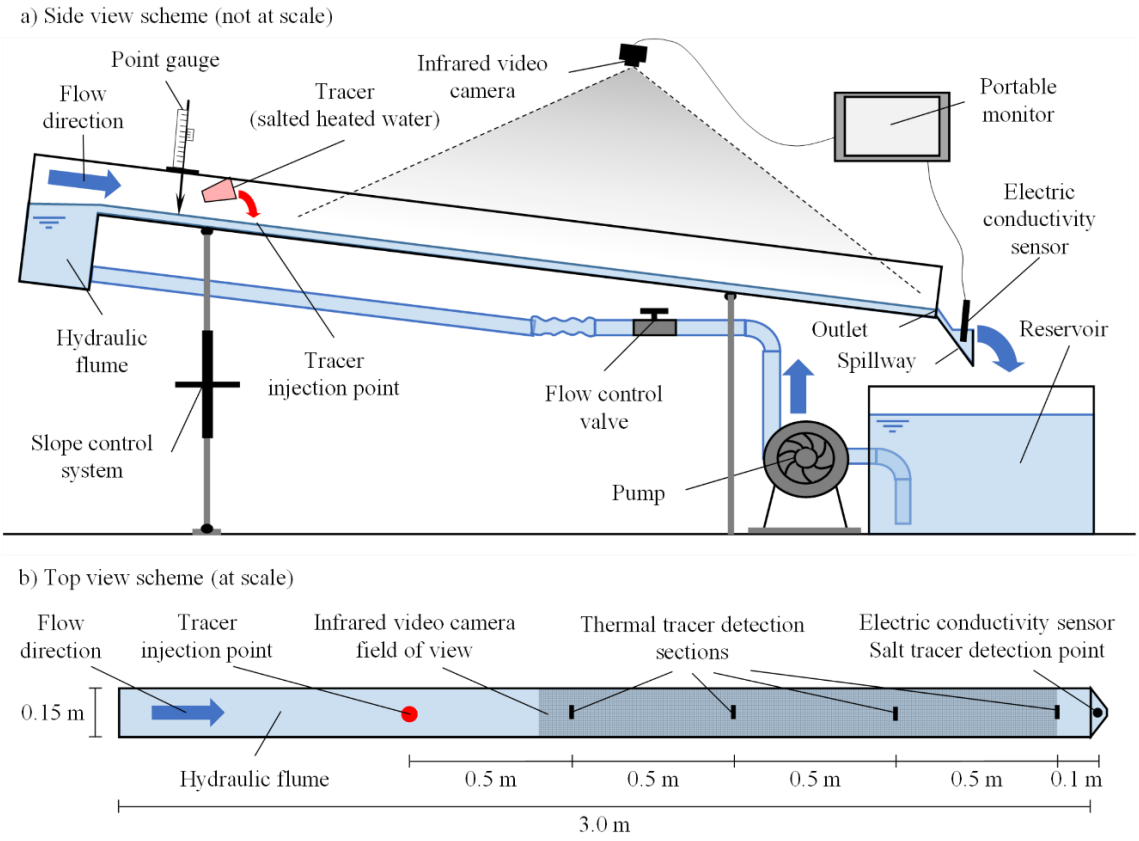

Figure 10.1. Schematic representation of the laboratory setup used in the experiments: a) Side view (not to scale); b) View from above (to scale).

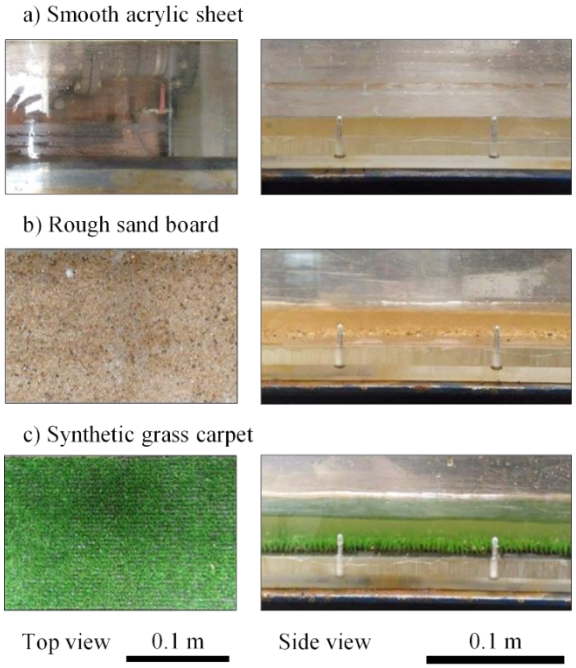

Figure 10.2. Photographs of the three bed surfaces used in the experiments: a) Smooth acrylic sheet; b) Rough sand board; and c) Synthetic grass carpet. View from above, without flowing water (left) and side view with flowing water (right).

Table 10.1. Simulated flows.

	Flow simulation	S (%)	Q (10^{-6} m^3 s^{-1})	h (10^{-3} m)	U_M (m s^{-1})
Smooth acrylic sheet	Acrylic_1	0.8	650	9.12	0.475
	Acrylic_2	0.8	856	11.06	0.516
	Acrylic_3	0.8	1158	13.31	0.580
	Acrylic_4	4.4	420	5.29	0.529
	Acrylic_5	4.4	696	7.45	0.623
	Acrylic_6	13.2	71	1.37	0.345
	Acrylic_7	13.2	164	1.77	0.619
	Acrylic_8	13.2	450	3.5	0.851
Rough sand board	Sand_1	0.8	47	8.95	0.035
	Sand_2	0.8	81	7.71	0.070
	Sand_3	0.8	210	17.72	0.079
	Sand_4	4.4	72	14.55	0.033
	Sand_5	4.4	259	9.70	0.178
	Sand_6	4.4	884	15.89	0.371
Synthetic grass carpet	Grass_1	0.8	94	25.07	0.025
	Grass_2	0.8	438	36.50	0.080
	Grass_3	0.8	1067	45.60	0.156
	Grass_4	4.4	75	n.a.m.	n.a.m.
	Grass_5	4.4	549	17.68	0.207
	Grass_6	4.4	1103	17.63	0.417
	Grass_7	13.2	52	n.a.m.	n.a.m.
	Grass_8	13.2	202	11.41	0.118
	Grass_9	13.2	1239	17.92	0.461

S for slope; Q for discharge; h for flow depth; U_M for mean flow velocity from discharge/depth measurements; n.a.m. for not able to measure.

10.4.2. Tracer techniques

Flow velocity was measured using salt and thermal tracer techniques. The two techniques were tested simultaneously in a double tracer consisting of salted-heated water (Figure 10.1a). This was made by adding common table salt to tap water, in a ratio of 5 g of salt per litre of water (corresponding to an electrical conductivity of approximately 9000 µS cm^{-1}), and heating this solution in an electrical kettle to a temperature well above the average flow water temperature (71.3 ± 5.2 ºC immediately before injecting the tracer into the flow). A volume of 10 ml of tracer per 100 ml s-1 of flow discharge was used in each flow velocity measurement. Salt concentration, temperature and volume of tracer were established in preliminary tests and shown to be appropriate, enabling the tracer to be detected in the flow by the two techniques. Any differences in density and viscosity between flow and tracer due to differences in salt concentration and temperature should be minimal and should not have a significant influence on the transport of the tracer in the flow. The tracer was injected manually into the flow in a quick movement, 2.1 m upslope of the channel outlet (Figure 10.1b).

The movement of the tracer in the flow was detected with (Figure 10.1): i) A CON-BTA conductivity sensor (from Vernier Software & Technology LLC, USA), with a temporal resolution of 0.2 s, an accuracy of ±3%, at the mid-range of 0-2000 µS cm^{-1}; and ii) An Optris PI-160 infrared video camera (from Optris GmbH, Germany), with a temporal resolution of 0.01 s, a thermal

resolution of 0.1 °C, an accuracy of ±2%, at the spectral range of 7.5–13.0 μm. The conductivity sensor was placed in a spillway immediately in front of the channel outlet (Figure 10.1a). The infrared camera was fixed to a metal structure 4 m above the flume, with the field of view (23° × 17°) covering 1.60 m of the flume length and the entire width of 0.15 m, providing thermal imaging of 156 × 13 pixels (Figure 10.1b).

The tracer techniques were applied three times for each simulated flow.

10.4.3. Data analyses

Flow velocity was estimated following three different automatic methodologies, as schematised in Figure 10.3: i) Velocities from the leading edge of the tracers (U_{LE}); ii) Velocities from the centroid of the tracers (U_C); and iii) Velocities from fitting the analytical solution of solute transport to data obtained from the tracers (U_{AS}). Estimated velocities from the three methodologies and two tracers were compared to mean flow velocity calculated using discharge/depth measurements, according to Equation 10.4:

$$U_M = \frac{Q}{hw} \tag{10.4}$$

where U_M is the mean flow velocity (m s^{-1}), Q is the flow discharge (m^3 s^{-1}), h is the flow depth (m) and w is the width of the hydraulic flume (m).

Hydraulic parameters for the different simulated flows are shown in Table 10.1.

Electrical conductivity and temperature data obtained with the tracer techniques were transformed in order to properly estimate flow velocities automatically. Firstly, threshold values of electrical conductivity and temperature were established to distinguish values associated with the tracer from values associated with the background flow. These threshold values corresponded to the maximum electrical conductivity and temperature measured in the 5 s before the injection of the tracer (EC_{MAX} and T_{MAX}), as schematised in Figure 10.3a. A maximum value instead of a mean value was chosen as a threshold value to be more certain that only values associated with the tracer were identified automatically. These threshold values were subtracted from the corresponding electrical conductivity and temperature measured during the passage of tracer (Figure 10.3b) and negative values were set to 0. Secondly, since absolute values of electrical conductivity and temperature were not important to estimate the flow velocity, they were normalised in order to compare the curves of solute and heat transport. This was done by dividing the electrical conductivity and temperature values by the respective concentration or temperature injected at the upper boundary. In the generalised form:

$$NG(x,t) = \frac{G(x,t)}{G(0,t)} = ti \times \frac{G(x,t)}{G_0} \tag{10.5a}$$

where NG represents either the dimensionless normalised values of solute concentration (NC, proportional to the electrical conductivity, NEC) or the dimensionless normalised values of tracer temperature (NT).

Since the tracer was injected manually into the flow in a quick movement in a very short time (i.e. approximated to a unit pulse input), the time for tracer injection (ti) was practically impossible to measure or estimate. Therefore, the normalised values were expressed as a ratio of the tracer injection time (Equation 10.5b), i.e. dimensionless values of electrical conductivity or temperature per second of tracer injection (NEC/t_i or NT/t_i in s^{-1}), as represented in Figure 10.3c. This normalisation assumes a consistent tracer injection time throughout the experiments.

$$\frac{NG}{t_i}(x,t) = \frac{G(x,t)}{G_0} \tag{10.5b}$$

These normalised values (Equation 10.5b) can vary between 0 and ∞ (greatly depend on the tracer injection time) and the integral area of the normalised curves with time is equal to 1.

The leading edge (U_{LE}) and centroid (U_C) velocities of the tracers were calculated automatically, following procedure schematised in Figure 10.3c. In the first case this was done by dividing the distance travelled from the injection of the tracer to the detection sections (2.1 m for the salt tracer and 0.5, 1.0, 1.5 and 2.0 m for the thermal tracer as schematised in Figure 10.2b) by the time taken from the tracer injection to the first rise (i.e. first non-zero value) in the normalised electrical conductivity and temperature (t_{LE}). In the second case, the travelled distance was divided by the time taken for the centroid of the normalised electrical conductivity and temperature graphs to arrive (t_C), calculated as follows:

$$t_C = \frac{\sum_{t=0}^{\infty}\left(\frac{NG}{t_i}(x,t)\times t\right)}{\sum_{t=0}^{\infty}\frac{NG}{t_i}(x,t)} \tag{10.6}$$

For each flow condition, velocities from fitting the analytical solution (Equation 10.2) to salt and thermal tracers' data (U_{AS}) were determined by minimising the sum of squared errors between modelled and experimentally observed data, as schematised in Figure 10.3c. The hydrodynamic dispersion coefficient (D_H) and thermal dispersion coefficient (D_T) were also determined. The performance of the numerical method was evaluated using the determination coefficient (r^2) to compare modelled and experimentally observed data. One-way analysis of variance (one-way ANOVA) with post hoc Tukey-Kramer honestly significant difference (HSD) test at levels of significance of 0.05 and 0.01 was performed as a multiple comparison of r^2 values to ascertain if the performance of the numerical methodology differed significantly between tracer techniques, bed surfaces and measuring distances to tracer injection point.

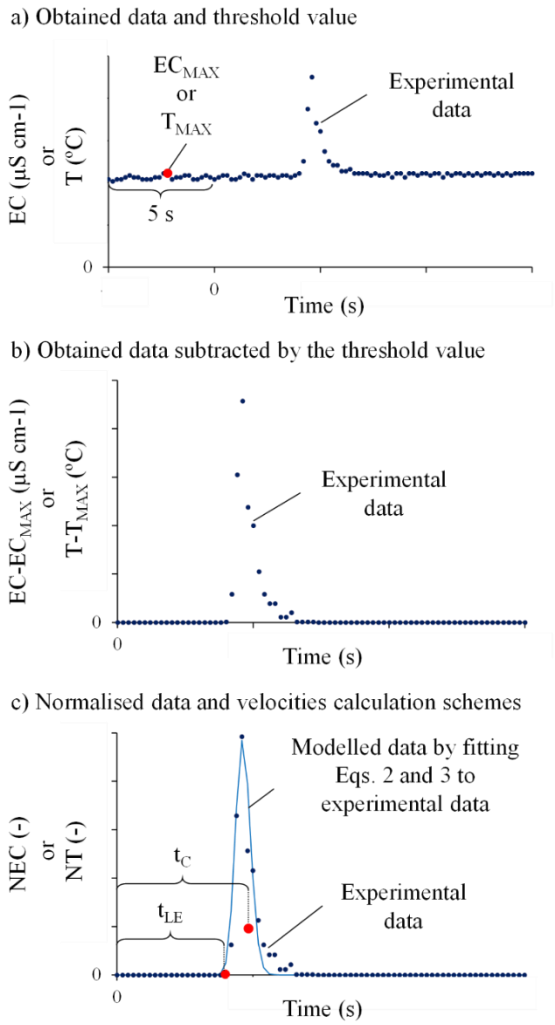

Figure 10.3. Procedure used to calculate the velocity of the salt and thermal tracers: a) Data observed experimentally from measurements with the electrical conductivity sensor or the infrared video camera and identification of the threshold value (ECMAX or TMAX); b) Observed data subtracted by the threshold value; and c) Data normalisation and identification of the time taken by the leading edge (t_{LE}) and centroid (t_C) of the tracers, as well as representation of the modelled data (solid line) fitted to the observed data (markers).

10.5. Results and discussion

Graphs of experimentally observed electrical conductivity and temperature data (markers) and the corresponding fitted analytical solute and heat transport curves (smooth solid curves) are shown in Figures 10.4 and 10.5, respectively; results of three simulated flows for the salt tracer and two simulated flows for the thermal tracer are shown. Velocity results for all bed surfaces and simulated flows, comprising a total of 23 different flow conditions, are shown in Table 10.2 (salt tracer) and Table 10.3 (thermal tracers). Salt tracer velocities (Figure 10.4 and Table 10.2) were measured 2.1 m from the tracer injection point and thermal tracer velocities were measured 0.5, 1.0, 1.5 and 2.0 m from the tracer injection point (Figure 10.5 and Table 10.3).

From Figures 10.4 and 10.5 it can be seen that, in general, the analytical solution of the solute and heat transport successfully modelled the electrical conductivity and temperature data observed in the salt and thermal tracer experiments. The modelled data simulated the peaks and the increasing and decreasing curves of the observed data well. As expected, due to diffusion effects the observed and modelled temperature peaks (Figure 10.5) decreased with increasing distance from the tracer injection point.

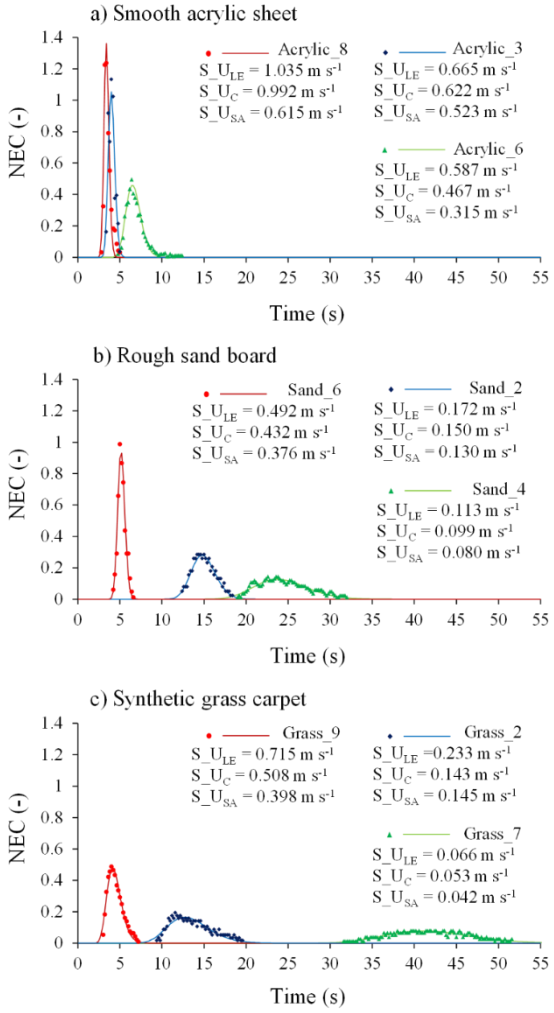

Figure 10.4. Salt tracer leading edge velocity (U_{LE}) and centroid (U_C) velocity, and velocity estimated from fitting the analytical solution of solute transport to electric conductivity data (U_{AS}) for the three bed surfaces: a) Smooth acrylic sheet; b) Rough sand board; c) Synthetic grass carpet. For each bed surface, data observed 2.1 m from the tracer injection point (markers) and the corresponding fitted modelled curves (solid lines) of three simulated flows are shown. For each simulated flow, data from one repetition is shown.

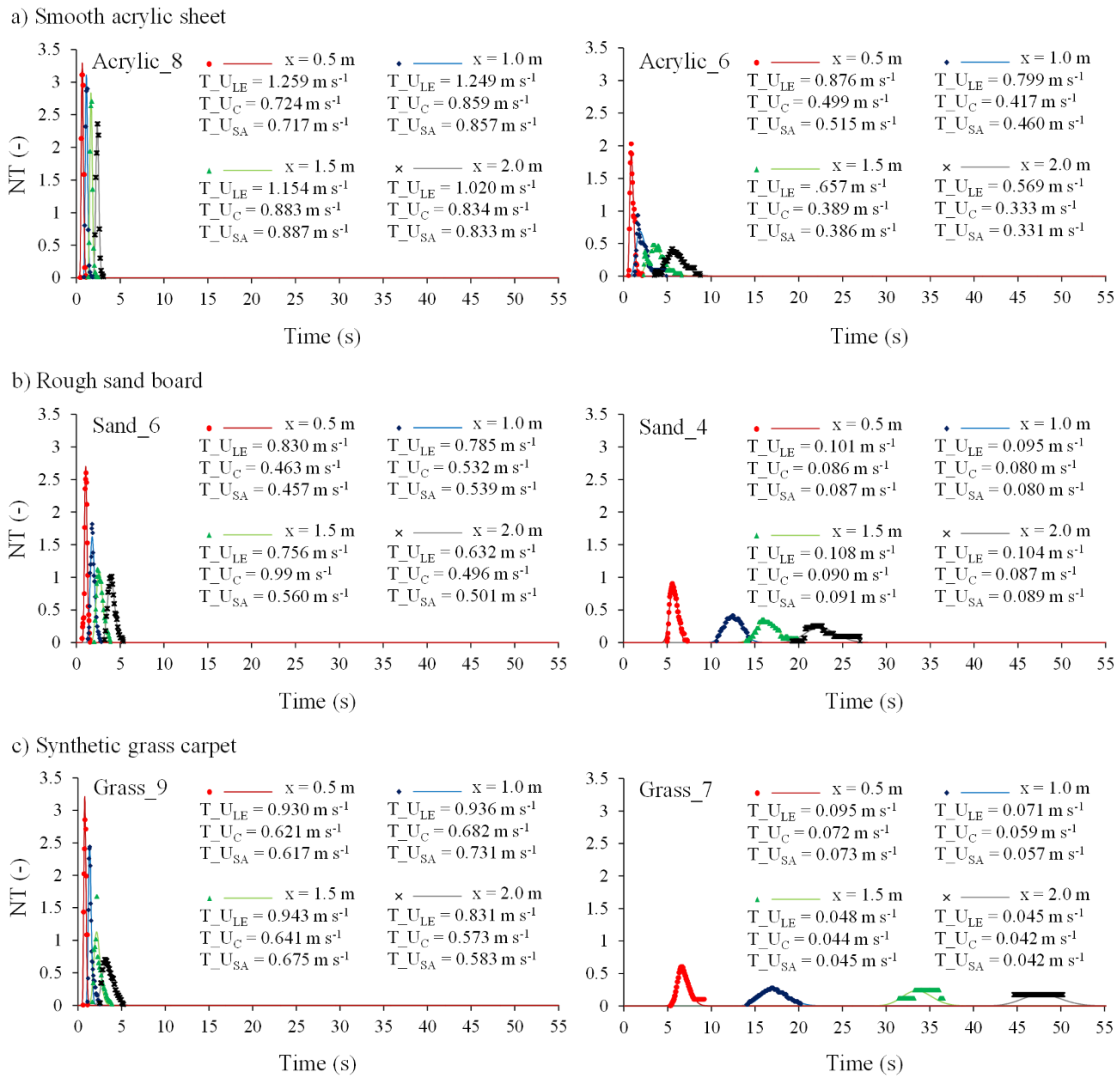

Figure 10.5. Thermal tracer leading edge (U_{LE}) and centroid (U_C) velocities, as well as velocities estimated from fitting the analytical solution of solute transport to temperature data (U_{AS}) for the three bed surfaces: a) Smooth acrylic sheet; b) Rough sand board; and c) Synthetic grass carpet. For each bed surface, data observed 0.5, 1.0, 1.5 and 2.0 m from the tracer injection point (markers) and the corresponding fitted modelled curves (solid lines) of two simulated flows are shown. For each simulated flow, data from one repetition is shown.

Determination coefficients (r^2) comparing modelled and experimentally observed data are shown in Figure 10.6; thermal tracer results correspond to temperature measurements at 0.5, 1.0, 1.5 and 2.0 m from the tracer injection point and salt tracer results correspond to electrical conductivity measurements at 2.1 m from the tracer injection point. For all simulated flows, on average, r^2 values higher than 0.85 were obtained. Generally, the solute transport model better represented the electrical conductivity data observed with the salt tracer than the temperature data observed with the thermal tracer. Also, the r^2 of the temperature data decreased with increasing distance from the tracer injection point. In previous studies of solute transport data (LEI et al., 2005, 2010, 2013; SHI et al., 2012) no clear relation has been observed between the model performance and the distance from the tracer injection point. As stated before, thermal tracers have been shown to be less

conservative than salt tracers (ABRANTES et al., 2018a; SCHUETZ et al., 2012), and therefore it is expected a lower performance of the heat transport model than the solute transport model. In any case, differences in the model performance between both tracer techniques and between different distances from the tracer injection point were never significant.

Table 10.2. Salt tracer velocities measured 2.1 m from the tracer injection point. Values are average of three repetitions.

	Salt tracer velocities (m s^{-1})		
Flow simulation	U_{LE}	U_C	U_{AS}
Acrylic_1	0.596	0.540	0.453
Acrylic_2	0.639	0.547	0.481
Acrylic_3	0.637	0.597	0.506
Acrylic_4	0.595	0.552	0.461
Acrylic_5	0.717	0.649	0.534
Acrylic_6	0.591	0.460	0.310
Acrylic_7	0.725	0.573	0.401
Acrylic_8	0.901	0.945	0.567
Sand_1	0.080	0.106	0.090
Sand_2	0.138	0.108	0.129
Sand_3	0.156	0.143	0.087
Sand_4	0.122	0.095	0.078
Sand_5	0.317	0.252	0.213
Sand_6	0.538	0.441	0.381
Grass_1	0.109	0.052	0.043
Grass_2	0.225	0.151	0.144
Grass_3	0.307	0.194	0.214
Grass_4	0.072	0.058	0.045
Grass_5	0.472	0.284	0.248
Grass_6	0.564	0.371	0.334
Grass_7	0.062	0.055	0.043
Grass_8	0.210	0.147	0.118
Grass_9	0.752	0.545	0.425

U_{LE} and U_C for salt tracer leading edge and centroid velocities; U_{AS} for velocities estimated from fitting the analytical solution of solute transport to electrical conductivity data.

The performance of the solute and heat transport models was not influenced by the flow velocity or bed slope; no clear relation was observed between them, as shown in previous studies for solute transport in LEI et al. (2005, 2010, 2013), RAHMA et al. (2013) and SHI et al. (2012). However, for both tracers, flow simulations on the synthetic grass carpet showed lower values of r^2 than those on the smooth acrylic sheet and rough sand board. It was expected that modelling the movement of a tracer in the flow over a rough element such as the synthetic grass carpet would be a more complex task due to the higher flow disturbances, higher diffusion, and higher exchanges of tracer between the flow and the rough element. In any case, differences in the model performance between the different simulated flows, bed surfaces and distances from the tracer injection point were never significant. While this was reported before in RAHMA et al. (2013) for the electrical conductivity data (salt tracer), it was a novelty for the temperature data (thermal tracer).

Table 10.3. Thermal tracer velocities measured 0.5, 1.0, 1.5 and 2.0 m from the tracer injection point. Values are average of three repetitions.

Flow simulation	Thermal tracer velocities (m s^{-1})											
	U_{LE}				U_C				U_{AS}			
	x (m)											
	0.5	1.0	1.5	2.0	0.5	1.0	1.5	2.0	0.5	1.0	1.5	2.0
Acrylic_1	0.763	0.707	0.635	0.601	0.660	0.617	0.596	0.595	0.453	0.456	0.387	0.414
Acrylic_2	0.787	0.813	0.762	0.695	0.544	0.714	0.698	0.670	0.429	0.443	0.489	0.456
Acrylic_3	0.843	0.867	0.839	0.754	0.760	0.763	0.757	0.756	0.489	0.577	0.588	0.554
Acrylic_4	0.846	0.803	0.695	0.638	0.604	0.647	0.642	0.625	0.524	0.419	0.387	0.418
Acrylic_5	0.948	0.983	0.931	0.819	0.750	0.793	0.759	0.774	0.555	0.683	0.546	0.523
Acrylic_6	0.872	0.795	0.654	0.566	0.507	0.599	0.372	0.370	0.415	0.372	0.311	0.326
Acrylic_7	1.214	1.177	1.001	0.769	0.912	0.721	0.753	0.669	0.647	0.668	0.502	0.398
Acrylic_8	1.265	1.256	1.160	1.025	0.937	0.827	0.843	0.924	0.581	0.731	0.806	0.700
Sand_1	0.125	0.125	0.119	0.091	0.06	0.079	0.079	0.079	0.079	0.079	0.077	0.056
Sand_2	0.138	0.132	0.122	0.115	0.099	0.117	0.115	0.118	0.100	0.097	0.094	0.089
Sand_3	0.304	0.203	0.181	0.170	0.334	0.259	0.208	0.162	0.162	0.114	0.093	0.104
Sand_4	0.101	0.094	0.107	0.104	0.115	0.11	0.105	0.100	0.083	0.076	0.087	0.084
Sand_5	0.576	0.463	0.420	0.328	0.431	0.308	0.295	0.263	0.334	0.272	0.245	0.184
Sand_6	0.830	0.785	0.756	0.632	0.598	0.568	0.567	0.519	0.487	0.459	0.455	0.470
Grass_1	0.128	0.111	0.091	0.083	0.048	0.061	0.074	0.087	0.078	0.066	0.057	0.052
Grass_2	0.418	0.267	0.229	0.190	0.231	0.175	0.198	0.177	0.268	0.186	0.184	0.120
Grass_3	0.379	0.372	0.357	0.334	0.319	0.336	0.283	0.293	0.272	0.266	0.257	0.229
Grass_4	0.092	0.060	0.044	0.043	0.057	0.038	0.030	0.048	0.051	0.034	0.025	0.023
Grass_5	0.682	0.571	0.486	0.427	0.477	0.292	0.323	0.305	0.429	0.350	0.288	0.253
Grass_6	0.690	0.698	0.694	0.681	0.861	0.522	0.516	0.519	0.515	0.529	0.522	0.487
Grass_7	0.094	0.071	0.047	0.045	0.061	0.051	0.036	0.035	0.069	0.054	0.039	0.038
Grass_8	0.288	0.228	0.140	0.173	0.154	0.111	0.109	0.144	0.180	0.132	0.090	0.110
Grass_9	0.923	0.929	0.936	0.825	0.845	0.744	0.503	0.688	0.539	0.631	0.586	0.508

U_{LE} and U_C for thermal tracer leading edge and centroid velocities; U_{AS} for velocities estimated from fitting the analytical solution of solute transport to temperature data; x distance from tracer injection point.

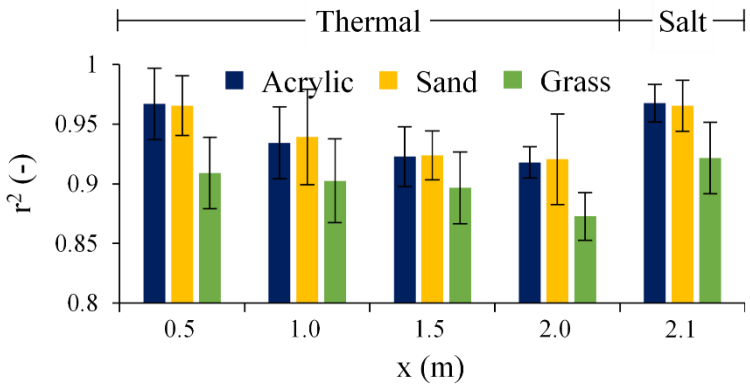

Figure 10.6. Determination coefficient (r^2) comparing modelled and experimentally observed data. Temperature data from thermal tracer measurements at 0.5, 1.0, 1.5 and 2.0 m from the tracer injection point and electrical conductivity data from salt tracer measurements at 2.1 m from the tracer injection point.

Ratios between the mean flow velocity (U_M) calculated from discharge/depth measurements and the leading edge (U_{LE}), centroid (U_C) and analytical solution (U_{AS}) velocities for both tracers are shown in Figure 10.7; thermal tracer results correspond to temperature measurements at 0.5, 1.0, 1.5 and 2.0 m from the tracer injection point and salt tracer results correspond to electrical conductivity measurements at 2.1 m from the tracer injection point.

For both tracers, the leading edge (Figure 10.7a) and centroid (Figure 10.7b) velocities were higher than mean flow velocity, with ratios lower than 1, as observed in ABRANTES et al. (2018a). The leading edge had the higher velocity values, and therefore lower ratios, varying between 0.23-0.94 for the salt tracer and between 0.30-0.83 for the thermal tracer (for measurements at 2.0 m from the tracer injection point), with average values of 0.62 and 0.60, respectively. As stated before, the leading edge is regarded as the surface flow velocity, which corresponds to the maximum (or near maximum) value of the flow velocity profile. These values are in accordance with Horton's theoretical value of 0.67 (HORTON et al., 1934) and with the range of approximately 0.2-0.9 found in the previous studies of DUNKERLEY (2001), EMMETT (1970), LI and ABRAHAMS (1997), LI et al. (1996), PLANCHON et al. (2005) and ZHANG et al. (2010). The centroid velocity, meanwhile, is regarded as the theoretical mean value of the flow velocity profile, if conservation of the tracer in the flow is assumed. However, since none of the tracers exhibited absolute conservation during the experiments, centroid velocities were higher than mean flow velocity. For the centroid velocities the corresponding ratios were 0.33-1.13 for the salt tracer and 0.33-0.93 for the thermal tracer, with average values of 0.77 and 0.68, respectively. The lower value of 0.33 came below the range of 0.7-0.9 observed by LI et al. (1996) and 0.6-1.0 observed by PLANCHON et al. (2005).

Velocities from fitting the analytical solutions of solute and heat transport to data obtained from both tracers (U_{AS}) gave the highest ratios (Figure 10.7c), with values ranging between 0.39-1.54 for the salt tracer and between 0.39-1.55 for the thermal tracer (for measurements at 2.0 m from the tracer injection point), with average values of 0.95 and 0.92, respectively. Therefore, on average,

velocities from the numerical methods, were the ones that better predicted the mean flow velocity calculated from discharge/depth measurements.

It should be noted that the ratios between the mean flow velocity and tracer velocities are the result of a very complex relationship between the shape of the flow velocity profile and the flow characteristics (e.g. velocity, depth, Reynolds number, Froude number) and the bed surface characteristics (e.g. roughness, slope), as shown in ABRANTES et al. (2018a), DUNKERLEY (2001), EMMETT (1970), LI and ABRAHAMS (1997), LI et al. (1996), PLANCHON et al. (2005) and ZHANG et al. (2010). In the present study, a strong positive correlation was found between these ratios and the flow regime. An increase in Reynolds and Froude numbers increases flow turbulence and flow speed, which results in a better mixing of the flow, and a less steep velocity profile, approaching the flow velocity profile mean and maximum values. Therefore, ratios between the mean flow velocity and tracer velocities closer to 1. In general, these ratios varied directly with flow velocity and slope and varied inversely with flow depth and bed roughness. In Figure 10.7, perceptible differences can be seen between the smooth acrylic sheet, the rough sand board and the synthetic grass carpet, with the two latter presenting lower values. Flow velocity estimation from tracers involves a large amount of uncertainty and caution is required when using these measurements. A more detailed analysis on the results of these tracer experiments and on the variation of these ratios with the flow and bed surface characteristics can be seen in ABRANTES et al. (2018a).

Thermal tracer velocities decreased with increasing distance from the tracer injection point, as can be seen by the higher values in Figure 10.7. This effect was observed in ABRANTES et al. (2018a) for the leading edge (Figure 10.7a) and centroid (Figure 10.7b) velocities and it can be related to two aspects. On the one hand, higher velocities closer to the tracer injection point can be caused by the disturbance of the tracer injection itself, even with the minimum distance of 0.5 m from the tracer injection point. On the other hand, the non-conservative aspect of the thermal tracer results in a decrease of tracer temperature as the distance from the tracer addition point increases, and therefore the tracer temperature slowly dissipates in the background water temperature. This effect had more impact on the leading edge than on the centroid because temperature dissipation occurs first in the interface between the tracer and the flow. At a lesser extent, the thermal analytical solution velocities (U_{AS}) also decreased with increasing distance to the tracer injection point (Figure 10.7c). On the contrary, in LEI et al. (2005, 2010, 2013), RAHMA et al. (2013) and SHI et al. (2012) a slight increase of the numerically determined velocities with increasing distance from the tracer injection point was observed with salt tracer measurements. In these studies, the flow was considered to still be accelerating as it passed through the measuring points. However, the main difference is that salt tracer measurements were conducted. As stated before, salt tracer was found to be more conservative than thermal tracer and the transport of salt has shown higher stability with increasing distance from the tracer injection point than the heat transport. Therefore, the accuracy of the flow velocity measurements seem to depend more on the volume and temperature of the thermal tracer (i.e. lower conservation may require a higher volume and/or temperature of the

thermal tracer) than on the volume and concentration of the salt tracer (i.e. higher conservation may require a lower volume and/or concentration of the salt tracer).

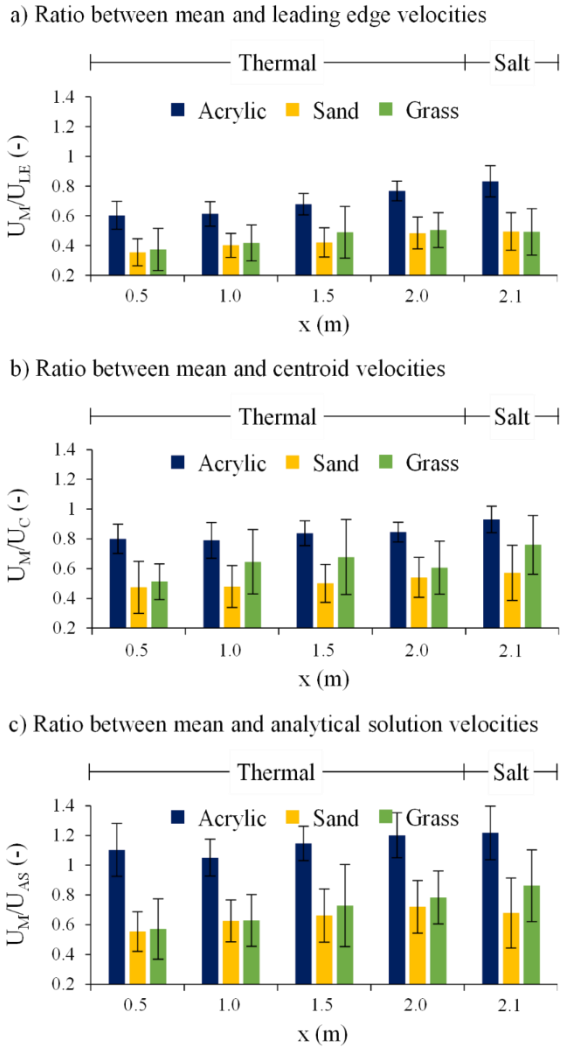

Figure 10.7. Ratio between mean flow velocity (U_M) calculated from discharge/depth measurements and: a) Leading edge velocity (U_{LE}); b) Centroid velocity (U_C); and c) Velocity from fitting the analytical solution of solute transport to observed data (U_{AS}). Data from thermal tracer measurements at 0.5, 1.0, 1.5 and 2.0 m from the tracer injection point and salt tracer measurements at 2.1 m from the tracer injection point.

Comparison between salt and thermal tracer velocities and between hydrodynamic and thermal dispersion coefficients is shown in Figure 10.8; results of temperature measurements at 2.0 m from the tracer injection point are shown to make comparison possible with electrical conductivity measurements at 2.1 m from the tracer injection point. The thermal and salt tracer techniques yielded very similar results with a good correlation with one another (r^2 values higher than 0.94 in Figure 10.8a). Generally, the thermal tracer resulted in slightly higher velocities than the salt tracer, with differences increasing with the flow velocity. Even so, differences between both tracers were never significant. A similar relationship between salt and thermal tracer techniques was noted in ABRANTES et al. (2018a) and SCHUETZ et al. (2012). Differences between the thermal and salt

tracing were very similar for the three tracer velocities (i.e. leading edge, centroid and analytical solution), as can be seen by the linear regressions in Figure 10.8a. In turn, differences between tracer techniques varied with the bed surface. On average, for the smooth acrylic sheet simulations the thermal tracer leading edge, centroid and analytical solution velocities were 8, 11 and 2% higher, respectively. For the rough sand board, the thermal tracer yielded 2 and 4% higher leading edge and centroid velocities, but 5% lower analytical solution velocities. For the synthetic grass carpet, the thermal tracer leading edge velocities were 11% lower, but the centroid and analytical solution velocities were 17 and 1% higher.

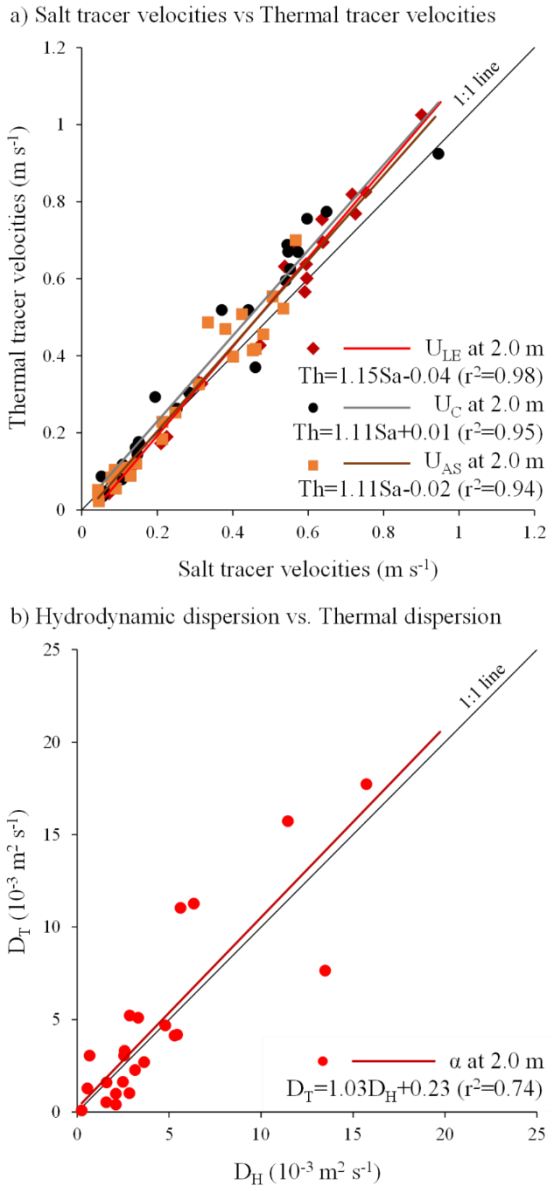

Figure 10.8. Comparison between salt and thermal tracer results: a) Leading edge (U_{LE}), centroid (U_C) and analytical solution (U_{AS}) velocities; and b) Hydrodynamic dispersion (D_H) against thermal dispersion (D_T). Salt and thermal tracer results from measurements taken 2.1 and 2.0 m, respectively, from the tracer injection point.

The correlation between hydrodynamic and thermal dispersion coefficients was not as marked as that between the tracers' velocities, as can be seen from the r^2 value of 0.74 in Figure 10.8b. On average, the thermal dispersion was higher than the hydrodynamic dispersion. This difference between dispersion coefficients can be explained. Both dispersion coefficients contain a component of pure diffusion (i.e. mass diffusion for solute transport and thermal diffusion for heat transport) and a component of advection (i.e. hydrodynamic dispersivity for solute transport and thermal dispersivity for heat transport). In the previous studies of de MARSILY (1986), RAU et al. (2012) and VANDENBOHEDE et al. (2009) it is suggested that while usually the hydrodynamic and thermal dispersivity coefficients are approximately equal, the thermal diffusion coefficient can be up to orders of magnitude greater than the mass diffusion coefficient. Therefore, the thermal dispersion coefficient can be approximately equal up to orders of magnitude greater than the hydrodynamic dispersion coefficient. This difference depends on the type of flow. For advection dominated flows, such as the shallow flows simulated in this study with high flow rates, the effect of the mechanical advection greatly exceeds that of the molecular diffusion and the effect of pure mass and thermal diffusion is minimal. Therefore, thermal dispersion was only 17% higher than hydrodynamic dispersion. As a comparison, in the study of de MARSILY (1986) of solute and heat transport by diffusion dominated flows in porous media, thermal dispersion coefficients up to approximately 500 times greater than hydrodynamic dispersion coefficients were observed. The higher thermal diffusivity ultimately explains the lower conservation of the thermal tracer than the salt tracer, as observed in ABRANTES et al. (2018a) and SCHUETZ et al. (2012).

10.6. Conclusions

A numerical methodology to estimate shallow flow velocity combining temperature data from thermal tracer measurements and an advection-dispersion heat transport model was tested. This methodology was compared to an identical methodology combining an advection-dispersion solute transport model with electrical conductivity data from salt tracer measurements. It can be concluded the proposed methodology can be used to estimate shallow flow velocity. The analytical solution of heat transport fitted the experimentally measured temperature data well under different shallow flow conditions, i.e. different flow discharges, bed slopes, bed surfaces. In fact, results from the numerical methodology predicted the mean flow velocity calculated from discharge/depth measurements better than other more traditional and well-established methodologies, such as measuring the leading edge and centroid of the tracer.

Differences were observed between salt and thermal tracer velocities and between hydrodynamic and thermal dispersion coefficients. These differences result from the lower conservative aspect of the thermal tracer than the salt tracer, which ultimately can be explained by the higher thermal diffusion than the mass diffusion. This results in thermal tracer velocities less accurate and less stable than the salt tracer velocities. However, it should be noted that for this study's shallow flows

and small measuring section, differences between both tracers were never significant. Also, some of these differences can also be explained due to some method errors, such as errors that occur due to differences in the response times and in the measurement temporal frequency between the infrared camera (thermal tracer) and the electrical conductivity sensor (salt tracer).

Velocity estimation from tracers in hydrologic research (e.g. soil erosion and solute transport studies) involves a large amount of uncertainty and caution is required when using these measurements, especially in the field. Tracking the movement of a thermal tracer in flowing water using an infrared camera has the advantage of measuring space-averaged flow velocity, which can greatly vary in space and time. For salt tracers this can only be achieved by installing multiple sensors, which can ultimately cause higher disturbance to the actual flow velocity. In this sense, the tested methodology using a thermal tracer can be a useful tool in such research areas. Further studies are therefore required to investigate performance of the numerical methodology in the presence of different hydrological processes (e.g. presence of sediments in the flow). Also, to achieve the best performance of the numerical methodology, further tests should be conducted using different volumes of tracer at different temperatures.

“Soil erosion is as old as agriculture. It began when the first heavy rain struck the first furrow turned by a crude implement of tillage in the hands or prehistoric man. It has been going on ever since, wherever man's culture of the earth has bared the soil to rain and wind.”

- Hugh Hammond Bennett and Walter Clay Lowdermilk

11. TWO-DIMENSIONAL (2D) NUMERICAL MODELLING OF RAINFALL INDUCED OVERLAND FLOW, INFILTRATION AND SOIL EROSION: COMPARISON WITH LABORATORY RAINFALL-RUNOFF SIMULATIONS ON A TWO-DIRECTIONAL SLOPE SOIL FLUME

11.1. Abstract

This paper presents an original two-dimensional (2D) numerical model of soil erosion and sediment transport resulting from rainfall induced overland flow. It is a spatial and temporal dynamic model combining physical and empirical laws and comprises: i) An overland flow module that solves the two-dimensional unsteady water flow equations on an infiltrating surface; ii) A soil infiltration module that uses a combined Horton-SCS scheme; and iii) A soil erosion and sediment transport module that solves the two-dimensional sediment transport equation, distinguishing between rill erosion, interrill erosion and sediment deposition.

The performance of the model was evaluated by comparing its results with observed data from laboratory rainfall-runoff experiments on a two-directional 2×2 m^2 soil flume set at 1% and 10% slopes in the x- and y-directions, respectively. The x-direction produced remarkably lower runoff and transported sediments than the y-direction. The numerical model significantly underestimated x-direction lower values of runoff and transported sediments. However, in the y-direction the model presented very good performance. Overall, in total terms (x- plus y-direction), the numerically simulated graphs of runoff and sediment transport were in very good agreement with corresponding experimental measurements, demonstrating the laboratory proof-of-concept of the model.

Keywords

Two-dimensional modelling; Overland flow; Soil erosion; Horton-SCS infiltration; Two-directional laboratory soil flume; Rainfall simulation

11.2. Introduction

Soil erosion has been widely recognized as a serious environmental degradation problem throughout the history (MONTGOMERY, 2007). It can reduce soil fertility and productivity and increase the transport of sediment and pollutants to freshwater bodies. Accurate prediction of soil erosion is therefore essential in land and water management.

Mathematical models are cost-effective tools for improving our understanding of erosion processes and predict its effects on soil and water quality. A robust mathematical model can provide a cost-effective tool by which many scenarios can be simulated and compared in order to find the best alternative of addressing a particular problem. Consequently, a wide spectrum of soil erosion models, ranging from simple empirical formulas, such as the Universal Soil Loss Equation (USLE, WISCHMEIER and SMITH, 1978) or its revised version (RUSLE, RENARD et al., 1997), to comprehensive physically based distributed descriptions, such as the KINematic runoff and EROSion (KINEROS, WOOLHISER et al., 1990), the Water Erosion Prediction Project (WEPP, FLANAGAN and NEARING, 1995), or the EUROpean Soil Erosion Model (EUROSEM, MORGAN et al., 1998), have been proposed for the prediction of soil erosion and sediment transport (BATISTA et al., 2019; SINGH and WOOLHISER, 2002).

Physically based models are generally the most scientifically robust and flexible models and provide an understanding of the fundamental and non-stationary processes involved in the detachment, transport and deposition of sediments and provide an access to their spatial and temporal variation (NEARING, 2000). However, due to the complexity of such processes, fully physically based models have not yet become a practical tool. Their parametrisation is complex, and they are data intensive. Also, such data always carry a level of uncertainty, are expensive and time consuming and, therefore, most of the times the amount of data needed is not readily available (STROOSNIJDER, 2005).

Reduced-scale laboratory experiments using soil flumes and rainfall simulators allow observing the fundamental mechanisms in the complex hydrologic processes (i.e. overland flow generation, infiltration, erosion) under controlled conditions. They allow to investigate effect of specific factors such as slope geometry, soil conditions and rainfall characteristics and allow for a quicker and easier way to access good-quality data, such as peak discharges, sediment concentrations and time to peaks. The availability of such good-quality data provides a good chance to evaluate the performance of numerical models and improve them (ABRANTES et al., 2015, 2019; CUOMO et al., 2016; DENG et al., 2005; ISIDORO and DE LIMA, 2013; SILVEIRA et al., 2016; SINGH and DE LIMA, 2018).

This paper presents an original two-dimensional (2D) numerical model of soil erosion and sediment transport resulting from rainfall induced overland flow. It is a spatial and temporal dynamic model combining physical and empirical laws and comprises three main modules: i) An overland flow module that solves the two-dimensional unsteady water flow equations on an infiltrating surface,

using the using the explicit finite-difference method based on the MacCormack operator-splitting scheme (GARCIA and KAHAWITA, 1986; MACCORMACK, 1971; SIMÕES, 2006); ii) A soil infiltration module that uses a modified version of the empirical Horton's infiltration equation with a calibration methodology of its parameters based on formal analogies with the SCS-CN method (GABELLANI et al., 2008); and iii) A soil erosion and sediment transport module that solves the two-dimensional sediment transport equation, dividing soil erosion in rill erosion, interrill erosion and sediment deposition processes (CAO et al., 2002; DENG et al., 2008). Specific procedures were used to handle the wet/dry front and, therefore, simulations can start on an initially dry surface. The performance of the model was evaluated by comparing its results with observed data from laboratory rainfall-runoff experiments on a two-directional free-drainage square soil flume. The experiments included four consecutive 5 min rainfall events of 211 mm h^{-1} average intensity.

11.3. Governing equations

11.3.1. Overland flow and soil erosion

Overland flow was described by the two-dimensional shallow-flow equations commonly referred to as the Saint-Venant equations, which include the equation of continuity and two equations of motion for the coordinate directions x and y (ZHANG and CUNDY, 1989):

$$\frac{\partial h}{\partial t}+\frac{\partial v_x h}{\partial x}+\frac{\partial v_y h}{\partial y}=p-i \tag{11.1}$$

$$\frac{\partial v_x h}{\partial t}+\frac{\partial}{\partial x}\left(v_x{}^2 h+\frac{1}{2}gh^2\right)+\frac{\partial v_x v_y h}{\partial y}=gh\left(-\frac{\partial Z}{\partial x}-S_{fx}\right) \tag{11.2}$$

$$\frac{\partial v_y h}{\partial t}+\frac{\partial v_x v_y h}{\partial x}+\frac{\partial}{\partial y}\left(v_y{}^2 h+\frac{1}{2}gh^2\right)=gh\left(-\frac{\partial Z}{\partial y}-S_{fy}\right) \tag{11.3}$$

where h is the water depth, v_x and v_y are the depth-averaged flow velocity components in the x and y directions, respectively, p is the rainfall intensity, i is the infiltration rate, g the gravitational constant, Z is the bed elevation, t is the time and S_{fx} and S_{fy} are the friction slopes in the x and y directions, respectively and were approximated by the Manning's formula and expressed in terms of conservation variables, as:

$$S_{fx}=\frac{n^2 v_x\left(v_x{}^2+v_y{}^2\right)^{1/2}}{h^{4/3}} \quad , \quad S_{fy}=\frac{n^2 v_y\left(v_x{}^2+v_y{}^2\right)^{1/2}}{h^{4/3}} \tag{11.4}$$

, where n is the Manning's roughness coefficient. Assumptions and derivation of Equations 11.1 to 11.3 can be found in detail in ZHANG and CUNDY (1989).

Equations used for soil erosion and sediment transport resulting from rainfall induced overland flow vary significantly due to different understanding and treatments of the sediment detachment, transport and deposition mechanisms (FLANAGAN and NEARING, 1995; MORGAN et al., 1998; WOOLHISER et al., 1990). Raindrop impact and/or overland flow can detach sediments from the soil surface. A critical force needs to be exerted by either a raindrop or a flow before detachment occur. Transport of detached material can occur as the result of raindrops and flow acting singly or together. Sediment deposition occurs when the flow can no longer support the suspended sediments, usually as result of a decrease in the flow transport capacity (KINNELL, 2005).

According to these principles, soil erosion was divided into three main mechanisms: i) Interrill erosion, that reflects the detachment and transport of sediments by the action of raindrops; ii) Rill erosion, that reflects the detachment and transport of sediments by the action of overland flow; and iii) Sediment deposition, that reflects the settling down of sediments. These mechanisms were described by the following two-dimensional sediment transport equation:

$$\frac{\partial hc}{\partial t} + \frac{\partial v_x hc}{\partial x} + \frac{\partial v_y hc}{\partial y} = e_i + e_r - d \tag{11.5}$$

, where c is the overland flow mass sediment concentration and e_i and e_r are the volumetric interrill and rill erosion, respectively, and d is the sediment deposition.

The right side of Equation 11.5 represents the constant exchange of sediment particles in the vertical between the soil surface and the flow, and its terms can be expressed as follows (CAO et al., 2002; DENG et al., 2008):

$$e_i = \rho_s \frac{p^2}{\omega_s} \exp^{(-\eta h)} \tag{11.6}$$

$$e_r = \begin{cases} 0 & \text{if} \quad \theta \le \theta_c \\ \rho_s \xi (\theta - \theta_c) \dfrac{1}{h d_s^{2/10}} \sqrt{v_x^2 + v_y^2} & \text{if} \quad \theta > \theta_c \end{cases} \tag{11.7}$$

$$d = \rho_s \omega_s \alpha c (1 - \alpha c)^2 \tag{11.8}$$

, where d_s is the mean sediment particle diameter, θ_c is the dimensionless critical Shields parameter for initiation of sediment movement and θ is the dimensionless flow shear stress and can be expressed as (LIU and BELJADID, 2017):

$$\theta = \frac{n^2}{(\rho_s / \rho - 1) d_s h^{1/3}} \left(v_x^2 + v_y^2 \right) \tag{11.9}$$

, where ρ and ρ_s are the density of clear water and sediment particles, respectively. ω_s is the settling velocity of a single sediment particle in tranquil water (CHENG, 1997):

$$\omega_s = \sqrt{\left(13.95\frac{\upsilon}{d_s}\right)^2 + 1.09 g d_s \left(\frac{\rho_s}{\rho} - 1\right)} - 13.95\frac{\upsilon}{d_s} \quad (11.10)$$

, where υ is the kinematic viscosity of water.

η, ξ and α are calibration parameters to control interrill erosion, rill erosion and sediment deposition, respectively. η represents the damping rate due to the water depth, ξ controls the erosion force of the of the overland flow and α describes the difference between the bed surface sediment concentration and the overland flow sediment concentration and can be approximated as:

$$\alpha = \min\left(2, \frac{1 - p_s}{c}\right) \quad (11.11)$$

, where p_s is the soil porosity

11.3.2. Infiltration

Infiltration was computed using a modified version of the Horton's infiltration equation (HORTON, 1933) with a calibration methodology of its parameters based on formal analogies with the SCS-CN method (USDA, 2004). The result was presented in GABELLANI et al. (2008) and is a general relation between SCS-CN and modified parameters of Horton's method.

HORTON (1933) proposed an exponential decay equation to describe the variation in time of the infiltration capacity of the soil during a rainfall event as:

$$f(t) = f_\infty + (f_0 - f_\infty)e^{-kt} \quad (11.12)$$

, where f(t) is the infiltration rate at time t from the beginning of the rainfall event, f_∞ and f_0 are the final (minimum) and initial (maximum) infiltration rates, respectively, and k is the exponential time decay coefficient.

The main restrictions to the application of Horton's equation in its original form are the difficulty of considering rainfall with intensities lower than f_0, the impossibility to describe the effect of dry periods inside the rainfall event, and the difficulty of obtaining reliable estimates for its parameters. This modified version of the Horton's infiltration accounts for a relation between the infiltration capacity and soil moisture conditions for a more successful parameter calibration and accounts for intermittent and low-intensity rainfall events, namely lower than f_0.

According to this methodology, the upper soil layer is modelled as a linear reservoir with a water volume V(t) varying in time between 0 for dry soil condition and V_{max} for saturated soil condition. V(t) varies with the infiltration in the upper soil layer i(t) and the percolation to deeper soil layers $i_p(t)$, according to the following mass-balance equation:

$$\frac{\partial V}{\partial t} = i(t) - i_p(t) \quad (11.13)$$

i(t) is simultaneously regulated by the rainfall intensity p(t) and the infiltration capacity f(t), as follows:

$$i(t) = \begin{cases} p(t) & \text{if} \quad p(t) \le f(t) \\ f(t) & \text{if} \quad p(t) > f(t) \end{cases} \tag{11.14}$$

Both f(t) and $i_p(t)$ vary linearly with V(t), as follows:

$$f(t) = f_0 - (f_0 - f_\infty)\frac{V(t)}{V_{max}} \tag{11.15}$$

$$i_p(t) = f_\infty \frac{V(t)}{V_{max}} \tag{11.16}$$

For dry soil condition, i.e. V(t) = 0, f(t) and $i_p(t)$ assume the values of f_0 and 0, respectively. For saturated soil condition, i.e. V(t) = V_{max}, both are equal to f_∞.

Substituting Equations 11.14 to 11.16 in Equation 11.13 and integrating it in Δt, results in:

$$V(t_{i+1}) = \begin{cases} \frac{p(t_i)V_{max}}{f_\infty} + e^{-\frac{f_\infty}{V_{max}}\Delta t}\left(V(t_i) - \frac{p(t_i)V_{max}}{f_\infty}\right) & \text{if} \quad p(t_i) \le f(t_i) \\ V_{max}\left(1 - e^{-\frac{f_0}{V_{max}}\Delta t}\right) + V(t_i)e^{-\frac{f_0}{V_{max}}\Delta t} & \text{if} \quad p(t_i) > f(t_i) \end{cases} \tag{11.17}$$

where $V(t_{i+1})$ is V(t) at $t = t_{i+1}$ and $p(t_i)$ and $f(t_i)$ are the values of p(t) and f(t) at $t = t_i$ and are assumed to be constant between t_i and t_{i+1}.

The calibration of the parameters f_0, f∞ and V_{max} was performed based on an analytical derivation of the Horton's equation and combination with the SCS-CN method (USDA, 2004), resulting in:

$$f_0 = -\frac{V_{max}}{0.8T_P}\ln\frac{V_{max}}{P + 0.8V_{max}} \tag{11.18}$$

$$f_\infty = c_f f_0 \tag{11.19}$$

, where T_P is the duration of the rainfall event, P is the cumulated rainfall of the event and c_f is a calibration parameter varying from 0 to 1. V_{max} can be compared the maximum retention capacity (S) of the SCS-CN method, calculated as:

$$V_{max} = S = 25.4\left(\frac{1000}{CN} - 10\right) \tag{11.20}$$

, where CN is the dimensionless curve number parameter.

It should be noted that this methodology is only valid from the moment that the cumulative rainfall (P) exceeds the initial abstraction Ia, i.e. P > Ia = 0.2S. Till that moment, all rainfall is considered to infiltrate into the upper soil layer, therefore becoming water input to the water reservoir, i.e. V(t).

11.4. Numerical methods

11.4.1. MacCormack operator-splitting scheme

In this paper, the governing equations were solved using the explicit finite-difference method based on the MacCormack operator-splitting scheme (GARCIA and KAHAWITA, 1986; MACCORMACK, 1971; SIMÕES, 2006). For simplification, Equations 11.1 to 11.3 and 11.5 were further rewritten in the following vector format:

$$\frac{\partial U}{\partial t}+\frac{\partial Ex}{\partial x}+\frac{\partial Ey}{\partial y}=gh\left(\frac{\partial Zx}{\partial x}+\frac{\partial Zy}{\partial y}\right)+G \tag{11.21}$$

, in which:

$$U=\begin{bmatrix} h \\ v_x h \\ v_y h \\ hc \end{bmatrix},\quad Ex=\begin{bmatrix} v_x h \\ v_x{}^2 h+\frac{1}{2}gh^2 \\ v_x v_y h \\ v_x hc \end{bmatrix},\quad Ey=\begin{bmatrix} v_y h \\ v_x v_y h \\ v_y{}^2 h+\frac{1}{2}gh^2 \\ v_y hc \end{bmatrix},$$

$$Zx=\begin{bmatrix} 0 \\ -Z \\ 0 \\ 0 \end{bmatrix},\quad Zy=\begin{bmatrix} 0 \\ 0 \\ -Z \\ 0 \end{bmatrix},\quad G=\begin{bmatrix} p-i \\ -ghS_{fx} \\ -ghS_{fy} \\ e-d \end{bmatrix} \tag{11.22}$$

Equation 23 was divided into two separate one-dimensional problems by the operator-splitting technique as:

$$\frac{\partial U}{\partial t}+\frac{\partial Ex}{\partial x}=gh\frac{\partial Zx}{\partial x}+G\quad,\quad \frac{\partial U}{\partial t}+\frac{\partial Ey}{\partial y}=gh\frac{\partial Zy}{\partial y}+G \tag{11.23}$$

, where the solution of U at time (n+l)Δt, for the computational point (i,j), i.e. U(iΔt,jΔt,(n+l)Δt), can be obtained as follows:

$$U_{i,j}^{n+1}=Lx_1\frac{\Delta t}{2}Ly_1\frac{\Delta t}{2}Ly_2\frac{\Delta t}{2}Lx_2\frac{\Delta t}{2}U_{i,j}^{n} \tag{11.24}$$

, where Lx and Ly are one-dimensional finite-difference operators, each one composed of a predictor-corrector computational sequence. In each of the Lx and Ly operators, the solution is advanced by a time step Δt/2 as if the derivatives in the other direction were absent. Therefore, each operator is computed twice to gain the solution at the next step.

Taking Lx_1 and Ly_1 operators as example, their solution can be written as:

Lx_1 predictor sequence (backward differences):

$$U_{i,j}^{p} = U_{i,j}^{o} - \frac{\Delta t}{2\Delta x}\left(Ex_{i,j}^{o} - Ex_{i-1,j}^{o}\right) + g\left(\frac{h_{i,j}^{o} + h_{i-1,j}^{o}}{2}\right)\frac{\Delta t}{2\Delta x}\left(Zx_{i,j}^{o} - Zx_{i-1,j}^{o}\right) + \frac{\Delta t}{2}\left(\frac{G_{i,j}^{o} + G_{i-1,j}^{o}}{2}\right) \tag{11.25}$$

Lx_1 corrector sequence (forward differences):

$$U_{i,j}^{c} = \frac{1}{2}\left[U_{i,j}^{o} + U_{i,j}^{p} - \frac{\Delta t}{2\Delta x}\left(Ex_{i+1,j}^{p} - Ex_{i,j}^{p}\right) + g\left(\frac{h_{i+1,j}^{p} + h_{i,j}^{p}}{2}\right)\frac{\Delta t}{2\Delta x}\left(Zx_{i+1,j}^{p} - Zx_{i,j}^{p}\right) + \frac{\Delta t}{2}\left(\frac{G_{i+1,j}^{o} + G_{i,j}^{o}}{2}\right)\right] \tag{11.26}$$

Ly_1 predictor sequence (forward differences):

$$U_{i,j}^{p} = U_{i,j}^{o} - \frac{\Delta t}{2\Delta y}\left(Ey_{i,j}^{o} - Ey_{i,j-1}^{o}\right) + g\left(\frac{h_{i,j}^{p} + h_{i,j-1}^{p}}{2}\right)\frac{\Delta t}{2\Delta y}\left(Zy_{i,j}^{o} - Zy_{i,j-1}^{o}\right) + \frac{\Delta t}{2}\left(\frac{G_{i,j}^{o} + G_{i,j-1}^{o}}{2}\right) \tag{11.27}$$

Ly_1 corrector sequence (backward differences):

$$U_{i,j}^{c} = \frac{1}{2}\left[U_{i,j}^{o} + U_{i,j}^{p} - \frac{\Delta t}{2\Delta y}\left(Ey_{i,j+1}^{p} - Ey_{i,j}^{p}\right) + g\left(\frac{h_{i,j+1}^{p} + h_{i,j}^{p}}{2}\right)\frac{\Delta t}{2\Delta y}\left(Zy_{i,j+1}^{p} - Zy_{i,j}^{p}\right) + \frac{\Delta t}{2}\left(\frac{G_{i,j+1}^{o} + G_{i,j}^{o}}{2}\right)\right] \tag{11.28}$$

, where the superscript o indicates that results from the previous operator (or time step in case of Lx_1) should be used and superscript p indicates that predicted quantities are used to obtain the corrected quantities denoted by the superscript c. Δx, Δy and Δt are space and time intervals, respectively. Lx_2 and Ly_2 are like Lx_1 and Ly_1 except that a forward difference is used in the predictor step and a backward difference is used in the corrector step.

Although derivatives are discretized to first-order accuracy, the operator-splitting technique achieve second-order accuracy in space and time. The stability of the scheme can be determined by the Courant-Friederichs-Lewy condition, which for the two-dimensional case is:

$$\Delta t \leq \frac{\Delta x \Delta y}{\sqrt{\Delta x^2 + \Delta y^2}} \frac{\mathrm{CFL}}{\left(\sqrt{v_x{}^2 + v_y{}^2} + \sqrt{gh}\right)_{\max}} \tag{11.29}$$

, where CFL is the Courant-Friederichs-Lewy number which can take values up to 1.

11.4.2. Initial conditions

The numerical model considers rain falling on initially dry soil bed. In terms of initial conditions this translates into flow depths, flow velocities and sediment concentrations all set equal to zero for all computational points. Also, it is possible that, after the rainfall event, the soil dries up again. This originates numerical complications that need to be solved using specific procedures. One is the surging of very shallow water depths, in which case velocities need a special treatment (ESTEVES et al., 2000). The other is the wetting/drying front that can originate computational negative water depths that need to be corrected for the next time step (MARTINS et al., 2017).

In the case of very shallow water depths, velocities need a special treatment because the motion of a very shallow flow is not correctly described by Equations 11.1 to 11.3. Also, unrealistically large values of the friction slope are computed when such water depths occur. Therefore, in this model, for water depths lower than 0.0001 m, velocities were computed considering the kinematic approximation, as follows:

$$v_x = \frac{1}{n} h^{\frac{2}{3}} \left|\frac{\partial Z}{\partial x}\right|^{\frac{1}{2}} \quad , \quad v_y = \frac{1}{n} h^{\frac{2}{3}} \left|\frac{\partial Z}{\partial y}\right|^{\frac{1}{2}} \tag{11.30}$$

In the case of negative depths, the following procedure was implemented. Firstly, after each time step, the computational points were differentiated between having negative depths ($\eta_{i,j} = 0$) and having null or positive depths ($\eta_{i,j} = 1$). Secondly, whenever a point with a negative depth is identified ($\eta_{i,j} = 0$), the sum of the positive depths of the four closer adjacent neighbours is calculated ($h_{sumi,j}$).

$$h_{sum_{i,j}} = (\eta h)_{i+1,j} + (\eta h)_{i-1,j} + (\eta h)_{i,j+1} + (\eta h)_{i,j-1} \quad \text{if} \quad \eta_{i,j} = 0 \tag{11.31}$$

Finally, if $h_{sumi,j}$ is greater than the absolute value of the negative depth of the respective point ($|h_{negi,j}|$), the negative depth is set to zero and the positive depths of the four neighbours that contributed to $h_{sumi,j}$ are reduced a fraction, as exemplified for the neighbour point $h_{i+1,j}$:

$$h_{i+1,j} = h_{i+1,j} - \frac{\left|h_{neg_{i,j}}\right| h_{i+1,j}}{h_{sum_{i,j}}} \quad \text{if} \quad \eta_{i,j} = 0 \quad \text{and} \quad \eta_{i+1,j} \quad \text{and} \quad h_{sum_{i,j}} > \left|h_{neg_{i,j}}\right| \tag{11.32}$$

If $h_{sumi,j} < |h_{negi,j}|$ the positive depths of the next four closer adjacent neighbours (e.g. diagonal neighbours) are added to the sum and the process is repeated.

11.4.3. Boundary conditions

In the numerical model, the physical domain was represented as a square divided in a uniform grid with longitudinal and transversal slope in x and y directions, respectively. Each direction is represented with a closed boundary (i.e. solid wall limiting the flow) at the upper end and an open

boundary (i.e. outlet) at the lower end. Geometry and boundary characteristics of the physical domain will be better explained in section 11.5.1.

Apart from the common elimination of the normal velocity component at the upper closed boundaries, an additional condition of zero tangential velocity at the wall has shown to improve the numerical solution (GARCIA and KAHAWITA, 1986; SIMÕES, 2006):

$$\begin{matrix} v_{x\,UB,j} = 0 \\ v_{x\,UB-1,j} = -v_{x\,UB+1,j} \end{matrix} \quad , \quad \begin{matrix} v_{y\,i,UB} = 0 \\ v_{y\,i,UB-1} = -v_{y\,i,UB+1} \end{matrix} \tag{11.33}$$

, where (UB,j) and (i,UB) represent the computational points at the upper closed boundaries in the x and y direction, respectively.

Since the flow was always supercritical, the lower open boundaries were considered free and no special treatment was necessary (GARCIA and KAHAWITA, 1986; SIMÕES, 2006).

11.5. Model application and simulation results

11.5.1. Experimental tests

To evaluate the proposed two-dimensional numerical model, data from laboratory rainfall-runoff experiments on a two-directional free-drainage square soil flume were used.

As schematised in Figure 11.1, the 2 × 2 m^2 soil flume has adjustable slope in two directions, i.e. slope in x-and y-directions. The flume was adjusted to a slope of 1% in the x-direction and 10% in the y-direction. Two gutters, each one placed along the downslope end of each slope direction, convey the surface runoff into two individual outlets.

The soil used in the experiments, characterised as sandy-loam (USDA, 1993), was comprised of 11.5% clay, 9.8% silt, 78.7% sand. Prior to the experiments, the soil was air-dried, sieved through a 5 mm mesh screen and well mixed to ensure uniformity. The soil was uniformly spread in the flume, flattened and tapped to attain a uniform bulk density of 1565 kg m^{-3} with a uniform thickness of 0.1 m and a smooth surface, i.e. without rough elements such as microtopographic protuberances. Laboratory permeability tests yielded a saturated hydraulic conductivity of 5.7 × 10^{-5} m s^{-1} and a saturated soil water content of 39%.

The rainfall simulator was comprised of three downward-oriented full-cone nozzles, a support structure, in which the nozzles were installed, and a hydraulic circuit connected to a water pump, water reservoir and tap water supply system from the public network. The nozzles were positioned in a straight line with its direction parallel to the direction of the higher slope (i.e. y-direction), with an equal spacing of 0.95 m between them at an average height of 2.5 m from the geometric centre of the flume soil surface. The working pressure on the nozzles was kept approximately constant at 50 kPa, producing rainfall at an average intensity of 211 mm h^{-1} at the soil flume surface, with a

uniformity coefficient of 64.6%, calculated according to CHRISTIANSEN (1942). Spatial distribution of the rainfall intensity at the soil surface is shown in Figure 11.2.

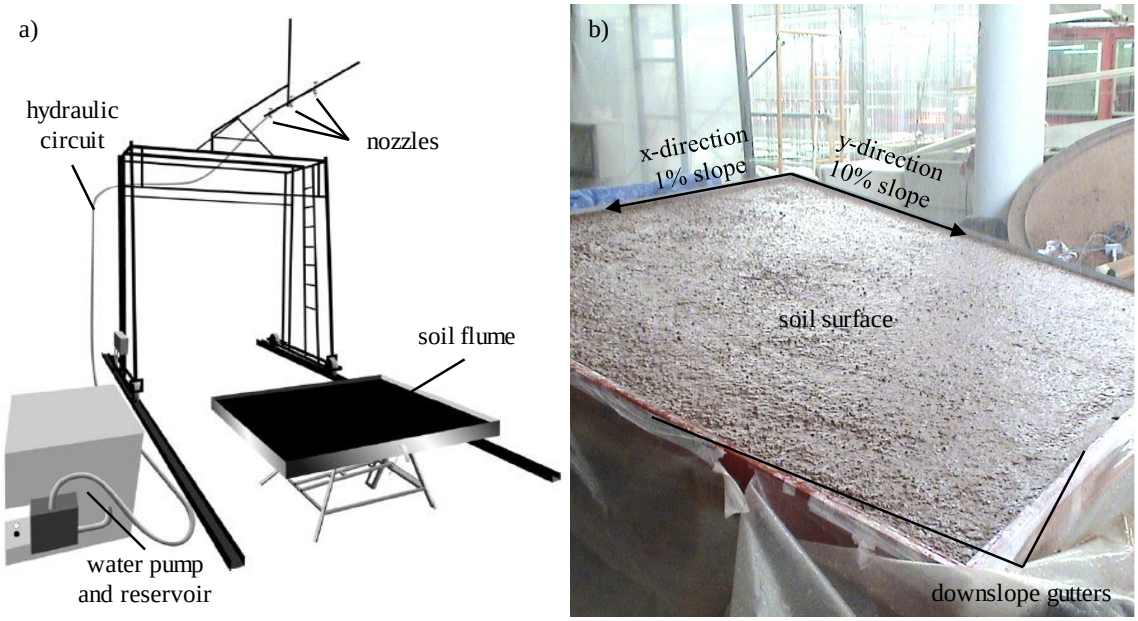

Figure 11.1. Experimental tests: a) Sketch of the laboratory set-up with the square soil flume and rainfall simulator comprising the water reservoir and pump, hydraulic circuit and nozzles (adapted from Deng et al., 2008); and b) Photograph of the 2 × 2 m^2 soil flume with adjustable slope in x-and y-directions (represented by the arrows), with indication of downslope gutters.

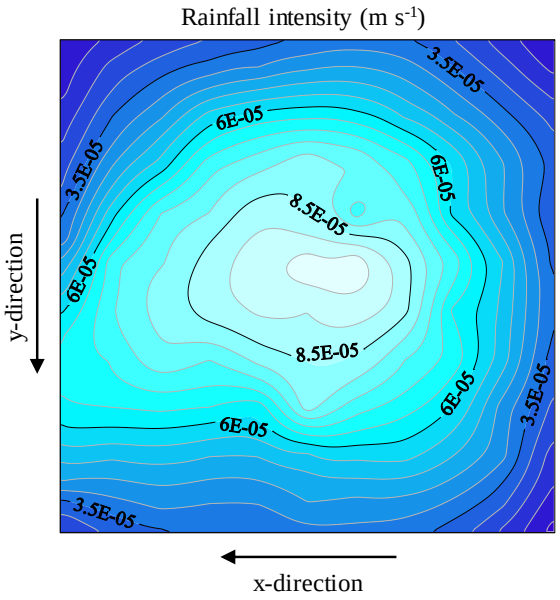

Figure 11.2. Rainfall intensity spatial distribution at the soil surface level. Major isohyets (black lines) are in m s^{-1}. Interval between minor isohyets (grey lines) is 0.5 × 10^{-5} m s^{-1}. The arrows represent the slope in x- and y-directions.

The experiments consisted on four rainfall simulations each lasting 5 min, with a 48 h interval of no rain between them. The first rainfall was simulated on an initially dry soil condition with a low soil water content of 0.1%. Initial soil moisture for the following events was the resulting from the previous rainfall simulations and drying period. Before the start of a new event, the amount of transported sediments in the previous event was replaced and the soil surface was levelled so that microrelief (e.g. rills) formed during the previous event was removed, resulting in a new smooth soil surface.

Samples of surface runoff of the x- and y-directions were collected separately at the two outlets located at the downslope end of the soil flume, using metal containers. Sediments transported by surface runoff were estimated by drying of samples in a low temperature oven.

11.5.2. Model parameterisation

The following parameters were estimated using the data collected from the laboratory experiments: i) Clear water density (ρ) and kinematic viscosity (υ), for water at a temperature of 20ºC, were fixed in 998.2 kg m^{-3} and 1.003×10^{-6} m^2 s^{-1}, respectively, according to VENNARD and STREET (1975); ii) Mean sediment particle diameter (d_s) was estimated from the soil granulometric analysis and was fixed to 4.0×10^{-4} m; iii) Soil porosity was estimated as equivalent to the saturated water content and was fixed to 0.39; and iv) Sediment particles density (ρ_s) was estimated using the measured soil bulk density of 1565 kg m^{-3} and estimated porosity of 0.39 and was fixed to 2566 kg m^{-3}.

The following parameters were estimated using the data from similar experimental work using the same laboratory set-up (i.e. soil, soil flume, rainfall simulator) and similar numerical work using similar numerical equations to express soil erosion (DENG et al., 2008): i) Manning's roughness coefficient (n) was fixed to 0.0265 s $m^{-1/3}$; and ii) Interrill and rill erosion control parameters (η and ξ) were fixed in 1.38 m^{-1} and 8.2×10^{-6} $m^{1.2}$, respectively.

The dimensionless critical Shields parameter (θ_c) was estimated from PETIT (1994) and was fixed in 0.047.

The parameters involved in the numerical simulation of infiltration (CN and c_f) were obtained after calibration till achievement of the best model performance. Such parameters are listed in Table 11.1.

Spatial discretization in both x- and y-directions (Δx and Δy) was fixed to 0.01 m.

Table 11.1. Infiltration parameters used in the proposed model, for each of the four rainfall-runoff events.

	Rainfall event			
Infiltration parameter	1st	2nd	3rd	4th
CN (-)	95.0	99.0	99.5	99.5
c_f (-)	0.200	0.050	0.050	0.025

11.5.3. Model evaluation

Different criteria were used to evaluate the performance of the numerical model. Firstly, the accuracy of estimated runoff peak (Q_p) and volume (V) and transported sediments peak (Qs_p) and total mass (Ms) and was quantified using the relative error (E_r):

$$E_r = \frac{Obs - Mod}{Obs} \times 100 \tag{11.34}$$

, where Obs and Mod represent the observed and modelled data, respectively.

Secondly, the goodness of fit of the shape of the estimated runoff hydrographs and graphs of transported sediments was quantified using the Coefficient of determination (r^2) and the Nash-Sutcliffe coefficient of efficiency (NS) according to NASH and SUTCLIFFE (1970):

$$r^2 = \left(\frac{\sum_{i=1}^{n} \left(\left(Obs_i - \overline{Obs} \right) \times \left(Mod_i - \overline{Mod} \right) \right)}{\sqrt{\left(\sum_{i=1}^{n} \left(Obs_i - \overline{Obs} \right)^2 \right) \times \left(\sum_{i=1}^{n} \left(Mod_i - \overline{Mod} \right)^2 \right)}} \right)^2 \tag{11.35}$$

$$NS = 1 - \frac{\sum_{i=1}^{n} \left(Obs_i - Mod_i \right)^2}{\sum_{i=1}^{n} \left(Obs_i - \overline{Obs} \right)^2} \tag{11.36}$$

, where Obs_i and Mod_i represent the observed and modelled data at point i, respectively, $\overline{Obs}$ and $\overline{Mod}$ represent the average observed and modelled data and n is the total number of data points.

11.5.4. Simulation results

Graphs of experimentally observed (markers) and numerically modelled (solid curves) runoff (left) and transported sediments (right) for the four simulated rainfall events, are shown in Figure 11.3. Results of experimentally observed (Obs) and numerically modelled (Mod) runoff peak (Q_p) and runoff volume (V) and transported sediments peak (Qs_p) and total mass (Ms), for the four rainfall-runoff events, are shown in Tables 11.2 and 11.3; the Relative error (E_r), the Coefficient of determination (r^2) and the Nash-Sutcliffe coefficient of efficiency (NS) comparing observed to modelled results are also shown.

When compared to the higher slope of 10% in the y-direction, the lower slope of 1% in the x-direction produced remarkably lower runoff and transported sediments (Figure 11.3). Overall, this situation was more pronounced in the numerical model than in the experimental tests (see E_r in Tables 11.2 and 11.3).

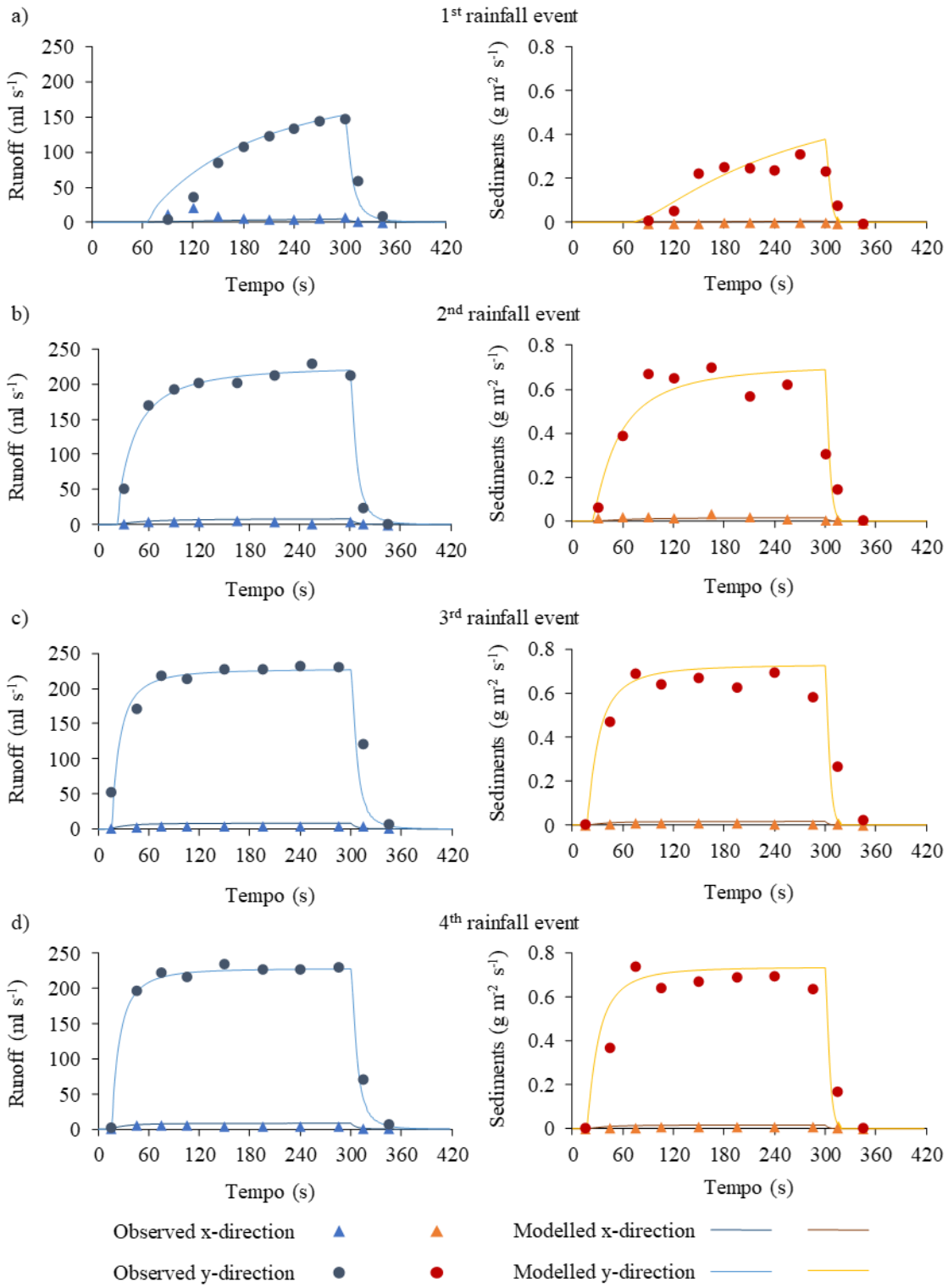

Figure 11.3. Graphs of observed (markers) and modelled (solid curves) runoff (left) and transported sediments (right) fin the x- and y-directions and for each of the four rainfall-runoff events: a) 1st rainfall event; b) 2nd rainfall event; c) 3rd rainfall event; and d) 4th rainfall event.

The numerical model significantly underestimated x-direction runoff and transported sediments, both in terms of peak and total amounts. In terms of numerical modelling goodness of fit, this situation translated in a good performance in the y-direction as opposed to a poor performance in the x-direction (see r^2 and NS in Tables 11.2 and 11.3). For the x-direction, NS was always negative for both runoff and transported sediments. For the y-direction, NS was always higher than 0.75 meaning a very good performance. Despite this results, r^2 values were always higher than 0.75, meaning a good correlation between observed and modelled data, even for the x-direction. Only runoff results in the x-direction in the first rainfall event showed a different behaviour from the other results. Here, x-direction runoff was overestimated and r^2 value was close to 0.

Table 11.2. Observed (Obs) and modelled (Mod) results of runoff peak (Q_p) and runoff volume (V) for the four rainfall-runoff events. Relative error (E_r), Coefficient of determination (r^2) and Nash-Sutcliffe coefficient of efficiency (NS) are shown.

			Runoff					
Rainfall event	Direction	Data	Q_p		V		r^2	NS
			ml s^{-1}	E_r (%)	l	E_r (%)		
1	x	Obs	22.94	79.57	2.39	69.47	0.02	-1.16
		Mod	4.69		0.73			
	y	Obs	149.06	-2.38	24.18	-6.56	0.93	0.90
		Mod	152.61		25.77			
	Total	Obs	157.67	0.23	26.58	0.29	0.96	0.95
		Mod	157.30		26.50			
2	x	Obs	5.34	-50.39	1.09	-80.33	0.51	-2.61
		Mod	8.03		1.97			
	y	Obs	228.73	4.03	55.70	-0.72	0.99	0.99
		Mod	219.52		56.09			
	Total	Obs	230.43	1.25	56.79	-2.25	0.99	0.98
		Mod	227.55		58.06			
3	x	Obs	4.58	-84.05	1.25	-82.28	0.80	-12.99
		Mod	8.43		2.28			
	y	Obs	232.15	2.41	64.11	2.15	0.96	0.92
		Mod	226.54		62.73			
	Total	Obs	236.66	0.71	65.36	0.54	0.96	0.92
		Mod	234.97		65.01			
4	x	Obs	5.96	-42.31	1.27	-81.39	0.83	-3.01
		Mod	8.49		2.30			
	y	Obs	237.82	4.15	63.68	0.51	0.99	0.98
		Mod	227.95		63.35			
	Total	Obs	241.80	2.22	64.95	-1.09	0.99	0.98
		Mod	236.44		65.66			

Table 11.3. Observed (Obs) and modelled (Mod) results of transported sediment peak (Qs_p) and total mass (Ms) for the four rainfall-runoff events. Relative error (E_r), Coefficient of determination (r^2) and Nash-Sutcliffe coefficient of efficiency (NS) are shown.

Rainfall event	Direction	Data	Transported sediments					
			$Qs_p \times 10^2$		Ms		r^2	NS
			g m^2 s^{-1}	E_r (%)	g	E_r (%)		
1	x	Obs	0.50	-13.70	2.31	-2.83	0.79	-0.79
		Mod	0.57		2.38			
	y	Obs	34.07	-10.89	188.97	-7.95	0.85	0.80
		Mod	37.78		204.00			
	Total	Obs	34.57	-10.93	191.28	-7.89	0.85	0.80
		Mod	38.35		206.38			
2	x	Obs	4.96	70.03	17.26	24.28	0.82	-0.08
		Mod	1.49		13.07			
	y	Obs	74.28	7.24	634.54	-3.81	0.85	0.80
		Mod	68.90		658.74			
	Total	Obs	75.61	6.90	651.80	-3.07	0.85	0.79
		Mod	70.39		671.81			
3	x	Obs	0.85	-88.47	6.86	-139.52	0.75	-8.97
		Mod	1.61		16.44			
	y	Obs	69.39	-4.46	690.12	-12.26	0.91	0.79
		Mod	72.49		774.73			
	Total	Obs	69.99	-5.87	696.33	-13.62	0.91	0.79
		Mod	74.10		791.17			
4	x	Obs	1.17	-39.22	9.28	-80.77	0.87	-2.02
		Mod	1.63		16.78			
	y	Obs	74.05	1.11	688.33	-14.39	0.88	0.76
		Mod	73.23		787.41			
	Total	Obs	74.69	-0.22	697.61	-15.28	0.88	0.76
		Mod	74.86		804.19			

As expected, due to the initial dry soil condition, observed time to runoff was significantly higher in the first rainfall event (60 s) when compared to the following events (20, 15 and 14 s). Also, the hydrograph and sediment transport graph in the first event presented significantly less steep rising limbs and lower peaks. The last three rainfall events presented similar results due to the similar initial wet condition of the soil (i.e. 24h dry period between rainfall events). In numerical terms, since infiltration parameters were calibrated according to each rainfall event, the initial soil moisture condition did not had a visible impact in the performance model.

Since runoff and transported sediments in the x-direction were almost meaningful, the numerical performance of the model in total terms (i.e. x- plus y-direction) was considered to be very good. Overall, runoff was slightly better modelled than sediment transport. However, as stated before, whereas the infiltration parameters were calibrated according to each rainfall event the sediment transport parameters were fixed for all rainfall events.

11.6. Conclusion

A two-dimensional mathematical model was developed for simulating soil erosion and sediment transport resulting from rainfall induced overland flow. The model comprised: i) Two-dimensional unsteady water flow equations on an infiltrating surface; ii) Combined Horton-SCS infiltration scheme; and iii) Two-dimensional sediment transport equation with three distinct soil erosion processes (interrill erosion, rill erosion and sediment deposition).

Overall, if the sum of the x- and y-direction results is considered, the numerically simulated graphs of runoff and sediment transport were in very good agreement with corresponding experimental measurements, demonstrating the laboratory proof-of-concept of the model. However, if x- and y-directions results are analysed separately, the numerical model was only able to properly simulate the runoff and sediment transport observed in the y-direction with the higher slope of 10%. A poor agreement was observed for the remarkably lower values of runoff and sediment transport observed in the x-direction with the lower slope of 1%. Overall, since the infiltration parameters were calibrated, the initial moisture condition of the soil did not had impact on the performance of the numerical model.

Although the agreement between the presented model and the experimental observations of runoff and sediment transport were satisfactory, a performance evaluation of the spatial and temporal evolution of flow velocity, flow depth, soil surface moisture conditions, soil surface microrelief development (e.g. rills) and rainfall characteristics, should be performed. Future experimental tests should contemplate such measurements, e.g. using new instrumental methodologies based on infrared thermography such as the ones presented in ABRANTES et al. (2014, 2016, 2017, 2018a, 2019), DE LIMA and ABRANTES (2014a, 2014b), DE LIMA et al. (2014a, 2014b, 2014c, 2015a, 2015b) and MUJTABA and DE LIMA (2018).

“No research is ever quite complete. It is the glory of a good bit of work that it opens the way for something still better, and this repeatedly leads to its own eclipse.”

- Mervin Gordon

"The outcome of any serious research can only be to make two questions grow where only one grew before."

- Thorstein Veblen

12. FINAL REMARKS

The first part of this chapter summarizes the overall conclusions reached during this doctoral study. The second part attempts to give an answer to the main research question of this Thesis. The third part presents some suggestions for future research.

12.1. Conclusions

The aim of this Thesis was to develop and investigate innovative techniques based on infrared thermography that can be used as sensing tools to assess different hydrologic processes that occur at the soil surface, namely in the study of surface runoff and water erosion. For that, seven specific objectives were defined in Chapter 1. Those research objectives were achieved during this doctoral study and the overall conclusions of this Thesis are drawn in the following paragraphs.

Objective 1. To develop, in laboratory, an innovative technique based on infrared thermography to assess morphological characteristics of soil surface.

- The technique allows to identify the spatial variability of soil surface microrelief, rill geometry and preferential flow paths at the soil surface;
- Visual thermal patterns distinguished in the infrared imaging are driven by differences in hot water depth at the soil surface, i.e. hot water concentrates more in lower morphologic features, therefore presenting different temperature than higher morphologic features;
- Thermal data can be converted into 3D models of the soil surface, using elevation point measurements.

Objective 2. To develop, in laboratory, innovative techniques based on infrared thermography to assess different hydraulic characteristics of soil surface.

- The technique allows to identify the spatial variability of soil surface permeability, macroporosity and soil water repellency;
- Visual thermal patterns distinguished in the infrared imaging are driven by differences in hot or cold water content in the soil and hot or cold water accumulation; i.e. hot or cold water infiltrates more in more permeable and less water repellent areas and flows preferentially to the macropores, therefore presenting different temperature than less permeable areas, more water repellent areas and areas without macropores;

- Thermal data can be converted into maps of soil surface permeability and soil water repellency, using point measurements of soil hydraulic conductivity and surface tension, respectively.

Objective 3. To investigate the applicability in real field conditions of an innovative technique based on infrared thermography to assess the hydraulic behaviour of the soil surface due to differences in soil water repellency.

- The applicability of the technique in real field conditions is comparable to the applicability in controlled laboratory conditions, presenting very similar experimental set-up, application methodology and measuring accuracy;
- The natural spatial variability of soil surface temperature in the field (i.e. before the application of the technique), requires an adaptation of the data treatment procedure.

Objective 4. To identify the strengths and drawbacks of the techniques based on infrared thermography developed in this doctoral study.

The following strengths of the techniques were identified:

- The techniques can be used in a very expedite way;
- The techniques are specifically useful to identify the spatial variability of morphologic structures and visualise preferential flow paths at the soil surface in the presence of mulch (i.e. organic residue covering the soil surface), where other techniques (e.g. photogrammetry and laser techniques) may not be applied with success;
- The easy handling and low cost of the equipment (i.e. infrared camera, recipient with water hotter or colder than the soil surface) compared with other techniques (e.g. laser scanners) make them useful for measuring the spatial variation of soil surface characteristics;
- The fast application makes them interesting techniques to obtain spatially distributed data, when compared to some time-consuming point measurement techniques (e.g. pin or relief meters, constant head permeameters, MED test);
- The techniques are independent of illumination condition, which is known to severely affect optical and laser measurement techniques; furthermore, the techniques based on infrared thermography can be used during night-time without artificial lighting.

The following drawbacks of the techniques were identified:

- Overall, the precision of the techniques in measure the spatial variation of soil surface characteristics is low compared with other more accurate measurement techniques (e.g. photogrammetry and laser techniques);
- The precision of some techniques relies on point measurements of surface morphology and hydraulic characteristics (e.g. with a pin meter, double ring infiltrometer, MED test);

- Due to heat propagation in the soil, sharp variations of soil surface characteristics (e.g. rill and macropores geometry) tend to be interpreted as being smoother;
- The assessment of a determined soil surface morphologic or hydraulic characteristic can be affected by the spatial variability of other soil surface morphologic and hydraulic characteristics; e.g. high variable soil surface morphology (e.g. rills, ponds, mounds) or the presence of macropores at the soil surface can affect the assessment of soil surface permeability or soil water repellency;
- The techniques themselves can affect the soil surface morphology and hydraulic characteristics, so a second test in easy erodible soils may obtain a slightly different result.

Objective 5. To investigate the use of thermal tracers and infrared video cameras to estimate the velocity of shallow flows.

- The visualization of the movement of a thermal tracer within flowing water, using an infrared camera, can be used to measure the surface velocity of distributed overland flows and concentrated rill flows, as well as to identify preferential flow paths at the surface of the water;
- Overall, thermal tracer velocities are slightly higher than velocities measured using other traditional and well-established tracer techniques, such as dye and salt tracers; however, differences are not significant;
- The correction factors used to estimate the mean flow velocity from the tracers' measurements greatly vary with the hydraulic characteristics of the flow (e.g. velocity, depth, Reynolds number, Froude number) and the characteristics of the bottom surface (e.g. roughness, slope);

The main advantage of using thermal tracers are:

- Higher visibility compared with the dye tracers, which leads to the estimation of flow velocity using smaller volume of tracer, and, therefore, smaller disturbances in the actual flow velocity;
- Easier image processing than dye tracers that usually require more sophisticated and specific light conditions that may not be always available, especially in field tests;
- The visualization of the movement of the tracer within the flow, which cannot be done with salt tracing;
- The possibility of measuring the flow velocity without the need of introducing any instrument (e.g. sensor) in the flow, causing less disturbances in the actual flow velocity;
- Non-necessity of a minimum water depth, which usually is needed to accurately measure flow velocity with some instruments (e.g. sensors);

- Thermal tracers are more environmentally friendly than dye and salt tracers; they are cleaner and more ecological, do not leave any residue in the water or the soil and cause very little temporal and spatial disturbance on the environment.

The main disadvantages of using thermal tracers are:

- Higher price of an infrared video camera compared with a regular optical video camera or an electrolyte sensor, despite recent falls in the cost of infrared equipment;
- The necessity of water hotter or colder than the flowing water may be an obstacle in remote field places;
- Thermal tracers are less conservative than salt tracers;
- Measuring flow velocity using the dye tracer can be faster and more intuitive than the thermal tracer, since the movement of the tracer can be simply observed by the operator without using any recording equipment; however, at the cost of a worst accuracy;

Objective 6. To develop a numerical approach to combine with thermal tracers to estimate basic hydraulic characteristics of shallow flows.

- The developed numerical approach by fitting an analytical solution of an advection–dispersion transport equation to temperature data from thermal tracers can be used to estimate the velocity and the dispersion coefficient (hydrodynamic or thermal) of shallow flows;
- Results from the numerical methodology predicted the mean flow velocity better than other more traditional and well-established methodologies, such as measuring the leading edge and centroid of the tracer.

Objective 7. To develop a two-dimensional (2D) rainfall induced water erosion numerical model.

- The mathematical model comprises a rainfall-runoff module using the 2D unsteady physically based Saint-Venant equations, a rainfall-infiltration module using a combined Horton-SCS empirical scheme and a water erosion and sediment transport module using a 2D transport rate-based advection equation and a detachment-transport-deposition approach, distinguishing between interrill erosion, rill erosion and sediment deposition;
- The governing equations are solved using an explicit finite-differences method based on the MacCormack operator-splitting scheme;
- The parameterization and calibration procedure of the model can be difficult due to the large amount of simulation parameters;
- Overall, the numerically simulated graphs of runoff and sediment transport are in very good agreement with corresponding experimental measurements; even so, lower volumes of runoff and sediment transport are not so well simulated as higher volumes.

12.2. Answer to research question

In Chapter 1, the following research question was presented to be discussed and analysed in this Thesis: **Can information collected at the soil surface level with techniques based on infrared thermography be useful to model and better understand surface hydrologic processes?**

The research presented in this doctoral study revealed that infrared thermography can be used as a ground-based sensing tool for acquisition of information on soil surface characteristics and flow hydraulics. These techniques have shown great potential to: i) Estimate the spatial variability of soil surface morphology where other techniques cannot be applied (e.g. presence of organic residues concealing the soil surface); ii) Estimate the spatial variability of soil surface hydraulic characteristics in a faster and expedite way, instead of multiple time-consuming point measurements that need to be grouped or scaled to bring out spatial coherence; and iii) Estimate the surface flow velocity in the occurrence of very shallow flows where many measurement equipment cannot be used.

One big advantage of these techniques is the possibility of qualitative real time monitoring of the spatial dynamics of some key processes in surface hydrology, using a fast and expedite methodology with a simple set-up and only one equipment, i.e. one infrared video camera. Usually, gathering such amount of data would normally require different types of equipment, more complex setups, time-consuming methodologies and specialized personal. However, in quantitative terms, the precision of some of these techniques relies on measurements with other more common techniques. As usual, such novel sensing tools will need thorough assessment to be routinely adopted in field monitoring practices. Their development will require extensive calibration, validation and collaboration from the scientific community.

Observations from these techniques can be used to complement observations from other techniques. Also, nowadays, the technological advances provide a great variety of equipment and technologies that can be combined, taking advantage each other's potentials, e.g. dual cameras with optical and infrared sensors to combine optical and infrared observations, infrared cameras couple with unmanned aerial vehicles to combine observations at different scales. Main attention should be drawn to the ability to complement these new observations with other observations from other techniques with different temporal and spatial resolutions, different precisions and different physical meanings.

No doubt, the information collected with these innovative techniques based on infrared thermography can be useful to calibrate and validate numerical models of surface hydrology, such as surface runoff and water erosion, as well as to better understand the underlying processes.

12.3. Future work

Further research could include:

- Extensive field testing at different spatial and temporal scales and different soil surface and hydraulic conditions to calibrate and validate these innovative techniques as suitable monitoring techniques for surface hydrology;
- Investigation on the use of infrared cameras to asses other hydrologic processes at the soil surface, such as ponding;
- Investigation on the use of dual cameras with infrared and optical sensors to assess surface hydrologic processes combining both observations;
- Coupling of infrared cameras with unmanned aerial vehicles to gather data at different spatial scales;
- Development of a numerical algorithm to analyse thermal imaging (or thermal and optical imaging) and automatically identify the different morphologic and hydraulic characteristics of the soil surface;
- Installation of equipment (e.g. infrared cameras, automatic thermal tracer devices) in natural systems or at existing observation stations to continuous automatic monitoring of surface hydrologic processes;
- Carry out of laboratory and field experiments focusing on water erosion, applying the developed innovative techniques based on infrared thermography, in order to validate the developed numerical model.

"The common facts of today are the products of yesterday's research."

- Duncan MacDonald

13. REFERENCES

ABRAHAMS, A.D. and ATKINSON, J.F. (1993). Relation between grain velocity and sediment concentration in overland flow. *Water Resources Research*, 29(9), 3021-3028. DOI:10.1029/93WR00771.

ABRAHAMS, A.D., PARSONS, A.J. and LUK, S.H. (1986). Field measurement of the velocity of overland flow using dye tracing. *Earth Surface Processes and Landforms*, 11(6), 653-657. DOI:10.1002/esp.3290110608.

ABRANTES, J.R.C.B. and DE LIMA, J.L.M.P. (2014). Termografia para determinação da microtopografia da superfície do solo em diferentes condições de cobertura morta. *Revista Brasileira de Ciências Agrárias*, 9(3), 445-453. DOI:10.5039/agraria.v9i3a3602.

ABRANTES, J.R.C.B., DE LIMA, J.L.M.P. and MONTENEGRO, A.A.A. (2015). Desempenho da modelagem cinemática do escoamento superficial para chuvas intermitentes em solos com cobertura morta. *Revista Brasileira de Engenharia Agrícola e Ambiental*, 19(2), 166-172. DOI:10.1590/1807-1929/agriambi.v19n2p166-172.

ABRANTES, J.R.C.B., DE LIMA, J.L.M.P., PRATS, S.A. and KEIZER, J.J. (2017). Assessing soil water repellency spatial variability using a thermographic technique: an exploratory study using a small-scale laboratory soil flume. *Geoderma*, 287, 98-104. DOI:10.1016/j.geoderma.2016.08.014.

ABRANTES, J.R.C.B., DE LIMA, J.L.M.P., PRATS, S.A. and KEIZER, J.J. (2016). Field assessment of soil water repellency using infrared thermography. *Forum Geographic*, 15(2), 12-18. DOI:10.5775/fg.2016.019.s.

ABRANTES, J.R.C.B., MORUZZI, R.B., DE LIMA, J.L.M.P., SILVEIRA, A. and MONTENEGRO, A.A.A. (2019). Combining a thermal tracer with a transport model to estimate shallow flow velocities. *Physics and Chemistry of the Earth*, 109, 59-69. DOI:10.1016/j.pce.2018.12.005.

ABRANTES, J.R.C.B., MORUZZI, R.B., SILVEIRA, A., DE LIMA, J.L.M.P. (2018a). Comparison of thermal, salt and dye tracing to estimate shallow flow velocities: novel triple tracer approach. *Journal of Hydrology*, 557, 362-377. DOI:10.1016/j.jhydrol.2017.12.048.

ABRANTES, J.R.C.B., PRATS, S.A., KEIZER, J.J., and DE LIMA, J.L.M.P. (2018b). Effectiveness of the application of rice straw mulching strips in reducing runoff and soil loss: Laboratory soil flume experiments under simulated rainfall. *Soil & Tillage Research*, 180, 238-249. DOI:10.1016/j.still.2018.03.015.

ALI, M., SEEGER, M., STERK, G. and MOORE, D. (2013). A unit stream power based sediment transport function for overland flow. *CATENA*, 101, 197-204. DOI:10.1016/j.catena.2012.09.006.

ALLAIRE, S.E., ROULIER, S. and CESSNA, A.J. (2009). Quantifying preferential flow in soils: a review of different techniques. *Journal of Hydrology*, 378(1-2), 179-204. DOI:10.1016/j.jhydrol.2009.08.013.

ALLMARAS, R.R., BURWELL, R.E., LARSON, W.E. and HOLT, R.F. (1966). *Total porosity and random roughness of the interrow zone as influenced by tillage.* Conservation Research Report No. 7. Washington, DC, USA: USDA. 22 pp.

APPLES, W.M. (2013). *Water redistribution at the soil surface: ponding and surface runoff in flat areas*. PhD Thesis, Wageningen University, Wageningen, The Netherlands. 164 pp.

BAARTMAN, J.E.M., JETTEN, V.G., RITSEMA, C.J. and DE VENTE, J. (2011). Exploring effects of rainfall intensity and duration on soil erosion at the catchment scale using open LISEM: Prado catchment, SE Spain. *Hydrological Processes*, 26 (7), 1034-1049. DOI:10.1002/hyp.8196.

BACHMANN, J., ELLIES, A. and HARTGE, K.H. (2000). Development and application of a new sessile drop contact angle method to assess soil water repellency. *Journal of Hydrology*, 231-232, 66-75. DOI:10.1016/S0022-1694(00)00184-0.

BADÍA-VILLAS, D., GONZÁLEZ-PÉREZ, J.A., AZNAR, J.M., ARJONA-GRACIA, B. and MARTÍ-DALMAU, C. (2014). Changes in water repellency, aggregation and organic matter of a mollic horizon burned in laboratory: soil depth affected by fire. *Geoderma*, 213, 400-407. DOI:10.1016/j.geoderma.2013.08.038.

BAGAVATHIAPPAN, S., SARAVANAN, T., PHILIP, J. and JAYAKUMAR, T. (2013). Infrared thermography for condition monitoring - a review. *Infrared Physics & Technology*, 60, 35-55. DOI:10.1016/j.infrared.2013.03.006.

BAKER, E.A., LAUTZ, L.K., MCKENZIE, J.M. and AUBRY-WAKE, C. (2019). Improving the accuracy of time-lapse thermal infrared imaging for hydrologic applications. *Journal of Hydrology*, 571, 60-70. DOI:10.1016/j.jhydrol.2019.01.053.

BAN, Y., LEI, T., LIU, Z. and CHEN, C. (2016). Comparison of rill flow velocity over frozen and thawed slopes with electrolyte tracer method. *Journal of Hydrology*, 534, 630-637. DOI:10.1016/j.jhydrol.2016.01.028.

BATISTA, P.V.G., DAVIES, J., SILVA, M.L.N. and QUINTON, J.N. (2019). On the evaluation of soil erosion models: are we doing enough? *Earth-Science Reviews*, 197, 102898. DOI:10.1016/j.earscirev.2019.102898.

BAUER, S.W. (2010). A modified Horton equation for infiltration during intermitente rainfall. *Hydrological Sciences Bulletin*, 19(2), 219-225. DOI:10.1080/02626667409493900.

BENTLEY, A. (1904). Studies of raindrops and raindrop phenomena. *Monthly Weather Review*, 32, 450-456. DOI:10.1175/1520-0493(1904)32<450:SORARP>2.0.CO;2.

BERGER, C., SCHULZE, M., RIEKE-ZAPP, D. and SCHULUNEGGER, F. (2010). Rill development and soil erosion: a laboratory study of slope and rainfall intensity. *Earth Surface Processes and Landforms*, 35 (12), 1456–1467. DOI:10.1002/esp.1989.

BEVEN, K. (2004). Robert E. Horton's perceptual model of infiltration processes. *Hydrological Processes*, 18 (17), 3447-3460.

BEVEN, K.J. and GERMANN, P.F. (1982). Macropores and water flow in soils. *Water Resources Research*, 18 (5), 1311-1325. DOI:10.1029/WR018i005p01311.

BEVEN, K.J. and GERMANN, P.F. (2013). Macropores and water flow in soils revisited. *Water Resources Research*, 49 (6), 3071-3092. DOI:10.1002/wrcr.20156.

BEVEN, K.J., KIRKBY, M.J., SCHOFIELD, N. and TAGG, A.F. (1984). Testing a physically-based flood forecasting model (TOPMODEL) for three U.K. catchments. *Journal of Hydrology*, 69(1-4), 119-143. DOI:10.1016/0022-1694(84)90159-8.

BEVEN, K.J., ZHANG, D. and MERMOUD, A. (2006). On the value of local measurements on prediction of pesticide transport at the field scale. *Vadoze Zone Journal*, 5(1), 222-233. DOI:10.2136/vzj2005.0016.

BJERKLIE, D.M., (2007). Estimating the bankfull velocity and discharge for rivers using remotely sensed river morphology information. *Journal of Hydrology*, 341(3-4), 144-155. DOI:10.1016/j.jhydrol.2007.04.011.

BJERKLIE, D.M., DINGMAN, S.L., VOROSMARTY, C.J., BOLSTER, C.H. and CONGALTON, R.G. (2003). Evaluating the potential for measuring river discharge from space. *Journal of Hydrology*, 278(1-4), 13-78. DOI:10.1016/S0022-1694(03)00129-X.

BLANCHOUD, H., MOREAU-GUIGON, E., FARRUGIA, F., CHEVREUIL, M. and MOUCHEL, J. M. (2007). Contribution by urban and agricultural pesticide uses to water contamination at the scale of the Marne watershed. *Science of the Total Environment*, 375(1-3), 168-179. DOI:10.1016/j.scitotenv.2006.12.009.

BLÖSCHL, G. et al. (2019). Twenty-three Unsolved Problems in Hydrology (UPH): a community perspective. *Hydrological Sciences Journal*, 64(10), 1141-1158, DOI:10.1080/02626667.2019.1620507

BOARDMAN, J., SHEPHEARD, M.L., WALKER, E. and FOSTER, I.D.L. (2009). Soil erosion and risk-assessment for on- and off-farm impacts: A test case using the Midhurst area, West Sussex, UK. *Journal of Environmental Management*, 90(8), 2578-2588. DOI:10.1016/j.jenvman.2009.01.018.

BOBBA, A.G., BUKATA, R.P. and JEROME, J.H. (1992). Digitally processed satellite data as a tool in detecting potential groundwater flow systems. *Journal of Hydrology*, 31(1-4), 25-62. DOI:10.1016/0022-1694(92)90212-E.

BOCHET, E., POESEN, J. and RUBIO, J.L. (2006). Runoff and soil loss under individual plants of a semi-arid Mediterranean shrubland: influence of plant morphology and rainfall intensity. *Earth Surface Processes and Landforms*, 31(5), 536-549. DOI:10.1002/esp.1351.

BONAR, S.A. and PETRE, S.J. (2015). Ground-based thermal imaging of stream surface temperatures: technique and evaluation. *North American Journal of Fisheries Management*, 35(6), 1209-1218. DOI:10.1080/02755947.2015.1091410.

BONNER, R., AYLWARD, A., HARLEY, C., KAPPELMEYER, U. and SHERIDAN, C.M. (2017). Heat as a hydraulic tracer for horizontal subsurface flow constructed wetlands. *Journal of Water Process Engineering*, 16, 183-192. DOI:10.1016/j.jwpe.2017.01.007.

BRADLEY, S.G. and STOW, C.D. (1974). The measurement of charge and size of raindrops: part I. The disdrometer. *Journal of Applied Meteorology*, 13(1), 114-130. DOI:10.1175/1520-0450(1974)013<0114:TMOCAS>2.0.CO;2.

BRAUD, I., DE CONDAPPA, D., SORA, J.M., HAVERKAMP, R., ANGULO-JARAMILLO, R., GALLE, S. and VAUCLIN, M. (2005). Use of scaled forms of the infiltration equation for the estimation of unsaturated soil hydraulics properties (the Beerkan method). *European Journal of Soil Science*, 56 (3), 361-374. DOI:10.1111/j.1365-2389.2004.00660.x.

BUTZEN, V., SEEGER, M., WIRTZ, S., HUEMANN, M., MUELLER, C., CASPER, M. and RIES, J.B. (2014). Quantification of Hortonian overland flow generation and soil erosion in a Central European low mountain range using rainfall experiments. *CATENA*, 113, 202-212. DOI:10.1016/j.catena.2013.07.008.

CALKINS, D. and DUNNE, T. (1970). A salt tracing method for measuring channel velocities in small mountain streams. *Journal of Hydrology*, 11(4), 379-392. DOI:10.1016/0022-1694(70)90003-X.

CANTÓN, Y., SOLÉ-BENET, A., DE VENTE, J., BOIX-FAYOS, C., CALVO-CASES, A., ASENSIO, C. and PUIGDEFÁBREGAS, J. (2011). A review of runoff generation and soil erosion across scales in semiarid south-eastern Spain. *Journal of Arid Environments*, 75(12), 1254-1261. DOI:10.1016/j.jaridenv.2011.03.004.

CAO, Z., PENDER, G., WALLIS, S. and CARLING, P. (2002). Computational dam-break hydraulics over erodible sediment bed. *Journal of Hydraulic Engineering*, 128(5), 460-72. DOI:10.1061/(ASCE)0733-9429(2004)130:7(689).

CARDENAS, M.B., HARVEY, J.W., PACKMAN, A.I. and SCOTT, D.T. (2008). Ground-based thermography of fluvial systems at low and high discharge reveals potential complex thermal heterogeneity driven by flow variation and bioroughness. *Hydrological Processes*, 22(7), 980-986. DOI:10.1002/hyp.6932.

CARRILLO, M.L.K., LETEY, J. and YATES, S.R. (1999). Measurement of initial soil-water contact angle of water repellent soils. *Soil Science Society of America Journal*, 63(3), 433-436. DOI:10.2136/sssaj1999.03615995006300030002x.

CERDÀ, A. (1996). Seasonal variability of infiltration rates under contrasting slope conditions in southeast Spain. *Geoderma*, 69 (3-4), 217-232. DOI:10.1016/0016-7061(95)00062-3.

CERDÀ, A. (2010). Seasonal and spatial variations in infiltration rates in badland surfaces under Mediterranean climatic conditions. *Water Resources Research*, 35(1), 319-328. DOI:10.1029/98WR01659.

CERDÀ, A., IBÁÑEZ, S. and CALVO, A. (1997). Design and operation of a small and portable rainfall simulator for rugged terrain. *Soil Technology*, 11(2), 163-170. DOI:10.1016/S0933-3630(96)00135-3.

CHAU, H.W., BISWAS, A., VUJANOVIC, V. and SI, B.C. (2014).Relationship between the severity, persistence of soil water repellency and the critical soil water content in water repellent soils. *Geoderma*, 221-222, 113-120. DOI:10.1016/j.geoderma.2013.12.025.

CHEN, C., BAN, Y., WANG, X. and LEI, T. (2017). Measuring flow velocity on frozen and non-frozen slopes of black soil through leading edge method. *International Soil and Water Conservation Research*, 5(3), 180-189. DOI:10.1016/j.iswcr.2017.02.004.

CHEN, X., SONG, J., CHENG, C., WANG, D. and LACKEY, S.O. (2009). A new method for mapping variability in vertical seepage flux in streambeds. *Hydrogeology Journal*, 17(3), 519-525. DOI:10.1007/s10040-008-0384-0

CHENG, N.S. (1997). Simplified settling velocity formula for sediment particle. *Journal of Hydraulic Engineering*, 123(2), 149-152. DOI:10.1061/(ASCE)0733-9429(1997)123:2(149).

CHRISTIANSEN, J.E. (1942). *Irrigation by Sprinkling*. California Agricultural Experiment Station Bulletin 670. Berkeley, CA, USA: University of California. 124 pp.

CLARKE, T. R. (1997). An empirical approach for detecting crop water stress using multispectral airborne sensors. *HortTechnology*, 7(1), 9-16. DOI:10.21273/HORTTECH.7.1.9.

COCHRANE, T.A. and FLANAGAN, D.C. (1996). Detachment in a simulated rill. *Transactions of the American Society of Agricultural Engineers* 40 (1), 111-119. DOI:10.13031/2013.21255.

COMINA, C., LASAGNA, M., DE LUCA, D.A. and SAMBUELLI, L. (2014). Geophysical methods to support correct water sampling locations for salt dilution gauging. *Hydrology and Earth System Science*, 18(8), 3195-3203. DOI:10.5194/hess-18-3195-2014.

COMITI, F., MAO, L., WILCOX, A., WOHL, E.E. and LENZI, M.A. (2007). Field-derived relationships for flow velocity and resistance in high-gradient streams. *Journal of Hydrology*, 340(1-2), 48-62. DOI:10.1016/j.jhydrol.2007.03.021.

COOK, H.F., VALDES, G.S.B. and LEE, H.C. (2006). Mulch effects on rainfall interception, soil physical characteristics and temperature under Zea mays L. *Soil & Tillage Research*, 91(1-2), 227-235. DOI:10.1016/j.still.2005.12.007.

COSENTINO, D., HALLETT, P.D., MICHEL, J.C. and CHENU, C. (2010). Do different methods for measuring the hydrophobicity of soil aggregates give the same trends in soil amended with residue? *Geoderma*, 159(1-2), 221-227. DOI:10.1016/j.geoderma.2010.07.015.

COZ, J.L., HAUET, A., PIEEFEU, G., DRAMAIS, G. and CAMENEN, B. (2010). Performance of image-based velocimetry LSPIV applied to flash-flood discharge measurements in

Mediterranean rivers. *Journal of Hydrology*, 394(1-2), 42-52. DOI:10.1016/j.jhydrol.2010.05.049.

CUOMO, S., DELLA SALA, M. and PIERRI, M. (2016). Experimental evidences and numerical modelling of runoff and soil erosion in flume tests. *CATENA*, 147, 61-70. DOI:10.1016/j.catena.2016.06.044.

DANIELESCU, S., MACQUARRIE, K.T.B. and FAUX, R.N. (2009). The integration of thermal infrared imaging, discharge measurements and numerical simulation to quantify the relative contributions of freshwater inflows to small estuaries in Atlantic Canada. *Hydrological Processes*, 23(20), 2847-2859. DOI:10.1002/hyp.7383.

DARBOUX, F. and HUANG, C. (2003). An instantaneous-profile laser scanner to measure soil surface microtopography. *Soil Science Society of America Journal*, 67(1), 92-99. DOI:10.2136/sssaj2003.9200.

DARBOUX, F., DAVY, PH., GASCUEL-ODOUX, C. and HUANG, C. (2001). Evolution of soil surface roughness and flowpath connectivity in overland flow experiments. *CATENA*, 46(2-3), 124-139. DOI:10.1016/S0341-8162(01)00162-X.

DAY, T.J. (1977). Observed mixing lengths in mountain streams. *Journal of Hydrology*, 35(1-2), 125-136. DOI:10.1016/0022-1694(77)90081-6.

DE LIMA, C.A., DE LIMA, J.L.M.P., MONTENEGRO, A.A.A., ABRANTES, J.R.C.B., MUJTABA, B. and SILVEIRA, A. (2018). Comparative evaluation of factors influencing seed displacement over the soil of nonconventional perennial crops: moringa (Moringa oleifera Lam.) and neem (Azadirachta indica A. Juss.). *Soil Science*, 182(8), 267-277. DOI:10.1097/SS.0000000000000219.

DE LIMA, J.L.M.P. and ABRANTES, J.R.C.B. (2014a). Can infrared thermography be used to estimate soil surface microrelief and rill morphology? *Catena*, 113, 314-322. DOI:10.1016/j.catena.2013.08.011.

DE LIMA, J.L.M.P. and ABRANTES, J.R.C.B. (2014b). Using a thermal tracer to estimate overland and rill flow velocities. *Earth Surface Processes and Landforms*, 39(10), 1293-1300. DOI:10.1002/esp.3523.

DE LIMA, J.L.M.P. and SINGH, V.P. (2002). The influence of the pattern of moving rainstorms on overland flow. *Advances in Water Resources*, 25(7), 817-828. DOI:10.1016/S0309-1708(02)00067-2.

DE LIMA, J.L.M.P., ABRANTES, J.R.C.B., SILVA JR., V.P., DE LIMA, M.I.P. and MONTENEGRO, A.A.A. (2014a). Mapping soil surface macropores using infrared thermography: exploratory laboratory study. *Scientific World Journal*, 2014, 845460. DOI:10.1155/2014/845460.

DE LIMA, J.L.M.P., ABRANTES, J.R.C.B., SILVA, JR., V.P. and MONTENEGRO, A.A.A. (2014b). Prediction of skin surface soil permeability by infrared thermography: a soil flume experiment. *Quantitative InfraRed Thermography Journal*, 11(2), 161-169. DOI:10.1080/17686733.2014.945325.

DE LIMA, J.L.M.P., CARVALHO, S.C.P. and DE LIMA, M.I.P. (2013a). Rainfall simulator experiments on the importance of when rainfall burst occurs during storm events on runoff and soil loss. *Zeitschrift für Geomorphologie*, 57(1), 91-109. DOI:10.1127/0372-8854/2012/S-00096.

DE LIMA, J.L.M.P., DE LIMA, M.I.P. and SINGH, V.P. (2005). The importance of the direction, speed, intensity and length of moving storms on water erosion. In A. FAZ CANO, R. ORTIZ SILLA and A.R. MERMUT (Eds.), *Advances in Geoecology 36 - Sustainable Use and Management of Soils: Arid and Semiarid Regions.* Reiskirchen, Germany: Catena Verlag. pp. 163-176.

DE LIMA, J.L.M.P., DINIS, P.A., SOUZA, C.S., DE LIMA, M.I.P., CUNHA, P.P., AZEVEDO, J.M., SINGH, V.P. and ABREU, J.M. (2011). Patterns of grain-size temporal variation of sediment transported by overland flow associated with moving storms: interpreting soil flume experiments. *Natural Hazards and Earth System Science*, 11, 2605-2615. DOI:10.5194/nhess-11-2605-2011.

DE LIMA, J.L.M.P., SILVA JR., V.P., ABRANTES, J.R.C.B., MONTENEGRO, A.A.A. and DE LIMA, M.I.P. (2014c). In situ observation of soil macropores using infrared thermography. *Die Bodenkultur: Journal of Land Management, Food and Environment*, 65(3-4), 57-62. Retrieved from https://boku.ac.at/en/fos/themen/die-bodenkultur/inhalte/band-65-2014/band-65-heft-3-4/de-lima-silva.

DE LIMA, J.L.M.P., SILVA, JR., V.P., DE LIMA, M.I.P., ABRANTES, J.R.C.B. and MONTENEGRO, A.A.A. (2015a). Revisiting simple methods to estimate drop size distributions: a novel approach based on infrared thermography. *Journal of Hydrology Hydromechanics*, 63(3), 220-227. DOI:10.1515/johh-2015-0025.

DE LIMA, J.L.M.P., SINGH, V.P. and DE LIMA, M.I.P. (2003). The influence of storm movement on water erosion: Storm direction and velocity effects. *CATENA*, 52(1), 39-56. DOI:10.1016/S0341-8162(02)00149-2.

DE LIMA, J.L.M.P., SOUZA, C.S. and SINGH, V.P. (2008). Granulometric characterization of sediments transported by surface runoff generated by moving storms. *Nonlinear Processes in Geophysics*, 15, 999-1011. DOI:10.5194/npg-15-999-2008.

DE LIMA, J.L.M.P., TAVARES, P., SINGH, V.P. and DE LIMA, M.I.P. (2009). Investigating the nonlinear response of soil loss to storm direction using a circular soil flume. *Geoderma*, 152(1-2), 9-15. DOI:10.1016/j.geoderma.2009.05.004.

DE LIMA, M.I.P. and GRASMAN, J. (1999). Multifractal analysis of 15-min and daily rainfall from a semi-arid region in Portugal. *Journal of Hydrology*, 220(1-2), 1-11. DOI:10.1016/S0022-1694(99)00053-0.

DE LIMA, M.I.P., ESPÍRITO SANTO, F., RAMOS, A.M. and DE LIMA, J.L.M.P. (2013b). Recent changes in daily precipitation and surface air temperature extremes in mainland Portugal, in the period 1941-2007. *Atmospheric Research*, 127, 195-209. DOI:10.1016/j.atmosres.2012.10.001.

DE LIMA, M.I.P., SCHERTZER, D., LOVEJOY, S. and DE LIMA, J.L.M.P. (2002). Multifractals and the study of extreme precipitation events: a case study from semi-arid and humid regions in Portugal. In V.P. SINGH, M. AL-RASHID and M.M. SHERIF (Eds.), *Surface Water Hydrology*. Rotterdam, The Netherlands: A.A. Balkema Publishers. pp. 195-211.

DE LIMA, R.L.P (2013). *Development of a method using infrared thermography for shallow flow visualization and quantitative estimation of velocity*. MSc Thesis, University of Coimbra, Coimbra, Portugal. 77 pp.

DE LIMA, R.L.P., ABRANTES, J.R.C.B., DE LIMA, J.L.M.P. and DE LIMA, M.I.P. (2015b). Using thermal tracers to estimate flow velocities of shallow flows: laboratory and field experiments. *Journal of Hydrology Hydromechanics*, 63(3), 255-262. DOI:10.1515/johh-2015-0028.

DE MARSILY, G. (1986). *Quantitative Hydrogeology: Groundwater Hydrology for Engineers*. San Diego, California, USA: Academic Press. 440 pp.

DE VENTE, J., POESEN, J., VERSTRAETEN, G., GOVERS, G., VANMAERCKE, M., ROMPAEY, A.V., ARABKHEDRI, M. and BOIX-FAYOS, C. (2013). Predicting soil erosion and sediment yield at regional scales: where do we stand? *Earth-Science Reviews*, 127, 16-29. DOI:10.1016/j.earscirev.2013.08.014.

DEBANO, L.F. (2000a). The role of fire and soil heating on water repellency in wildland environments: a review. *Journal of Hydrology*, 231-232, 195-206. DOI:10.1016/S0022-1694(00)00194-3.

DEBANO, L.F. (2000b). SWR in soils: a historical overview. *Journal of Hydrology*, 231-232, 4-32. DOI:10.1016/S0022-1694(00)00180-3.

DEHVARI, A. and HECK, R.J. (2007). Comparison of object-based and pixel based infrared airborne image classification methods using DEM thematic layer. *Journal of Geography and Regional Planning*, 2(4), 86-96. DOI:10.5897/JGRP2009.5B0C0A51198.

DEKKER, L.W. and RITSEMA, C.J. (1994). How water moves in a water-repellent sandy soil: 1. Potential and actual water-repellency. *Water Resources Research*, 30(9), 2507-2517. DOI:10.1029/94WR00749.

DEKKER, L.W., RITSEMA, C.J., OOSTINDIE, K., MOORE, D. and WESSELING, J.G. (2009). Methods for determining soil water repellency on field-moist samples. Water Resources Research 45(4), W00D33. DOI:10.1029/2008WR007070.

DENG Z.Q. DE LIMA J.L.M.P. and SINGH V.P. (2005). Transport rate-based model for overland flow and solute transport: Parameter estimation and process simulation. *Journal of Hydrology*, 315(1-4), 220-235. DOI:10.1016/j.jhydrol.2005.03.042.

DENG, Z.Q., DE LIMA, J.L.M.P. and JUNG, H.S. (2008). Sediment transport rate-based model for rainfall-induced soil erosion. *CATENA*, 76 (1), 54-62. DOI:10.1016/j.catena.2008.09.005.

DIS4ME (2013). *EU Research Project - DESERTLINKS*. Retrieved from http://www.kcl.ac.uk/projects/desertlinks/accessdis4me.htm. Accessed at 7 November 2013.

DOERR, S.H. and THOMAS, A.D. (2000). The role of soil moisture in controlling water repellency: new evidence from forest soils in Portugal. *Journal of Hydrology*, 231-232, 134-147. DOI:10.1016/S0022-1694(00)00190-6

DOERR, S.H., SHAKESBY, R.A. and WALSH, R.P.D. (1998). Spatial variability of hydrophobicity in fire-prone eucalyptus and pine forests, Portugal. *Soil Science*, 163(4), 313-324. DOI:10.1097/00010694-199804000-00006.

DOERR, S.H., SHAKESBY, R.A. and WALSH, R.P.D. (2000). Soil water repellency: its causes, characteristics and hydro-geomorphological significance. *Earth-Science Reviews*, 51(1-4), 33-65. DOI:10.1016/S0012-8252(00)00011-8.

DONG, W. and WANG, Q. (2013). Modeling soil solute release into runoff and transport with runoff on a Loess slope. *Journal of Hydrologic Engineering*, 18(5), 527-535. DOI:10.1061/(ASCE)HE.1943-5584.0000622.

DUGDALE, S.J., BERGERON, N.E. and ST-HILAIRE, A. (2013). Temporal variability of thermal refuges and water temperature patterns in an Atlantic salmon river. *Remote Sensing of Environment* 136, 358-373. DOI:10.1016/j.rse.2013.05.018.

DUGDALE, S.J., KELLEHER, C.A., MALCOLM, I.A., CALDWELL, S. and HANNAH, D.M. (2019). Assessing the potential of drone-based thermal infrared imagery for quantifying river temperature heterogeneity. Hydrological Processes, 33(7), 1152-1163. DOI:10.1002/hyp.13395.

DUNKERLEY, D. (2001). Estimating the mean speed of laminar overland flow using dye injection-uncertainty on rough surfaces. *Earth Surface Processes and Landforms*, 26(4), 363-374. DOI:10.1002/esp.185.

DUNKERLEY, D. (2003). An optical tachometer for short-path measurement of flow speeds in shallow overland flows: improved alternative to dye timing. *Earth Surface Processes and Landforms*, 28(7), 777-786. DOI:10.1002/esp.468.

DUNNE, T. and BLACK, R. (1970). Partial area contributions to storm runoff in a small New England watershed. *Water Resources Research* 6(5), 1296-1311. DOI:10.1029/WR006i005p01296.

EGEA, G., PADILLA-DÍAZ, C.M., MARTINEZ-GUANTER, J., FERNÁNDEZ, J.E. and PÉREZ-RUIZ, M. (2017). Assessing a crop water stress index derived from aerial thermal imaging and infrared thermometry in super-high density olive orchards. *Agricultural Water Management*, 187, 210-221. DOI:10.1016/j.agwat.2017.03.030.

EIGEL, J.D. and MOORE, I.D. (1983). A simplified technique for measuring raindrop size and distribution. *Transactions of the American Society of Agricultural Engineers*, 26 (4), 1079-1084. DOI:10.13031/2013.34080.

EITEL, J.U.H., WILLIAMS, C.J., VIERLING, L.A., AL-HAMDAN, O.Z. and PIERSON, F.B. (2011). Suitability of terrestrial laser scanning for studying surface roughness effects on concentrated flow erosion processes in rangelands. *CATENA* 87 (3), 398-407. DOI:10.1016/j.catena.2011.07.009.

ELRICK, D.E. and REYNOLDS, W.D. (1992). Methods for analyzing constant-head well permeameter data. *Soil Science Society of America Journal* 56 (1), 320-323. DOI:10.2136/sssaj1992.03615995005600010052x.

EMERY, W.J. and YU, Y. (1997). Satellite sea surface temperature patterns. *International Journal of Remote Sensing*, 18 (2), 323-34. DOI:10.1080/014311697219097.

EMMETT, W.W. (1970). *The Hydraulics of Overland Flow on Hillslopes*. Geological Survey Professional Paper 662-A. Washington, D.C., USA: U.S. Government Printing Office. 74 pp.

ESTEVES, M., FAUCHER, X., GALLE, S. and VAUCLIN, M. (2000). Overland flow and infiltration modelling for small plots during unsteady rain: numerical results versus observed values. *Journal of Hydrology*, 228(3-4), 265-282. DOI:10.1016/S0022-1694(00)00155-4.

FAN, J.C. and WU, M.F. (1999). Effects of soil strength, texture, slope steepness and rainfall intensity on interrill erosion of some soils in Taiwan. In D.E. STOTT, R.H. MOTHAR and D.C. STEIHARDT (Eds.), *Sustaining the Global Farm - Selected Papers from the 10th International Soil Conservation Organization Meeting*. West Lafayette, IN, USA: Purdue University. pp. 588-593.

FAVIS-MORTLOCK, D.T. (1998). A self-organizing dynamic systems approach to the simulation of rill initiation and development on hillslopes. *Computers & Geosciences*, 24(4), 353-372. DOI:10.1016/S0098-3004(97)00116-7.

FAVIS-MORTLOCK, D.T., BOARDMAN, J., PARSONS, A.J. and LASCELLES, B. (2000). Emergence and erosion: a model for rill initiation and development. *Hydrological Processes*, 14 (11-12), 2173-2205. DOI:10.1002/1099-1085(20000815/30)14:11/12<2173::AID-HYP61>3.0.CO;2-6.

FERREIRA, C.S.S., WALSH, R.P.D., SHAKESBY, R.A., KEIZER, J.J., SOARES, D., GONZÁLEZ-PELAYO, O., COELHO, C.O.A. and FERREIRA, A.J.D. (2016). Differences in overland flow, hydrophobicity and soil moisture dynamics between Mediterranean woodland types in a peri-urban catchment in Portugal. *Journal of Hydrology*, 533, 473-485. DOI:10.1016/j.jhydrol.2015.12.040.

FINKNER, S.C., NEARING, M.A., FOSTER, G.R. and GILLEY, E. (1989). A simplified equation for modeling sediment transport capacity. *Transactions of the American Society of Agricultural Engineers*, 32(5), 1545-1550. DOI:10.13031/2013.31187.

FLANAGAN, D.C. and NEARING, M.A. (1995). *USDA-Water Erosion Prediction Project: Hillslope Profile and Watershed Model Documentation*. NSERL Report No. 10. West Lafayette, IN, USA: USDA-ARS.

FLETCHER, T.D., ANDRIEU, H. and HAMEL, P. (2013). Understanding, management and modelling of urban hydrology and its consequences for receiving waters: a state of the art. *Advances in Water Resources*, 51, 261-279. DOI:10.1016/j.advwatres.2012.09.001.

FLURY, M. and FLÜHLER, H. (1993). Brilliant Blue FCF as a dye tracer for solute transport studies: a toxicological overview. *Journal of Environmental Quality*, 23(5), 1108-1112. DOI:10.2134/jeq1994.00472425002300050037x.

FLURY, M. and WAI, N.N. (2003). Dyes as tracers for vadose zone hydrology. *Reviews of Geophysics*, 41(1), 1002. DOI:10.1029/2001RG000109.

FLURY, M., FLÜHLER, H., JURY, W.A. and LEUENBERGER, J. (1994). Susceptibility of soils to preferential flow of water: a field study. *Water Resources Research*, 30(7), 1945-1954. DOI:10.1029/94WR00871.

FOHRER, N., BERKENHAGEN, J., HECKER, J.M. and RUDOLPH, A. (1999). Changing soil and surface conditions during rainfall: Single rainstorm/subsequent rainstorms. *CATENA*, 37(3-4), 355-375. DOI:10.1016/S0341-8162(99)00026-0.

FULTON, J. and OSTROWSKI, J. (2008). Measuring real-time streamflow using emerging technologies: Radar, hydroacoustics, and the probability concept. *Journal of Hydrology*, 357(1-2), 1-10. DOI:10.1016/j.jhydrol.2008.03.028.

GABELLANI, S., SILVESTRO, F., RUDARI, R. and BONI, G. (2008). General calibration methodology for a combined Horton-SCS infiltration scheme in flash flood modeling. *Natural Hazards and Earth System Sciences*, 8, 1317-1327. DOI:10.5194/nhess-8-1317-2008.

GABRIELLI, C.P., MCDONNELL, J.J. and JARVIS, W.T. (2012). The role of bedrock groundwater in rainfall–runoff response at hillslope and catchment scales. *Journal of Hydrology*, 450-451, 117-133. DOI:10.1016/j.jhydrol.2012.05.023.

GADE, R. and MOESLUND, T.B. (2014). Thermal cameras and applications: a survey. *Machine Vision and Applications*, 25, 245-262. DOI:10.1007/s00138-013-0570-5.

GARCÍA MORENO, R., DÍAZ ÁLVAREZ, M.C., TARQUIS, M., PAZ GONZÁLEZ, A. and SAA REQUEJO, A. (2010). Shadow analysis of soil surface roughness compared to the chain set method and direct measurement of micro-relief. *Biogeosciences*, 7, 2477-2487. DOI:10.5194/bg-7-2477-2010.

GARCIA MORENO, R., SAA REQUEJO, A., TARQUIS ALONSO, A.M., BARRINGTON, S. and DÍAZ, M.C. (2008). Shadow analysis: A method for measuring soil surface roughness. *Geoderma*, 146(1-2), 201-208. DOI:10.1016/j.geoderma.2008.05.026.

GARCIA, R. and KAHAWITA, R.A. (1986). Numerical solution of the St. Venant equations with the MacCormack finite-differece scheme. *International Journal for Numerical Methods in Fluids*, 6(5), 259-274. DOI:10.1002/fld.1650060502.

GARCIA-NAVARRO, P. and SAVIRON, J.M. (1992). McCormack's method for the numerical simulation of one-dimensional discontinuous unsteady open channel flow. *Journal of Hydraulic Research*, 30(1), 95-105. DOI:10.1080/00221689209498949.

GILLEY, J.E. and KOTTWITZ, E.R. (1995). Random roughness assessment by the pin and chain method. *Applied Engineering in Agriculture*, 12(1), 39-43. DOI:10.13031/2013.25437.

GIMÉNEZ, R. and GOVERS, G. (2002). Flow detachment by concentrated flow on smooth and irregular beds. *Soil Science Society of America Journal*, 66(5), 1475-1483. DOI:10.2136/sssaj2002.1475.

GIMÉNEZ, R., PLANCHON, O., SILVERA, N. and GOVERS, G. (2004). Longitudinal velocity patterns and bed morphology interaction in a rill. *Earth Surface Processes and Landforms*, 29(1), 105-114. DOI:10.1002/esp.1021.

GÓMEZ, J.A. and NEARING, M.A. (2005). Runoff and sediment losses from rough and smooth soil surfaces in a laboratory experiment. *CATENA*, 59 (3), 253-266. DOI:10.1016/j.catena.2004.09.008.

GOMI, T., SIDLE, R.C., UENO, M., MIYATA, S. and KOSUGI, K. (2008). Characteristics of overland flow generation on steep forested hillslopes of central Japan. *Journal of Hydrology*, 361(3-4), 275-290. DOI:10.1016/j.jhydrol.2008.07.045.

GOVERS, G. (1992). Relationship between discharge, velocity and flow area for rills eroding loose, non layered materials. *Earth Surface Processes and Landforms*, 17(5), 515-528. DOI:10.1002/esp.3290170510.

GOVERS, G. and POESEN, J. (1988). Assessment of the interrill and rill contributions to total soil loss from an upland field plot. *Geomorphologie*, 1(4), 343-354. DOI:10.1016/0169-555X(88)90006-2.

GOVERS, G., GIMÉNEZ, R. and OOST, K.V. (2007). Rill erosion: exploring the relationship between experiments, modelling and field observations. *Earth-Science Reviews*, 84 (3-4), 87-102. DOI:10.1016/j.earscirev.2007.06.001.

GOVERS, G., VAN OOST, K. and POESEN, J. (2006). Responses of a semi-arid landscape to human disturbance: a simulation study of the interaction between rock fragment cover, soil erosion and land use change. *Geoderma*, 133(1-2), 19-31. DOI:10.1016/j.geoderma.2006.03.034.

GRANT, O.M., TRONINA, L., JONES, L., JONES, H.G. and CHAVES, M.M. (2007). Exploring thermal imaging variables for the detection of stress responses in grapevine under different irrigation regimes. *Journal of Experimental Botany*, 58(4), 815-825. DOI:10.1093/jxb/erl153.

GREENE, D. (2001). Architecture and the rain. *The Journal of Architecture*, 6(2), 195-200. DOI:10.1080/13602360110048212.

GRIFFITH, C.G., WOODLEY, W.L., GRUBE, P.G., MARTIN, D.W., STOUT, J. and SIKDAR, D.N. (1978). Rain estimation from geosynchronous satellite imagery: visible and infrared studies. *Monthly Weather Review*, 106(8), 1153-1171. DOI:10.1175/1520-0493(1978)106<1153:REFGSI>2.0.CO;2.

HANSEN, B., SCHJØNNING, P. and SIBBESEN, E. (1999). Roughness indices for estimation of depression storage capacity of tilled soil surfaces. *Soil & Tillage Research*, 52(1-2), 103-111. DOI:10.1016/S0167-1987(99)00061-6.

HARDIE, M., LISSON, S., DOYLE, R. and COTCHING, W. (2013). Determining the frequency, depth and velocity of preferential flow by high frequency soil moisture monitoring. *Journal of Contaminant Hydrology*, 144, 66-77. DOI:10.1016/j.jconhyd.2012.10.008.

HASHIMOTO, Y., INO, T., KRAMER, P.J., NAYLOR, A.W. and STRAIN, B.R. (1984). Dynamic analysis of water stress of sunflower leaves by means of a thermal image processing system. *Plant Physiology*, 76, 266-269. DOI:10.1104/pp.76.1.266.

HAVERKAMP, R., DEBIONNE, S., VIALLET, P., ANGULO-JARAMILLO, R. and DE CONDAPPA, D. (2006). Soil properties and moisture movement in the unsaturated zone. In J.W. DELLEUR (Ed.), *The Handbook of Groundwater Engineering*. Boca Raton, FL, USA: CRC Press. pp. 6.1-6.59.

HEATHWAITE, A.L. (2010). Multiple stressors on water availability at global to catchment scales: understanding human impact on nutrient cycles to protect water quality and water availability in the long term. *Freshwater Biology*, 55(s1), 241-257. DOI:10.1111/j.1365-2427.2009.02368.x.

HESSEL, R. and TENGE, A. (2008). A pragmatic approach to modelling soil and water conservation measures with a catchment scale erosion model. *CATENA*, 74(2), 119-126. DOI:10.1016/j.catena.2008.03.018.

HOGG, S.E. (1982). Sheetfloods, sheetwash, sheetflow, or ...? *Earth-Science Reviews*, 18(1), 59-76. DOI:10.1016/0012-8252(82)90003-4.

HOLDEN, J., KIRKBY, M.J., LANE, S.N., MILLEDGE, D.G., BROOKES, C.J., HOLDEN, V. and MCDONALD, A.T. (2008). Overland flow velocity and roughness properties in peatlands. *Water Resources Research*, 44(6), W06415. DOI:10.1029/2007WR006052.

HOOK, S.J., PRATA, F.J., ALLEY, R.E., ABTAHI, A., RICHARDS, R.C., SCHLADOW, S.G. and PÁLMARSSON, S. (2003). Retrieval of lake bulk and skin temperatures using along-track scanning radiometer (ATSR-2) data: a case study using Lake Tahoe, California. *Journal of Atmospheric and Oceanic Technology*, 20(4), 534-548. DOI:10.1175/1520-0426(2003)20<534:ROLBAS>2.0.CO;2.

HORTON, R.E. (1933). The role of infiltration in the hydrologic cycle. *Transactions of the American Geophysical Union*, 14(1), 446-460. DOI:10.1029/TR014i001p00446.

HORTON, R.E. (1940). An approach towards physical interpretation of infiltration capacity. *Soil Science Society of America Journal*, 5, 399-417. DOI:10.2136/sssaj1941.036159950005000C0075x

HORTON, R.E., LEACH, H.R. and VLIET, V.R. (1934). Laminar sheet flow. *Transactions of the American Geophysical Union*, 15(2), 393-404. DOI:10.1029/TR015i002p00393.

HUANG, C. (1998). Quantification of soil microtopography and surface roughness. In P. BAVEYE, J.Y. PARLANGE and B.A. STEWART (Eds.), *Fractals in Soil Science*. Boca Raton, FL, USA: CRC Press. pp. 143-168.

HUANG, Y., CHEN, X., LI, F., ZHANG, J., LEI, T., LI, J., CHEN, P. and WANG, X. (2018). Velocity of water flow along saturated loess slopes under erosion effects. *Journal of Hydrology*, 561, 304-311. DOI:10.1016/j.jhydrol.2018.03.070.

ISIDORO J.M.G.P. and DE LIMA J.L.M.P. (2013). An analytical closed form solution for 1D kinematic overland flow under moving rainstorms. *Journal of Hydrological Engineering*, 18(9), 1148-1156. DOI:10.1061/(ASCE)HE.1943-5584.0000740.

ISIDORO, J.M.G.P. (2012). *Modelling the influence of storm movement and wind-driven rainfall on overland flow in urban areas*. PhD Thesis, University of Coimbra, Coimbra, Portugal. 207 pp.

JAJARMIZADEH, M., HARUN, S. and SALARPOUR, M. (2012). A review on theoretical consideration and types of models in hydrology. *Journal of Environmental Science and Technology*, 5(5), 249-261. DOI:10.3923/jest.2012.249.261.

JAN, C.D., CHEN, T.H. and LO, W.C. (2007). Effect of rainfall intensity and distribution on groundwater level fluctuations. *Journal of Hydrology*, 332(3-4), 348-360. DOI:10.1016/j.jhydrol.2006.07.010.

JARVIS, N.J. (2007). A review of non-equilibrium water flow and solute transport in soil macropores: Principles, controlling factors and consequences for water quality. *European Journal of Soil Science*, 58, 523-546. DOI:10.1111/j.1365-2389.2007.00915.x.

JESTER, W. and KLIK, A. (2005). Soil surface roughness measurement-methods, applicability, and surface representation. *CATENA*, 64(2-3), 174-192. DOI:10.1016/j.catena.2005.08.005.

JETTEN, V., GOVERS, G. and HESSEL, R. (2003). Erosion models: quality and spatial predictions. *Hydrological Processes* 17 (5), 887-900. DOI:10.1002/hyp.1168.

JINKANG, DU., SHUNPING, X., YOUPENG, X., XU, C. and SINGH, V.P. (2007). Development and testing of a simple physically-based distributed rainfall-runoff model for storm runoff simulation in humid forested basins. *Journal of Hydrology*, 336(3-4), 334-346. DOI:10.1016/j.jhydrol.2007.01.015.

JODEAU, M., HAUET, A., PAQUIER, A., LE COZ, J. and DRAMAIS, G. (2008). Application and evaluation of LS-PIV technique for the monitoring of river surface velocities in high flow conditions. *Flow Measurement and Instrumentation*, 19(2), 117-127. DOI:10.1016/j.flowmeasinst.2007.11.004.

JOMAA, S., BARRY, D.A., BROVELLI, A., HENG, B.C.P., SANDER, G.C., PARLANGE, J.Y. and ROSE, C.W. (2012). Rain splash soil erosion estimation in the presence of rock fragments. *CATENA*, 92, 38-48. DOI:10.1016/j.catena.2011.11.008.

JONES, D.M.A. (1992). Raindrop spectra at the ground. *Journal of Applied Meteorology*, 31(10), 1219-1225. DOI:10.1175/1520-0450(1992)031<1219:RSATG>2.0.CO;2.

JORDÁN, A., ZAVALA, L.M. and GIL, J. (2010). Effects of mulching on soil physical properties and runoff under semi-arid conditions in Southern Spain. *CATENA*, 81(1), 77-85. DOI:10.1016/j.catena.2010.01.007.

JOSS, J. and WALDVOGEL, A. (1969). Raindrop size distribution and sampling size errors. *Journal of the Atmospheric Sciences*, 26(3), 566-569. DOI:10.1175/1520-0469(1969)026<0566:RSDASS>2.0.CO;2.

JULIEN, P.Y. and SIMMONS, D.B. (1985). Sediment transport capacity of overland flow. *Transactions of the American Society of Agricultural Engineers*, 28(3), 755-762. DOI:10.13031/2013.32333.

KAGABO, D.M., STROOSNIJDER, L., VISSER, S.M. and MOORE, D. (2013). Soil erosion, soil fertility and crop yield on slow-forming terraces in the highlands of Buberuka, Rwanda. *Soil & Tillage Research*, 128, 23-29. DOI:10.1016/j.still.2012.11.002.

KALFF, A., DOWNING, J.A. and SMITH, T.T. (1985). Rainfall, agriculture, livestock and human density in the dry regions of Kenya. *Journal of Arid Environments*, 9, 173-183. DOI:10.1016/S0140-1963(18)31499-X.

KAMPHORST, E.C. and DUVAL, Y. (2001). Validation of a numerical method to quantify depression storage by direct measurements on moulded surfaces. *CATENA*, 43(1), 1-14. DOI:10.1016/S0341-8162(00)00123-5.

KAMPHORST, E.C., JETTEN, V., GUÉRIF, J., PITKÄNEN, J., IVERSEN, B.V., DOUGLAS, J.T. and PAZ, A. (2000). Predicting depressional storage from soil surface roughness. *Soil Science Society of America Journal*, 64(5), 1749-1758. DOI:10.2136/sssaj2000.6451749x.

KANTOUSH, S.A., SCHLEISS, A.J., SUMI, T. and MURASAKI, M. (2011). LSPIV implementation for environmental flow in various laboratory and field cases. Journal of Hydro-environment Research, 5(4), 263-276. DOI:10.1016/j.jher.2011.07.002.

KEIZER, J.J., COELHO, C.O.A., MATIAS, M.J.S., DOMINGUES, C.S.P. and FERREIRA, A.J.D. (2005a). Soil water repellency under dry and wet antecedent weather conditions for selected land-cover types in the coastal zone of central Portugal. *Soil Research*, 43(3), 297-308. DOI:10.1071/SR04095.

KEIZER, J.J., COELHO, C.O.A., SHAKESBY, R.A., DOMINGUES, C.S.P., MALVAR, M.C., PEREZ, I.M.B., MATIAS, M.J.S. and FERREIRA, A.J.D. (2005b). The role of soil water repellency in overland flow generation in pine and eucalypt forest stands in coastal Portugal. *Soil Research*, 43(3), 337-349. DOI:10.1071/SR04085.

KEIZER, J.J., DOERR, S.H., MALVAR, M.C., FERREIRA, A.J.D. and PEREIRA, V.M.F.G. (2007). Temporal and spatial variations in topsoil water repellency throughout a crop-rotation cycle on sandy soil in north central Portugal. *Hydrological Processes*, 21(17), 2317-2324. DOI:10.1002/hyp.6756.

KEIZER, J.J., DOERR, S.H., MALVAR, M.C., PRATS, S.A., FERREIRA, R.S.V., OÑATE, M.G., COELHO, C.O.A. and FERREIRA, A.J.D. (2008). Temporal variation in topsoil water

repellency in two recently burnt eucalypt stands in north-central Portugal. *CATENA*, 74(3), 192-204. DOI:10.1016/j.catena.2008.01.004.

KEIZER, J.J., FERREIRA, A.J.D., COELHO, C.O.A., DOERR, S.H., MALVAR, M.C., DOMINGUES, C.S.P., PEREZ, I.M.B., RUIZ, C. and FERRARI, K. (2005c). The role of tree stem proximity in the spatial variability of soil water repellency in a eucalypt plantation in coastal Portugal. *Soil Research*, 43(3), 251-259. DOI:10.1071/SR04096.

KELLY, J.L., DULAI, H., GLENN, C.R. and LUCEY, P.G. (2018). Integration of aerial infrared thermography and in situ radon-222 to investigate submarine groundwater discharge to Pearl Harbor, Hawaii, USA. *Limnology and Oceanography*, 64(1), 238-257. DOI:10.1002/lno.11033.

KETEMA, A. and DWARAKISH, G.S. (2019). Water erosion assessment methods: a review. *Journal of Hydraulic Engineering*. DOI: 10.1080/09715010.2019.1567398

KIDRON, G.J. (2007). Millimeter-scale microrelief affecting runoff yield over microbiotic crust in the Negev Desert. *CATENA*, 70(2), 266-273. DOI:10.1016/j.catena.2006.08.010.

KIM, Y., MUSTE, M., HAUET, A., KRAJEWSKI, W.F., KRUGER, A. and BRADLEY, A. (2008). Stream discharge using mobile large-scale particle image velocimetry: a proof of concept. *Water Resources Research*, 44(9), W09502. DOI:10.1029/2006WR005441.

KIMIAGHALAM, N., GOHARROKHI, M. and CLARK, S.P. (2016). Assessment of wide river characteristics using an acoustic Doppler current profiler. *Journal of Hydraulic Engineering*, 21(12), 06016012. DOI:10.1061/(ASCE)HE.1943-5584.0001447.

KING, P.M. (1981) Comparison of methods for measuring severity of water repellence of sandy soils and assessment of some factors that affect its measurement (Australia). *Australian Journal of Soil Research*, 19(3), 275-285. DOI:10.1071/SR9810275.

KINNELL, P.I.A. (2005). Raindrop-impact-induced erosion processes and prediction: a review. *Hydrological Processes*, 19(14), 2815-2844. DOI:10.1002/hyp.5788.

KNAPEN, A., POESEN, J., GOVERS, G., GYSEELS, G. and NACHTERGAELE, J. (2007). Resistance of soils to concentrated flow erosion: a review. *Earth-Science Reviews*, 80(1-2), 75-109. DOI:10.1016/j.earscirev.2006.08.001.

KNOLLENBERG, R.G. 1970. The optical array: An alternative to scattering or extinction for airborne particle size determination. *Journal of Applied Meteorology*, 9(1), 86-103. DOI:10.1175/1520-0450(1970)009<0086:TOAAAT>2.0.CO;2.

KÖHNE, J.M., KÖHNE, S. and ŠIMŮNEK, J. (2009). A review of model applications for structured soils: a) water flow and tracer transport. *Journal of Contaminant Hydrology*, 104(1-4), 4-35. DOI:10.1016/j.jconhyd.2008.10.002.

KREIBICH, H., PIROTH, K., SEIFERT, I., MAIWALD, H., KUNERT, U., SCHWARZ, J., MERZ, B. and THIEKEN, A.H. (2009). Is flow velocity a significant parameter in flood damage modelling? *Natural Hazards and Earth System Sciences*, 9(5), 1679-1692. DOI:10.5194/nhess-9-1679-2009.

LEGOUT, C., DARBOUX, F., NÉDÉLEC, Y., HAUET, A., ESTEVES, M., RENAUX, B., DENIS, H. and CORDIER, S. (2012). High spatial resolution mapping of surface velocities and depths for shallow overland flow. *Earth Surface Processes and Landforms*, 37(9), 984-993. DOI:10.1002/esp.3220.

LEI, T., CHUO, R., ZHAO, J., SHI, X. and LIU, L. (2010). An improved method for shallow water flow velocity measurement with practical electrolyte inputs. *Journal of Hydrology*, 390(1-2), 45-56. DOI:10.1016/j.jhydrol.2010.06.029.

LEI, T., NEARING, M.A., HAGHIGHI, K. and BRALTS, V.F. (1998). Rill erosion and morphological evolution: a simulation model. *Water Resources Research*, 34(11), 3157-3168. DOI:10.1029/98WR02162.

LEI, T., XIA, W., ZHAO, J., LIU, Z. and ZHANG, Q. (2005). Method for measuring velocity of shallow water flow for soil erosion with an electrolyte tracer. *Journal of Hydrology*, 301(1-4), 139-145. DOI:10.1016/j.jhydrol.2004.06.025.

LEI, T., YAN, Y., SHI, X., CHUO, R. and ZHAO, J. (2013). Measuring velocity of water flow within a gravel layer using an electrolyte tracer method with a Pulse Boundary Model. *Journal of Hydrology*, 500, 37-44. DOI:10.1016/j.jhydrol.2013.07.025.

LEIBUNDGUT, C.H., MALOSZEWSKI, P., KÜLLS, C.H., (2009). *Tracers in Hydrology*. Chichester, West Sussex, UK: John Wiley & Sons Ltd. 432 pp.

LEIGHTON-BOYCE, G., DOERR, S.H., SHAKESBY, R.A. and WALSH, R.P.D. (2007). Quantifying the impact of soil water repellency on overland flow generation and erosion: a new approach using rainfall simulation and wetting agent on in situ soil. *Hydrological Processes*, 21(17), 2337-2345. DOI:10.1002/hyp.6744.

LEIGHTON-BOYCE, G., DOERR, S.H., SHAKESBY, R.A., WALSH, R.P.D., FERREIRA, A.J.D., BOULET, A.K. and COELHO, C.O.A. (2005). Temporal dynamics of water repellency and soil moisture in eucalypt plantations, Portugal. *Australian Journal of Soil Research*, 43(3), 269-280. DOI:10Ð1071/SR04082.

LETEY, J. (1969). Measurement of contact angle, water drop penetration time, and critical surface tension. In L.F. DEBANO and J. LETEY (Eds.), *Proceedings of the Symposium on Water-Repellent Soils*. Riverside, CA, USA: University of California. pp. 43-47.

LETEY, J., CARRILLO, M.L.K. and PANG, X.P. (2000). Approaches to characterize the degree of water repellency. *Journal of Hydrology*, 231-232, 61-65. DOI:10.1016/S0022-1694(00)00183-9.

LETEY, J., OSBORN, J. and PELISHEK, R.E. (1962). Measurement of liquid-solid contact angles in soil and sand. *Soil Science*, 93(3), 149-153. DOI:10.1097/00010694-196203000-00001.

LI, G. and ABRAHAMS, A.D. (1997). Effect of saltating sediment load on the determination of the mean velocity of overland flow. *Water Resources Research*, 33(2), 341-347. DOI:10.1029/96WR02937.

LI, G., ABRAHAMS, A.D. and ATKINSON, J.F. (1996). Correction factors in the determination of mean velocity of overland flow. *Earth Surface Processes and Landforms*, 21(6), 509-515. DOI:10.1002/SICI1096-983719960621:6<509::AID-ESP613>3.0.CO;2-Z.

LI, X.Y., CONTRERAS, S. and SOLÉ-BENET, A. (2008). Unsaturated hydraulic conductivity in limestone dolines: influence of vegetation and rock fragments. *Geoderma*, 145(3-4), 288-294. DOI:10.1016/j.geoderma.2008.03.018.

LIANG, D., CHEN, J.M., CHONG, K.J.Y. and MCCORKELL, C. (2012). Thermal imaging study of temperature fields in shallow flows. *Measurement*, 45(5), 1015-1022. DOI:10.1016/j.measurement.2012.01.042.

LIN, D., GRUNDMANN, J. and ELTNER, A. (2019). Evaluating Image Tracking Approaches for Surface Velocimetry With Thermal Tracers. *Water Resources Research*, 55(4), 3122-3136. DOI:10.1029/2018WR024507.

LIU, Q.Q., XIANG, H. and SINGH, V.P. (2006). A simulation model for unified interrill erosion and rill erosion on hillslopes. *Hydrological Processes*, 20(3), 469-486. DOI:10.1002/hyp.5915.

LIU, X. and BELJADID, A. (2017). A coupled numerical model for water flow, sediment transport and bed erosion. *Computers and Fluids*, 154, 273-284. DOI:10.1016/j.compfluid.2017.06.013.

LOCH, R.J. (1979). The measurement and description of rill erosion. In *The Hydrology of Areas of Low Precipitation - Proceedings of the Canberra Symposium.* IAHS-AISH Publ. No. 128. Wallingford, UK: IAHS. pp. 429-433.

LOCH, R.J. (2000). Effects of vegetation cover on runoff and erosion under simulated rain and overland flow on a rehabilitated site on the Meandu Mine, Tarong, Queensland. *Australian Journal of Soil Research*, 38(2), 299-312. DOI:10.1071/SR99030.

LOUCHART, X., VOLTZ, M., ANDRIEUX, P. and MOUSSA R. (2001). Herbicide transport to surface waters at field and watershed scales in a Mediterranean vineyard area. *Journal of Environmental Quality*, 30(3), 982-991. DOI:10.2134/jeq2001.303982x.

LUO, L.F., LIN, H.S. and LI, S.C. (2010). Quantification of 3-D soil macropore networks in different soil types and land uses using computed tomography. *Journal of Hydrology*, 393(1-2), 53-64. DOI:10.1016/j.jhydrol.2010.03.031.

MACCORMACK, R.W. (1971). Numerical solution of the interaction of a shock wave with a laminar boundary layer. In M. Holt (Ed.), *Proceedings of the Second International Conference on Numerical Methods in Fluid Dynamics*. Lecture Notes in Physics, 8. Heidelberg, Germany: Springer. pp. 151-163.

MAGARVEY, R.H. (1957). Stain method of drop-size determination. *Journal of Meteorology*, 14(2), 182-184. DOI:10.1175/1520-0469(1957)014<0182:SMODSD>2.0.CO;2.

MALVAR, M.C., PRATS, S.A., NUNES, J.P. and KEIZER, J.J. (2016). Soil water repellency severity and its spatio-temporal variation in burnt eucalypt plantations in north-central Portugal. *Land Degradation and Development*, 27(5), 1463-1478. DOI:10.1002/ldr.2450.

MANCILLA, G.A., CHEN, S. and MCCOOL, D.K. (2005). Rill density prediction and flow velocity distributions on agricultural areas in the Pacific Northwest. *Soil & Tillage Research*, 84(1), 54-66. DOI: DOI:10.1016/j.still.2004.10.002.

MANFREDA, S., MCCABE, M.F., MILLER, P.E., LUCAS, R., PAJUELO MADRIGAL, V., MALLINIS, G., BEN DOR, E., HELMAN, D., ESTES, L., CIRAOLO, G., MÜLLEROVÁ, J., TAURO, F., DE LIMA, M.I.P., DE LIMA, J.L.M.P., MALTESE, A., FRANCES, F., CAYLOR, K., KOHV, M., PERKS, M., RUIZ-PÉREZ, G., SU, Z., VICO, G. and TOTH, B. (2018). On the use of Unmanned Aerial Systems for environmental monitoring. *Remote Sensing*, 2018(10), 641. DOI:10.3390/rs10040641.

MANNAERTS, C.M. and GABRIELS, D. (2000). A probabilistic approach for predicting rainfall soil erosion losses in semiarid areas. *CATENA*, 40(4), 403-420. DOI:10.1016/S0341-8162(00)00089-8.

MARTINEZ-MENA, M., CASTILLO, V. and ALBALADEJO, J. (2001). Hydrological and erosional response to natural rainfall in a semi-arid area of south-east Spain. *Hydrological Processes*, 15(4), 557-571. DOI:10.1002/hyp.146.

MARTÍNEZ-MURILLO, J.F., NADAL-ROMERO, E., REGÜÉS, D., CERDÀ, A. and POESEN, J. (2013). Soil erosion and hydrology of the western Mediterranean badlands throughout rainfall simulation experiments: a review. *CATENA*, 106, 101-112. DOI:10.1016/j.catena.2012.06.001.

MARTINS, R., LEANDRO, J. and DJORDJEVIĆ, S. (2018). Wetting and drying numerical treatments for the Roe Riemann scheme. *Journal of Hydraulic Research*, 56(2), 256-267. DOI:10.1080/00221686.2017.1289256.

MATAIX-SOLERA, J. and DOERR, S.H. (2004). Hydrophobicity and aggregate stability in calcareous topsoils from fire-affected pine forests in southeastern Spain. *Geoderma*, 118(1-2), 77-88. DOI:10.1016/S0016-7061(03)00185-X.

MATSUSHI, Y., HATTANJI, T. and MATSUKURA, Y. (2006). Mechanisms of shallow landslides on soil-mantled hillslopes with permeable and impermeable bedrocks in the Boso Peninsula, Japan. *Geomorphology*, 76 (1-2), 92-108. DOI:10.1016/j.geomorph.2005.10.003.

MAURICE, L., ATKINSON, T.C., WILLIAMS, A.T., BARKER, J.A. and FARRANT, A.R. (2010). Catchment scale tracer testing from karstic features in a porous limestone. *Journal of Hydrology*, 389(1-2), 31-41. DOI:10.1016/j.jhydrol.2010.05.019.

MAYOR, A.G., BAUTISTA, S. and BELLOT, J. (2009). Factors and interactions controlling infiltration, runoff, and soil loss at the microscale in a patchy Mediterranean semiarid landscape. *Earth Surface Processes and Landforms* 34 (12), 1702-1711. DOI:10.1002/esp.1875.

MEJÍAS, M., BALLESTEROS, B.J., ANTÓN-PACHECO, C., DOMÍNGUEZ, J.A., GARCIA-ORELLANA, J., GARCIA-SOLSONA, E.G. and MASQUÉ, P. (2012). Methodological study of submarine groundwater discharge from a karstic aquifer in the Western Mediterranean Sea. *Journal of Hydrology*, 464-465, 27-40. DOI:10.1016/j.jhydrol.2012.06.020.

MERRILL, S.D., HUANG, C., ZOBECK, T.M. and TANAKA, D.L. (2001). Use of the chain set for scale-sensitive and erosion-relevant measurement of soil surface roughness. In D.E. STOTT, R.H. MOTHAR, and D.C. STEIHARDT (Eds.), *Sustaining the Global Farm - Selected papers from the 10th International Soil Conservation Organization Meeting.* West Lafayette, IN, USA: USDA. pp. 594-600.

MERRIT, W.S., LETCHER, R.A. and JAKEMAN, A.J. (2003). A review of erosion and sediment transport models. *Environmental Modelling & Software*, 18(8-9), 761-799. DOI:10.1016/S1364-8152(03)00078-1.

MEYER, L.D. (1981). How rain intensity affects interrill erosion. *Transactions of the American Society of Agricultural Engineers*, 24(6), 1472-1475. DOI:10.13031/2013.34475.

MINEO, S. and PAPPALARDO, G. (2019). InfraRed Thermography presented as an innovative and non-destructive solution to quantify rock porosity in laboratory. *International Journal of Rock Mechanics and Mining Sciences*, 115, 99-110. DOI:10.1016/j.ijrmms.2019.01.012.

MIURA, S. HIRAI, K. and YAMADA, T. (2002). Transport rates of surface materials on steep forested slopes induced by raindrop splash erosion. *Journal of Forest Research*, 7(4), 201-211. DOI:10.1007/BF02763133.

MONTENEGRO, A.A.A., ABRANTES, J.R.C.B., DE LIMA, J.L.M.P., SINGH, V.P. and SANTOS, T.E.M. (2013a). Impact of mulching on soil and water dynamics under intermittent simulated rainfall. *CATENA*, 109, 139-149. DOI:10.1016/j.catena.2013.03.018.

MONTENEGRO, A.A.A., DE LIMA, J.L.M.P., ABRANTES, J.R.C.B. and SANTOS, T.E.M. (2013b). Impact of mulching on soil and water conservation in semiarid catchment: simulated rainfall in the field and in the laboratory. *Die Bodenkultur: Journal of Land Management, Food and Environment*, 64(3-4), 79-85. Retrieved from https://boku.ac.at/en/fos/themen/die-bodenkultur/inhalte/band-64-2013/band-64-heft-3-4/montenegro#c89101.

MONTGOMERY, D.R. (2007). *Dirt: The Erosion of Civilizations*. Berkeley, CA, USA: University of California Press. 296 pp.

MORGAN, R.P.C., QUINTON, J.N., SMITH, R.E., GOVERS, G., POESEN, J.W.A., AUERSWALD, K., CHISCI, G., TORRI, D. and STYCZEN, M.E. (1998). The European Soil Ersoion Model (EUROSEM): a dynamic approach for predicting sediment transport from fields and small catchments. *Earth Surfaces Processes and Landforms*, 23, 527-544. DOI:10.1002/(SICI)1096-9837(199806)23:6<527::AID-ESP868>3.0.CO;2-5.

MÜGLER, C., PLANCHON, O., PATIN, J., WEILL, S., SILVERA, N., RICHARD, P. and MOUCHEA, E. (2011). Comparison of roughness models to simulate overland flow and tracer transport experiments under simulated rainfall at plot scale. *Journal of Hydrology*, 402(1-2), 25-40. DOI:10.1016/j.jhydrol.2011.02.032.

MUJTABA, B. and DE LIMA, J.L.M.P. (2018). Laboratory testing of a new thermal tracer for infrared-based PTV technique for shallow overland flows. *CATENA*, 169, 69-79. DOI:10.1016/j.catena.2018.05.030.

MUSTE, M., YU, K., PRATT, T. and ABRAHAM, D. (2004a). Practical aspects of ADCP data use for quantification of mean river flow characteristics; part II: fixed-vessel measurements. *Flow Measurement and Instrumentation*, 15(1), 17-28. DOI:10.1016/j.flowmeasinst.2003.09.002.

MUSTE, M., YU, K., PRATT, T. and SPASOJEVIC, M. (2004b). Practical aspects of ADCP data use for quantification of mean river flow characteristics; part I: moving-vessel measurements. *Flow Measurement and Instrumentation*, 15(1), 1-16. DOI:10.1016/j.flowmeasinst.2003.09.001.

NASH, J.E. and SUTCLIFFE, J.V. (1970). River flow forecasting through conceptual models part I: a discussion of principles. *Journal of Hydrology*, 10(3), 282-290. DOI:10.1016/0022-1694(70)90255-6.

NEARING, M.A. (1998). Why soil erosion models over-predict small soil losses and under-predict large soil losses. *CATENA*, 32(1), 15-22. DOI:10.1016/S0341-8162(97)00052-0.

NEARING, M.A. (2000). Evaluating soil erosion models using measured plot data: accounting for variability in the data. *Earth Surface Processes and Landforms*, 25, 1035-1043. DOI:10.1002/1096-9837(200008)25:9<1035::AID-ESP121>3.0.CO;2-B.

NEARING, M.A. FOSTER, G.R., LANE, L.J. and FINKNER, S.C. (1989). A process-based soil erosion model for USDA - Water Erosion Prediction Project technology. *Transactions of the American Society of Agricultural Engineers*, 32(5), 1587-1593. DOI:10.13031/2013.31195.

NEZLOBIN, D., RUBIN, H., LAVEE, H., SARAH, P. and SACHS, E. (2013). Runoff initiation from raindrops falling onto planar inclined surface. *Experimental Thermal and Fluid Science*, 46, 8-19. DOI:10.1016/j.expthermflusci.2012.11.004.

NIAZI, A., BENTLEY, L.R. and HAYASHI, M. (2017). Estimation of spatial distribution of groundwater recharge from stream baseflow and groundwater chloride. *Journal of Hydrology*, 546, 380-392. DOI:10.1016/j.jhydrol.2017.01.032.

O'SHAUGHNESSY, S.A., EVETT, S.R., COLAIZZI, P.D. and HOWELL, T.A. (2011). Using radiation thermography and thermometry to evaluate crop water stress in soybean and cotton. *Agricultural Water Management*, 98(10), 1523-1535. DOI:10.1016/j.agwat.2011.05.005.

OELZE, L., SABATIER, J.M. and RASPET, R. (2003). Roughness measurements of soil surfaces by acoustic backscatter. *Soil Science Society of America Journal*, 67(1), 241-250. DOI:10.2136/sssaj2003.2410.

OWOR, M., TAYLOR, R.G., TINDIMUGAYA, C. and MWESIGWA, D. (2009). Rainfall intensity and groundwater recharge: empirical evidence from the Upper Nile Basin. *Environmental Research Letters*, 4(3), 035009. DOI:10.1088/1748-9326/4/3/035009.

PADILLA, C., ONDA, Y., IIDA, T., TAKAHASHI, S. and UCHIDA, T. (2014). Characterization of the groundwater response to rainfall on a hillslope with fractured bedrock by creep deformation and its implication for the generation of deep-seated landslides on Mt. Wanitsuka, Kyushu Island. *Geomorphology*, 204, 444-458. DOI:10.1016/j.geomorph.2013.08.024.

PANAGOS, P. and KATSOYIANNIS, A. (2019). Soil erosion modelling: The new challenges as the result of policy developments in Europe. *Environmental Research*, 172, 470-474. DOI:10.1016/j.envres.2019.02.043.

PAQUET, E., GARAVAGLIA, F., GARÇON, R. and GAILHARD, J. (2013). The SCHADEX method: a semi-continuous rainfall–runoff simulation for extreme flood estimation. *Journal of Hydrology*, 495, 23-27. DOI:10.1016/j.jhydrol.2013.04.045.

PARSONS, A.J. (2019). How reliable are our methods for estimating soil erosion by water? *Science of the Total Environment*, 676, 215-221. DOI:10.1016/j.scitotenv.2019.04.307.

PARSONS, A.J. and STONE, P.M. (2006). Effects of intra-storm variations in rainfall intensity on interrill runoff and erosion. *CATENA*, 67(1), 68-78. DOI:10.1016/j.catena.2006.03.002.

PARSONS A.J. and WAINWRIGHT, J. (2006). Depth distribution of interrill overland flow and the formation of rills. *Hydological Processes*, 20(7), 1511-1523. DOI:10.1002/hyp.5941.

PASCHALIS, A., FATICHI, S., MOLNAR, P., RIMKUS, S. and BURLANDO, P. (2014). On the effects of small scale space–time variability of rainfall on basin flood response. *Journal of Hydrology*, 514, 313-327. DOI:10.1016/j.jhydrol.2014.04.014.

PAZ-FERREIRO, J., BERTOL, I. and VIDAL VÁZQUEZ, E. (2008). Quantification of tillage, plant cover, and cumulative rainfall effects on soil surface microrelief by statistical, geostatistical and fractal indices. *Nonlinear Processes in Geophysics*, 15(4), 575-590. DOI:10.5194/npg-15-575-2008.

PEARSON, J.E. and MARTIN, G.E. (1957). *An Evaluation of Raindrop Sizing and Counting Techniques. Scientific Report No. 1*. Urbana, IL, USA: Illinois State Water Survey and University of Illinois. 116 pp.

PÉREZ-LATORRE, F.J., DE CASTRO, L. and DELGADO, A. (2010). A comparison of two variable intensity rainfall simulators for runoff studies. *Soil & Tillage Research*, 107(1), 11-16. DOI:10.1016/j.still.2009.12.009.

PERRET, J., PRASHER, S.O., KANTZAS, A. and LANGFORD, C. (1999). Three-dimensional quantification of macropore networks in undisturbed soil cores. *Soil Science Society of America Journal*, 63, 1530-1543. DOI:10.2136/sssaj1999.6361530x.

PEUGEOT, C., ESTEVES, M., GALLE, S., RAJOT, J.L. and VANDERVAERE, J.P. (1997). Runoff generation processes: results and analysis of field data collected at the East Central Supersite of the HAPEX-Sahel experiment. *Journal of Hydrology* 188-189, 179-202. DOI:10.1016/S0022-1694(96)03159-9.

PFISTER, L., MCDONNELL, J.J., HISSLER, C. and HOFFMAN, L. (2010). Ground-based thermal imagery as a simple, practical tool for mapping saturated area connectivity and dynamics. Hydrological Processes, 24(21), 3123-3132. DOI:10.1002/hyp.7840.

PLANCHON, O., ESTEVES, M., SILVERA, N. and LAPETITE, J.M. (2001). Microrelief induced by tillage: measurement and modelling of Surface Storage Capacity. *CATENA*, 46(2-3), 141-157. DOI:10.1016/S0341-8162(01)00163-1.

PLANCHON, O., SILVERA, N., GIMENEZ, R., FAVIS-MORTLOCK, D., WAINWRIGHT, J., LE BISSONNAIS, Y. and GOVERS, G. (2005). An automated salt-tracing gauge for flow-velocity measurement. Earth Surface Processes and Landforms, 30(7), 833-844. DOI:10.1002/esp.1194.

POESEN, J., DE LUNA, E., FRANCA, A., NACHTERGAELE, J. and GOVERS, G. (1999). Concentrated flow erosion rates as affected by rock fragment cover and initial soil moisture content. *CATENA*, 36(4), 315-329. DOI:10.1016/S0341-8162(99)00044-2.

POESEN, J., NACHTERGAELE, J., VERSTRAETEN, G. and VALENTIN, C. (2003). Gully erosion and environmental change: importance and research needs. *CATENA*, 50(2-4), 91-113. DOI:10.1016/S0341-8162(02)00143-1.

POHL, C. and VAN GENDEREN, J.L. (1998). Review article Multisensor image fusion in remote sensing: concepts, methods and applications. *International Journal of Remote Sensing*, 19(5), 823-854. DOI:10.1080/014311698215748. DOI:10.1080/014311698215748.

PRATS, S.A., ABRANTES, J.R.C.B., COELHO, C.O.A., KEIZER, J.J. and DE LIMA, J.L.M.P. (2018). Comparing topsoil charcoal, ash, and stone cover effects on the postfire hydrologic and erosive response under laboratory conditions. *Land Degradation and Environment*, 29(7), 2102-2111. DOI:10.1002/ldr.2884.

PRATS, S.A., ABRANTES, J.R.C.B., CREMA, I.P., KEIZER, J.J. and DE LIMA, J.L.M.P. (2015). Testing the effectiveness of three forest residue mulch application schemes for reducing postfire runoff and soil erosion using indoor simulated rain. *FLAMMA*, 6(3), 113–116. Retrieved from https://sites.google.com/site/flammafgr/texto/volumen-6-2015/6-3-2015/6-3-3.

PRATS, S.A., ABRANTES, J.R.C.B., CREMA, I.P., KEIZER, J.J. and DE LIMA, J.L.M.P. (2017). Runoff and soil erosion mitigation with sieved forest residue mulch strips under controlled laboratory conditions. *Forest Ecology and Management*, 396, 102–112. http://dx.doi.org/10.1016/j.foreco.2017.04.019.

PRICE, J., ROCHEFORT, L. and QUINTY, F. (1998). Energy and moisture considerations on cutover peatlands: surface microtopography, mulch cover and Sphagnum regeneration. *Ecological Engineering*, 10(4), 293-312. DOI:10.1016/S0925-8574(98)00046-9.

RAHMA, A.E., LEI, T., SHI, X., DONG, Y., ZHOU, S. and ZHAO, J. (2013). Measuring flow velocity under straw mulch using the improved electrolyte tracer method. *Journal of Hydrology*, 495, 121-125. DOI:10.1016/j.jhydrol.2013.04.049.

RAU, G.C., ANDERSEN, M.S. and ACWORTH, R.I. (2012). Experimental investigation of the thermal dispersivity term and its significance in the heat transport equation for flow in sediments. *Water Resources Research*, 48(3), W03511. DOI:10.1029/2011WR011038.

RENARD, K., FOSTER, G.R., WEESIES, G.A., MCCOOL, D.K. and YODER, D.C. (1997). *Predicting Soil Erosion by Water: A Guide to Conservation Planning with the Revised Universal Soil Loss Equation (RUSLE)*. Agricultural Handbook 703. Tucson, AZ, USA: USDA-ARS. 407 pp.

REYNOLDS, W.D. and ELRICK, D.E. (1985). In situ measurement of field-saturated hydraulic conductivity, sorptivity, and the [alpha]-parameter using the Guelph permeameter. *Soil Science*, 140(4), 292-302. Retrieved from https://journals.lww.com/soilsci/Fulltext/1985/10000/IN_SITU_MEASUREMENT_OF_FIELD_SATURATED_HYDRAULIC.8.aspx.

RICCHETTI, E. (2001). Visible-infrared and radar imagery fusion for geological application: a new approach using DEM and sun-illumination model. *International Journal of Remote Sensing*, 22(11), 2219-2230. DOI:10.1080/713860801. DOI:10.1080/713860801.

RICHARDS, L.A. (1931). Capillary conduction of liquids through porous mediums. *Journal of Applied Physics*, 1(5), 318-333. DOI:10.1063/1.1745010.

RIEKE-ZAPP, D.H. and NEARING, M.A. (2005). Digital close range photogrammetry for measurement of soil erosion. *The Photogrammetric Record*, 20(109), 69-87. DOI:10.1111/j.1477-9730.2005.00305.x.

RITSEMA, C.J. and DEKKER, L.W. (1994). How water moves in a water repellent sandy soil: 2. dynamics of fingered flow. Water Resources Research, 30(9), 2519-2531. DOI:10.1029/94WR00750.

ROCKSTRÖM, J., FOLKE, C., GORDON, L., HATIBU, N., JEWITT, G., PENNING DE VRIES, F., RWEHUMBIZA, F., SALLY, H., SAVENIJE, H. and SCHULZE, R. (2004). A watershed approach to upgrade rainfed agriculture in water scarce regions through Water System Innovations: an integrated research initiative on water for food and rural livelihoods in balance with ecosystem functions. *Physics and Chemistry of the Earth*, 29(15-18), 1109-1118. DOI:10.1016/j.pce.2004.09.016.

ROCKSTRÖM, J., KARLBERG, L., WANI, S.P., BARRON, J., HATIBU, N., OWEIS, T., BRUGGEMAN, A., FARAHANI, J. and QIANG, Z. (2010). Managing water in rainfed agriculture: the need for a paradigm shift. *Agricultural Water Management*, 97(4), 543-550. DOI:10.1016/j.agwat.2009.09.009.

RODRÍGUEZ-CABALLERO, E., CANTÓN, Y., CHAMIZO, S., AFANA, A. and SOLÉ-BENET, A. (2012). Effects of biological soil crusts on surface roughness and implications for runoff and erosion. *Geomorphology*, 145-146, 81-89. DOI:10.1016/j.geomorph.2011.12.042.

ROGALSKI, A. (2011). Recent progress in infrared detector technologies. *Infrared Physics & Technology*, 54(3), 136-154. DOI:10.1016/j.infrared.2010.12.003.

RÖMKENS, M.J.M., HELMING, K. and PRASAD, S.N. (2001). Soil erosion under different rainfall intensities, surface roughness, and soil water regimes. *CATENA*, 46(2-3), 103-123. DOI:10.1016/S0341-8162(01)00161-8.

RÖMKENS, M.J.M., PRASAD, S.N. and WHISLER, F.D. (1990). Surface sealing and infiltration. In M.G. ANDERSON and T.P. BURT (Eds.), *Process Studies in Hillslope Hydrology*. Chichester, West Sussex, UK: John Wiley & Sons Ltd. pp. 127-172.

ROUTSCHEK, A. SCHMIDT, J., ENKE, W. and DEUTSCHLAENDER, TH. (2014). Future soil erosion risk: results of GIS-based model simulations for a catchment in Saxony/Germany. *Geomorphology*, 206, 299-306. DOI:10.1016/j.geomorph.2013.09.033.

SAAVEDRA, C. (2005). *Estimating spatial patterns of soil erosion and deposition in the Andean region using geo-information techniques*. Phd Thesis, Wageningen University, Wageningen, The Netherlands, 265 pp.

SANKEY, J.B., EITEL, J.U.H., GLENN, N.F., GERMINO, M.J. and VIERLING, L.A. (2011). Quantifying relationships of burning, roughness, and potential dust emission with laser altimetry of soil surfaces at submeter scales. *Geomorphology*, 135(1-2), 181-190. DOI:10.1016/j.geomorph.2011.08.016.

SANTOS, J.M., VERHEIJEN, F.G.A., WAHREN, F.T., WAHREN, A., FEGER, K.H., BERNARD-JANNIN, L., RIAL-RIVAS, M.E., KEIZER, J.J. and NUNES, J.P. (2013). Soil water repellency dynamics in pine and eucalypt plantations in Portugal: a high resolution time series. *Land Degradation and Development*, 27(5), 1334-1343. DOI:10.1002/ldr.2251.

SANTOS, T.E.M. and MONTENEGRO, A.A.A. (2012). Erosividade e padrões hidrológicos de precipitação no Agreste Central pernambucano. *Revista Brasileira de Engenharia Agrícola e Ambiental*, 16(8), 971-880. DOI:10.1590/S1415-43662012000800009.

SANTOS, T.E.M., SILVA, D.D. and MONTENEGRO, A.A.A. (2010). Temporal variability of soil water content under different surface conditions in the semiarid region of the Pernambuco state. *Revista Brasileira de Ciência do Solo*, 34(5), 1733-1741. DOI:10.1590/S0100-06832010000500025.

SCHAUMANN, G. E., BRAUN, B., KIRCHNER, D., ROTARD, W., SZEWZYK, U. and GROHMANN, E. (2007). Influence of biofilms on the water repellency of urban soil samples. *Hydrological Processes*, 21(17) 2276-2284. DOI:10.1002/hyp.6746 DOI:10.1002/hyp.6746.

SCHUETZ, T. and WEILER, M. (2011). Quantification of localized groundwater inflow into streams using ground-based infrared thermography. *Geophysical Research Letters*, 38(3), L03401. DOI:10.1029/2010GL046198.

SCHUETZ, T., WEILER, M., LANGE, J. and STOELZLE, M. (2012). Two-dimensional assessment of solute transport in shallow waters with thermal imaging and heated water. *Advances in Water Resources*, 43, 67-75. DOI:10.1016/j.advwatres.2012.03.013.

SHAHRAEENI, E. and OR, D. (2010). Thermo-evaporative fluxes from heterogeneous porous surfaces resolved by infrared thermography. *Water Resources Research*, 46(9), W09511. DOI:10.1029/2009WR008455.

SHAHRAEENI, E. and OR, D. (2011). Quantification of subsurface thermal regimes beneath evaporating porous surfaces. *International Journal of Heat and Mass Transfer*, 54(19–20), 4193–4202. DOI:10.1016/j.ijheatmasstransfer.2011.05.024.

SHAKESBY, R.A. (2011). Post-wildfire soil erosion in the Mediterranean: review and future research directions. *Earth-Science Reviews*, 105(3-4), 71-100. DOI:10.1016/j.earscirev.2011.01.001.

SHAKESBY, R.A., COELHO, C.O.A., FERREIRA, A.D., TERRY, J.P. and WALSH, R.P.D. (1993). Wildfire impacts on soil erosion and hydrology in wet Mediterranean forest, Portugal. *International Journal of Wildland Fire*, 3(2), 95-110. DOI:10.1071/WF9930095.

SHARMA, M.L., GANDER, G.A. and HUNT, C.G. (1980). Spatial variability of infiltration in a watershed. *Journal of Hydrology*, 45(1-2), 101-122. DOI:10.1016/0022-1694(80)90008-6.

SHI, X., LEI, T., YAN, Y. and ZHANG, F. (2016). Determination and impact factor analysis of hydrodynamic dispersion coefficient within a gravel layer using an electrolyte tracer method. *International Soil and Water Conservation Research*, 4(2), 87-92. DOI:10.1016/j.iswcr.2016.05.001.

SHI, X., ZHANG, F., LEI, T., CHUO, R., ZHOU, S. and YAN, Y. (2012). Measuring shallow water flow velocity with virtual boundary condition signal in the electrolyte tracer method. *Journal of Hydrology*, 452-453, 172-179. DOI:10.1016/j.jhydrol.2012.05.046.

SILVA, J.R.L., MONTENEGRO, A.A.A. and SANTOS, T.E.M. (2012). Caracterização física e hidráulica de solos em bacias experimentais do semiárido brasileiro, sob manejo conservacionista. *Revista Brasileira de Engenharia Agrícola e Ambiental*, 16(1), 27-36. DOI:10.1590/S1415-43662012000100004.

SILVEIRA, A., ABRANTES, J.R.C.B., DE LIMA, J.L.M.P. and LIRA, L.C. (2016). Modelling runoff on ceramic tile roofs using the kinematic wave equations. *Water Science and Technology*, 73(11), 2824-2831. DOI:10.2166/wst.2016.148.

SIMÕES, N.E. (2006). Modelação bidimensional de escoamentos variáveis em superfície livre: aplicação ao estudo de cheias. MSc thesis. University of Coimbra, Coimbra, Portugal. 123 pp.

ŠIMŮNEK, J. and HOPMANS, J.W. (2002). Parameter optimization and non linear fitting. In J.H. DANE and G.C. TOPP (Eds.), *Methods of Soil Analysis: Part 1 - Physical Methods*. Madison, WI, USA: SSSA. pp. 139-157.

SINGH V.P. (1996). *Kinematic Wave Modelling in Water Resources: Surface-Water Hydrology*. New York, NY, USA: John Wiley & Sons Ltd. 1424 pp.

SINGH, R., SUBRAMANIAN, K. and REFSGAARD, J.C. (1999). Hydrological modelling of a small watershed using MIKE SHE for irrigation planning. *Agricultural Water Management*, 41(3), 149-166. DOI:10.1016/S0378-3774(99)00022-0.

SINGH, V.P. and DE LIMA, J.L.M.P. (2018). One-dimensional linear kinematic wave solution for overland flow under moving storms using the method of characteristics. *Journal of Hydrologic Engineering*, 23(7), 04018029. DOI:10.1061/(ASCE)HE.1943-5584.0001676.

SINGH, V.P. and WOOLHISER, D.A. (1976). Sensitivity of linear and nonlinear surface runoff models to input errors. *Journal of Hydro*logy, 29(3-4), 243-249. DOI:10.1016/0022-1694(76)90039-1.

SINGH, V.P. and WOOLHISER, D.A. (2002). Mathematical modeling of watershed hydrology. *Journal of Hydrologic Engineering*, 7(4), 270-292. DOI:10.1061/(ASCE)1084-0699(2002)7:4(270).

SLAYMAKER, O. (2003). The sediment budget as conceptual framework and management tool. *Hydrobiologia*, 494(1-3), 71-82. DOI:10.1023/A:1025437509525.

SMITH, J.A., BAECK, M.L., MEIERDIERCKS, K.L., MILLER, A.J. and KRAJEWSKI, W.F. (2007). Radar rainfall estimation for flash flood forecasting in small urban watersheds. *Advances in Water Resources*, 30(10), 2087-2097. DOI:10.1016/j.advwatres.2006.09.007.

SMITH, M.B., KOREN, V.I., ZHANG, Z. REED, S.M., PAN, J.J. and MOREDA, F. (2004). Runoff response to spatial variability in precipitation: an analysis of observed data. *Journal of Hydrology*, 298(1-4), 267-286. DOI:10.1016/j.jhydrol.2004.03.039.

SOLÉ-BENET, A., CALVO, A., CERDÀ, A., LÁZARO, R., PINI, R. and BARBERO, J. (1997). Influences of micro-relief patterns and plant cover on runoff related processes in badlands from Tabernas (SE Spain). *CATENA*, 31(1-2), 23-38. DOI:10.1016/S0341-8162(97)00032-5.

SOLIMAN, A.S., RAHMAN, M.E.A. and HECK, R.J. (2010). Comparing time-resolved infrared thermography and X-ray computed tomography in distinguishing soil surface crusts. *Geoderma*, 158(3–4), 101-109. DOI:10.1016/j.geoderma.2010.02.008.

SORACCO, C.G., LOZANO, L.A., BALBUENA, R., RESSIA, J.M. and FILGUEIRA, R.R. (2012). Contribution of macroporosity to water flux of a soil under different tillage systems. *Revista Brasileira de Ciência do Solo*, 36(4), 1149-1156. DOI:10.1590/S0100-06832012000400009.

STOLTE, J. (1997). *Manual for Soil Physical Measurements*. Technical Document No. 37. Wageningen, The Netherlands: DLO-Staring Center. 77 pp.

STONESTROM, D.A. and CONSTANTZ, J. (2003). *Heat as a Tool for Studying the Movement of Ground Water Near Streams*. Circular 1260. Reston, Virginia, USA: U.S. Geological Survey. 105 pp.

STROOSNIJDER, L. (2005). Measurement of erosion: is it possible? *CATENA*, 64, 162-173. DOI:10.1016/j.catena.2005.08.004.

STROOSNIJDER, L. (2012). *Myths in Land Degradation and Development*. Wageningen, The Netherlands: Wageningen University. 36 pp.

SUMN, G. (1988). *Precipitation: Process and Analysis*. Chichester, West Sussex, UK: John Wiley & Sons Ltd. 472 pp.

TACONET, O., BERNARD, R. and VIDAL-MADJAR, D. (1986). Evapotranspiration over an agricultural region using a Surface Flux/Temperature model based on NOAA-AVHRR data. *Journal of Climate and Applied Meteorology*, 25(3), 284–307. DOI:10.1175/1520-0450(1986)025<0284:EOAARU>2.0.CO;2.

TAKKEN, I. and GOVERS, G. (2000). Hydraulics of interrill overland flow on rough, bare soil surfaces. *Earth Surface Processes and Landforms*, 25(13), 1387-1402. DOI:10.1002/1096-9837(200012)25:13<1387::AID-ESP135>3.0.CO;2-D.

TATARD, L., PLANCHON, O., WAINWRIGHT, J., NORD, G, FAVIS-MORTLOCK, D., SILVERA, N., RIBOLZI, O., ESTEVES, M. and HUANG, C.H. (2008). Measurement and modelling of high-resolution flow-velocity data under simulated rainfall on a low-slope sandy soil. *Journal of Hydrology*, 348(1-2), 1-12. DOI:10.1016/j.jhydrol.2007.07.016.

TAURO, F. and GRIMALDI, S. (2017). Ice dices for monitoring stream surface velocity. *Journal of Hydro-environment Research*, 14, 143-149. DOI:10.1016/j.jher.2016.09.001.

TAURO, F., GRIMALDI, S., PETROSELLI, A. and PORFIRI, M. (2012a). Fluorescent particle tracers for surface flow measurements: A proof of concept in a natural stream. *Water Resources Research*, 48(6), W06528. DOI:10.1029/2011WR011610.

TAURO, F., GRIMALDI, S., PETROSELLI, A., RULLI, C. and PORFIRI, M. (2012b). Fluorescent particle tracers in surface hydrology: A proof of concept in a semi-natural hillslope. *Hydrology and Earth System Sciences*, 16(8), 2973-2983. DOI:10.5194/hess-16-2973-2012.

TAURO, F., PAGANO, G., PORFIRI, M. and GRIMALDI, S. (2012c). Tracing of shallow water flows through buoyant fluorescent particles. *Flow Measurement and Instrumentation*, 26, 93-101. DOI:10.1016/j.flowmeasinst.2012.03.007.

TAURO, F., PORFIRI, M. and GRIMALDI, S. (2014). Orienting the camera and firing lasers to enhance large scale particle image velocimetry for streamflow monitoring. *Water Resources Research*, 50(9), 7470-7483. DOI:10.1002/2014WR015952.

TAURO, F., PORFIRI, M. and GRIMALDI, S. (2016). Surface flow measurements from drones. *Journal of Hydrology*, 540, 240-245. DOI:10.1016/j.jhydrol.2016.06.012.

TAURO, F., SELKER, J., VAN DE GIESEN, N., ABRATE, T., UIJLENHOET, R., PORFIRI, M., MANFREDA, S., CAYLOR, K., MORAMARCO, T., BENVENISTE, J., CIRAOLO, G.,

ESTES, L., DOMENEGHETTI, A., PERKS, M.T., CORBARI, C., RABIEI, E., RAVAZZANI, G., BOGENA, H., HARFOUCHE, A., BROCCA, L., MALTESE, A., WICKERT, A., TARPANELLI, A., GOOD, S., ALCALA, J.M.L., PETROSELLI, A., CUDENNEC, C., BLUME, T., HUT, R. and GRIMALDI, S. (2018). Measurements and Observations in the XXI century (MOXXI): innovation and multi-disciplinarity to sense the hydrological cycle. *Hydrological Sciences Journal*, 63(2), 169-196. DOI:10.1080/02626667.2017.1420191.

TAZIOLI, A., (2011). Experimental methods for river discharge measurements: comparison among tracers and current meter. *Hydrological Sciences Journal*, 56(7), 1314-1324. DOI:10.1080/02626667.2011.607822.

TETZLAFF, B., FRIEDRICH, K., VORDERBRÜGGE, T., VEREECKEN, H. and WENDLAND, F. (2013). Distributed modelling of mean annual soil erosion and sediment delivery rates to surface waters. *CATENA*, 102, 13-20. DOI:10.1016/j.catena.2011.08.001.

TETZLAFF, D. and UHLENBROOK, S. (2005). Significance of spatial variability in precipitation for process-oriented modelling: results from two nested catchments using radar and ground station data. *Hydrology and Earth System Sciences*, 9, 29-41. DOI:10.5194/hess-9-29-2005.

TILLMAN, R.W., SCOTTER, D.R., WALLIS, M.G. and CLOTHIER, B.E. (1989). Water repellency and its measurement by using intrinsic sorptivity. *Australian Journal of Soil Research*, 27(4), 637–644. DOI:10.1071/SR9890637.

TONOLLA, D., ACUÑA, V., UEHLINGER, U., FRANK, T. andTOCKNER, K. (2010). Thermal heterogeneity in river floodplains. *Ecosystems*, 13(5), 727-740. DOI:10.1007/s10021-010-9350-5.

TORRI, D., POESEN, J., BORSELLI, L., BRYAN, R. and ROSSI, M. (2012). Spatial variation of bed roughness in eroding rills and gullies. *CATENA*, 90, 76-86. DOI:10.1016/j.catena.2011.10.004.

TOTIN, E., STROOSNIJDER, L. and AGBOSSOU, E. (2013). Mulching upland rice for efficient water management: a collaborative approach in Benin. *Agricultural Water Management*, 125, 71-80. DOI:10.1016/j.agwat.2013.04.012.

TRUMAN, C.C., STRICKLAND, T.C., POTTER, T.L., FRANKLIN, D.H., BOSCH, D.D. and BEDNARZ, C.W. (2007). Variable rainfall intensity and tillage effects on runoff, sediment and carbon losses from a loamy sand under simulated rainfall. *Journal of Environmental Quality*, 36(5), 1495-1502. DOI:10.2134/jeq2006.0018.

TURNER, R., PANCIERA, R., TANASE, M.A., LOWELL, K., HACKER, J.M. and WALKER, J.P. (2014). Estimation of soil surface roughness of agricultural soils using airborne LiDAR. *Remote Sensing of Environment*, 140, 107-117. DOI:10.1016/j.rse.2013.08.030.

URBANEK, E., HALLETT, P., FEENEY, D. and HORN, R. (2007). Water repellency and distribution of hydrophilic and hydrophobic compounds in soil aggregates from different tillage systems. *Geoderma*, 140(1-2), 147-155. DOI:10.1016/j.geoderma.2007.04.001.

URRESTARAZU, M. (2013). Infrared thermography used to diagnose the effects of salinity in a soilless culture. *Quantitative InfraRed Thermography* Journal, 10(1), 1-8. DOI:10.1080/17686733.2013.763471.

USDA (1993). *Soil Survey Manual*. USDA-SCS Handbook 18. Washington, DC, USA: U.S. Government Publishing Office. 639 pp.

USDA (2004). *National Engineering Handbook, Section 4. Hydrology, Chapter 10. Estimation of Direct Runoff from Storm Rainfall*. Washington, DC, USA: U.S. Government Publishing Office. 79 pp.

VAN DER HEIJDEN, G., LEGOUT, A., POLLIER, B., BRÉCHET, C., RANGER, J. and DAMBRINE, E. (2013). Tracing and modeling preferential flow in a forest soil: potential impact on nutrient leaching. *Geoderma* 195-196, 12-22. DOI:10.1016/j.geoderma.2012.11.004.

VAN LEEUWEN, C.C.E., CAMMERAAT, E.L.H., DE VENTE, J. and BOIX-FAYOS, C. (2019). The evolution of soil conservation policies targeting land abandonment and soil erosion in Spain: A review. *Land Use Policy*, 83, 174-186. DOI:10.1016/j.landusepol.2019.01.018.

VAN LOON, E.E. (2001). *Overland flow: interacting models with measurements*. PhD Thesis, Wageningen University, Wageningen, The Netherlands, 185 pp.

VAN'TWOUDT, B.D. (1959). Particle coatings affecting the wettability of soils. *Journal of Geophysical Research*, 64(2), 263-267. DOI:10.1029/JZ064i002p00263.

VANDENBOHEDE, A., LOUWYCK, A. and LEBBE, L. (2009). Conservative solute versus heat transport in porous media during push-pull tests. *Transport in Porous Media*, 76(2), 265-287. DOI:10.1007/s11242-008-9246-4.

VENNARD, J.K. and STREET, R.L. (1975). *Elementary Fluid Mechanics*. New York, NY, USA: Wiley. 350 pp.

VERBIST, K., CORNELIS, W.M., SCHIETTECATTE, W., OLTENFREITER, G., VAN MEIRVENNE, M. and GABRIELS, D. (2007). The influence of a compacted plow sole on saturation excess runoff. *Soil & Tillage Research*, 96(1-2), 292-302. DOI:10.1016/j.still.2007.07.002.

VEREECKEN, H., KASTEEL, R., VANDERBORGHT, J. and HARTER, T. (2007). Upscaling hydraulic properties and soil water flow processes in heterogeneous soils: a review. *Vadose Zone Journal*, 6(1), 1-28. DOI:10.2136/vzj2006.0055.

VIDAL VÁZQUEZ, E., VIVAS MIRANDA, J.G. and PAZ GONZÁLEZ, A. (2005). Characterizing anisotropy and heterogeneity of soil surface microtopography using fractal models. *Ecological Modelling*, 182(3-4), 337-353. DOI:10.1016/j.ecolmodel.2004.04.012.

VIEIRA, D.C.S., PRATS, S.A., NUNES, J.P., SHAKESBY, R.A., COELHO, C.O.A. and KEIZER, J.J. (2014). Modelling runoff and erosion, and their mitigation, in burned Portuguese forest using the revised Morgan-Morgan-Finney model. *Forest Ecology and Management*, 314, 150-165. DOI:10.1016/j.foreco.2013.12.006.

VILLHOLTH, K.G., JENSEN, K.H. and FREDERICIA, J. (1998). Flow and transport processes in a macroporous subsurface-drained glacial till soil I: field investigations. *Journal of Hydrology*, 207(1-2), 98-120. DOI:10.1016/S0022-1694(98)00129-2.

WANG, J., FU, B.J., QIU, Y., CHEN, L.D. and WANG, Z. (2001). Geostatistical analysis of soil moisture variability on Da Nangou catchments of the loess plateau, China. *Environmental Geology*, 41(1-2), 113-116. DOI:10.1007/s002540100350.

WARNER, W.S. (1995). Mapping a three-dimensional soil surface with hand-held 35 mm photography. *Soil & Tillage Research*, 34(3), 187-197. DOI:10.1016/0167-1987(95)00462-2.

WIJEWARDANA, N.S., MÜLLER, K., MOLDRUP, P., CLOTHIER, B., KOMATSU, T., HIRADATE, S., DE JONGE, L.W. and KAWAMOTO, K., (2016). Soil-water repellency characteristic curves for soil profiles with organic carbon gradients. *Geoderma*, 264, 150-159. DOI:10.1016/j.geoderma.2015.10.020.

WILSON, G.V., JARDINE, P.M., LUXMORE, R.J., ZELAZNY, L.W., LIETZKE, D.A. and TODD, D.E. (1991). Hydrogeochemistry processes controlling subsurface transport from an upper subcatchment of Walker Branch watershed during storm events. 1. Hydrologic transport processes. *Journal of Hydrology*, 123(3-4), 297-316. DOI:10.1016/0022-1694(91)90096-Z.

WIRTZ, S., SEEGER, M. and RIES, J.B. (2012). Field experiments for understanding and quantification of rill erosion process. *CATENA*, 91, 21-34. DOI:10.1016/j.catena.2010.12.002.

WISCHMEIER, W.H. and SMITH, D.D. (1978). *Predicting rainfall erosion losses: a guide to conservation planning*. Agricultural Handbook No. 537. Washington, DC, USA: USDA, 58 pp.

WMO (2012). *International Glossary of Hydrology*. Geneva, Switzerland: WMO. 473 pp.

WOOLHISER, D.A., SMITH, R.E., GOODRICH, D.C., 1990. *KINEROS, A kinematic runoff and erosion model: Documentation and user manual*. ARS-77. West Lafayette, IN, USA: USDA. 130 pp.

WU, J., ZHANG, R. and YANG, J. (1996). Analysis of rainfall-recharge relationships. *Journal of Hydrology*, 177(1-2), 143-160. DOI:10.1016/0022-1694(95)02935-4.

XU, X., KIELY, G. and LEWIS, C. (2009). Estimation and analysis of soil hydraulic properties through infiltration experiments: comparison of BEST and DL fitting methods. *Soil Use and Management*, 25(4), 354-361. DOI:10.1111/j.1475-2743.2009.00218.x.

YAN, L.J. YU, X.X., LEI. T.W., ZHANG, Q.W. and QU, L.Q. (2008). Effects of transport capacity and erodibility on rill erosion processes: a model study using the Finite Element method. *Geoderma*, 146(1-2), 114-120. DOI:10.1016/j.geoderma.2008.05.009.

ZHANG, G.H., LIU, Y., HAN, Y. and ZHANG, X.C. (2009). Sediment transport and soil detachment on steep slopes: I. Transport Capacity estimation. *Soil Science Society of America Journal*, 73(4), 1291-1297. DOI:10.2136/sssaj2008.0145.

ZHANG, G.H., LUO, R.T., CAO, Y., SHEN, R.C. and ZHANG, X.C. (2010). Correction factor to dye-measured flow velocity under varying water and sediment discharges. *Journal of Hydrology*, 389(1-2), 205-213. DOI:10.1016/j.jhydrol.2010.05.050.

ZHANG, W. and CUNDY, T.W. (1989). Modelling of two dimensional overland flow. *Water Resources Research*, 25(9), 2019-2035. DOI:10.1029/WR025i009p02019.

ZHUANG, X., WANG, W., MA, Y., HUANG, X. and LEI, T. (2018). Spatial distribution of sheet flow velocity along slope under simulated rainfall conditions. *Geoderma*, 321, 1-7. DOI:10.1016/j.geoderma.2018.01.036.

ZOBECK, T.M. and ONSTAD, C.A. (1987). Tillage and rainfall effects on random roughness: a review. *Soil & Tillage Research*, 9(1), 1-20. DOI:10.1016/0167-1987(87)90047-X.

ZRIBI, M., GORRAB, A. and BAGHADADI, N. (2014). A new soil roughness parameter for the modelling of radar backscattering over bare soil. *Remote Sensing of Environment*, 152, 62-73. DOI:10.1016/j.rse.2014.05.009.

APPENDIX A

This appendix presents a list of publications authored and co-authored by the author of this Thesis, published and submitted to national and international journals, conferences and meetings, that emerged from the research presented in this Thesis. This list does not include the articles included in Chapters 3 to 11 of this Thesis (see section 1.4), nor other publications listed in the Curriculum Vitae of the author.

Articles in journals

- ABRANTES, J.R.C.B. and DE LIMA, J.L.M.P. (2014). Termografia para determinação da microtopografia da superfície do solo em diferentes condições de cobertura morta. *Revista Brasileira de Ciências Agrárias*, 9(3), 445-453. DOI:10.5039/agraria.v9i3a3602.
- DE LIMA, J.L.M.P., SILVA JR., V.P., ABRANTES, J.R.C.B., MONTENEGRO, A.A.A. and DE LIMA, M.I.P. (2014). In situ observation of soil macropores using infrared thermography. *Die Bodenkultur: Journal of Land Management, Food and Environment*, 65(3-4), 57-62. Retrieved from https://boku.ac.at/en/fos/themen/die-bodenkultur/inhalte/band-65-2014/band-65-heft-3-4/de-lima-silva.
- DE LIMA, R.L.P., ABRANTES, J.R.C.B., DE LIMA, J.L.M.P. and DE LIMA, M.I.P. (2015). Using thermal tracers to estimate flow velocities of shallow flows: laboratory and field experiments. *Journal of Hydrology and Hydromechanics*, 63(3), 259-266. DOI:10.1515/johh-2015-0028.
- DE LIMA, J.L.M.P., SILVA JR., V.P., DE LIMA, M.P.I., ABRANTES, J.R.C.B. and MONTENEGRO, A.A.A. (2015). Revisiting simple methods to estimate drop size distributions: a novel approach based on infrared thermography. *Journal of Hydrology and Hydromechanics*, 63(3), 224-231. DOI:10.1515/johh-2015-0025.
- DA SILVA, J.R.L., SILVA JR., V.P., DE LIMA, J.L.M.P., MONTENEGRO, A.A.A. and ABRANTES, J.R.C.B. Exploratory in situ study on the effect of vegetal mulching impact on soil surface temperature in semiarid Brazil. Submitted to *Die Bodenkultur* in January 2019. Under Review.
- SILVA JR., V.P., MONTENEGRO, A.A.A., DA SILVA, J.R.L., DE LIMA, J.L.M.P. and ABRANTES, J.R.C.B. Estimating soil moisture and hydraulic conductivity of two soils in the Brazilian semiarid using infrared thermography. Submitted to *Quantitative InfraRed Thermography Journal* in January 2019. Under review.

Articles in conferences and meetings

- DE LIMA, J.L.M.P. and ABRANTES, J.R.C.B. (2013). The use of infrared thermography to estimate soil surface microrelief. In *Proceedings of 8th Simpósio de Meteorologia e Geofísica da APMG and 14th Encontro Luso-Espanhol de Meteorologia*. 18-20 March 2013, Ericeira, Portugal. 6 pp. Oral presentation by J.L.M.P. de Lima.
- ABRANTES, J.R.C.B. and DE LIMA, J.L.M.P. (2014). Utilização de termografia para a estimativa de velocidades e profundidades de escoamentos superficiais pouco profundos e

caracterização do microrelevo. In *Proceedings of 12º Congresso da Água, 16º Encontro de Engenharia Sanitária e Ambiental (ENaSB) and XVI Simpósio Luso-Brasileiro de Engenharia Sanitária e Ambiental (SILUBESA)*. 5-7 March 2014, Lisboa, Portugal. 11 pp. Oral presentation by J.R.C.B. Abrantes.

- DE LIMA, J.L.M.P., ABRANTES, J.R.C.B., SILVA JR., V.P., DE LIMA, M.I.P. and MONTENEGRO, A.A.A. (2014). Mapeamento de macroporos superficiais utilizando termografia por infravermelhos. In *Proceedings of UMS 2014 - VI Congresso sobre o Uso e Manejo do Solo*. 19-21 March 2014, Recife, PE, Brazil. 4 pp. Oral presentation by J.L.M.P. de Lima.
- DE LIMA, J.L.M.P. and ABRANTES, J.R.C.B. (2014). Use of thermal tracers to characterize overland flow velocities. In *Proceedings of 3rd IAHR Europe Congress*. 14-16 April 2014, Porto, Portugal. 7 pp. Oral presentation by J.R.C.B. Abrantes.
- SILVA JR., V.P., DE LIMA, J.L.M.P., DE LIMA, M.I.P., MONTENEGRO, A.A.A. and ABRANTES, J.R.C.B. (2014). Caracterização da distribuição do diâmetro de gotas da chuva: Utilização de termografia por infravermelhos. In *Proceedings of XII Simpósio de Recursos Hídricos do Nordeste*. 4-7 November 2014, Natal, RN, Brazil. 10 pp. Oral presentation by J.L.M.P. de Lima.
- DE LIMA, J.L.M.P., ABRANTES, J.R.C.B., SILVA JR., V.P.,MONTENEGRO, A.A.A. and DE LIMA, M.I.P. (2015). Validação de uma nova tecnologia termográfica para a monitorização da superfície do solo. In *Proceedings of 12º Simpósio de Hidráulica e Recursos Hídricos dos Países de Língua Portuguesa (SILUSBA) and XXI Simpósio Brasileiro de Recursos Hídricos*. 22-27 November 2015, Brasília, DF, Brazil. 10 pp. Oral presentation by A.A.A. Montenegro.
- MONTENEGRO, A.A.A., DOS SANTOS, T.E.M., DE LIMA, J.L.M.P., SILVA, D.D. ABRANTES, J.R.C.B. and BORGES, T.K.S. 2016. Desempenho de cobertura morta no controle de processos hidrológicos, de aquecimento do solo e no incremento da produção agrícola. In *Proceedings of XIII Simpósio de Recursos Hídricos do Nordeste*. 8-11 November 2016, Aracaju, SE, Brazil. 10 pp. Oral presentation by A.A.A. Montenegro.
- DE LIMA, J.L.M.P., ABRANTES, J.R.C.B., ISIDORO, J.M.G.P. and DE LIMA, M.I.P. (2019). Avaliação de características da superfície do solo usando termografia por infravermelhos. In *Proceedings of 30º Congresso ABES*. 16-19 June 2019, Natal, RN, Brazil. 5 pp. Oral presentation by J.M.G.P. Isidoro.

Abstracts in conferences and meetings

- DE LIMA, J.L.M.P. and ABRANTES, J.R.C.B. (2013). A thermographic technique to characterize soil surface microrelief: application at the laboratory scale. In *Book of Abstracts of EGU General Assembly 2013*. EGU2013-6455. 7-12 April 2013, Vienna, Austria. Oral presentation by J.L.M.P. de Lima.
- ABRANTES, J.R.C.B. and DE LIMA, J.L.M.P. (2013). Aplicação de termografia como instrumento de apoio à gestão de ecossistemas: estimativa de velocidades do escoamento e caracterização da microtopografia da superfície do solo. In *Book of Abstracts of VIII Congresso Ibérico de Gestão e Planeamento da Água*. 5-7 December 2013, Lisboa, Portugal. Poster presentation by J.R.C.B. Abrantes.
- ABRANTES, J.R.C.B., DE LIMA, J.L.M.P., SILVA JR., V.P. and MONTENEGRO, A.A.A. (2014). Mapping soil permeability using infrared thermography. In *Book of Abstracts of 15th Biennial Conference ERB 2014*. 9-13 September 2014, Coimbra, Portugal. Poster presentation by J.R.C.B. Abrantes.
- DE LIMA, J.L.M.P, ABRANTES, J.R.C.B., SILVA JR., V.P., DE LIMA, M.I.P. and MONTENEGRO, A.A.A. (2014). Locating soil macropores with thermography. In *Book of*

Abstracts of 15th Biennial Conference ERB 2014. 9-13 September 2014, Coimbra, Portugal. Oral presentation by J.R.C.B. Abrantes.

- ABRANTES, J.R.C.B., DE LIMA, J.L.M.P., PRATS, S.A. and KEIZER, J.J. (2016). Caracterização da variabilidade espacial da hidrofobicidade do solo: Utilização de termografia por infravermelhos. In *Book of Abstracts of UMS 2016 - VII Congresso sobre o Uso e Manejo do Solo*. 13-15 June 2016, Coimbra, Portugal. Poster presentation by J.R.C.B. Abrantes.
- DE LIMA, J.L.M.P., ABRANTES, J.R.C.B., SILVA JR., V.P., MONTENEGRO, A.A.A., DE LIMA, M.I.P., GONÇALVES, J.M., PRATS, S.A. and KEIZER, J.J. (2016). Monitorização da superfície do solo usando termografia por infravermelhos. In *Book of Abstracts of UMS 2016 - VII Congresso sobre o Uso e Manejo do Solo*. 13-15 June 2016, Coimbra, Portugal. Oral presentation by J.L.M.P. de Lima.
- DE LIMA, J.L.M.P., ABRANTES, J.R.C.B., PRATS, S.A. and KEIZER, J.J. (2016). Assessing soil water repellency spatial variability using infrared thermographic. In *Book of Abstracts of 16th Biennial Conference ERB 2016*. 5-8 September 2016, Bucharest, Romania. Oral presentation by J.L.M.P. de Lima.
- ABRANTES, J.R.C.B., DE LIMA, J.L.M.P., PRATS, S.A., LIRA, L.M.C. and KEIZER, J.J. (2016). Using infrared thermography to assess soil water repellency: laboratory and field tests. In *Book of Abstracts of Reunión Internacional Fuegored 2016*. 23-26 November 2016, Aveiro, Portugal. Poster presentation by S.A. Prats.
- DE LIMA, J.L.M.P., ABRANTES, J.R.C.B., MUJTABA, B., SILVA JR., V.P., DE LIMA, R.L.P., SANTOS, L.I.V., NAGEL, G.W., VARGA, M., MONTENEGRO, A.A.A., DE LIMA, M.I.P., GONÇALVES, J.M., PRATS, S.A., KEIZER, J.J., ISIDORO, J.M.P.G. and SILVEIRA, A. (2017). Using thermal infrared imagery for quantifying soil surface processes. In *Book of Abstracts of ERB 2017 Steering Committee Meeting*. 1 September 2017, Sopron, Hungary. Oral presentation by J.L.M.P. de Lima.
- ABRANTES, J.R.C.B., DE LIMA, J.L.M.P., MORUZZI, R.B. and SILVEIRA, A. (2017). Comparing thermal, salt and dye tracers to estimate shallow flow velocities. In *Book of Abstracts of EcoHCC'17 - 4th International Conference on Ecohydrology, Soil and Climate Change*. 21-23 September 2017, Figueira da Foz, Portugal. Oral presentation by J.R.C.B. Abrantes.
- ABRANTES, J.R.C.B., DE LIMA, J.L.M.P., PRATS, S.A., KEIZER, J.J., DE LIMA, M.I.P. and MONTENEGRO, A.A.A. (2017). Using infrared thermography to assess soil water repellency: Laboratory and field applications. In *Book of Abstracts of IAHS Measurements and observations in the XXI Century (MOXXI) and WMO Hydro-Hub Joint Meeting 2017*. 4-5 December 2017, Geneva, Switzerland. Oral presentation by J.R.C.B. Abrantes.
- ABRANTES, J.R.C.B., DE LIMA, J.L.M.P., MORUZZI, R.B., SILVEIRA, A. and A.A.A. MONTENEGRO. (2018). Traçadores térmicos na deteção de velocidade de escoamentos superficiais pouco profundos. In *Book of Abstracts of UMS 2018 - VIII Congreso sobre o Uso e Manejo do Solo*. 25-27 June 2018, A Coruña, Spain. Poster presentation by J.R.C.B. Abrantes.
- ABRANTES, J.R.C.B. and DE LIMA, J.L.M.P. (2018). Detecting the movement of very shallow surface flows by means of thermal tracers: results from laboratory to field tests. In *Book of Abstracts of 17th Biennial Conference ERB 2018*, 11-14 September 2018, Darmstadt, Germany. Oral presentation by J.R.C.B. Abrantes.